Atmospheric Escape in Exoplanets: a Journey From Gas Giants to Earth Twins

Dos Santos, Leonardo

UNIVERSITÉ DE GENÈVE
Département d'Astronomie

FACULTÉ DES SCIENCES
Professeur David Ehrenreich
Professeur Vincent Bourrier

Atmospheric Escape In Exoplanets: A Journey From Gas Giants To Earth Twins

THÈSE

présentée à la Faculté des Sciences de l'Université de Genève
pour obtenir le grade de Docteur des sciences,
mention Astronomie et Astrophysique

par

Leonardo Augusto Gonçalves DOS SANTOS

de

Itajubá (Brésil)

Thèse N^{o} 5590

GENÈVE
Observatoire Astronomique de l'Université de Genève
2021

UNIVERSITÉ DE GENÈVE

FACULTÉ DES SCIENCES

DOCTORAT ÈS SCIENCES, MENTION ASTRONOMIE ET ASTROPHYSIQUE

Thèse de Monsieur Leonardo Augusto GONÇALVES DOS SANTOS

intitulée :

«Atmospheric Escape In Exoplanets: A Journey From Gas Giants To Earth Twins»

La Faculté des sciences, sur le préavis de Monsieur D. EHRENREICH, professeur associé et directeur de thèse (Département d'astronomie), Monsieur V. BOURRIER, professeur assistant et codirecteur de thèse (Département d'astronomie), Madame A. VERHAMME, professeure assistante (Département d'astronomie), Madame A. DE ALMEIDA VIDOTTO, professeure (School of Physics, Trinity College Dublin and Leiden Observatory, Leiden University, Leiden, The Netherlands), Monsieur D. K. SING, professeur (Henry Rowland Department of Physics and Astronomy, The Johns Hopkins University, Baltimore, USA), autorise l'impression de la présente thèse, sans exprimer d'opinion sur les propositions qui y sont énoncées.

Genève, le 14 septembre 2021

Thèse - 5590 -

Le Doyen

N.B. - La thèse doit porter la déclaration précédente et remplir les conditions énumérées dans les "Informations relatives aux thèses de doctorat à l'Université de Genève".

“ *Ano passado eu morri, mas esse ano eu não morro.* ”

Belchior

I dedicate this thesis to my brothers Julio and Marco, to my mother Benedita,
and to the memory of my father Eric, whose unending support was vital
to the success of my scientific endeavor.

Acknowledgements

There have been too many people and institutions that made their mark in the last four years of my scientific endeavor. In particular, I would like to thank David Ehrenreich and Vincent Bourrier for their mentoring, sharing of knowledge, and for giving me a fair chance when most were not willing to. To all my colleagues and friends at the Observatory of Geneva: Heather Cegla, Emily Rickman, Helen Giles, Louise Nielsen, Karina Rojas, Manu Stalport, Nicolas Unger, Omar Attia, Elisabeth Matthews, a big thank you for every beer, every dinner, every beach hangout, every barbecue, every moment that we shared; and especially to Julia Seidel for putting up with my shenanigans, but I know I have been the best office mate ever.

Furthermore, I would like to acknowledge: Munazza Alam, for the companionship and the times we chatted and commiserated during graduate school, as well as for our successful collaborations. Raphaëlle Haywood for being incredibly welcoming and inclusive, and for fostering interesting science and social discussions. My previous supervisors Jorge Meléndez and Hektor Monteiro for being overall great supporters, for inspiring me to reach beyond what I thought I was capable of. Jarita Holbrook for her unyielding leadership in making academia a more just workplace, and her mentoring in my times of greatest need. Mercedes López-Morales for being an incredible role model and collaborator. Aline Vidotto for her patience when I reached out to her with a river of questions, which ended in a very fruitful discussion and collaboration. Chani Nava, for the spontaneous friendship and our adventures in Iceland. Kevin France, Allison Youngblood, Jacob Bean, Andreas Seifahrt, and David Sing for being excellent hosts when I was visiting.

More than seven billion people inhabit this little mote of cosmic dust we know as the Earth, of which 59% are unable to meet their most basic of human needs – food, health, shelter, and education. Our world is ravaged by extreme poverty, greed, violence, and uncertainty. And yet, somewhere in ourselves we have found an unstoppable drive to look to the sky and wonder. It is, thus, truly an enormous privilege to be an astronomer. I am very grateful for the opportunities I was given and confidence deposited in me in the last nine years since I decided that studying the universe should be my occupation. I owe so much to my people, that I do not think I will ever be able to return the favor. But I vow to do whatever rests in my power to leave this world a little bit more peaceful than I found it.

Abstract

Most planets are surrounded by a layer of material in gas phase with varying levels of physical and chemical properties. The planetary upper atmosphere invariably extend to space with decreasing levels of density and increasing gas particle velocities the higher we are in altitude. Some of these particles are so fast that they can unbind from the gravitational pull of the planet, and eventually escape it. Although seemingly mundane in our lives, this process of evaporation is precisely what transformed Mars from a world covered by rivers and oceans into a desolate, uninhabitable planet. More than 4000 exoplanets have been discovered to date, and most of them orbit closer to their host star than Mercury orbits the Sun. Their extreme environments drive atmospheric escape rates high enough to strip them of a large fraction of their primordial envelopes, and we have the tools to observe this process happening. In this manuscript, I will describe in detail the state-of-the-art hypothesis and theories to explain atmospheric escape in exoplanets, as well as the leading-edge techniques to observe it. We shall embark on a journey from gas giants to Earth twins, in which we search for the faintest signatures of their evolution imprinted in their thin, upper atmospheres. To this end, we employ transmission spectroscopy, a technique that consists in measuring the light of their host stars filtered through the thin gaseous limbs of a transiting exoplanet, and inferring the properties of their atmospheres. Our observations are carried out in ultraviolet wavelengths using the *Hubble Space Telescope* and in infrared using ground-based telescopes. Leveraging what we learned in this journey, we shall also explore the possibility of probing the presence of water and habitability of Earth-like exoplanets using the future *LUVOIR* mission.

Resumé

La plupart des planètes sont entourées d'une couche de matière en phase gazeuse présentant une myriade de propriétés physiques et chimiques différentes : l'atmosphère. La haute atmosphère planétaire s'étend invariablement vers l'espace, sa densité décroissants et la vitesse de ses particules gazeuses crossant au fur et à mesure que l'on s'élève en altitude. Certaines de ces particules sont si rapides qu'elles peuvent se libérer de l'attraction gravitationnelle de la planète, et à terme s'évader. Même si cela pourrait nous paraître quelque peu prosaïque, ce processus d'évaporation est précisément ce qui a transformé Mars d'un monde couvert de rivières et d'océans en une planète désolée et inhabitable. Plus de 4 000 exoplanètes ont été découvertes à ce jour, et la plupart d'entre elles orbitent plus près de leur étoile hôte que Mercure ne tourne autour du Soleil. Leurs environnements extrêmes entraînent des taux d'échappement atmosphérique suffisamment élevés pour les dépouiller d'une grande partie de leurs enveloppes primordiales, et nous disposons des outils nécessaires pour observer ce mécanisme. Dans ce manuscrit, je décrirai en détail les hypothèses et les théories les plus récentes pour expliquer l'échappement atmosphérique des exoplanètes, ainsi que les techniques de pointe pour l'observer. Nous embarquerons dans un voyage, des géantes gazeuses aux jumelles de la Terre, au cours duquel nous partirons à la recherche des plus faibles signatures de leur évolution au sein de leurs minces hautes atmosphères. À cette fin, nous employons la spectroscopie de transmission, une technique qui consiste à mesurer la lumière de leurs étoiles hôtes filtrée à travers les fines couches gazeuses des exoplanètes en transit, pour en déduire les propriétés de leurs atmosphères. Nos observations sont réalisées dans les longueurs d'onde ultraviolettes en utilisant le *Hubble Space Telescope*, ainsi que dans l'infrarouge en utilisant des télescopes au sol. Tirant parti de ce que nous avons appris au cours de ce voyage, nous explorerons également la possibilité de sonder la présence d'eau et étudier l'habitabilité d'exoplanètes semblables à la Terre en utilisant la future mission *LUVOIR*.

Table of contents

Chapter 1

Atmospheres of distant worlds

> “ *Can you hear me, Major Tom?* ”
>
> *David Bowie*

To say that the discovery of the first extra-solar planet around a solar-type star in 1995 by Mayor and Queloz [128] was revolutionary is an understatement. The finding of the Jupiter-mass planet 51 Peg b through the radial velocities (RV) method [see, e.g., 133] ushered the development of a whole new sub-field of astrophysics known as Exoplanetary Science. As of the writing of this manuscript, this new research area produced more than 7.5k refereed publications and almost 240k citations, as tracked by the Astrophysics Data System[1]. The feat of discovery notwithstanding, what struck the scientific community at the time as odd was that this planet orbited too close to its host star, 51 Peg, when compared to the planets in the Solar System: at a separation of staggering 0.05 au, which is almost 8 times closer than Mercury is to the Sun. However, the skepticism against 51 Peg b started to crumble away when, by mid-1996, the roster of known exoplanets had already grown to 10 [156]. All of these were massive, Jupiter-sized planets orbiting very close to their host stars, so the community aptly named them *hot Jupiters*.

But how hot can these planets actually be? One estimate we can quickly draw is the equilibrium temperature $T_{\rm eq}$, which is a theoretical temperature at which the planet irradiates all the energy it receives from its host star assuming the planet is a black body. This estimate is independent from the presence of an atmosphere, and can be calculated as:

$$T_{\rm eq} = T_{\rm eff,*}\,(1-a)^{1/4}\sqrt{\frac{R_*}{2D}}, \tag{1.1}$$

[1] Available at https://ui.adsabs.harvard.edu.

where $T_{\mathrm{eff},*}$ is the effective temperature of the host star, a is the planetary albedo, R_* is the host star radius, and D is the distance from the host star. For 51 Peg b, eq. 1.1 yields an equilibrium temperature of 1935 K if we assume an albedo of zero. As of today, the hottest known exoplanet is KELT-9 b, with an equilibrium temperature of $\sim$4000 K [71], which would mean this planet is as hot as a K-type star on its day side. On the other hand, there are also several discovered exoplanets with equilibrium temperatures as mild as the Earth, such as K2-18 b with 284 K [154]. We can also use the properties of the host star to calculate the bolometric incident flux S_{inc} at the location of the planet with the following equation:

$$\frac{S_{\mathrm{inc}}}{S_\oplus} = \left(\frac{T_{\mathrm{eff},*}}{5778\ K}\right)^4 \left(\frac{R_*}{R_\oplus}\right)^2 \left(\frac{a}{1\ \mathrm{au}}\right)^{-2}, \tag{1.2}$$

where a is the semi-major axis of the planetary orbit. S_{inc} is given in units of bolometric incident flux at the Earth ($S_\oplus$).

With the exception of hot Jupiters, which are rare, planets that orbit close to their host stars, although very different from our Solar System, are actually very common [e.g., 89]. One of the reasons most of our discoveries are of short-period planets owes to the fact that they are easier to detect than longer-period ones. Since they have short orbital periods, they produce stronger signals in radial velocities; and since they transit more frequently [190], it is easier to find them when we serendipitously survey the sky. With more than 4000 exoplanets discovered to date (Fig. 1.1), there are many open questions that the scientific community wants to answer: How do their atmospheres look like? Are these planetary configurations stable through astronomical timescales? How are they formed? How do they evolve? And ultimately: can they sustain life?

1.1 The structure of hot gas giant atmospheres

Objects like stars and planets exist because the internal, outward pressure balances out the gravitational force pulling material inward. This phenomenon is called hydrostatic equilibrium, and it implies that pressure is always decreasing in the direction outward from the center of the object. At a certain point, the density of material encircling the object of interest becomes low enough that photons emerge from it unhindered, and can potentially reach our telescopes on Earth. This interface between our object of interest and space is an atmosphere. Astronomy has a long history of simultaneously modeling stars and planets and observing their atmospheres in a virtuous circle of experimentation, aimed at understanding the structure and evolution of celestial bodies.

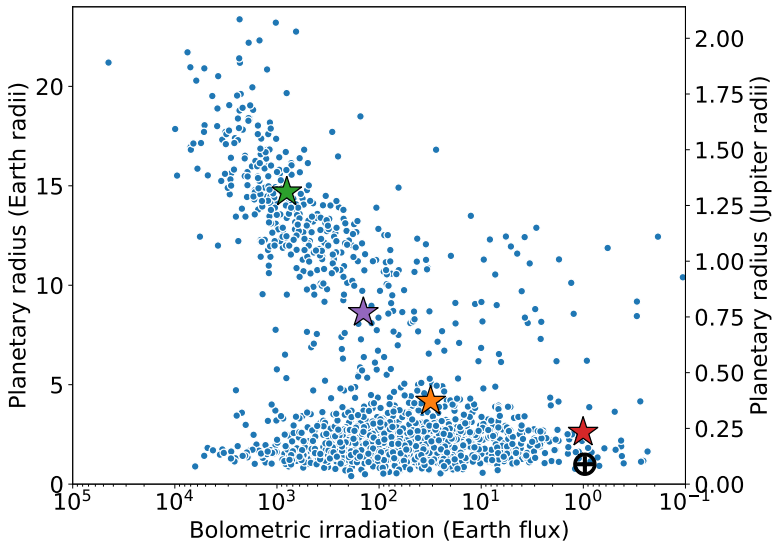

Fig. 1.1 Population of exoplanets with known radius and bolometric irradiation (taken from the NASA Exoplanets Archive on 01 Feb 2021). The star symbols represent the planets that will be discussed in this manuscript: WASP-127 b (green), WASP-29 b (purple), GJ 436 b (orange), and K2-18 b (red); the Earth is represented with the $\oplus$ symbol.

Following the seminal discovery of 51 Peg b, the first attempt at modeling an irradiated extrasolar giant planet (EGP) was done by Guillot et al. [77]. Using techniques very similar to those applied in modeling the evolution of brown dwarfs [22] and longer-period EGPs [155], the objectives of Guillot et al. were: i) to investigate the relation between the luminosity and temperature of irradiated EGPs, and ii) to assess if these worlds can survive against the intense mass loss driven by stellar irradiation. Among their findings, the authors conclude that not only can irradiated EGPs survive evaporation, but signals of their evolution would be imprinted in their spectra. Later, Seager and Sasselov [158] would reach a similar conclusion and predict that the external irradiation produces measurable changes in the emerging planetary spectrum when compared to an isolated brown dwarf.

Despite being hot, short-period EGPs are sufficiently cool that chemistry plays an important role in determining the composition and structure of their photosphere. Furthermore, a relatively deep radiative zone emerges due to external irradiation from their host stars [77]. In such case, atmospheric heating is not efficiently redistributed by convective motion, but is instead distributed by zonal winds from the day side to the night side [23].

The outermost layers of a planetary atmosphere above tens or hundreds of km see a sharp increase in temperature (see Fig. 1.2) at the thermosphere due to the absorption of high-energy (wavelengths shorter than ultraviolet) photons. This region is also known as the

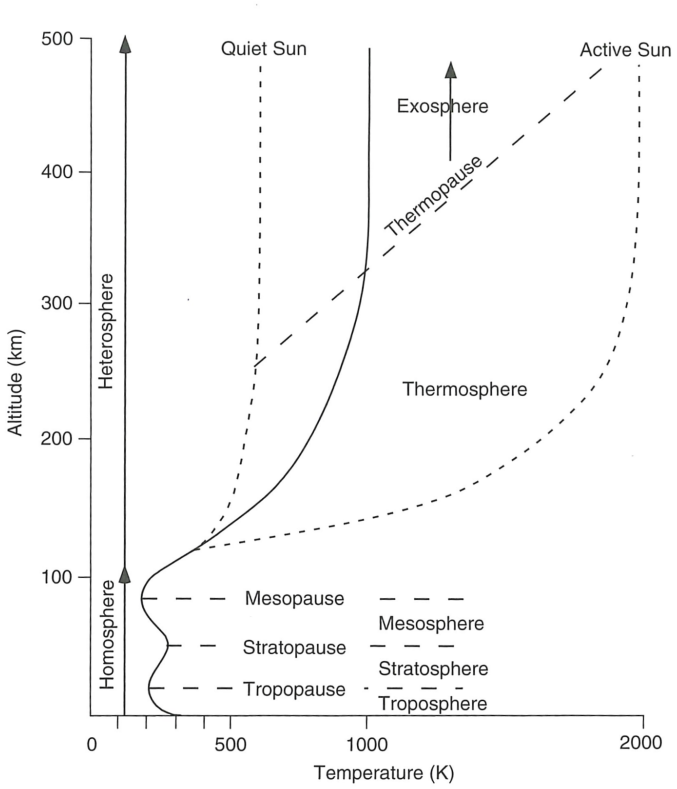

Fig. 1.2 Temperature profile of the Earth's atmosphere and its nomenclature. Adapted from Catling and Kasting [29]. Despite being at a different regime of physical properties, the overall behavior and nomenclature also apply for EGPs.

upper atmosphere. Hot gas giants like HD 209458 b orbit so close to their host stars, that they receive enough irradiation that their upper atmospheres exhibit an expanding outward wind that reach supersonic velocities (we discuss this phenomenon in more detail in Sect. 1.2). The densities and wind velocities in the upper atmosphere depend mainly on the composition and the temperature of the gas, the planetary mass and the atmospheric mass loss rate. One useful, simplified way to understand the structure of this upper atmosphere is by using an isothermal Parker wind model driven by gas pressure [146]. This model was originally designed to explain the solar wind, but it has been adapted to describe winds in EGPs as well. In this model, a steady-state, spherically-symmetric wind follows the equation of mass conservation:

$$\dot{M} = 4\pi r^2 \rho(r) v(r), \tag{1.3}$$

where $\dot{M}$ is the mass loss rate, r is the radial distance (altitude), ρ is the gas density, and v is the wind velocity. This model also follows the momentum equation:

$$v\frac{dv}{dr}+\frac{1}{\rho}\frac{dp}{dr}+\frac{GM_{\rm pl}}{r^2}=0, \tag{1.4}$$

where G is the gravitational constant, p is the thermal pressure and $M_{\rm pl}$ is the planetary mass. The isothermal Parker wind model assumes that the sound speed $v_{\rm s}$ is constant in the upper atmosphere, allowing for a significant simplification of the problem:

$$v_{\rm s}=\sqrt{\frac{kT_0}{\mu}}, \tag{1.5}$$

where T_0 is the gas temperature (assumed to be constant) and μ is the mean molecular weight. For EGPs, whose outflows are mostly made of atomic and ionized H, typical values of μ are near 1.0 in unit of proton mass. It is convenient to normalize the radii, velocities and densities to, respectively, the radius at the sonic point[2] ($r_{\rm s}$), speed of sound, and density at the sonic point ($\rho_{\rm s}$). The resulting equations describing the radial profiles of velocity and density are:

$$\tilde{v}(r)\exp\left[\frac{-\tilde{v}(r)^2}{2}\right]=\left(\frac{1}{\tilde{r}}\right)^2\exp\left[-\frac{2}{\tilde{r}}+\frac{3}{2}\right]\text{ and} \tag{1.6}$$

$$\tilde{\rho}(r)=\exp\left[\frac{2}{\tilde{r}}-\frac{3}{2}-\frac{\tilde{v}^2}{2}\right], \tag{1.7}$$

where $\tilde{r}$, $\tilde{v}$, and $\tilde{\rho}$ are the normalized radius, velocity, and density, respectively. Eq. 1.6 has many solutions, but we are only interested in the solution that represents an escaping atmosphere, i.e., the one with velocities increasing asymptotically with radius. As an example, I calculated the structure of the upper atmosphere of the hot Jupiter HD 209458 b assuming an escape rate of 8×10^8 g s^{-1} and a temperature of 9000 K [152], and the resulting structure for the upper atmosphere is shown in Fig. 1.3.

1.2 Atmospheric escape and evolution

Classically, the term *atmospheric escape* has loosely been used to refer to planetary outflows at the layers where the atmosphere becomes so thin that the particles can move unhindered by collisions [140]. This terminology seems to have been coined by Spitzer [171]. But the first physical description of "atmospheres evaporating into space" using kinetic theory dates back to an abstract presented in 1846 by Waterston [187] and published much later in 1892 by Waterston and Rayleigh [188]. The description of flows in and above the upper

[2]The sonic point is defined as the point where the velocity of the outflow becomes supersonic.

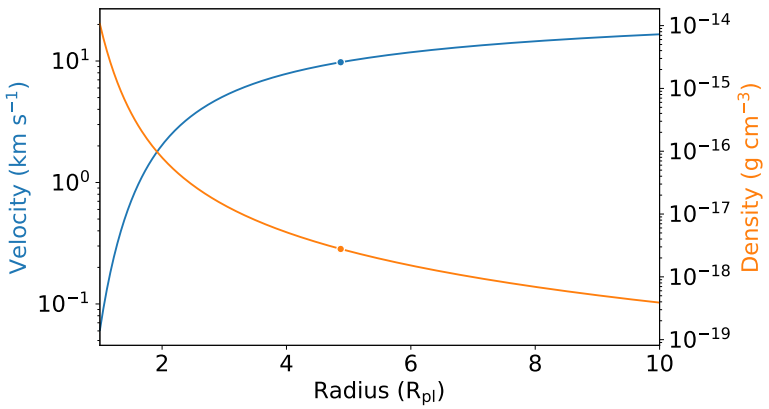

Fig. 1.3 Structure of the upper atmosphere of HD 209458 b. The circles mark the speed of sound and density at the sonic point.

atmosphere is called planetary aeronomy. Although the first studies of atmospheric escape focused on the theoretical implications of kinetic theory, evidence started to emerge showing that this process could indeed yield observable signatures in the planets of the Solar System. For example, the excess of helium (He) over hydrogen (H) in the atmospheres of the outer planets [140] is one of the motivators to explore atmospheric escape and evolution. Changes in the geochemistry of the Earth and Mars, at astronomical time scales, has been presented as evidence for atmospheric evolution in rocky planets [e.g., 150].

In planets outside the Solar System, the discovery of a large H cloud around the hot Jupiter HD 209458 b [182] quickly followed the discovery of sodium (Na) in its atmosphere [33], both observed with the *Hubble Space Telescope* (*HST*)[3]. Using the transmission spectroscopy technique (see Section 1.3), Vidal-Madjar et al. [182] observed that the stellar Lyman-α emission decreases by approximately 15% during the transit of HD 209458 b, in staggering contrast with the 1.5% transit depth seen in optical wavelengths [56]. Such a large additional transit absorption can only be caused by an extended cloud of neutral H around the planet, which would cover much more of the stellar light than the opaque disk of the planet. Since atomic H cannot be sustained for a long time around a planet without eventually being ionized or swept away by radiation pressure, there has to be a source of H that feeds the cloud around the planet with a constant stream of neutral atoms; or, in other words, the planet must be losing large amounts of H to space. In fact, Bourrier and Lecavelier des Etangs [18] concluded that the planet loses mass in a total rate of 10^9 to 10^{11} g s^{-1}, which is equivalent to shedding approximately one Deimos (the Martian satellite) per year.

[3]The detection of Na has since been challenged by high-resolution, ground-based observations reported by Casasayas-Barris et al. [28], which claim that it was a false positive caused by the Rossiter-McLaughlin effect.

In the following material of Section 1.2 we shall briefly overview the main processes of atmospheric escape for planets exposed to stellar wind and radiation. We refer the reader to the excellent review of Gronoff et al. [74] for a detailed description on these various processes, as well as their implications for both exoplanets and the Solar System planets. We show a schematic image depicting the many atmospheric escape processes in Fig. 1.7.

1.2.1 Temperature-driven, thermal escape

One of the earliest descriptions of upper atmospheric escape was presented by Jeans [93], which assumed an isothermal atmosphere in hydrostatic equilibrium. Such a model assumes that the velocities of particles in the upper atmosphere follow a Maxwell-Boltzmann distribution [127], and applies kinetic theory to describe the process. In this scenario, any particles that possess enough potential energy to escape the gravitational well of the planet are effectively lost to infinity (see Eq. 1.8) [171]. However, such a model is only applicable when the kinetic flow is unhindered by collisions. Thus, it is convenient to establish a layer above which the collisions are less likely to happen than a flow free of particle impacts. This limit is called the *exobase*, and is defined as the radius above which the mean free path of gas particles l is equal to scale height H of the atmosphere. The atmospheric layer above the exobase is called the *exosphere*. The layer below the exobase is known as the *thermosphere*, and it plays an important role in escape because that is where the processes of atmospheric heating and cooling happen [75].

As explained by Chamberlain [32], in reality atmospheres cannot be completely hydrostatic in their nature in order to guarantee that the atmosphere has a finite mass. There must be an atmospheric expansion, even if just slightly. The larger this velocity of expansion, the more the flow departs from a hydrostatic description. Thus, in practice, we establish two regimes for atmospheric escape: i) Jeans regime, where hydrostatic equilibrium is sufficiently accurate to describe escape, and ii) hydrodynamic regime, in which there is a supersonic or near transonic bulk motion of gas through the upper atmosphere.

Jeans escape

It is useful to define the escape parameter as:

$$\lambda_{\mathrm{J}} \equiv \frac{GM_{\mathrm{pl}}m}{kT_{\mathrm{J}}r_{\mathrm{J}}}, \tag{1.8}$$

where m is the atomic mass of the gas particle, T_{J} and r_{J} are, respectively, the temperature and radius at the exobase. If the gas particles have relatively small thermal energy compared to the gravitational potential, then $\lambda_{\mathrm{J}} \gtrsim 1$, and we have escape in Jeans regime. In the Earth,

if we assume a thermospheric temperature of 1000 K, we obtain $\lambda_J \sim 1-10$, squarely inside the Jeans regime. The Earth's exosphere is mostly made of H [174, see Fig. 1.4], which escapes from the upper atmosphere through the photodissociation of water vapor molecules.

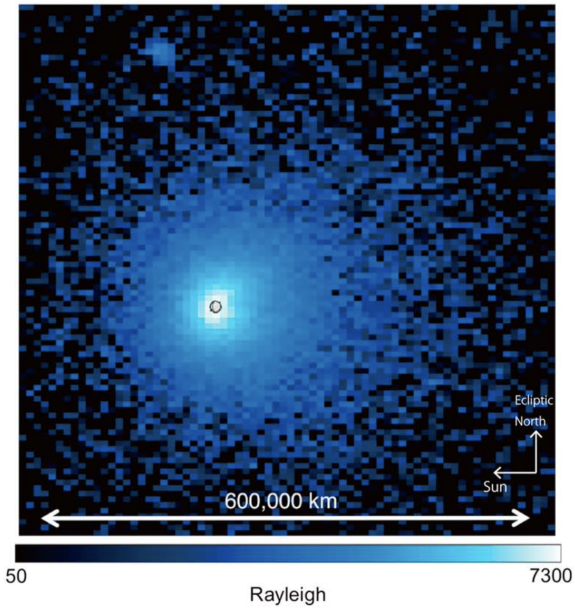

Fig. 1.4 Direct image of the Earth's exosphere. The extended cloud of gas scatters solar Lyman-α photons, which were detected by the LAICA instrument aboard the Procyon satellite at a distance of 0.1 au from the Earth [adapted from 97].

In kinetic theory, a parcel of gas just below the exobase will have particles whose velocities follow a Maxwellian distribution in which their most probable speed is $U = \sqrt{2kT_J/m}$. It is possible to rewrite Eq. 1.8 in terms of velocities:

$$\lambda_J = \frac{v_{esc}^2}{U^2}, \tag{1.9}$$

where $v_{esc} = \sqrt{2GM/r_J}$ is the escape velocity at the exobase. Assuming an exobase altitude of 500 km for the Earth, the escape velocity at that location is 40 km s^{-1}. In the Jeans regime, most particles that reach the exobase with a speed above v_{esc} will find themselves unhindered by collisions against other particles, and will effectively leave the planet. On the Earth, the Jeans escape rate of H is 6×10^{26} atoms s^{-1}, or approximately 1×10^3 g s^{-1} [174]. On Mars, this rate is approximately one third of that observed on the Earth [91], and on Venus it is eight orders of magnitude lower [107].

Hydrodynamic escape

Gross [75] argued that, in their youth, the thermospheres of terrestrial planets in the Solar System were rich in hydrogen (mixing ratios exceeding a few percent), and that consequently hydrodynamic escape dominated their early atmospheric evolution. Gross' insight was that, in these cases, the exospheric temperatures would be so high ($T_J > 10\,000$ K), that a selective escape of gases would be impossible, and instead they would have a bulk motion of gas in the upper atmosphere, or a so-called planetary wind. Since the escape is not selective in such a case, not only lighter species such as H and He will escape to the exosphere at a large rate, but also heavy metals such as O, Mg, Si, and Fe – this point will be important when I discuss observational techniques in Section 1.3.

The physical description of a hydrodynamically expanding wind can become encumbering, so I refer the reader to the seminal work of Watson et al. [189] for the first simplified formulation of hydrodynamic escape in planets with H-He dominated atmospheres. This so called *energy-limited formalism* has a semi-arbitrary limit of validity in which the high-energy-photons deposition radius must not be causally connected to the exosphere. In other words, the formulation of Watson et al. [189] applies when the exobase is located above the sonic point. More recently, García Muñoz [67] pointed out that planetary winds from hot exoplanets may not necessarily be transonic, since stellar wind can confine the planetary outflow to a so called subsonic breeze. In extreme cases, such as those of close-in hot Jupiters, the exobase can be located beyond the Roche lobe, leading to copious escape rates in a process known as "geometric blow-off" [113].

Based on the solar wind model of Parker [146], Murray-Clay et al. [134] presented a simplified one-dimensional hydrodynamic escape model for hot Jupiters. This treatment starts from the three basic equations of mass continuity, momentum and energy conservation. The latter includes heating by photoionization, cooling due to work done by the expanding gas, and cooling from radiation and conduction. In the case of hot Jupiter orbiting a solar-type star, Murray-Clay et al. [134] conclude that as much as 83% of heating goes into work to expand the upper atmosphere, implying that the mass loss rate is energy limited (this is not the case for planets with extremely high levels of ionizing irradiation). Accordingly, the energy-limited mass loss rate is given by:

$$\dot{M}_{\rm e-lim} \sim 6 \times 10^9 \text{ g s}^{-1} \left(\frac{\varepsilon}{0.3}\right) \left(\frac{R_p}{10^{10} \text{ cm}}\right)^3 \left(\frac{0.7 M_J}{M_p}\right) \left(\frac{F_{\rm EUV}}{450 \text{ erg s}^{-1} \text{ cm}^{-2}}\right), \quad (1.10)$$

where ε is the fraction of photon energy deposited as heat (analogous to the efficiency factor used in other formulations; see, e.g., [152, 55]) and $F_{\rm EUV}$ is incoming flux of EUV (extreme

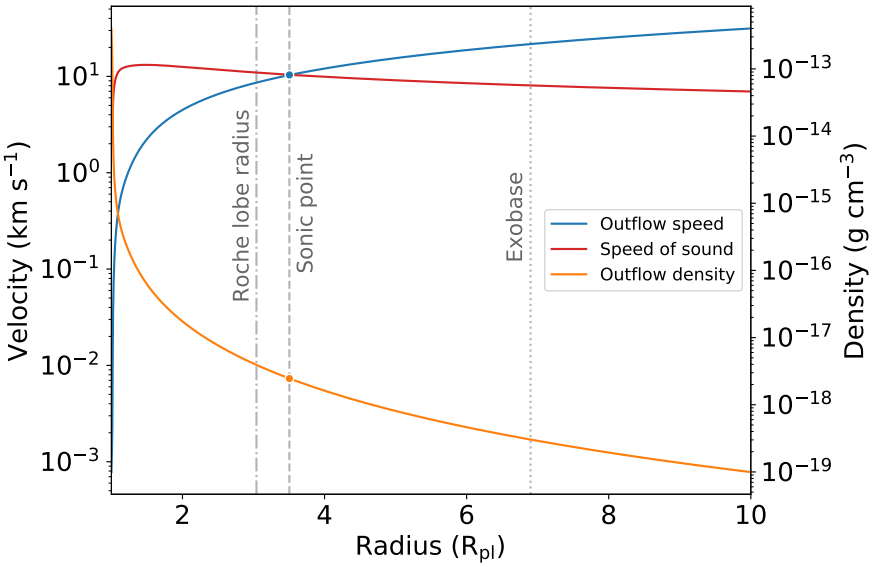

Fig. 1.5 One-dimensional structure of the upper atmosphere of the hot Jupiter HD 209458 b using a self-consistent hydrodynamic escape model similar to that of Murray-Clay et al. [134] and Allan and Vidotto [3]. The results of the model were provided as courtesy of A. Vidotto.

ultraviolet) irradiation. For HD 209458 b, it yields a maximum mass loss rate of $\sim 10^{10}$ g s^{-1}. Erkaev et al. [55] presented a hydrodynamic model for this planet that takes into account the effect of the Roche lobe in escape and is also widely used by the community [e.g., 104, 137]. The advantage of the model of Salz et al. [152] is that it maintains the formulation analogous to the energy-limited case, even when the regime is not energy limited. The aforementioned forward modelling approaches yield mass loss rates consistent with that inferred by Bourrier and Lecavelier des Etangs [18] using a data-driven particle model. The energy-limited formulation for evaporation, however, yield inaccurate mass loss for rates for extremely irradiated and low-density planets, as well as those with hydrostatic exospheres; for such cases, Kubyshkina et al. [103] presented an updated description called the "hydro-based approximation" that results in more accurate escape rates.

As we shall see in Section 1.3.1, such a high escape rate for HD 209458 b has the potential to produce deep absorption signals in transmission spectroscopy, in particular in the core of the H I Lyman-α line at 1215.6702 Å. The problem is that the core of the line is mostly absorbed by the interstellar medium (ISM), which is rich in H I, so only the wings of the Lyman-α line are observable for stars that are not the Sun. The hydrodynamical model of Murray-Clay et al. [134] predicts an absorption of approximately 5% in the wings of the Lyman-α line, which is inconsistent with the 15% absorption first reported by Vidal-Madjar

et al. [182] and later by Ehrenreich et al. [54]. As we will see in Section 1.2.2, other non-thermal mechanisms, such as radiation pressure, interactions with the stellar wind and charge exchange, can accelerate H I particles to higher velocities [18] and thus explain the signature observed by HD 209458 b and other planets [20, 185].

1.2.2 Non-thermal processes

Some processes of atmospheric escape are not directly due to the thermal motion of gas particles. They are usually related to chemical reactions, particle impacts, interactions with the stellar wind or a gravitational potential, and ion flows through magnetic fields. For planets that already lost their primary atmosphere, some of these processes contribute to a significant fraction of their mass loss rate.

Roche lobe overflow

When planets orbit extremely close to their host star, part of their atmosphere may also escape due to the stellar gravitational potential. In such a configuration, the gas passes through the inner Lagrangian point of the system, is accelerated to a few hundred km s^{-1} (subsonic), and forms an accretion disk. Lai et al. [106] discusses the application of a formalism to describe Roche lobe overflow in the WASP-12 system, and suggests that the accretion stream formed between and planet and star can produce an earlier transit signature [see also 13, 176]. Li et al. [116] further predicted that, due to intense tidal forces, the surface of WASP-12 b is distorted into an oblate shape, and that it loses its atmosphere at a rate of 10^{-7} M_{Jup} yr^{-1}, or 6×10^{15} g s^{-1} (see Fig. 1.6).

Photochemical loss

Some exothermic chemical reactions in the upper atmosphere can provide enough kinetic energy to atoms that they escape the planet at high velocities. These particles are also known as energetic neutral atoms, or ENAs. The most relevant reactions are:

1. Ion recombination: It can lead to the escape of heavy atoms from rocky planets, such as N and O in Mars and the Earth [e.g., 163, 197].

2. Photodissociation: Caused by impacts of photons, electrons, and protons, which has been proposed to explain the hot oxygen geocorona [161].

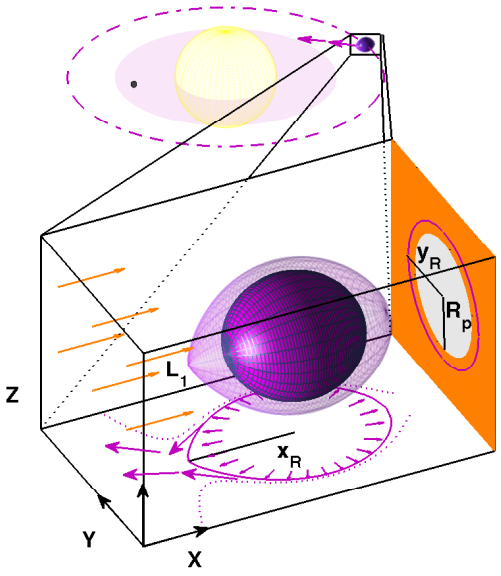

Fig. 1.6 Model of the oblate envelope and atmospheric escape of WASP-12 b (purple surface). Adapted from Li et al. [116]. Stellar photons are represented by the orange arrows, L_1 is the inner Lagrangian point of the system, and the flow of escaping material is shown as purple arrows. The black dot is a hypothetical inner planet suggested by Li et al. [116].

Charge exchange

Charge exchange contribute to atmospheric escape in planets in two different ways. In the first, also know as charge exchange in trapped particles, fast energetic ions trapped in the magnetic field of a planet may exchange charges with slow neutrals in the environment, creating ENAs. Since they are now neutral, these fast particles are able to escape the magnetic field. This process is ubiquitous in the magnetized planets of the Solar System [e.g., 163]. The second avenue consists on interactions between atmospheric or exospheric neutrals with the stellar wind, which is rich in fast energetic ions. These ions then become ENAs by exchanging charges, and access the thermosphere, where it increases the heating, thereby contributing to atmospheric escape [35]. Holmström et al. [87] has further suggested that some of these newly-produced ENAs originating from charge exchange contribute to the in-transit absorption seen in the hot Jupiter HD 209458 b, but this conclusion has been a matter of intense debate since then [e.g., 88, 112, 134, 18, 42].

Impacts

When energetic particles or large bodies collide with the atmosphere or the surface of a planet, the exchange of kinetic energy may knock off planetary particles, which in turn

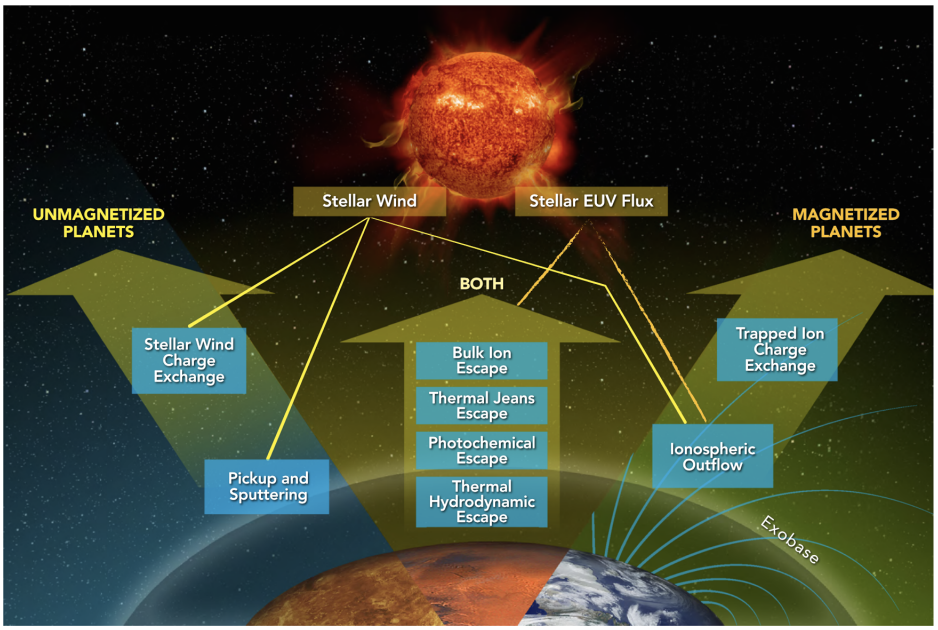

Fig. 1.7 Summary of the various processes of atmospheric escape in planets exposed to high-energy irradiation and stellar wind. Adapted from Gronoff et al. [74].

are susceptible to escape the planet. When the collision is between an incoming ion and a planetary particle, this process is known as sputtering [e.g., 81, 92]. Impacts of larger bodies, such as collisions with planetesimals, can knock off planetary particles and even induce hydrodynamic escape loss via deposition of thermal energy [157].

Ion outflow

For magnetized planets, the heating of electrons and ions can result in their escape through open magnetic field lines, where they join the stellar wind flow. If these particles follow closed field lines, they will be trapped in the magnetosphere. This process is also known as polar wind or polar escape in the literature. In the Earth, polar escape accounts for approximately 10% of H escape in the form of ions [79], and Garcia-Sage et al. [70] have suggested that ion loss may be a threat to the survival of atmospheres of Earth-like planets orbiting M dwarfs in their habitability zone.

Ion pickup

When neutral atoms in non-magnetized planets are ionized by stellar UV irradiation, charge exchange, or electron impact, they can be picked by stellar wind and achieve high velocities, effectively escaping the planet [e.g., 38].

1.3 Spectroscopic techniques to measure atmospheric escape in exoplanets

The first observation of an exoplanetary atmosphere was reported in Charbonneau et al. [33], with the detection of Na in the hot Jupiter HD 209458 b, a signal that had previously been predicted by Seager and Sasselov [159]. The technique utilized by the authors is called transmission spectroscopy. In summary, this technique searches for changes in the host star spectrum during the planetary transit that could be attributed to absorption by the thin, transparent lower-atmosphere present at the limbs of the planet. Put simply, the transmission spectrum Φ is given by:

$$\Phi(\lambda) = 1 - \frac{F_{\rm in}(\lambda)}{F_{\rm out}(\lambda)}, \tag{1.11}$$

where $F_{\rm out}$ is the out-of-transit spectrum of the host star and $F_{\rm in}$ is the observed in-transit spectrum. However, at high spectral resolution, the wavelength of the excess absorption of a planetary atmosphere follows the Doppler velocities of the planet or, in other words, its phase. In such a case, the formal definition of an exoplanet transmission spectrum ϕ[4] in function of the planetary phase θ and wavelength λ is the following:

$$\phi(\theta,\lambda) = 1 - \frac{f_{\rm in}(\theta,\lambda)}{F_{\rm out}(\lambda)}. \tag{1.12}$$

It is also convenient to define the transmission spectrum in the rest frame of the planet by Doppler shifting the spectrum according to:

$$\lambda_{\rm p}(\theta) = \lambda\left(\frac{c}{\Delta v(\theta)} + 1\right), \tag{1.13}$$

where Δv is the difference between radial velocity of the planet at a particular phase θ and the reference velocity of the observer, and $\lambda_{\rm p}$ will be the resulting wavelength in the rest frame of the planet. Finally, we can define the transmission spectrum Φ independent from the planetary phase by taking the mean of $\phi(\theta,\lambda_{\rm p})$ over the range of θ observed in transit:

$$\Phi(\lambda_{\rm p}) = \frac{1}{\Delta\theta}\int \phi(\theta,\lambda_{\rm p})d\theta. \tag{1.14}$$

As we will see in Sect. 1.3.1, and Chapters 2 and 3, light curves are also routinely used to study transit spectra and search for in-transit excess absorption that could indicate the presence of an atmosphere.

[4] We use lower-case to denote the dependence of the in-transit spectra to the orbital phase θ.

The ratio of the lower-atmosphere area to the disk of the star is in the order of 10^{-3} to 10^{-4} in the optical and near-infrared [159], thus requiring very strong spectroscopic features to be detectable [e.g., 192, 165]. That is not the case, however, for the exosphere, which can extend to several planetary radii. In fact, Coustenis et al. [37] predicted that some ionized species in the exosphere of the hot Jupiter 51 Peg b have transitions in the optical that could reach 1% to 2% in-transit absorption.

The first successful observation to detect an exoplanet exosphere and its atmospheric escape was achieved by Vidal-Madjar et al. [182], not at optical wavelengths, but in the ultraviolet with *HST*. Shortly after that, hydrodynamically escaping metals were also detected using UV spectroscopy [180]. More recently, the helium (He) triplet in infrared (1.083 μm) was also confirmed to be a tracer of atmospheric escape [170]. In the optical wavelengths, the Hα line has also been used to study escaping atmospheres in ultra-hot Jupiters [94].

1.3.1 Neutral hydrogen in Lyman-α

The main spectroscopic channel to probe atomic H in exoplanet atmospheres is the Lyman-α line in the far-ultraviolet (central wavelength 1215.6702 Å). Currently, the only telescope able to observe at this wavelength is *HST*. The technique consists in performing a time-series observation of the Lyman-α line of the host star before, during and after the planetary transit. Since the observable Lyman-α profile of stars beyond the Solar System is heavily affected by interstellar medium absorption, we do not have access to the emission line core[5], and the flux in the wings are significantly attenuated. The classical approach used in Lyman-α transit spectroscopy is to separate the profile in different channels that probe specific velocities: the blue wing traces material being driven away from the star, and the red wing traces gas inflowing into the host star. The profile can further be divided into ranges of interest where we do not expect planetary signals to appear (i.e., flux-stable ranges), or where there is strong contamination by the Earth's geocoronal emission.

Since an exosphere can extend to many planetary radii, its properties are strongly affected by the environment in the vicinity of the planet. While the vertical outflow near the surface can accelerate the upper atmosphere up to velocities of only a few tens of km s^{-1}, radiation pressure and interactions with the stellar wind can drive velocities of more than 100 km s^{-1}. Because of these properties, exospheres usually assume a cometary shape [see, e.g., 132], thus observable exospheric Lyman-α signatures usually display asymmetries when compared to a traditional transit light curve at longer wavelengths [111, 109, 19].

[5]Except for specific cases of stars with high radial velocity; see, e.g., the case of Kepler-444 [17] and Barnard's Star [59].

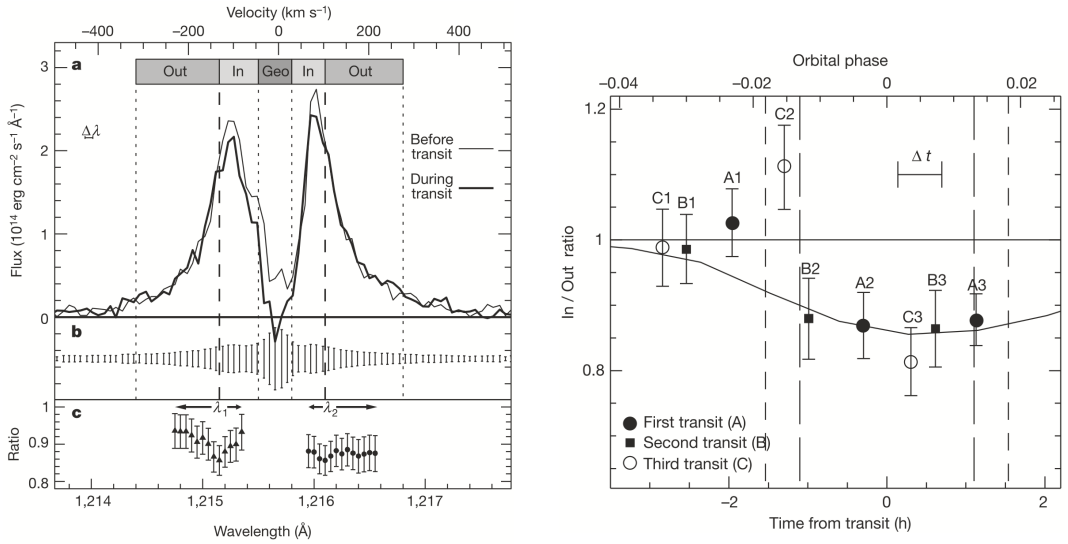

Fig. 1.8 Lyman-α transit spectroscopy of the hot Jupiter HD 209458 b. *Left panel:* In- and out-of-transit Lyman-α profiles of the host star (a) and its uncertainties (b); the ratio between the in- and out-of-transit spectra are shown in the inset (c). *Right panel:* Light curve of the Lyman-α band pass phase-folded to the orbital period of the planet. The vertical dashed lines delimit the transit contact times. Adapted from Vidal-Madjar et al. [182].

A characteristic exospheric signature consists in a decrease of flux in the stellar Lyman-α line during the planetary transit, and can be accompanied by a long egress, as well as a pre-transit absorption (see Fig. 1.8). This flux variation occurs more prominently in the blue wing, since most of the material is driven away from the star to high velocities by a combination of radiation pressure and stellar wind, but can also be present in the red wing too, but less prominently than the blue wing [19, 47]. The precision with which we can measure these signatures with the most cutting edge instruments and techniques is in the order of a few percent. Thus, currently, we can only measure signatures of planets with large atmospheric escape rates (see Chapter 4).

Observing exoplanet signals in the ultraviolet has some specific challenges that we do not encounter at longer wavelengths:

- Inactive stars less massive than the Sun do not have enough continuum flux, meaning that planetary signals can only be detected in emission lines where we have flux.
- The Lyman-α line is formed across a wide range of temperatures in the stellar atmosphere, and is difficult to model.
- The interstellar medium does not only absorb in Lyman-α, but also in other emission lines and the extreme ultraviolet wavelengths.

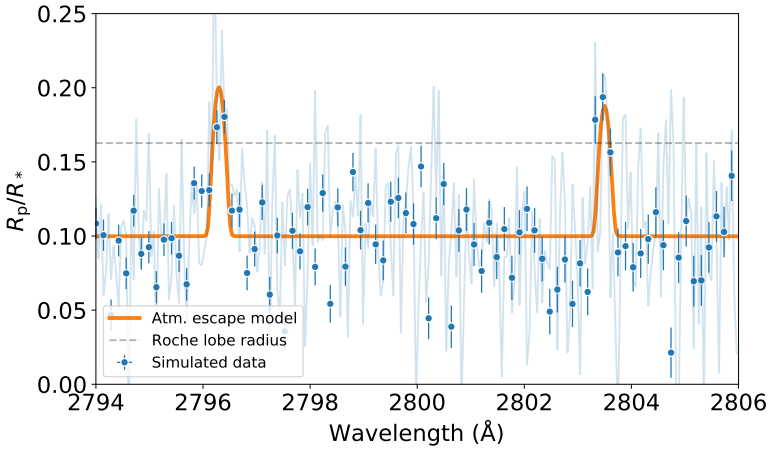

Fig. 1.9 Simulated transmission spectrum of the ultra-hot Jupiter WASP-76 b near the Mg doublet in NUV using the STIS spectrograph on *HST*. The simulation is based on a self-consistent hydrodynamic escape model courtesy of A. Vidotto.

- This wavelength range is extremely susceptible to variability due to stellar activity (see Sect. 1.4).

These observations can be used to assess the high-energy environment around exoplanets and to estimate maximum atmospheric escape rates. The latter depends on the amount of EUV irradiation that reaches the planet (see Eq. 1.10 and the energy-limited formulation of Lecavelier Des Etangs [110]). The challenge in this estimate lies on the fact that the EUV emission of stars that are not the Sun is mostly absorbed by the interstellar medium, similar to the Lyman-α line. However, both can be reconstructed using different techniques [see, e.g., 191, 195, 121, 19, 49].

1.3.2 Metallic species in the ultraviolet

Exospheres of planets whose atmospheric escape happens hydrodynamically may also be populated by heavier species than H, such as carbon (C), nitrogen (N), oxygen (O), silicon (Si), magnesium (Mg; see Fig. 1.9), and even iron (Fe). There are several lines in ultraviolet wavelengths accessible to *HST* that trace such species. Metals can also contribute to absorption in the stellar continuum at near-ultraviolet (NUV) wavelengths [e.g., 58, 120, 126].

Despite the lack of a continuum emission for cool stars, the STIS and COS spectrographs on *HST* have the capabilities to detect the strongest metallic UV emission lines. Thus, the transit spectroscopy technique used in Lyman-α can be similarly applied for metals, with

the advantage that they have less to no ISM absorption. The drawback is that these lines are much weaker and narrower than Lyman-α, limiting the precision with which we can measure transit depths and outflow velocities.

To this date, hydrodynamic escape of metals has only been confidently observed in hot Jupiters [180, 58, 117, 11, 181, 166], and a tentative detection was made for the super-Earth π Men c [68]. A characteristic signal of escaping metals in hot Jupiters produces an excess transit depth of a few to several percent. Usually, these heavier species are carried to the Roche lobe at high velocities, essentially forming a metal-rich exosphere [166]. Ionized metal species can be sensitive to planetary magnetic fields, forming controlled outflows and producing asymmetric transits if the field is strong enough [1]. Transit asymmetries for escaping metals are a matter of debate in the literature; early results pointed out to the presence of a magnetospheric bow shock around WASP-12 b [e.g., 106], but additional observations ruled out a stable early ingress [136], and the possibility of a variable bow shock remains open [184].

1.3.3 Metastable neutral helium in the infrared

Initially theorized by Seager and Sasselov [159], transmission spectroscopy of the metastable He triplet at 1.083 μm has recently been shown to be a reliable technique to estimate atmospheric escape rates and study planetary outflows [139]. The spin of electrons in atomic He can exist in two states: singlet (parallel) and triplet (anti-parallel). Since the radiative decay of He triplet has a lifetime of 2.2 h, the de-population of He in this state is relatively slow, hence the moniker metastable (see Fig. 1.11). As the name implies, the triplet possesses three transitions (spectral lines), of which two are blended, and they are routinely observed in the atmospheres of stars [e.g., 50] and galactic centers [e.g., 115].

Among the advantages of the He triplet over the UV tracers, two of them are that it can be observed from the ground and, in some cases, at higher spectral resolution [e.g., 4, see Fig. 1.10]. This allows the study of bulk velocities of planetary winds in transmission. By fitting metastable He winds to observed transmission spectra, we can infer model-dependent atmospheric escape rates and upper atmospheric temperatures. In Appendix A I present a Python implementation of such a model that can be fit to observations. Furthermore, in Chapter 2, I will discuss the observation of metastable He in the hot Jupiter WASP-127 b carried out with the Gemini/Phoenix spectrograph.

The drawback of transmission spectroscopy with the He triplet over other tracers is that it seems to occur for a limited range of stellar types. Oklopčić [138] points out that populating the metastable He triplet requires a relatively hard high-energy spectrum, with strong EUV fluxes (which ionizes the He ground-state) and weak mid-UV irradiation (which ionizes the

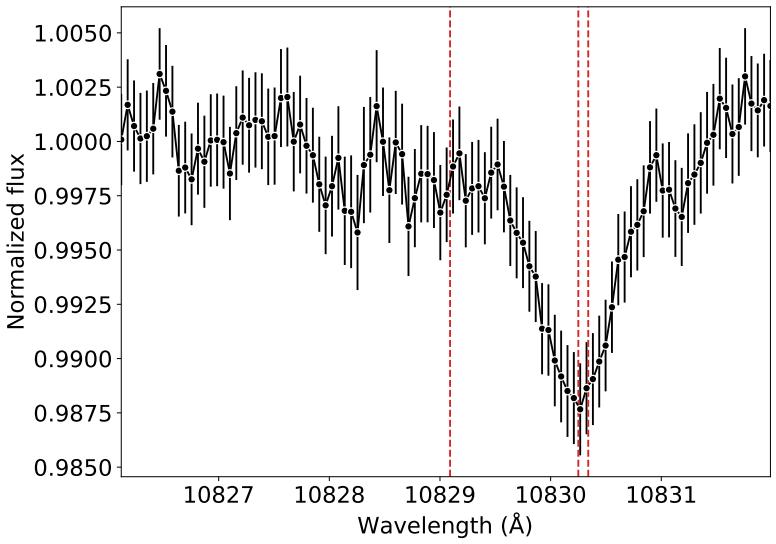

Fig. 1.10 Metastable He transmission spectrum of the warm Neptune HAT-P-11 b obtained with the CARMENES spectrograph [4]. The dashed vertical lines represent the rest wavelengths of the triplet.

He triplet). This ideal condition seems to arise around K-type stars, but detections have been found for planets orbiting other stellar types as well [5, 145], albeit more rarely.

1.3.4 Other hydrogen features in the optical

Since H is the most abundant element in the atmospheres of gas giants, and it is also the lightest element, it comes to no surprise that other H spectral lines can exhibit signatures of atmospheric absorption at high altitudes during a planetary transit. Ballester et al. [7] reported on the discovery of an excess absorption of $0.03\% \pm 0.006\%$ absorption in HD 209458 b by atomic H in the Balmer jump and continuum using the 1st-order CCD observations with *HST* and the G430M grating. They conclude that a large population of hot H in the upper atmosphere is needed to explain this excess absorption. The technique they used is not spectroscopically resolved, and instead they use broadband, high-precision photometry corrected for instrumental systematics to achieve these results.

The first detection of excited H in an exoplanet's atmospheres was reported by Jensen et al. [94] for the archetypal hot Jupiters HD 209458 b and HD 189733 b. Jensen et al. applied transmission spectroscopy (very similar to the technique described in Sect. 1.3.3) of the Hα line to data obtained with the High-Resolution Spectrograph in the Hobby-Eberly Telescope between 2006 and 2008. In the case of HD 189733 b, the authors combined both the Hα and Lyman-α detections to estimate the necessary temperature to excite enough atomic H to

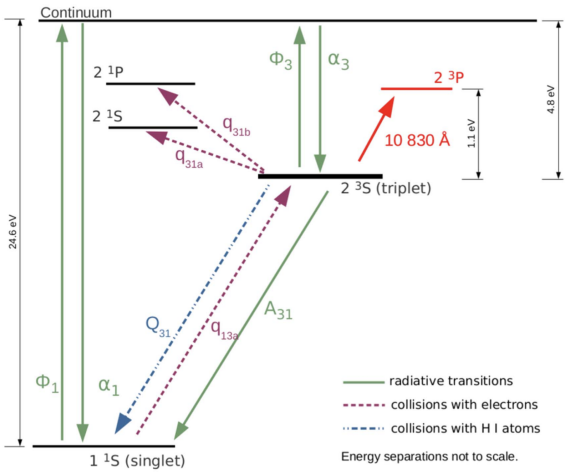

Fig. 1.11 Atomic structure of the He atom, with the radiative and collisional transitions relevant for the population of the metastable He spectral lines (shown in red) [adapted from 139].

produce the observed in-transit Hα absorption, inferring an upper limit of 26 000 K. Jensen et al. argue that such temperatures can only be found in the upper atmosphere, and conclude that the Hα absorption must be produced at very low-densities, likely near the exosphere. Although the host star HD 189733 is very active and atmospheric signals must be analyzed with caution, Cauley et al. [30] provides further evidence that the observed Hα absorption is likely planetary and not only due to activity.

Using the high-resolution, ground-based spectrograph CARMENES, Yan and Henning [194] reported the detection of H in the atmosphere of the hottest planet known to date, KELT-9 b. This result was later replicated with HARPS spectrograph and reported in Wyttenbach et al. [193]. KELT-9 b shows in-transit absorption in the Hα, Hβ, and Hγ with velocities reaching up to 50 km s^{-1} (see Fig. 1.12); Wyttenbach et al. argue that the best explanation for the observed transmission spectrum of KELT-9 b requires that the thermosphere is expanding hydrodynamically, and they retrieve a mass loss rate of $\dot{m} = 10^{12.8\pm0.3}$ g s^{-1} in local thermodynamic equilibrium (LTE) conditions, and $\dot{m} = 10^{14.3^{+1.2}_{-1.4}}$ g s^{-1} for the non-LTE case.

1.4 Effects of stellar activity on planets and observations

Stellar activity is an umbrella term that refers to the changes in the stellar surface flux arising from the bulk motion of plasma in the chromosphere [82]. This phenomenon is closely tied to the stellar magnetic fields, hence sometimes referred to as magnetic activity. The reason

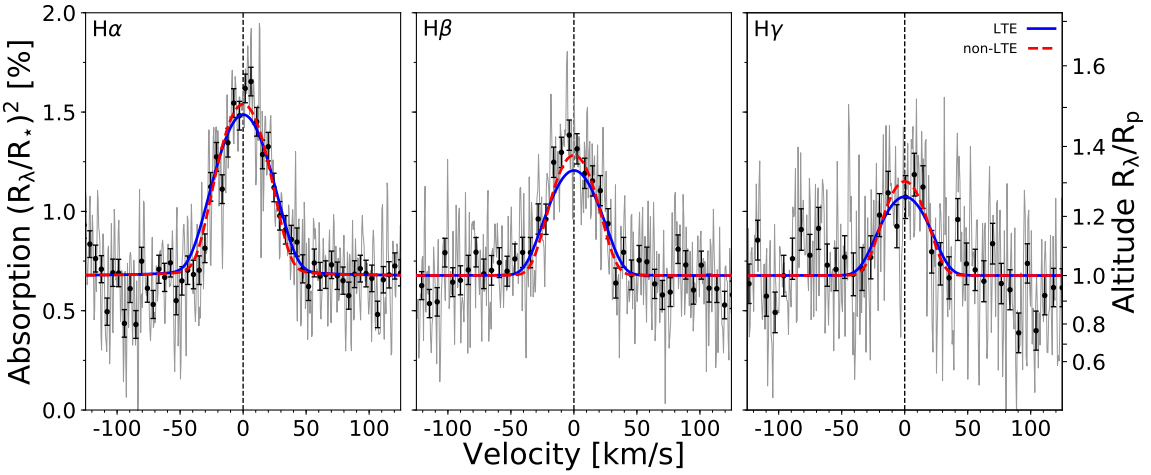

Fig. 1.12 Hα, Hβ, and Hγ transmission spectra of KELT-9 b measured with the HARPS spectrograph [193].

why this subject warrants a whole section of this manuscript is because the observation of atmospheric escape is performed in wavelengths that also trace stellar chromospheric activity. Since planetary signals are not always as deep as the Lyman-α absorption of GJ 436 b [51], their amplitudes can be of similar size as stellar activity modulations. We, therefore, need a framework that allow us to disentangle planetary signals from stellar activity.

This is also a long-standing problem in the detection of exoplanets with the radial velocities method, where planet-induced signals have amplitudes with the same size or even smaller than activity signals (which sometimes are also called stellar noise or jitter). Although to a lesser extent, stellar activity also poses an obstruction to the detection of exoplanets with the transit method, however it is not uncommon to find transiting worlds around very young and active stars [e.g., 118, 40, 135, 147].

The stellar activity effects relevant for the study atmospheric escape and evolution of exoplanets are three: high-energy irradiation environment around exoplanets, flares, and modulation due to the emergence of magnetically active regions.

1.4.1 High-energy environment around exoplanets

As we briefly discussed in Section 1.2.1, the X-rays and extreme ultraviolet (XUV) irradiation arriving at a planet plays an important role in controlling the physical and chemical properties of their atmospheres. For late-type stars, the Lyman-α line constitutes the bulk of their far-UV irradiation budget [62], and it can be used to estimate the ISM-absorbed EUV fluxes of stars in the solar neighborhood. Such observations are essential to study the photochemistry

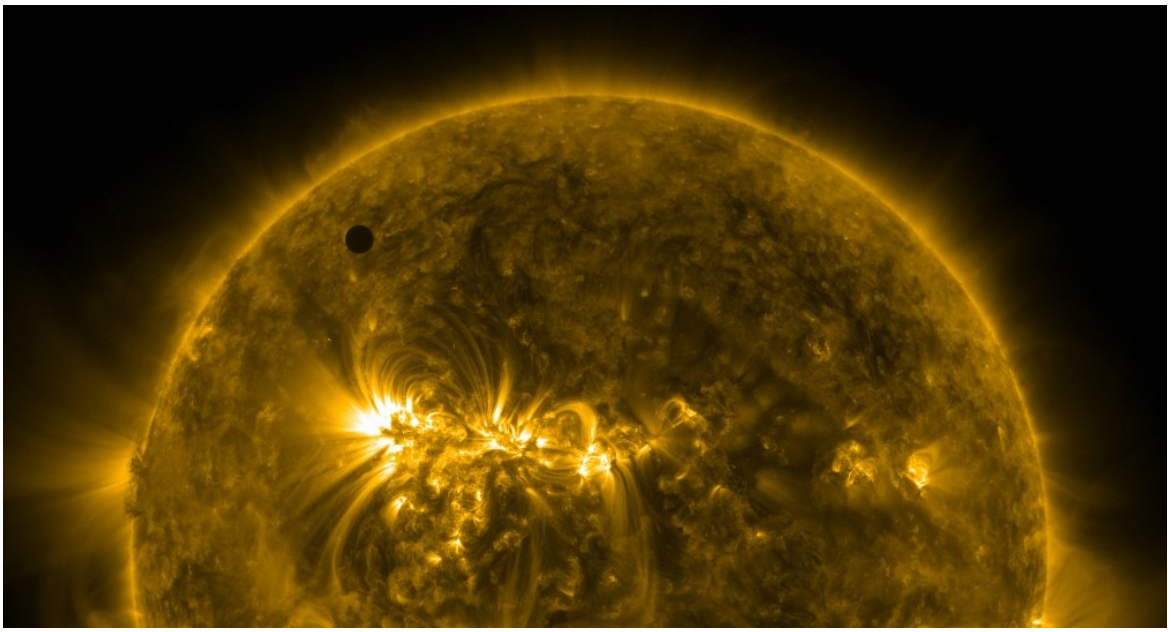

Fig. 1.13 Transit of Venus observed in 171 Å by the Atmospheric Imaging Assembly (AIA) instrument of the Solar Dynamics Observatory (SDO). This wavelength corresponds to the Fe IX spectral line formed between the upper transition region and corona of the Sun, and is very sensitive to stellar activity. Courtesy of NASA/SDO and the AIA, EVE, and HMI science teams.

in the upper atmospheres and habitability of these small planets [e.g., 160, 130, 96, 2, 169], regardless of whether or not these planets are ever probed with UV transits.

In particular, XUV irradiation is proposed as one of the main drivers for the expansion and evaporation of hot exoplanet atmospheres. Since low-mass stars (G-type and later) are more active in their early lives than at solar age [e.g., 167, 168, 149, 178, 48, 105], it is expected that atmospheric escape is the most intense in the first $\sim$100 Myr of a planet's life (see Chapter 3). So, in principle, one could expect that high chromospheric-activity levels should be correlated with large escape rates and thus strong atmospheric escape signals. But, in reality, the observability of escape signatures is more complicated. Recent observational and theoretical studies show that some planets orbiting active stars may have undetectable Lyman-α or metastable He in-transit absorption [e.g., 66, 98, 26, 196]. We further discuss this aspect in Chapters 2 and 3.

1.4.2 Flaring activity

Flares have been observed in the Sun since the antiquity. However, one event reported by Carrington [27] and Hodgson [86] is of particular interest because the authors described

what is, to date, the strongest solar magnetic storm in scientific record. The authors go on to narrate their observations of large spots in the solar surface, their quick evolution in timescales of a few minutes, which are followed by an increase in solar brightness unlike any other astronomical event on record. Flares and eruptions like this are caused by the reconnection of magnetic fields near activity regions, which leads to the release of copious amounts of energy and the acceleration of charged particles.

Events like the one described by Carrington [27] and Hodgson [86] are extremely rare: the last one of similar scale occurred in 2012, but it did not hit the Earth [6]. But smaller solar flares occur more frequently and are habitually observed in the Sun. Their occurrence follows a predictable power-law where the cumulative distribution ψ of flares more energetic than a reference energy of $E_{\rm ref}$ is:

$$\psi(E) = \kappa \left(\frac{E}{E_{\rm ref}} \right)^{-\alpha}, \tag{1.15}$$

where κ is a proportionality factor and α is the index of the power-law (always positive).

While flares and eruptions were initially observed in our own star, we can routinely apply what we learned from the Sun to other stars. A characteristic flare light curve displays an fast, impulsive increase in brightness followed by a slower, exponential decrease in flux. For example, Gryciuk et al. [76] report on a phenomenological model of X-ray solar flares using two temporal profiles: one Gaussian deposition function to describe the energy release, and an exponential decay function representing the energy loss. In equation form, the flare flux in function of time $f(t)$ is the following:

$$f(t) = \int_0^t g(x)h(t-x)dx, \tag{1.16}$$

where

$$g(t) = A \exp \left[\frac{-(t-B)^2}{C^2} \right], \tag{1.17}$$

and

$$h(t) = \exp(-Dt), \tag{1.18}$$

where A, B, C, and D and the shape parameters that reflect the following five free parameters: the amplitude of the flare, the time of peak flux, the rise time to reach peak flux, the decay time, and the baseline flux, respectively. We use this formulation to describe the large scale flare observed in the quiet M dwarf GJ 3470 in Bourrier et al. [16] (see also Fig. 1.14).

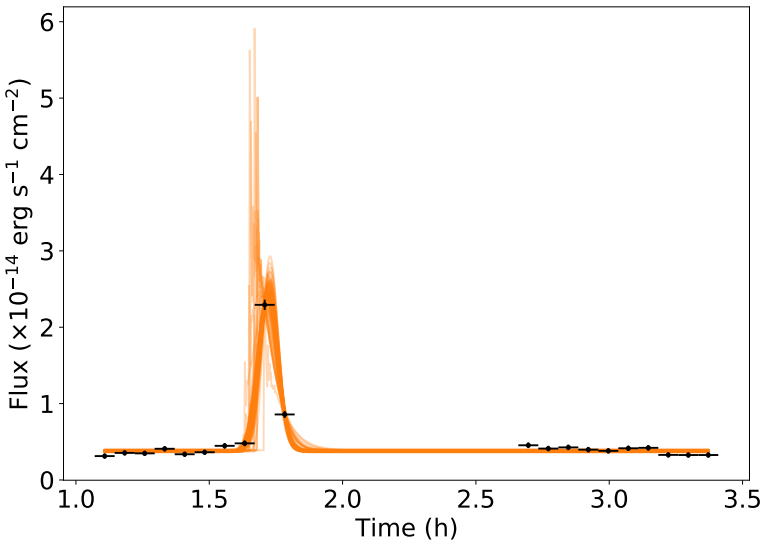

Fig. 1.14 Ultraviolet flare light curve of the quiet M dwarf GJ 3470 (black data points) and a family of models (orange) fit to the data [16].

As we shall see in Section 3.1, even magnetically quiet M dwarf stars show flaring activity, particularly in UV. Since short wavelengths trace the stellar chromosphere, it is only natural that they display more variability to flares than longer wavelengths. In some cases, flares are observed only in UV wavelengths; Loyd et al. [122] argue that UV-only flares are the result of small-scale magnetic reconnections that are only capable of heating the transition region and the chromosphere. Loyd et al. [122] found that the inactive M dwarf GJ 876 displays transition-region flares at a rate $\sim$1000 times that of the Sun. Furthermore, its flares can reach fluxes at least ten times stronger than the quiescent flux in the timescales of hours to days [61].

The increase in XUV flux caused by flares can potentially affect the atmospheric escape rate of exoplanets. For the case of GJ 3470 b, the energy released in the largest flare reported by Bourrier et al. [16] could have increased the mass loss rate of the planet by up to 320% at its highest and decreased the photoionization lifetime of H by half. However, numerical simulations suggest that the mass loss rates do not increase in proportion to the flare energy [31, 137]. In addition, the response time of the upper atmosphere to flares may be longer than the flare duration [14]. Thus, in practice, it may be challenging to observe the escape response to flares in exoplanets. To date, the only planet for which there are pieces of evidence for such an interaction is HD 189733 b, as reported in, e.g., Lecavelier des Etangs et al. [111] and Bourrier et al. [21].

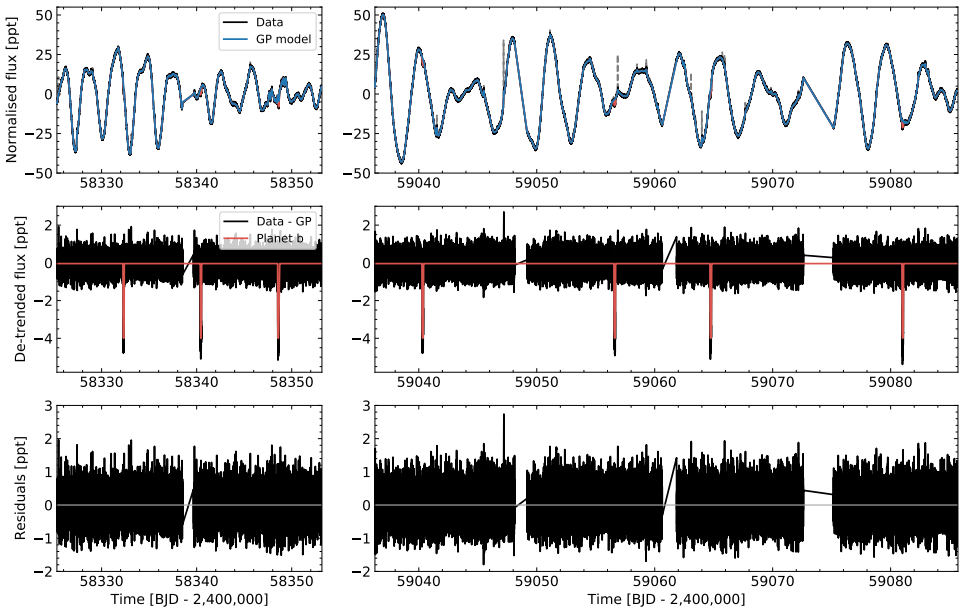

Fig. 1.15 Wide-band, red-optical light curve of the young planet-hosting star DS Tuc A obtained with the *TESS* satellite. The modulation is caused by the emergence and evolution of large spots in the stellar surface. The light curve also shows transits of the planet DS Tuc A b. This behavior is fit with a Gaussian Process model (GP) coupled with a transit model. Flares are also present in the time series. Courtesy of L. D. Nielsen.

1.4.3 Modulation induced by activity regions

The emergence of activity regions in a stellar surface also affects the observed disk-integrated fluxes of planet-hosting stars. This modulation by stellar rotation is routinely observed in stars both active and inactive using extensive time series observations. Transit surveys, such as *CoRoT* (Convection, Rotation and planetary Transits), *Kepler* and *TESS* (Transiting Exoplanet Survey Satellite) are ideal methods to observe this type of stellar activity because of their extensive and continuous monitoring (see Fig. 1.15). This effect is also extremely wavelength-dependent. Since activity is closely tied to the stellar chromosphere, spectral features that are formed in this region tend to be more sensitive to modulation.

For example, the emission core in the Ca H & K absorption lines at 393 and 397 nm, whose fluxes constitute the $R'_{\rm HK}$ activity index, have been used as tracers for chromospheric activity for several decades [179]. Long-term observations in this spectral channel have demonstrated the potential to measure stellar activity cycles and rotational modulation [e.g.,

83, 36]. In the infrared, the He triplet at 1.083 μm can also exhibit activity modulation [63], and can affect observations of transmission spectroscopy [78].

Such long-term time series are, unfortunately, challenging to achieve in the ultraviolet. Only space telescopes are capable of observing in the UV, and they often suffer from oversubscription and intermittency. For example, observations in the UV with *HST* are usually limited to five consecutive exposures interspersed by Earth occultations. One of the most observed stars in the UV is the planet-hosting M dwarf GJ 436. In Section 3.1, we will discuss in detail the analysis of this extensive dataset in the frame of stellar activity and atmospheric escape in the warm Neptune GJ 436 b.

However, there is one star for which we do have uninterrupted, long-term monitoring in the UV and short wavelengths: the Sun, thanks to the Solar Dynamics Observatory (SDO) and ground-based solar telescopes. The solar fluxes at many wavelength channels available in SDO are publicly available at the LASP Interactive Solar Irradiance Datacenter (LISIRD)[6]. In the case of atmospheric escape, we are particularly interested in the solar Lyman-α line, whose irradiance was measured every 60 s by the MEGS-P diode of the EVE instrument on SDO (Fig. 1.16). The main time scales of variability at display here are the solar magnetic cycle over several years and the rotational period of 27 days (see also Fig. 1.17 for a zoom-in at short time scales). The modulation is the result of a combination of brightenings caused by faculae and shorter-duration dimmings caused by sunspots [102].

The solar Lyman-α modulation is in the order of a few to several percent, depending on the time scale. This poses a problem because the amplitudes of transmission spectroscopy signatures in the UV are also in this order of magnitude. Thus, unless an experiment is reproduced several times, in-transit signatures can be inconclusive. One avenue to circumvent this problem is to perform simultaneous observations at different wavelengths. For example, an exoplanetary exosphere will only produce an absorption in Lyman-α, but not in the Ca H & K lines; but the latter does trace chromospheric variability present in Lyman-α (Fig. 1.17), so observing both channels at the same time allows us, in principle, to tease apart planetary signals from variability.

[6]https://lasp.colorado.edu/lisird/.

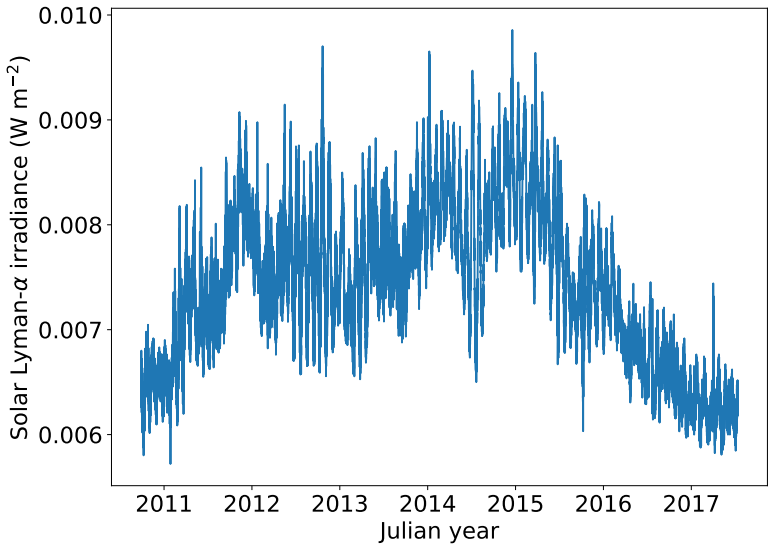

Fig. 1.16 Solar Lyman-α flux measured by SDO/EVE with a cadence of 60 s. The longest-term variability is caused by the solar magnetic cycle. Shorter time-scale varibility is the result of a combination of brightenings and dimmings with period of 27 days corresponding to the solar rotation and the emergence of activity regions.

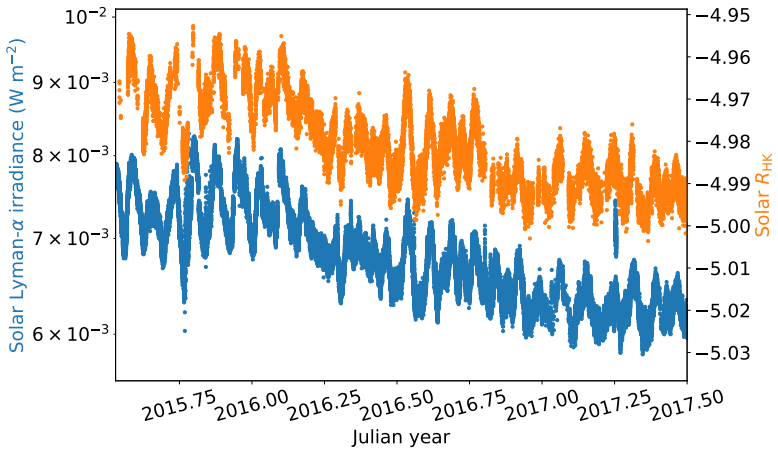

Fig. 1.17 Simultaneous observations of the solar Lyman-α flux with SDO/EVE and the activity index R'_{HK} with the ground-based HARPS-N spectrograph. Both channels trace chomospheric variability in the Sun, and match each other with a Spearman-r correlation index of 0.92. HARPS-N data is courtesy of X. Dumusque.

Chapter 2

Exploring the limits to detect atmospheric escape in gas giants

> *“ You see but you do not observe. The distinction is clear. ”*
>
> *Sherlock Holmes*

By 2003, the discovery of a hot Jupiter exoplanet was not as sensational as it once was a few years earlier. However, the question of how these gas giant exoplanets existed at such close proximity to their host star was persistent. In particular, Vidal-Madjar et al. [182] and Lammer et al. [108] were the first to propose an observational evidence for atmospheric evolution in short-period exoplanets: they claimed that hydrodynamic escape in hot, H-rich gas giants would cause a complete evaporation of their envelopes, explaining the lack of such planets observed at orbital distances shorter than 0.04 au. Baraffe et al. [8] would later postulate a critical mass below which evaporation strongly changes their radius size with time, and that HD 209458 b might be below this mass threshold. Finally, Lecavelier des Etangs et al. [113] posed an interesting scenario: if lower mass planets can show significantly more dramatic mass loss, what would we see when we started finding more and more smaller transiting planets?

As we have seen in Chapter 1, hydrodynamic atmospheric escape driven by X-rays and extreme-UV irradiation is thought to be one of the key determining factors of the demographics in short-period exoplanets [141]. But a persistent open question in this field is whether close-in gas giant exoplanets have hydrodynamically unstable thermospheres [152], which was originally proposed by Watson et al. [189] and confirmed for only a handful of exoplanets. On one side, this has led the community to rely on efficiency parametrizations (usually assuming a semi-arbitrary value between 0.1 and 1.0) to estimate escape rates from hot Jupiters to sub-Neptunes [162]. On the other hand, the severe lack of observed cases

limits modeling efforts to artificial planets instead of fitting them to actual observations. This gap between modeling and observations have an important downstream effect: It remains largely unconstrained whether the atmospheres of terrestrial planets can survive hydrodynamic escape in their lifetimes [e.g., 59]. Thus, increasing the sample of observations of hydrodynamic escape in exoplanets is fundamental to better understand the role of escape in their evolution.

2.1 Search for helium in the upper atmosphere of the hot Jupiter WASP-127 b using Gemini/Phoenix

By 2018, most observations of atmospheric escape and extended atmospheres had been performed with Lyman-α transmission spectroscopy with *HST*. However, the breakthrough discovery of Spake et al. [170] demonstrated that the metastable He triplet at 1.083 μm is one viable probe for atmospheric escape and is devoid of ISM absorption. Ground-based studies following up that discovery were performed with the CARMENES spectrograph, which is located in the Northern Hemisphere. By then, the only ground-based, high-resolution spectrograph that could observe in this window in the Southern Hemisphere was the Phoenix spectrograph. In the project we discuss here, we leveraged the uniqueness of Phoenix in this context to open the doors for probing atmospheric escape in planets located in the southern sky. In order to do that, we observed the transit of the low-density hot Jupiter WASP-127 b.

As we shall see, our search yielded a non-detection of He in WASP-127 b. We concluded that, despite the instrument being able to measure the transmission spectrum down to a precision of $\sim$1.9% per wavelength bin, on average, a detection was not possible because of a relatively low level of high-energy irradiation arriving at the planet. We discuss this possibility in more detail in Sect. 2.2. Unfortunately, the Phoenix spectrograph has since been retired because it was deemed non-competitive against other instruments available at the Gemini South telescope; however, no other instruments in the facility have access to the He triplet. Future instruments will be made available in the Southern Hemisphere that are capable of observing the He triplet, such as CRIRES+ and NIRPS.

This Section has previously been published in dos Santos et al. [45], and is reproduced with permission © ESO.

A&A 640, A29 (2020)
https://doi.org/10.1051/0004-6361/202038802

Astronomy & Astrophysics

Search for helium in the upper atmosphere of the hot Jupiter WASP-127 b using Gemini/Phoenix

Leonardo A. dos Santos[1], David Ehrenreich[1], Vincent Bourrier[1], Romain Allart[1], George King[2,3], Monika Lendl[1], Christophe Lovis[1], Steve Margheim[4], Jorge Meléndez[5], Julia V. Seidel[1], and Sérgio G. Sousa[6]

[1] Observatoire astronomique de l'Université de Genève, 51 chemin des Maillettes, 1290 Versoix, Switzerland
e-mail: leonardo.dossantos@unige.ch
[2] Department of Physics, University of Warwick, Gibbet Hill Road, Coventry, CV4 7AL, UK
[3] Centre for Exoplanets and Habitability, University of Warwick, Gibbet Hill Road, Coventry, CV4 7AL, UK
[4] Gemini Observatory/NSF's NOIRLab, Casilla 603, La Serena, Chile
[5] Universidade de São Paulo, Departamento de Astronomia do IAG/USP, Rua do Matão 1226, Cidade Universitária, 05508-900 São Paulo, SP, Brazil
[6] Instituto de Astrofísica e Ciências do Espaço, Universidade do Porto, CAUP, Rua das Estrelas, 4150-762 Porto, Portugal

Received 1 July 2020 / Accepted 12 July 2020

ABSTRACT

Large-scale exoplanet search surveys have shown evidence that atmospheric escape is a ubiquitous process that shapes the evolution and demographics of planets. However, we lack a detailed understanding of this process because very few exoplanets that have been discovered to date could be probed for signatures of atmospheric escape. Recently, the metastable helium triplet at 1.083 μm has been shown to be a viable window for the presence of He-rich escaping envelopes around short-period exoplanets. Our objective is to use, for the first time, the Phoenix spectrograph to search for helium in the upper atmosphere of the inflated hot Jupiter WASP-127 b. We observed one transit and reduced the data manually since no pipeline is available. We did not find a significant in-transit absorption signal indicative of the presence of helium around WASP-127 b, and we set a 90% confidence upper limit for excess absorption at 0.87% in a 0.75 Å passband covering the He triplet. Given the large scale height of this planet, the lack of a detectable feature is likely due to unfavorable photoionization conditions for populating the metastable He I triplet. This conclusion is supported by the inferred low coronal and chromospheric activity of the host star and the old age of the system, which result in a relatively mild high-energy environment around the planet.

Key words. planets and satellites: atmospheres – stars: individual: WASP-127 – techniques: spectroscopic

1. Introduction

The results from surveys of transiting exoplanets are fundamental to obtain a global overview of the exoplanet population in the solar neighborhood. One of the most important discoveries of these surveys is that the population of giant planets displays a dearth of hot, Neptune-sized worlds (Lecavelier Des Etangs 2007; Mazeh et al. 2016). One of the main explanations proposed for this feature is atmospheric loss: planets start their lives with a thick envelope that is rich in volatiles, which is gradually eroded by the high-energy stellar irradiation (e.g., Lammer et al. 2003). However, very few exoplanets have been revealed to be losing their atmospheres (e.g., Vidal-Madjar et al. 2003; Lecavelier des Etangs et al. 2010; Haswell et al. 2012; Ehrenreich et al. 2015; Bourrier et al. 2018; Sing et al. 2019), which sets a limit on how sophisticated escape models can be used to explain observational results.

Classical observations for studying atmospheric escape have been performed in the ultraviolet (UV), mostly using the transmission spectroscopy technique in the Lyman-α (H I) line at 1215.67 Å. The escape of heavier particles has also been detected in the UV around highly-irradiated, nearby hot-Jupiters (e.g., Vidal-Madjar et al. 2004; Ben-Jaffel & Ballester 2013; Sing et al. 2019). These UV observations can only be performed from space since the Earth's atmosphere is opaque to these wavelengths. Another limitation of Lyman-α transit spectroscopy is that the interstellar medium (ISM) efficiently absorbs the core of the line, so we can only access information at high Doppler velocities (i.e., above ~30 km s^{-1}, depending on the radial velocity of the host star). Furthermore, the Lyman-α emission line, including its wings, is completely absorbed for distances larger than ~100 pc.

More recently, Oklopčić & Hirata (2018) have revised the prediction of Seager & Sasselov (2000) that the metastable He I triplet at 1.083 μm can be used in transmission to study atmospheric properties of transiting planets, including escape. This wavelength window is not affected by ISM absorption. To date, several studies have come out exploiting this new technique (e.g., Spake et al. 2018; Allart et al. 2018; Mansfield et al. 2018; Nortmann et al. 2018; Kreidberg & Oklopčić 2018; Allart et al. 2019; Alonso-Floriano et al. 2019; Kirk et al. 2020; Ninan et al. 2020; Gaidos et al. 2020; Vissapragada et al. 2020). Since there are more cases of planets that are amenable to infrared transit spectroscopy than in the UV, and as it is impossible to probe all of them with the few instruments currently available, the community would benefit from including Phoenix in the roster of those capable of conducting He I transmission spectroscopy.

Our objective in this study is to search for He in the upper atmosphere of the inflated hot Jupiter WASP-127 b (Lam et al. 2017) and assess the capability of an alternative spectrograph in the Southern Hemisphere for this purpose. The

orbital and planetary parameters of WASP-127 b were recently updated with a joint analysis of TESS and Euler photometry as well as CORALIE radial velocities, yielding a radius of $R_{\rm pl} = 1.311^{+0.025}_{-0.029}\ R_{\rm Jup}$, a mass of $M_{\rm pl} = 0.165^{+0.021}_{-0.017}\ M_{\rm Jup}$, and an orbital semi-major axis of $a_{\rm pl} = 0.0484^{+0.0013}_{-0.0009}$ au (Seidel et al., in prep.). The planet has recently been shown to display a feature-rich transmission spectrum from near-UV to near-infrared wavelengths (Chen et al. 2018; Spake et al. 2019), thus bringing further evidence that WASP-127 b is a promising target for atmospheric characterization.

2. Observation and data reduction

We observed one transit of WASP-127 b in the night of 17 March 2019 by using the visiting instrument Phoenix spectrograph (Hinkle et al. 2003) installed on the Gemini South Telescope (PI: dos Santos, Director's discretionary time program GS-2019A-DD-105). This observation was a pilot study to assess the feasibility of using the Phoenix spectrograph to measure He extended atmospheres around transiting exoplanets. We used the J9232 slit with an aperture of 0.25 arcsec (three pixels), resulting in a nominal resolving power of $R \sim 65\,000$ near the He triplet. The exposure times were set to 900 s and we obtained 24 spectra covering the transit and the out-of-transit baseline. Two in-transit exposures had to be discarded because of high noise levels, possibly caused by the passage of clouds.

The Phoenix spectrograph is neither cross-dispersed nor stabilized like other high-resolution spectrographs that are currently used for cutting-edge exoplanet science; this lack of wavelength stability does not, however, preclude us from using it to conduct transmission spectroscopy studies. Phoenix is capable of spectroscopy across the 1−5 μm region, and the wavelength coverage is limited to the bandpass of the blocking filter mounted on the instrument and the finite size of the detector. The spectrograph does not possess an automatic data reduction pipeline, so we performed the reduction manually using `IRAF` and the packages `CCDPROC` and `CCDRED`. Besides the science exposures, the full data set also consists of 11 dark exposures, 20 flat-field exposures, and eight telluric standard exposures. The uncertainties of all exposures were calculated assuming a gain of 9.2 electrons per analog-to-digital unit (ADU) and a readout noise of 40 electrons per pixel. All of the uncertainties quoted in this study were calculated by propagating the uncertainties of the raw data in all of the steps of the data reduction and analysis process.

All exposures were trimmed in the wavelength dispersion direction, removing the first 100 pixels and the last 24 pixels to avoid noisy regions. The dark and flat-field frames were combined as a median with 3σ clipping to produce the master dark and flat-field frames. We subtracted the dark from the master flat-field and normalized it by its overall mean to obtain the response function of the detector.

The levels of sky background are highly variable near 1 μm. The strategy to perform sky subtraction with Phoenix observations consists in alternating the position of the stellar spectrum in the detector between each exposure. These positions are named A and B, and consecutive observations follow the pattern ABBA; each pair AB or BA is subtracted of each other's exposure, resulting in images without a sky and dark-current background (see Fig. 1). All telluric and science frames are then divided by the normalized master flat-field image.

The spectra are finally extracted using `IRAF`'s task `APALL` from each exposure. The only manual step is to set the initial aperture location in the spatial direction. This is done by finding the center of the stellar profile in two cross-dispersion cuts; one is in the upper and one is in the lower part of the detector. We then fit the spectral trace with a third-order polynomial and two iteration steps using the two previously mentioned points as a starting point for the fit. The width of the spectral trace is calculated automatically by the `APALL` task. We extracted the spectra for the science and telluric standard exposures using a regular box extraction algorithm.

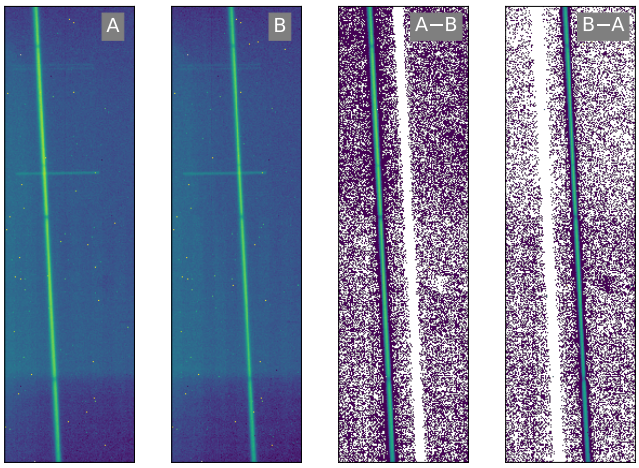

Fig. 1. Two consecutive science exposures (*left*) with spectra in different positions were subtracted of each other to remove the sky background (*right*).

We performed the wavelength calibration using the `IRAF`'s tasks `IDENTIFY` and `DISPCOR`; as a reference, we used the telluric lines available in the wavelength range of the spectra (1080.76–1084.62 nm). The average root mean square (RMS) of the wavelength calibration is ∼0.001 nm per pixel or ∼0.28 km s^{-1} in Doppler space, which represents the internal precision of the wavelength calibration. We measured the wavelength stability of Phoenix near the 1.083 μm He triplet and found that it is, on average, ∼1.6 pixels or ∼2.2 km s^{-1} in Doppler space. For comparison purposes, the Doppler trajectory of the planet WASP-127 b during transit varies between approximately −30 and +30 km s^{-1}. Each spectra of WASP-127 is corrected for the barycentric radial velocity calculated with `barycorrpy`, a Python implementation of the algorithm by Wright & Eastman (2014), and then shifted to the stellar rest frame. The last step of the data reduction is to normalize the spectra of WASP-127; this is achieved by fitting the continuum of the spectra with the task `CONTINUUM`. For the sake of consistency, we fit the continuum of all spectra with three cubic spline pieces. The average signal-to-noise ratio (S/N) of the spectra near the He triplet is ∼26. In the beginning of the observation, there is no telluric contamination in the wavelength range of interest near the He triplet (see Fig. 2). But we found a feature during the transit near 1083.35 nm that could be caused by telluric lines (see Fig. 3). This feature is, however, far from the wavelength range of the He I triplet, so there was no need to correct for it in our analysis.

3. Results and discussion

Since the spectra are normalized, we lose information about the flux decrease by the opaque disk of WASP-127 b; our analysis is thus only sensitive to excess absorption caused by the planet's atmosphere at specific spectral lines. In total, we obtained ten spectra outside the transit, and we combined them to produce

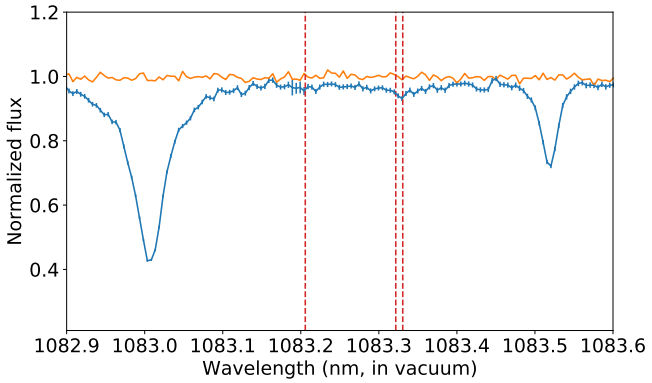

Fig. 2. Out-of-transit spectrum of WASP-127 around the He triplet (blue) and a telluric standard spectrum for reference (orange). The vertical-dashed lines represent the central wavelengths of each line in the triplet.

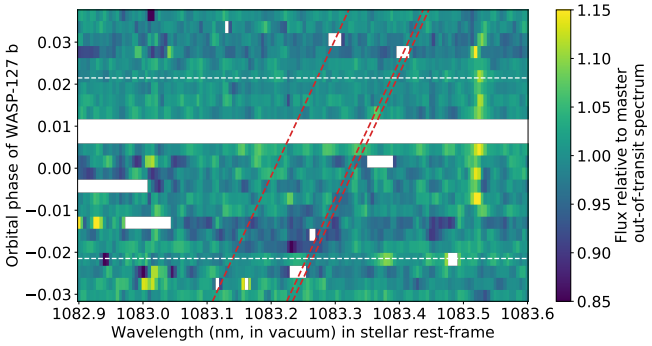

Fig. 3. Time series of the ratio between the individual spectra and the master out-of-transit spectrum; absorptions are positive and white regions represent bad pixels or discarded exposures. The horizontal-dashed lines represent the phases of ingress and egress of WASP-127 b. The dashed-red lines represent the central wavelength of the He triplet in the planetary rest frame.

a master out-of-transit spectrum (see Fig. 2). Contrary to previously observed targets, such as WASP-107 and HAT-P-11, the host star WASP-127 does not exhibit strong absorption lines of He in its spectrum. However, this does not preclude us from searching for an in-transit signal produced by the transiting planet since it would produce absorption in the stellar continuum instead. In fact, we expect that it improves the search for planetary He by increasing the local S/N (more photons than if there was a stellar line) and by avoiding flux variations due to the shifting stellar line in the planet rest frame.

The time series of the ratio between the individual spectra obtained during the observation and the master out-of-transit spectrum is shown in Fig. 3. The horizontal structure between phases −0.02 and −0.01 in Fig. 3 is likely due to normalization issues caused by the lower S/N of these exposures. Based on the technique of Wyttenbach et al. (2015), we computed an individual transmission spectrum as $f_{t,k} = 1 - f_{\mathrm{in,k}}/F_{\mathrm{out}}$, where $f_{\mathrm{in,k}}$ is the kth in-transit spectrum and F_{out} is the master out-of-transit spectrum. We note that $f_{\mathrm{in,k}}$ was calculated by shifting the spectrum of WASP-127 to the planetary rest frame. The final transmission spectrum F_t was computed by combining the individual ones as a median, and the result is shown in Fig. 4.

The average precision of the transmission spectrum of WASP-127 b is 1.9% per wavelength bin. This level of uncertainty is comparable to the one obtained for one transit of

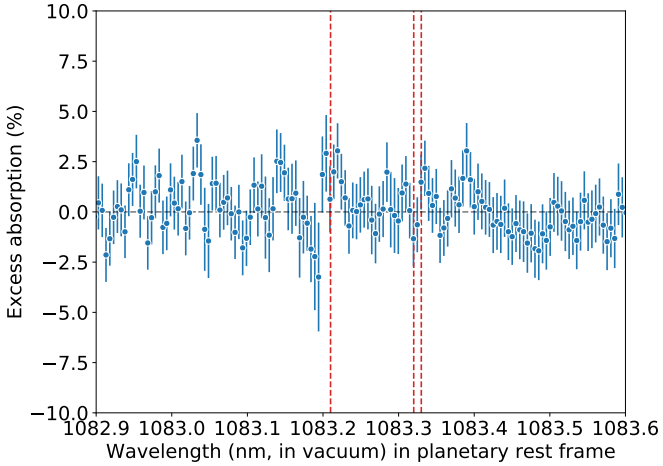

Fig. 4. Transmission spectrum of WASP-127 b around the He triplet. Absorption is positive.

WASP-107 b with the CARMENES spectrograph (Allart et al. 2019). For comparison purposes, the number of measured spectra in both programs is similar, both WASP-127 and WASP-107 possess similar J magnitudes, but the Gemini South Telescope has a mirror size of 8.1 m, while CARMENES is installed on a 3.5 m telescope.

An inspection of the spectral ratio time series and the transmission spectrum does not reveal a strong planetary absorption in the He triplet. We computed the integrated flux inside the wavelength range [1083.280, 1083.355] nm, the same bandwidth as in (Allart et al. 2019), and found an in-transit excess absorption consistent with null, 0.42% ± 0.36%, which corresponds to an upper limit of 0.87% at 90% confidence. In this project, we used a slit width of 0.25 arcsec (three pixels), but future projects with this instrument could benefit from a higher S/N if the widest slit width were used (0.34 arcsec, or four pixels). In this case, there would be some loss in spectral resolution ($R \sim 50\,000$), but given that the instrument is not stabilized in the first place and that the final error in wavelength calibration is ∼1.6 pixels, such a loss is not expected to severely affect how well we are able to trace atmospheric signals in Doppler space for short-period, massive exoplanets.

WASP-127 b and its host star are not as well studied as other systems for which we currently have detected He absorption signals. Using the most up-to-date planetary parameters (Seidel et al., in prep.), and assuming a mean molecular weight of 2.3 m_{H}, we calculated the lower-atmosphere scale height H_{eq} of WASP-127 b as 2109^{+313}_{-231} km. This is the largest scale height for a planet with a published He I transmission spectroscopy study to date (see, e.g., Alonso-Floriano et al. 2019, and references therein). The resulting 90% confidence upper limit for the ratio between the equivalent height of the absorbing atmosphere $\delta_{R_{\mathrm{pl}}}$ and the lower atmosphere scale height H_{eq} is 18.77. Converting this upper limit to an estimate of atmospheric escape rate is complicated by the number of unknowns, such as the temperature of the escaping material, the actual extreme ultraviolet (EUV) irradiation that the planet receives, the departure of the extended atmosphere from axial symmetry and from local thermal equilibrium.

For comparison purposes, we plotted this result in the high-energy irradiation versus $\delta_{R_{\mathrm{pl}}}/H_{\mathrm{eq}}$ in Fig. 5. There are currently no publicly available observations of WASP-127 in X-rays or UV wavelengths, so we needed to estimate the high-energy

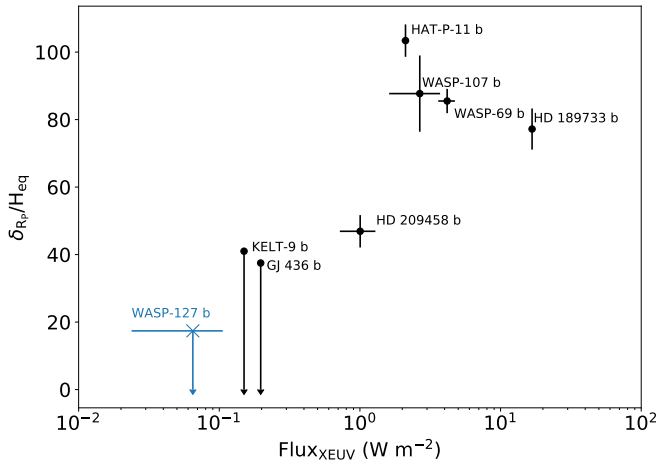

Fig. 5. He I ionizing irradiation ($\lambda < 504$ Å) versus the equivalent height of the absorbing He I particles in the upper atmosphere of WASP-127 b. The high-energy irradiation was estimated with two different methods (see main text), which define the limits of the horizontal uncertainty. The data points for other targets were measured by Nortmann et al. (2018) and Alonso-Floriano et al. (2019).

irradiation of the planet. We used two approaches for this estimate: (i) using an SED model of a similar star (HD 330075, same G5-type as WASP-127) from the `X-exoplanets` database[1] (Sanz-Forcada et al. 2011); and (ii) using the age and $B-V$ relations from Jackson et al. (2012) and extrapolating the X-rays luminosity to $\lambda = 504$ Å. The ionizing flux that populates the metastable He I triplet is limited to wavelengths that are shorter than 504 Å (XEUV; Oklopčić 2019). These techniques yield XEUV irradiation levels of 0.092 and 0.024 W m^{-2} at the semi-major axis of WASP-127 b, respectively. Despite possessing a large scale height, one of the explanations for the lack of detectable He I in the upper atmosphere of WASP-127 b is that the planet receives very little high-energy irradiation compared to planets with a detectable signal. This also seems to be the case for GJ 436 b and KELT-9 b.

Lam et al. (2017) estimated the age of the WASP-127 system using the isochrones method, which is reliable for old Sun-like stars (see, e.g., Spina et al. 2018), and they derived a value of 11.41 ± 1.80 Gyr. The old age of the host star and consequently its relatively weak high-energy output could be part of the explanation as to why there is no detectable He in WASP-127 b. However, the nondetection in the young planet K2-100 b (see the discussion in Gaidos et al. 2020), which is under a stronger X-EUV irradiation than WASP-127 b, shows that the atmospheric escape history also affects the detectability of the He I feature.

4. Conclusions

We have presented a pilot study to assess the feasibility of using the Phoenix spectrograph, a visiting instrument on the Gemini South telescope, to detect He I in transmission around transiting hot-Jupiters. We used a standard procedure to reduce the data to allow for reproducibility. The observed spectra had an average S/N of ~26 near the He I triplet. In total, we measured 12 exposures of 900 s during the transit of WASP-127 b, ten of which were out of transit and two exposures were discarded because of cloud coverage.

The final transmission spectrum of WASP-127 b near the He I triplet has an average precision of 1.9% per wavelength bin. For reference purposes, a transit observation of WASP-107 b using the CARMENES spectrograph rendered a comparable precision for its transmission spectrum; both host stars have a similar J magnitude and were observed for a similar amount of time. This result illustrates the potential to use the Phoenix spectrograph as a viable alternative for this purpose. We do not detect an in-transit excess absorption due to the presence of He, and we constrain it to 0.42% ± 0.36% between the wavelength range [1083.280, 1083.355] nm. To date, WASP-127 b has displayed the least amount of atmospheric He I absorption relative to its scale height when compared to other detections and nondetections. The most likely explanation for this lack of metastable He in the upper atmosphere of WASP-127 b is the low amount of ionizing irradiation (1–504 Å) from its host star, which in turn can be related to the old age of the system (11.40 ± 1.80 Gyr).

There are two main limitations when using the Phoenix spectrograph to conduct He searches in transmission: i) the lack of an automated pipeline renders the data reduction processes difficult to perform and reproduce; and ii) since this is a visiting instrument, its availability on the Gemini South telescope is dictated by the demand of the community during the first phase of the call for observing proposals. Given the promising results we have presented, we hope that this pilot study encourages the community to apply for observing time using Phoenix and to develop an automated pipeline to reduce its data. Until the date of the observation, this was the only spectrograph available in the Southern Hemisphere with a promising prospect to conduct this type of observation. In the near future, other southern instruments such as CRIRES+ (Follert et al. 2014) and NIRPS (Wildi et al. 2017) will be able to perform such studies; however, having an extra instrument would help distribute the pressure that would otherwise concentrate onto the newer spectrographs.

Acknowledgements. L.A.d.S. thanks the Gemini Observatory staff and K. Hinkle for the technical support during data analysis, and K. Lam for the discussion on stellar parameters. The authors thank the anonymous referee for the swift and helpful review. This project has received funding from the European Research Council (ERC) under the European Union's Horizon 2020 research and innovation programme (project FOUR ACES; grant agreement No 724427), and it has been carried out in the frame of the National Centre for Competence in Research PlanetS supported by the Swiss National Science Foundation (SNSF). J.M. thanks FAPESP, grant number 2018/04055-8. S.G.S is supported by FCT – Fundação para a Ciência e a Tecnologia through national funds and by FEDER – Fundo Europeu de Desenvolvimento Regional through COMPETE2020 - Programa Operacional Competitividade e Internacionalização by these grants: PTDC/FIS-AST/32113/2017 and POCI-01-0145-FEDER-32113; PTDC/FIS-AST/28953/2017 and POCI-01-0145-FEDER-028953. This study is based on observations obtained at the international Gemini Observatory, a program of NOIRLab, which is managed by the Association of Universities for Research in Astronomy (AURA) under a cooperative agreement with the National Science Foundation on behalf of the Gemini Observatory partnership: the National Science Foundation (United States), National Research Council (Canada), Agencia Nacional de Investigación y Desarrollo (Chile), Ministerio de Ciencia, Tecnología e Innovación (Argentina), Ministério da Ciência, Tecnologia, Inovações e Comunicações (Brazil), and Korea Astronomy and Space Science Institute (Republic of Korea). We used the open source software SciPy (Virtanen et al. 2020), NumPy (van der Walt et al. 2011), IPython (Perez & Granger 2007), Jupyter (Kluyver et al. 2016), Astropy (Astropy Collaboration 2013), and Matplotlib (Hunter 2007).

References

Allart, R., Bourrier, V., Lovis, C., et al. 2018, Science, 362, 1384
Allart, R., Bourrier, V., Lovis, C., et al. 2019, A&A, 623, A58
Alonso-Floriano, F. J., Snellen, I. A. G., Czesla, S., et al. 2019, A&A, 629, A110
Astropy Collaboration (Robitaille, T. P., et al.) 2013, A&A, 558, A33

[1] Available at `http://sdc.cab.inta-csic.es/xexoplanets/jsp/homepage.jsp`

Ben-Jaffel, L., & Ballester, G. E. 2013, A&A, 553, A52
Bourrier, V., Lecavelier des Etangs, A., Ehrenreich, D., et al. 2018, A&A, 620, A147
Chen, G., Pallé, E., Welbanks, L., et al. 2018, A&A, 616, A145
Ehrenreich, D., Bourrier, V., Wheatley, P. J., et al. 2015, Nature, 522, 459
Follert, R., Dorn, R. J., Oliva, E., et al. 2014, SPIE, 9147, 476
Gaidos, E., Hirano, T., Mann, A. W., et al. 2020, MNRAS, 495, 650
Haswell, C. A., Fossati, L., Ayres, T., et al. 2012, ApJ, 760, 79
Hinkle, K. H., Blum, R. D., Joyce, R. R., et al. 2003, Proc. SPIE Conf. Ser., 4834, 353
Hunter, J. D. 2007, Comput. Sci. Eng., 9, 90
Jackson, A. P., Davis, T. A., & Wheatley, P. J. 2012, MNRAS, 422, 2024
Kirk, J., Alam, M. K., López-Morales, M., & Zeng, L. 2020, AJ, 159, 115
Kluyver, T., Ragan-Kelley, B., Pérez, F., et al. 2016, in Positioning and Power in Academic Publishing: Players, Agents and Agendas, eds. F. Loizides, & B. Schmidt (Amsterdam: IOS Press), 8
Kreidberg, L., & Oklopčić, A. 2018, Res. Notes Am. Astron. Soc., 2, 44
Lam, K. W. F., Faedi, F., Brown, D. J. A., et al. 2017, A&A, 599, A3
Lammer, H., Selsis, F., Ribas, I., et al. 2003, ApJ, 598, L121
Lecavelier Des Etangs, A. 2007, A&A, 461, 1185
Lecavelier des Etangs, A., Ehrenreich, D., Vidal-Madjar, A., et al. 2010, A&A, 514, A72
Mansfield, M., Bean, J. L., Oklopčić, A., et al. 2018, ApJ, 868, L34
Mazeh, T., Holczer, T., & Faigler, S. 2016, A&A, 589, A75
Ninan, J. P., Stefansson, G., Mahadevan, S., et al. 2020, ApJ, 894, 97
Nortmann, L., Pallé, E., Salz, M., et al. 2018, Science, 362, 1388
Oklopčić, A. 2019, ApJ, 881, 133
Oklopčić, A., & Hirata, C. M. 2018, ApJ, 855, L11
Perez, F., & Granger, B. E. 2007, Comput. Sci. Eng., 9, 21
Sanz-Forcada, J., Micela, G., Ribas, I., et al. 2011, A&A, 532, A6
Seager, S., & Sasselov, D. D. 2000, ApJ, 537, 916
Sing, D. K., Lavvas, P., Ballester, G. E., et al. 2019, AJ, 158, 91
Spake, J. J., Sing, D. K., Evans, T. M., et al. 2018, Nature, 557, 68
Spake, J. J., Sing, D. K., Wakeford, H. R., et al. 2019, MNRAS, submitted [arXiv:1911.08859]
Spina, L., Meléndez, J., Karakas, A. I., et al. 2018, MNRAS, 474, 2580
van der Walt, S., Colbert, S. C., & Varoquaux, G. 2011, Comput. Sci. Eng., 13, 22
Vidal-Madjar, A., Lecavelier des Etangs, A., Désert, J.-M., et al. 2003, Nature, 422, 143
Vidal-Madjar, A., Désert, J.-M., Lecavelier des Etangs, A., et al. 2004, ApJ, 604, L69
Virtanen, P., Gommers, R., Oliphant, T. E., et al. 2020, Nat. Methods, 17, 261
Vissapragada, S., Knutson, H. A., Jovanovic, N., et al. 2020, AJ, 159, 278
Wildi, F., Blind, N., Reshetov, V., et al. 2017, Proc. SPIE Conf. Ser., 10400, 1040018
Wright, J. T., & Eastman, J. D. 2014, PASP, 126, 838
Wyttenbach, A., Ehrenreich, D., Lovis, C., Udry, S., & Pepe, F. 2015, A&A, 577, A62

2.2 Addendum to dos Santos et al. [45]

After the publication of dos Santos et al. [45], we attempted to model the metastable helium triplet transmission spectrum of WASP-127 b using the `p-winds` code. The high-energy spectrum of the host star is currently unknown, since it was never observed. So, in order to model the upper atmosphere of the planet, we take the high-energy spectrum of a similar G5-type star, HD 330075, from the `X-exoplanets` database. This spectrum was modeled using a coronal model based on Sanz-Forcada et al. [153], however it does not reach the longer wavelengths between 1200-2600 Å that we need to model the metastable He. So we concatenate the high-energy spectrum above with a Phoenix SED model for a star similar to WASP-127 b. The resulting spectrum arriving at the planet is shown in the left panel of Fig. 2.1.

We estimate an energy-limited mass loss rate of 2×10^{10} g s^{-1} at an optimistic 100% efficiency. At this rate, and assuming a planetary wind temperature of 9000 K, the resulting population of metastable He around WASP-127 b is extremely low compared to other planets with detections: approximately 10^{-6} cm^{-3} for WASP-127 b (see right panel of Fig. 2.1), and 10^{1} cm^{-3} for HAT-P-11 b (see Appendix A). This result provides a quantitative explanation for the non-detection obtained in dos Santos et al. [45]. From this result and others [e.g., 98], a clear trend has been emerging showing that only gas giants with high levels of energetic irradiation are capable of maintaining a detectable metastable He atmosphere.

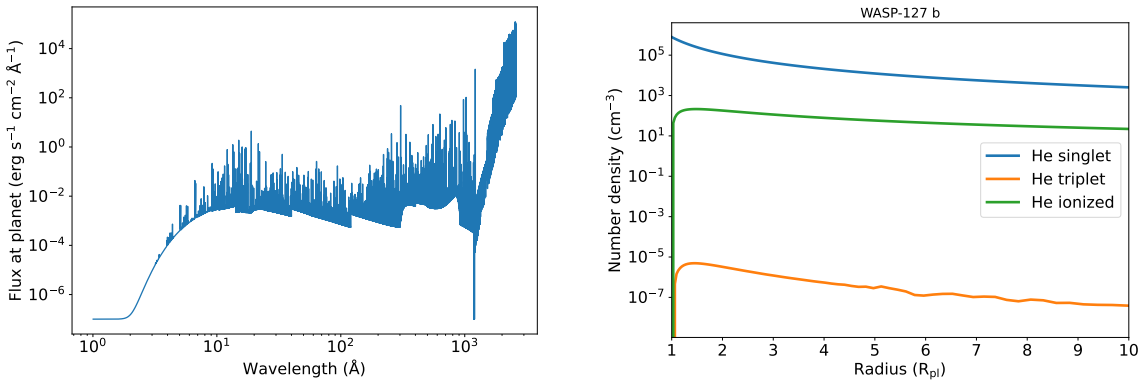

Fig. 2.1 *Left panel*: Assumed high-energy spectrum arriving at the planet WASP-127 b based on the coronal and SED models of a similar G5-type star. *Right panel:* Distribution of He in the upper atmosphere of WASP-127 b.

2.3 Non-detection of atmospheric escape in the warm Saturn-sized planet WASP-29 b

The Panchromatic Comparative Exoplanetary Treasury (PanCET) program is, to date, the largest *Hubble Space Telescope* observing campaign dedicated to extrasolar planets, with a total of 498 orbits. The main objective of this large program was to build a legacy dataset of transmission spectra, covering the ultraviolet to infrared, of a sample of transiting gas giants and Neptunes. Taking inspiration from the recently published studies of escape of neutral H [51] and metals [11], part of this program was dedicated to observe atmospheric escape in UV. In total, five targets were observe in far-UV, among them WASP-29 b, which we discuss in this Section; GJ 436 b was also observed, and we discuss the results for this planet in Chapter 3.

We did not detect any convincing planetary signals in the analysis of six transits of WASP-29 b. The spectral time series is mostly stable, and some of the observed variations are not repeatable, indicating possible contamination by stellar activity. Although we obtained only non-detections, we conclude that it is still possible that this warm Saturn-sized planet is undergoing atmospheric escape at a rate as high as 4×10^9 g s^{-1}, given the level of high-energy irradiation it receives. Future observations in He transmission spectroscopy may be able to pin down the escape rate of WASP-29 b. We also present an estimate of the unobservable EUV spectrum of the host WASP-29, which was inferred from a joint analysis of the UV data X-rays observations obtained with the *XMM-Newton* observatory.

This Section has previously been published in dos Santos et al. [44], and is reproduced with permission © ESO.

A&A 649, A40 (2021)
https://doi.org/10.1051/0004-6361/202140491

Astronomy & Astrophysics

HST PanCET program: non-detection of atmospheric escape in the warm Saturn-sized planet WASP-29 b

L. A. dos Santos[1], V. Bourrier[1], D. Ehrenreich[1], J. Sanz-Forcada[2], M. López-Morales[3], D. K. Sing[4,5], A. García Muñoz[6], G. W. Henry[7], P. Lavvas[8], A. Lecavelier des Etangs[9], T. Mikal-Evans[10], A. Vidal-Madjar[9], and H. R. Wakeford[11]

[1] Observatoire astronomique de l'Université de Genève, Chemin Pegasi 51b, 1290 Versoix, Switzerland
e-mail: leonardo.dossantos@unige.ch
[2] Centro de Astrobiología (CSIC-INTA), 28692 Villanueva de la Cañada, Madrid, Spain
[3] Center for Astrophysics, Harvard & Smithsonian, 60 Garden Street, Cambridge, MA 02138, USA
[4] Department of Earth & Planetary Sciences, Johns Hopkins University, Baltimore, MD, USA
[5] Department of Physics & Astronomy, Johns Hopkins University, Baltimore, MD, USA
[6] AIM, CEA, CNRS, Université Paris-Saclay, Université de Paris, 91191 Gif-sur-Yvette, France
[7] Tennessee State University, Center of Excellence in Information Systems, Nashville, TN 37203, USA
[8] Groupe de Spectrométrie Moléculaire et Atmosphérique, Université de Reims, Champagne-Ardenne, CNRS UMR 7331, 51687 Reims Cedex 2, France
[9] Institut d'Astrophysique de Paris, CNRS, UMR 7095 & Sorbonne Universités UPMC Paris 6, 98 bis bd Arago, 75014 Paris, France
[10] Kavli Institute for Astrophysics and Space Research, Massachusetts Institute of Technology, Cambridge, MA, USA
[11] School of Physics, University of Bristol, HH Wills Physics Laboratory, Tyndall Avenue, Bristol BS8 1TL, UK

Received 3 February 2021 / Accepted 29 March 2021

ABSTRACT

Short-period gas giant exoplanets are susceptible to intense atmospheric escape due to their large scale heights and strong high-energy irradiation. This process is thought to occur ubiquitously, but to date we have only detected direct evidence of atmospheric escape in hot Jupiters and warm Neptunes. The latter planets are particularly more sensitive to escape-driven evolution as a result of their lower gravities with respect to Jupiter-sized planets. But the paucity of cases for intermediate, Saturn-sized exoplanets at varying levels of irradiation precludes a detailed understanding of the underlying physics in atmospheric escape of hot gas giants. Aiming to address this issue, our objectives here are to assess the high-energy environment of the warm ($T_{\rm eq}$ = 970 K) Saturn WASP-29 b and search for signatures of atmospheric escape. We used far-ultraviolet observations from the *Hubble* Space Telescope to analyze the flux time series of H I, C II, Si III, Si IV, and N V during the transit of WASP-29 b. At 88 pc, a large portion of the Lyman-α core of the K4V-type host WASP-29 is attenuated by interstellar medium absorption, limiting our ability to probe the escape of H at velocities between −84 and +35 km s^{-1}. At 3σ confidence, we rule out any in-transit absorption of H I larger than 92% in the Lyman-α blue wing and 19% in the red wing. We found an in-transit flux decrease of $39\%^{+12\%}_{-11\%}$ in the ground-state C II emission line at 1334.5 Å. But due to this signal being significantly present in only one visit, it is difficult to attribute a planetary or stellar origin to the ground-state C II signal. We place 3σ absorption upper limits of 40, 49, and 24% on Si III, Si IV, and for excited-state C II at 1335.7 Å, respectively. Low activity levels and the faint X-ray luminosity suggest that WASP-29 is an old, inactive star. Nonetheless, an energy-limited approximation combined with the reconstructed EUV spectrum of the host suggests that the planet is losing its atmosphere at a relatively large rate of 4×10^9 g s^{-1}. The non-detection at Lyman-α could be partly explained by a low fraction of escaping neutral hydrogen, or by the state of fast radiative blow-out we infer from the reconstructed Lyman-α line.

Key words. stars: individual: WASP-29 – stars: chromospheres – planets and satellites: atmospheres – ISM: kinematics and dynamics

1. Introduction

The large population of transiting exoplanets yields the best opportunity to perform demographic studies aiming to characterize and understand their atmospheres. One of the main techniques to do so is transmission spectroscopy, which consists in measuring wavelength-dependent changes in the stellar spectrum when a planet transits its host star. The largest atmospheric signals of exoplanets detected to date have been obtained with transmission spectroscopy in far- and near-ultraviolet (FUV, NUV). This wavelength range traces the outermost parts of the atmospheres of transiting planets, where the lightest particles are susceptible to atmospheric escape. This has been observed in planets with H- and He-dominated atmospheres, such as the warm Neptunes GJ 436 b (Kulow et al. 2014; Ehrenreich et al. 2015; Bourrier et al. 2016; Lavie et al. 2017; dos Santos et al. 2019), GJ 3470 b (Bourrier et al. 2018b), the hot-Jupiters HD 209458 b (Vidal-Madjar et al. 2003, 2004, 2013; Ehrenreich et al. 2008), HD 189733 b (Lecavelier des Etangs et al. 2010, 2012; Bourrier et al. 2013), WASP-12 b (Fossati et al. 2010) and WASP-121 b (Sing et al. 2019), and tentatively for the temperate sub-Neptune K2-18 b (dos Santos et al. 2020b).

These signals point to the presence of H-rich, extended atmospheres and mass loss in both ends of the gas giant demographic, but the middle range that includes hot and warm Saturn-sized planets remains poorly explored (Fig. 1). Direct and indirect

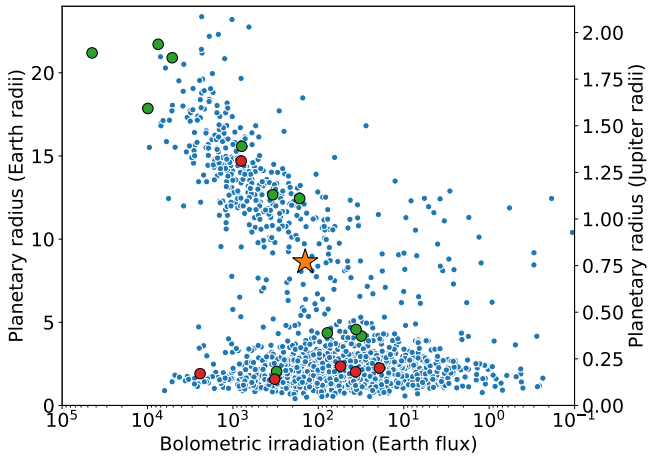

Fig. 1. Population of exoplanets with known radius and bolometric irradiation (taken from the NASA Exoplanets Archive on 01 Feb. 2021). Planets with confirmed atmospheric escape signatures of H, He or metals are shown as green symbols. Non-detections are shown as red symbols. WASP-29 b is represented as a star symbol.

observational evidence has shown that mass loss is one of the most important drivers for atmospheric evolution in short-period Neptune-sized exoplanets, as well as planetary migration and formation (e.g., Szabó & Kiss 2011; Beaugé & Nesvorný 2013; Mazeh et al. 2016; Helled et al. 2016; Matsakos & Königl 2016; Owen & Lai 2018; Bourrier et al. 2018b; McDonald et al. 2019; Armstrong et al. 2020); although, readers can refer to Cubillos et al. (2017), Kite et al. (2019), and Vidotto & Cleary (2020) for possible counterpoints. Such a conclusion is backed up by a strong theoretical framework as well (e.g., Lecavelier Des Etangs 2007; Rogers et al. 2011; Sanz-Forcada et al. 2011; Kurokawa & Nakamoto 2014; Tian 2015; Salz et al. 2016a). For a detailed review on the subject, readers can look to Owen (2019). This atmospheric evolution results in close-in Neptunes having short lifetimes, imprinting a feature in the population of known transiting exoplanets known as the hot-Neptune desert (Szabó & Kiss 2011; Mazeh et al. 2016; Bourrier et al. 2018b).

Hot Jupiters have been shown to be too massive to lose a significant fraction of their atmospheres due to photoevaporation (e.g., García Muñoz 2007; Hubbard et al. 2007; Ehrenreich & Désert 2011; Allan & Vidotto 2019). However, García Muñoz & Schneider (2019) have proposed that ultra-hot Jupiters orbiting early-type stars, such as KELT-9 b, may have lifetimes of less than 1 Gyr due to near-ultraviolet energy deposited through Balmer absorption. The lack of direct observational constraints on mass loss for Saturn-sized planets at the borders of the hot-Neptune desert contributes to the aforementioned poorly explored demographic. By directly detecting and assessing the current atmospheric rate and other properties of a sample of planetary systems, it is possible to tease apart the respective roles of planetary formation, migration, stellar wind, and photoevaporation in shaping the observed demographics of gas giants (Jin et al. 2014; Owen & Lai 2018; Vidotto & Cleary 2020).

One of the objectives of the *Hubble* Space Telescope Panchromatic Comparative Exoplanetology (HST PanCET) program is to address questions about atmospheres of gas giant transiting planets at a demographic level. One of the targets of this program is WASP-29 b, a low-density and moderately irradiated Saturn-sized planet orbiting every 3.92 d around a K4V-type star first discovered by Hellier et al. (2010, the stellar and planetary parameters are listed in Table 1). A previous attempt at

Table 1. Stellar and planetary parameters of the WASP-29 system.

Stellar parameters of WASP-29		Ref.
Radius	$0.813^{+0.033}_{-0.015}\ R_\odot$	(a)
Mass	$0.825 \pm 0.033\ M_\odot$	(b)
Eff. temperature	4731^{+44}_{-95} K	(a)
Proj. rot. velocity	1.5 ± 0.6 km s^{-1}	(b)
Radial velocity	24.48 ± 0.43 km s^{-1}	(a)
Distance	87.82 ± 0.31 pc	(a)
Sp. type	K4V	(c)
Planetary parameters of WASP-29 b		**Ref.**
Radius	$0.792^{+0.056}_{-0.035}\ R_{\rm Jup}$	(b)
Mass	$0.245^{+0.023}_{-0.022}\ M_{\rm Jup}$	(b)
Density	0.61 ± 0.12 g cm^{-3}	(b)
Eq. temperature	$970.0^{+32.0}_{-31.0}$ K	(c)
Orbital period	3.9227186 ± 0.0000068 d	(b)
Semi-major axis	$0.04566^{+0.00060}_{-0.00062}$ au	(b)
Ref. time (BJD)	$2455830.18886 \pm 0.00016$	(b)
Transit duration	$2.6486^{+0.0170}_{-0.0151}$ h	(b)
Orbital inclination	88.80 ± 0.70 deg	(b)
Eccentricity	<0.059	(b)

References. (a) Gaia Collaboration (2018), (b) Bonomo et al. (2017), (c) Gibson et al. (2013).

studying the atmosphere of WASP-29 b using ground-based, low-resolution (R < 1000) transmission spectroscopy between 515 and 720 nm yielded a featureless spectrum (Gibson et al. 2013). In particular, the lack of a broad Na feature indicates that either the planet does not have neutral Na in its upper atmosphere, or that clouds and hazes obscure the broad wings of the feature, resulting in a narrow absorption that is not detectable at low spectral resolution.

In this paper, we report on the data analysis and results of several transits of WASP-29 b observed with HST in FUV, aiming to detect and study its upper atmosphere. In particular, we are interested in addressing the following open issues: (i) how the high-energy environment around WASP-29 b influences the observable signatures of atmospheric escape; (ii) what escape rates should we expect for hot Saturns similar to WASP-29 b; and (iii) whether it shows signals of hydrodynamic escape such as hot Jupiters and warm Neptunes. This manuscript has the following structure: in Sect. 2 we describe the HST observations and data reduction; in Sects. 3 and 4 we present the analysis of the flux time series and the search for planetary signals in transmission; in Sect. 5 we discuss the reconstruction of the unobservable high-energy spectrum of WASP-29; and in Sect. 6 we present the conclusions of this work.

2. Description of observations

We observed six transits of WASP-29 b in the HST PanCET program (GO-14767, PIs: D. Sing and M. López-Morales), of which three were performed with the Cosmic Origins Spectrograph (COS; Visits A, B, and C) and three with the Space Telescope Imaging Spectrograph (STIS; Visits D, E, and F). Each transit was observed in a single visit with five orbits in time-tag mode. The uncertainty of the transit midpoint time propagated to our latest exposure (21 August 2019) is 7.6 min, based on the ephemeris of Bonomo et al. (2017). The COS observations were

Table 2. Observations log of WASP-29 in the HST PanCET program.

Visit	Orbit	Start time (UT)	Exp. time (s)	Phase (h)
		COS spectroscopy		
A	1	2018-05-19 15:49:32	2182.144	−3.54
	2	2018-05-19 17:08:21	2706.112	−2.01
	3	2018-05-19 18:43:40	2706.112	−0.42
	4	2018-05-19 20:20:47	2706.176	+1.20
	5	2018-05-19 22:01:53	2706.176	+2.85
B	1	2018-07-17 12:30:51	2182.112	−3.97
	2	2018-07-17 13:56:29	2706.144	−2.47
	3	2018-07-17 15:31:55	2706.176	−0.88
	4	2018-07-17 17:09:16	2706.112	+0.74
	5	2018-07-17 18:48:57	2706.144	+2.40
C	1	2018-11-04 09:01:12	2182.208	−4.48
	2	2018-11-04 10:29:04	2706.208	−3.09
	3	2018-11-04 12:04:32	2706.208	−1.51
	4	2018-11-04 13:41:15	2706.176	+0.11
	5	2018-11-04 15:20:13	2706.208	+1.80
		STIS spectroscopy		
D	1	2019-08-09 20:50:56	1751.159	−3.90
	2	2019-08-09 22:14:23	1983.173	−2.48
	3	2019-08-09 23:49:48	1983.189	−0.89
	4	2019-08-10 01:25:12	1983.179	+0.70
	5	2019-08-10 03:00:36	1983.195	+2.29
E	1	2019-08-17 17:54:04	1751.138	−3.14
	2	2019-08-17 19:21:08	1983.132	−1.66
	3	2019-08-17 20:56:28	1983.115	−0.07
	4	2019-08-17 22:31:47	1983.187	+1.52
	5	2019-08-18 00:07:06	1983.183	+3.11
F	1	2019-08-21 15:37:18	1751.147	−3.57
	2	2019-08-21 17:04:49	1983.181	−2.08
	3	2019-08-21 18:40:08	1983.015	−0.49
	4	2019-08-21 20:15:27	1983.193	+1.10
	5	2019-08-21 21:50:46	1983.197	+2.69

Notes. Phases are in relation to the orbit of WASP-29 b.

set to spectroscopic element G130M centered at 1291 Å and a circular aperture with diameter 2.5 arcsec, yielding wavelength ranges [1134, 1274] Å and [1290, 1429] Å. The STIS observations were set to spectroscopic element G140M centered at 1222 Å and a slit with dimensions 52×0.1 arcsec (the observations log is shown in Table 2), yielding a wavelength range [1194, 1248] Å.

2.1. Data reduction

The COS data were reduced automatically by the instrument pipeline. The STIS data required some custom reduction due to strong background contamination in some exposures. The custom STIS reduction consists in using the pipeline flat-fielded frames to extract the spectra and perform background removal. We extracted the spectra following a similar procedure as in dos Santos et al. (2020b), in which we manually set the cross-dispersion positions of the spectra and the background; the extraction box width was kept the same as in the pipeline reduction. We determined, by visual inspection, the spectrum

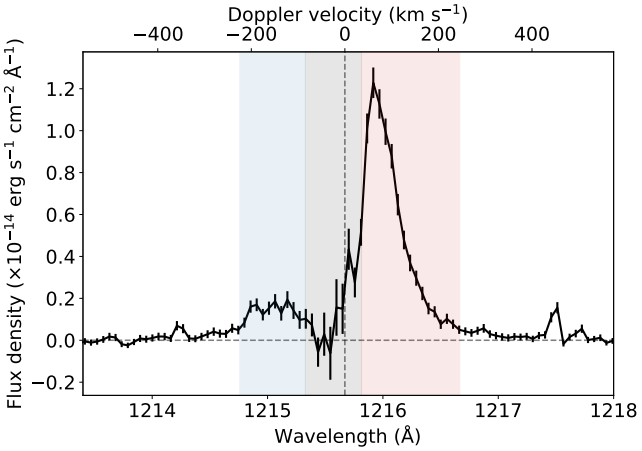

Fig. 2. Observed Lyman-α spectrum of WASP-29 with HST-STIS in a total exposure time of 8 h. The gray band represents the wavelength span with strong geocoronal contamination (removed in data reduction). The blue and red regions represent the respective blue and red wings. The Doppler velocities are in the stellar rest frame.

cross-dispersion positions to be $y = 189$ px and set the background to be centered 20 px away from the spectrum. We combined all STIS exposures to produce a high signal-to-noise Lyman-α spectrum, which is shown in Fig. 2. We used the time-tag information of the STIS and COS exposures to produce four subexposures per orbit.

2.2. Treatment of uncertainties

WASP-29 is a faint star in FUV, which means the observed count rates are limited to just a few photons per exposure (except for the Lyman-α line, which is the brightest feature in this wavelength region). In this regime, the uncertainties of the flux measurements do not follow a Gaussian distribution, but rather a Poisson distribution. Both pipelines of STIS and COS (respectively `calstis` and `calcos`) can calculate the uncertainties of FUV observations using Poisson confidence intervals. In particular, `calcos` produces confidence intervals calculated with the methodology outlined in Gehrels (1986), while `calstis` returns confidence intervals assuming Gaussian noise[1].

Due to the non-Gaussian nature of these uncertainties, care has to be taken when propagating them. This is particularly important when calculating the final uncertainties of, for example, transmission spectra, fluxes inside a pass band that is several pixels wide, or combined exposures to produce a higher signal-to-noise spectrum. It is unclear if this is the same effect seen by Wilson et al. (2017), who reported overestimated flux uncertainties produced by the `calcos` pipeline.

In this work, when computing light curves of spectral lines and combining spectra from COS, we work with the raw or net counts and, at the final step, convert them to the physical flux in order to perform a proper treatment of uncertainties. The 1σ uncertainties are calculated from the confidence intervals of a Poisson distribution based on the raw number of counts registered in the detector, which includes background sources. The conversion between counts and physical flux is performed using the tabulated sensitivity of the detector. The STIS Lyman-α spectra possess count rates at least one order of magnitude higher

[1] Except for time-tag split data processed with the `inttag` method of `calstis`, which also produces uncertainties based on the methodology of Gehrels (1986).

Table 3. Correlation between Lyman-α red wing fluxes and jitter data.

	Visit D		Visit E		Visit F	
	Spearman-r	p-value	Spearman-r	p-value	Spearman-r	p-value
$V_{\rm d,dom}$	−0.547	0.012	+0.223	0.346	−0.293	0.210
$V_{\rm d,roll}$	−0.505	0.023	+0.206	0.384	−0.200	0.398
$V_{\rm s,dom}$	−0.030	0.900	−0.260	0.269	−0.186	0.431
$V_{\rm s,roll}$	+0.164	0.490	+0.268	0.254	+0.006	0.980
Longitude	−0.090	0.705	+0.147	0.535	+0.268	0.254
Latitude	−0.017	0.945	−0.376	0.102	−0.134	0.574
Right ascension	+0.365	0.113	−0.129	0.587	+0.487	0.029
Declination	−0.564	0.010	+0.202	0.394	−0.215	0.363

than those of COS, so the assumption of Gaussian uncertainties is appropriate for STIS spectra.

2.3. Search for instrumental systematics

The engineering jitter files of HST contain telemetry and pointing information that can be used to understand potential systematic trends in long-slit observations with STIS. This method was first used by Sing et al. (2019) and we apply our implementation of the technique. The main source of systematic trends in STIS data is slit losses, which are caused by two effects: (i) changes in the position of the target star in the slit, both in the dispersion and cross-dispersion directions, and (ii) changes in the point-spread function (PSF) seen by the detector due to thermal variations of the telescope – also known as breathing. Previous ultraviolet studies with HST have shown that these systematic trends are more important the brighter is the observed star (e.g., Bourrier et al. 2017c, 2018a; Sing et al. 2019), and are not present in COS spectroscopy (dos Santos et al. 2019).

The pointing of the telescope can be traced by the right ascension and declination data present in the jitter data, but what matters in our case is the position of the target in relation to the slit. While we do not know exactly where our target is in relation to the slit at a sub-pixel level, we can gather this information from the jitter data of the guide stars. Usually, HST observations are performed with two guide stars, called dominant and roll; their positions in relation to the V_2 and V_3 axes of the telescope are traced to sub-pixel levels; since the slit is not aligned to the reference axes of the telescope, we need to rotate the dominant and roll position vectors to the slit reference frame – we call these new vectors $V_{\rm d}$ (dispersion direction) and $V_{\rm s}$ (spatial, or cross-dispersion direction).

In order to infer if the jitter trends cause slit losses in the STIS exposures, we searched for correlations between the observed Lyman-α red wing emission fluxes of the time-tag split data and the jitter data using the Spearman-r coefficient (Spearman 1904). The results are shown in Table 3. Despite Visit E displaying the strongest jitter trends, the correlation with the Lyman-α fluxes are weak, with p-values above 0.10. In relative terms, the strongest (anti-)correlations are seen in Visit D, where the guide star $V_{\rm d}$ vector and the declination have Spearman-r coefficients around 0.50 in modulus. Nevertheless, in absolute terms, these coefficients are below the threshold of 0.75 in modulus to be considered significant. Thus we conclude that there are negligible jitter trends in our STIS dataset.

We also searched for breathing effects by phase folding the subexposures to the orbit of HST and comparing the data to Fourier decomposition models (as in Bourrier et al. 2017c). We evaluated the likelihood of breathing effects by comparing the Bayesian Information Criterion (BIC) of models with varying orders fitted to the observed data. In all visits a flat model with no systematics is favored against higher order models: ΔBIC = 20 for Visit D, ΔBIC = 9 for Visit E, and ΔBIC = 12 for Visit F.

3. Lyman-α emission time series

The Lyman-α emission line (H I) is the strongest feature in the far-ultraviolet spectrum of cool stars (Linsky 2017) and plays an important role in the photochemistry of planetary atmospheres (Segura et al. 2005). For stars other than the Sun, the Lyman-α emission is partially or completely absorbed by the interstellar medium (ISM). For the nearest stars, the core of the line is inaccessible, but its wings can still be observed, yielding the usual double-peaked profile (Fig. 2). The shape of this observed profile will depend on the properties of the intrinsic stellar emission, the physical properties of the ISM, and the radial velocity of the observed star.

Atmospheric signatures in hot transiting exoplanets have been previously detected as a large (>10%) absorption in the Lyman-α line, which traces exospheric H I atoms (e.g., Vidal-Madjar et al. 2003; Lecavelier des Etangs et al. 2012; Ehrenreich et al. 2015; Bourrier et al. 2018b). Such a signal indicates the presence of a H-rich exospheric cloud being accelerated by radiation pressure and interactions with the stellar wind through charge exchange. We searched for a similar feature in the Lyman-α transit time series of WASP-29. At first, this search was performed by visual inspection of the Lyman-α profiles (Fig. 3). Upon concluding that there was no obvious signal, we performed a light curve analysis of the fluxes in the blue and red wing bandpasses. We define these bandpasses by the limits of the geocoronal contamination ([−60, +60] km s^{-1} in the heliocentric restframe, or [−84, +35] km s^{-1} in the stellar restframe) and the approximate limits where the stellar flux is above the 1σ noise floor of the instrument. This yields the blue and red wing bandpass limits as [−224, −84] km s^{-1} and [+35, +245] km s^{-1}, respectively.

In a single STIS exposure, we can measure the Lyman-α blue wing flux with a mean precision of 41.6, 30.4, and 29.1%, respectively for visits D, E, and F. In the case of the red wing fluxes, the mean precision values are 10.4, 9.5, and 9.9%, respectively. Due to potential stellar flux modulation in the time scales that separate the visits, we normalize each time series by the out-of-transit flux. This baseline is measured as the average flux in orbits 1, 2, and 5 of each visit. We fit the normalized light curves to transit models calculated with `batman` (Kreidberg 2015) and estimate

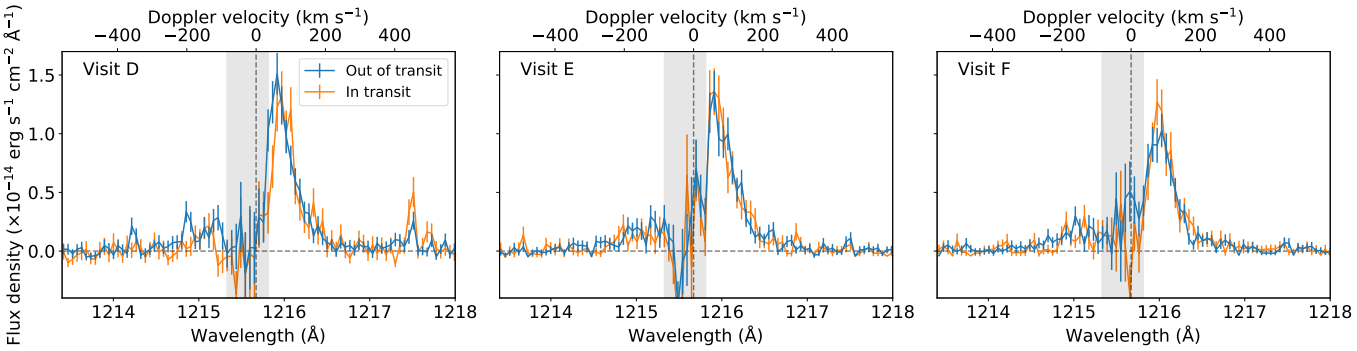

Fig. 3. In- and out-of-transit Lyman-α spectra of WASP-29 in Visits D, E, and F. The shaded region represents the interval where there is strong geocoronal contamination. We do not detect an obvious in-transit absorption signal.

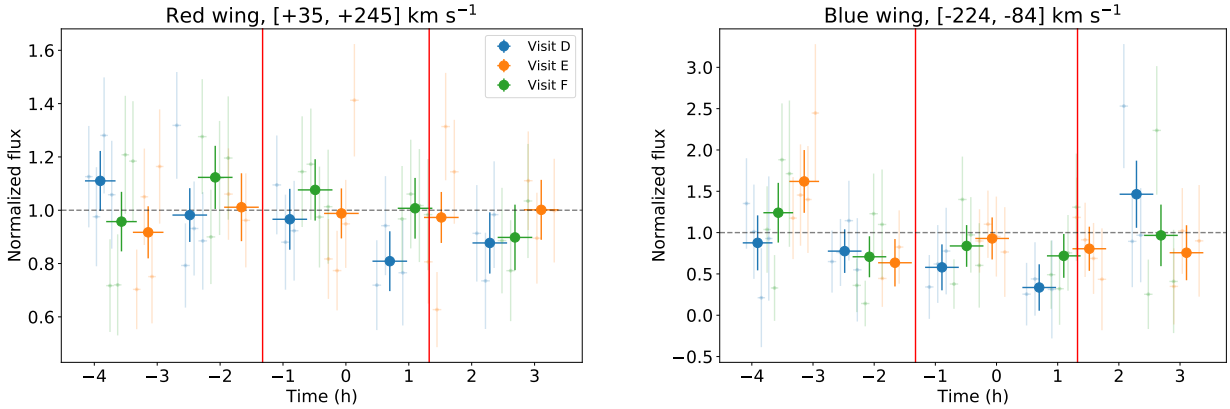

Fig. 4. Normalized Lyman-α light curves of WASP-29. The vertical red lines represent the times of first and fourth contacts of the transit of WASP-29 b. Each HST orbit is represented as a full symbol, while semi-transparent symbols represent sub-exposures within each orbit.

the uncertainties of the fit using the Markov chain Monte Carlo ensemble sampler implementation of `emcee` (Foreman-Mackey et al. 2013). We fix the orbital parameters of WASP-29 b to the values shown in Table 1 and vary only the depth $(R_p/R_*)^2$.

There is a flux decrease of ∼20% in the Lyman-α red wing in Visit D, a feature that is seen in the in- and out-of-transit Lyman-α profiles in Fig. 3, and the light curve of the red wing in Fig. 4. For comparison, GJ 436 shows an episodic red wing in-transit absorption as well (dos Santos et al. 2019), but its origin remains unknown. Since this feature is not repeated in the other STIS observations of our program, we deem it unlikely to arise from the exosphere of WASP-29 b. Since the absorption takes place near the core of the Lyman-α emission of WASP-29, it is possible that the decrease in flux can be caused by stellar activity modulation. Similar to the case of HD 97658 in Bourrier et al. (2017c), stellar activity is expected to modulate the wavelength region nearest to the line core, which is formed at higher temperatures in the stellar corona, than its wings.

We did not find evidence to support Lyman-α flux absorption during the transit of WASP-29 b. Using the technique described above and by combining all the visits, we rule out any in-transit absorption depth larger than 49% (92%) in the blue wing at 1σ (3σ) confidence. For the red wing light curves, we rule out any in-transit absorption signals above 9% (19%) at 1σ (3σ) confidence.

For comparison, the H I detection in HD 209458 b showed an in-transit depth of $15\% \pm 4\%$ in two bandpasses near the line core, between Doppler velocities −130 and +100 km s^{-1} (excluding the wavelength interval with geocoronal emission contamination; Vidal-Madjar et al. 2003). The hot-Jupiter HD 189733 b displays H I transit depths of $14.4 \pm 3.6\%$ between Doppler velocities −230 km s^{-1} and −140 km s^{-1} (Bourrier et al. 2013). The warm Neptunes GJ 436 b and GJ 3470 b display Lyman-α transit depths around 50% in the Doppler velocity interval [−120, −40] km s^{-1} (Ehrenreich et al. 2015; Bourrier et al. 2018b).

4. Metallic species time series

To date, all detections of exospheric metals in transiting planets have been found in the hot Jupiters HD 209458 b (Vidal-Madjar et al. 2004, 2013; Linsky et al. 2010), HD 189733 b (Ben-Jaffel & Ballester 2013), WASP-12 b (Fossati et al. 2010) and WASP-121 b (Sing et al. 2019). Sing et al. (2019) argue that exospheric metals in WASP-121 b can be observed in transmission when the exobase extends beyond the Roche lobe, allowing heavier species in the upper atmosphere to escape the planet. A search for such features in GJ 436 b, which benefited from a more extensive dataset covering several years, resulted in non-detections only (Lavie et al. 2017; Loyd et al. 2017; dos Santos et al. 2019). We perfomed a similar analysis for the three transits of WASP-29 b; the host star is fainter than GJ 436, thus we could analyze fewer spectral lines in the COS spectrum. The COS profiles of C II, Si III, Si IV, and N V are shown in Fig. 5, and their respective transit light curves are shown in Fig. 6.

Similarly to the Lyman-α analysis, we fit the observed time series with transit light curve models to assess the absorption depth and its statistical significance. We found that the stellar flux in the line that arises from the ground-level state C II (1334.5 Å) decreases by $39\%^{+12\%}_{-11\%}$; but we cannot rule out

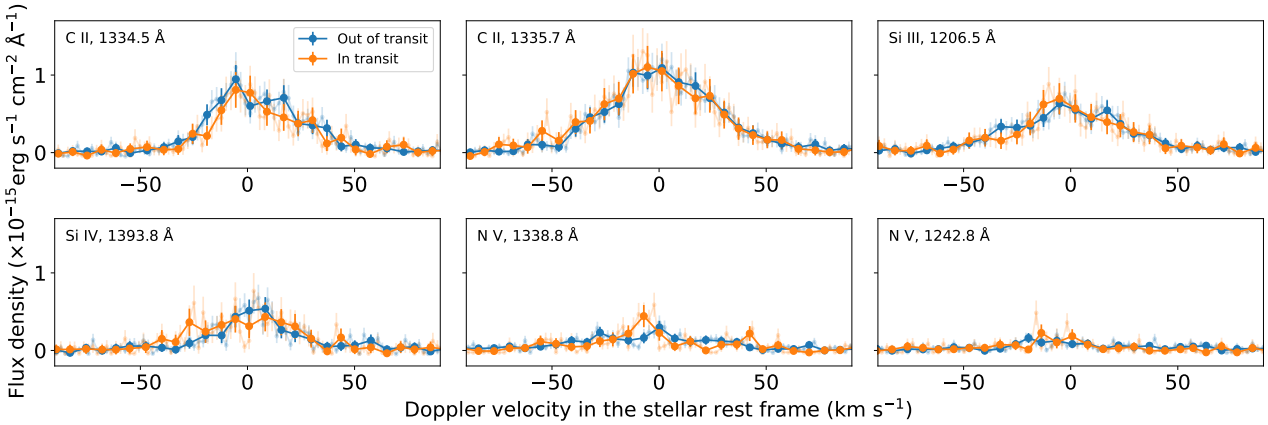

Fig. 5. In- and out-of-transit metallic spectral lines of WASP-29 in Visits A, B, and C.

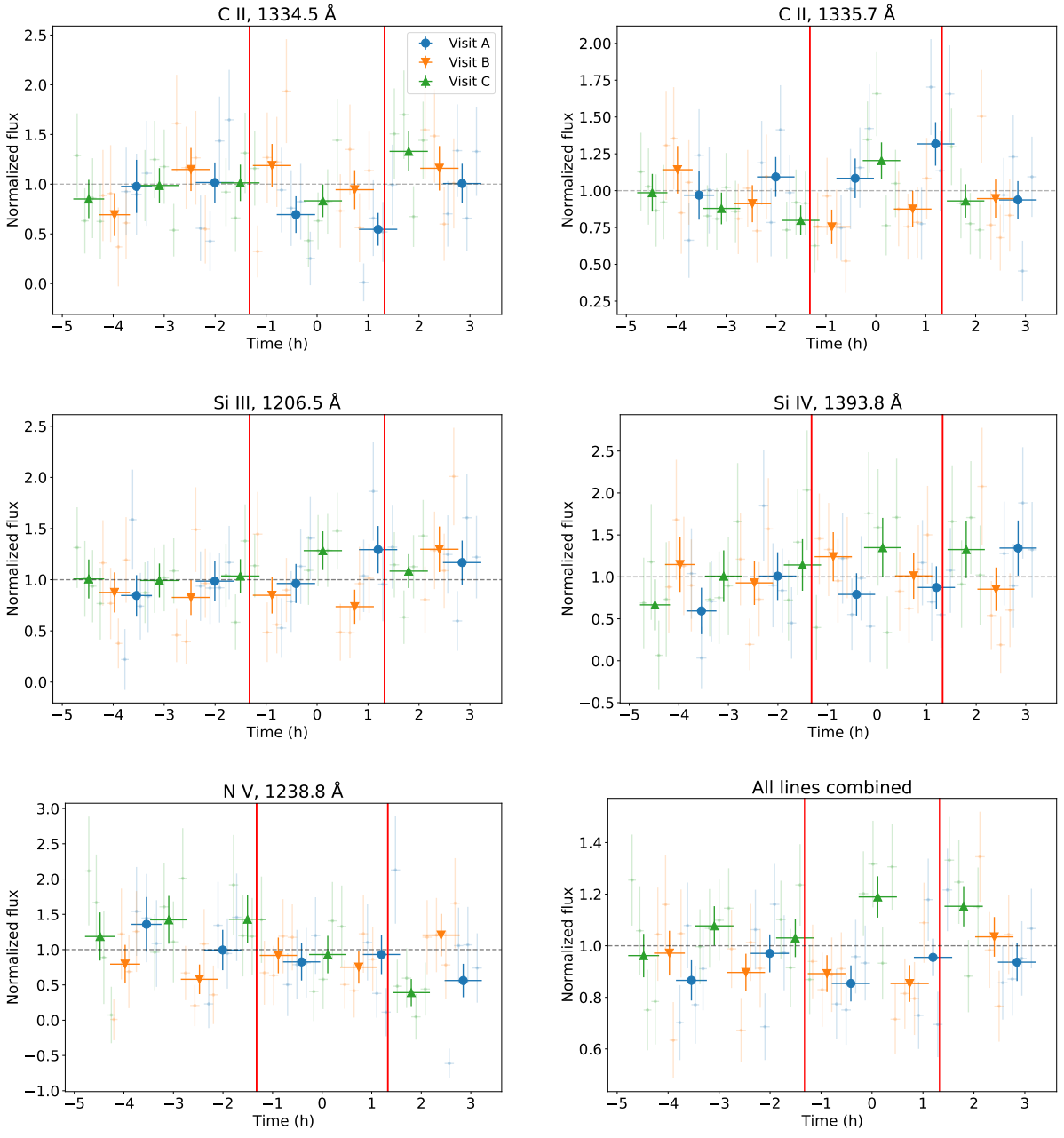

Fig. 6. Light curves of the metallic species emission lines of WASP-29 in the COS visits. The vertical red lines represent the times of first and fourth contacts of the transit of WASP-29 b. Each HST orbit is represented as a full symbol, while semi-transparent symbols represent sub-exposures within each orbit.

Table 4. Observed fluxes of WASP-29 and upper limits of the in-transit absorption depth for WASP-29 b.

Species	Wavelength (Å)	Integration range (km s^{-1})	Flux ($\times 10^{-16}$ erg s^{-1} cm^{-2})	Transit depth	
				1σ	3σ
C II	1334.5	[−60, +60]	1.94 ± 0.11	$39\%^{+12\%}_{-11\%}$	$39\%^{+40\%}_{-31\%}$
C II	1335.7	[−80, +80]	2.88 ± 0.12	<10%	<24%
Si III	1206.5	[−80, +80]	1.33 ± 0.07	$11\% \pm 9\%$	<40%
Si IV	1393.8	[−60, +60]	0.92 ± 0.07	<17%	<49%
N V	1238.8	[−80, +80]	0.63 ± 0.04	<31%	<70%

possible stellar variability effects that could mimic planetary signals since a similar "dip" is also seen before the transit between −5 and −4 h in relation to the transit center. Furthermore, no clear-cut signal is seen in the combined C II spectra (Fig. 5). For comparison, Linsky et al. (2010) detected an in-transit absorption of $7.8 \pm 1.3\%$ in the combined flux of the C II doublet for HD 209458 b using COS spectra; that result matched well the marginal 2σ detection of Vidal-Madjar et al. (2004), which was performed with the STIS spectrograph. García Muñoz et al. (2021) reported a 3.4σ detection of excited-level C II during one transit of the super-Earth π Men c that is consistent with ions filling the Roche lobe of the planet and moving away from the star. The decrease in C II flux that we observe in WASP-29 b is dominated by Visit A only, while Visits B and C are consistent with flat light curves. Since the signal in Visit A is not repeatable, we deem this decrease in flux as unrelated to the planet WASP-29 b.

The normalized light curve of the line arising from the excited-level C II atom (1335.7 Å) is suggestive of a W-shaped time series. Such a transit light curve could be indicative of FUV limb-brightening in the stellar host, a well known phenomenon in the Sun (Minnis 1955). The effect is clearer when we look at the time-tag subexposures, which are shown as semi-transparent points in Fig. 6. This behavior would not arise from the shape of the planetary atmosphere, but from the limb-brightened chromosphere and transition region of the host star. However, more observations would be needed to confirm this feature for WASP-29 b. Since the excited-level C II line is the strongest feature in the COS spectra after Lyman-α, it dominates the flux of the "all lines combined" light curve (lower right panel in Fig. 6) and the W-shape remains present. The COS light curves show that there are no obvious signatures of Si III, Si IV or N V ions populating the exosphere of WASP-29 b. We calculated the 1 and 3σ upper limits for the in-transit absorption depth and the observed COS fluxes, and the results are shown in Table 4.

5. The high-energy environment of WASP-29 b

The STIS and COS observations provide useful information about the stellar UV irradiation and its impact on the planet upper atmosphere, as well as constraints on the ISM. They also allow us to interpret the non-detections of atmospheric signals and to predict signals that could be observed in other wavelengths. The ISM absorbs a large portion of the stellar emission at short wavelengths, including the Lyman-α emission and the extreme ultraviolet (EUV) spectrum, so they need to be reconstructed.

5.1. Reconstruction of the intrinsic Lyman-α line

We used the STIS observations of WASP-29 to reconstruct its intrinsic Lyman-α spectrum following the standard method used in, for example, Bourrier et al. (2017a) and Bourrier et al. (2018b). In short, we fit the observed spectrum to a model of the intrinsic emission line attenuated by ISM absorption (H I and deuterium), scaled for distance, and convolved with the instrumental response. The model is oversampled in wavelength and rebinned over the STIS spectral table after convolution; the fit yields an estimate of the intrinsic emission and certain properties of the ISM in the line of sight.

Since no signatures of planetary absorption or stellar variability were found in any of the visits, the reconstruction was performed using all available spectra averaged into one master spectrum per visit. In all visits we excluded from the fit the velocity range $[-60, 60]$ km s^{-1} (heliocentric rest frame), which is too contaminated by geocoronal emission. We fit the three master spectra together using the Markov chain Monte Carlo (MCMC) software package *emcee* (Foreman-Mackey et al. 2013). K dwarfs can show either double-peaked or single-peaked Lyman-α profiles, depending on the presence of a self-reversal[2] in their core (e.g., Wood et al. 2005; Youngblood et al. 2016; Bourrier et al. 2017b). We found that a single-peaked Voigt profile provides the best fit to the WASP-29 intrinsic Lyman-α line. The theoretical intrinsic line profile is defined by its centroid, its temperature (assuming pure thermal broadening), its Voigt damping parameter, and its total flux $F_{\mathrm{Ly}-\alpha}(1\,\mathrm{au})$. Except for the total flux, all properties were set to the same value for the three visits. The line centroid was fixed to the systemic velocity of WASP-29 (24.48 km s^{-1}, as in Table 1). The absorption profile of the ISM along the line of sight is common to the three visits, and defined by its column density of neutral hydrogen $\log_{10} N_{\mathrm{ISM}}(\mathrm{H\,I})$, its Doppler broadening parameter $b_{\mathrm{ISM}}(\mathrm{H\,I})$, and its heliocentric radial velocity $v_{\mathrm{ISM}/\odot}$. The D I/H I ratio was set to 1.5×10^{-5} (e.g., Hébrard & Moos 2003; Linsky et al. 2006). We adopted the Lyman-α oscillator strength $f = 0.41641$ from the NIST database[3]. The Doppler broadening of the ISM toward WASP-29 is not constrained by its saturated Lyman-α line absorption profile, and was fixed to the value of the Local Interstellar Cloud (LIC).

We obtain a minimum χ^2 of 166 for 151 degrees of freedom (reduced $\chi^2 = 1.1$). The best-fit model for the line averaged over the three visits is shown in Fig. 7. The LISM kinematic calculator[4], a dynamical model of the local ISM (Redfield & Linsky 2008), predicts that the line of sight toward WASP-29 crosses the LIC cloud with a heliocentric radial velocity of −1.29 km s^{-1}. This is in very good agreement with our

[2] A self-reversal in Lyman-α happens in some stars, like the Sun, because there is a layer in of absorbing material in the stellar atmosphere between the region where the line is formed and the outermost stellar layers (see, e.g., Warren et al. 1998).

[3] Available in https://physics.nist.gov/PhysRefData/ASD/lines_form.html

[4] http://sredfield.web.wesleyan.edu/

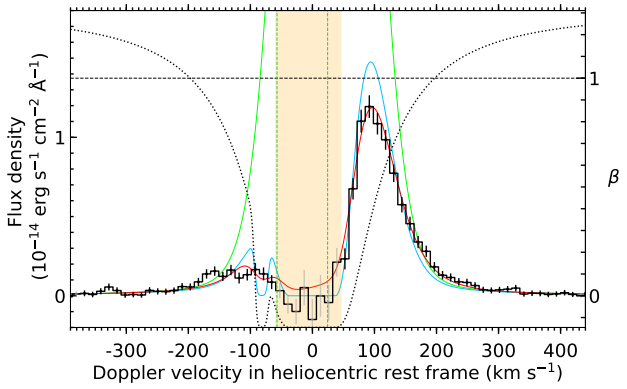

Fig. 7. Lyman-α line profile of WASP-29 averaged over the three visits. The black histogram shows the observed spectra, fit over points with black error bars. The orange band shows the region strongly contaminated by geocoronal emission to be excluded from the fit. The green full line is the best fit for the intrinsic stellar line profile, and the green dotted line represents the zero velocity in the stellar rest frame. It yields the blue profile after absorption by the interstellar medium, whose profile is plotted as a dotted black line (ISM absorption in the range 0–1 has been scaled to the vertical axis range). The red line shows the line profile fit to the data, after convolution with the STIS instrumental profile. The theoretical intrinsic stellar line profile also corresponds to the profile of the ratio β between radiation pressure and stellar gravity, which is shown in the right y-axis.

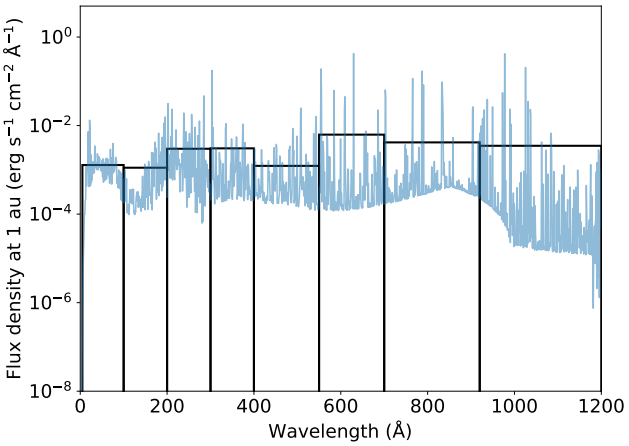

Fig. 8. Synthetic X+EUV spectrum of WASP-29 in high resolution (blue) and low resolution (black).

derived value of -0.1 ± 2.6 km s^{-1}. Our best-fit column density ($\log_{10} N_{\rm ISM}$(H I) = 18.55 ± 0.04 cm^{-2}) is also consistent with the range of values expected for a star at a distance of 87.8 pc (Fig. 14 in Wood et al. 2005).

The total flux in the observed and reconstructed Lyman-α lines shows no significant variations between the three visits, strengthening the long-term stability of the stellar UV emission. The average line flux $F_{{\rm Ly}-\alpha}(1\,{\rm au}) = 17.6^{+2.1}_{-1.6}$ erg s^{-1} cm^{-2} yields a rotation period of about 20 days for WASP-29 from the empirical relation in Youngblood et al. (2016). In Fig. 7, the β parameter is the ratio between radiation pressure and stellar gravity; our reconstruction shows that radiation pressure from WASP-29 Lyman-α line overcomes its gravity by a factor of seven at velocities between [−100 and 100] km s^{-1} in the stellar rest frame. This is much larger than the factor 3 associated with the K0 dwarfs HD 189733 and HD 97658 (Bourrier et al. 2013, 2017c), or even the factor ∼4.5 associated with the G0 dwarf HD 209458 (Bourrier & Lecavelier des Etangs 2013), suggesting that the putative neutral hydrogen exosphere of WASP-29 b is quickly accelerated away from the planet in a strong regime of radiative blow-out.

5.2. Reconstruction of the X-rays and extreme ultraviolet spectrum

The results for COS observations allow us to provide constraints on the X-rays and extreme ultraviolet (X+EUV) emission of WASP-29, a part of its high-energy spectrum that is widely absorbed by the ISM and not straightforward to measure directly. WASP-29 was also observed by *XMM-Newton* (Prop. ID: 80479, PI: J. Sanz-Forcada) in 14 May 2017. During the 6.9 ks exposure only an upper-limit detection was made ($S/N = 2$) in the European Photon Imaging Camera (EPIC). We measured an X-ray luminosity of $L_{\rm X} < 3.4 \times 10^{26}$ erg s^{-1} in the 0.12–2.48 keV spectral range (5–100 Å). Based on this upper limit, we used a coronal model to construct the synthetic spectrum in the region 1–1200 Å, following Sanz-Forcada et al. (2011). We used the EPIC spectra to model the coronal temperatures, and the well-constrained COS fluxes (Sect. 4) to model the transition region. The model-derived fluxes at 1 au in different EUV bands are 2.74 erg s^{-1} cm^{-2} (100–920 Å), and 0.78 erg s^{-1} cm^{-2} (100–504 Å), for the first ionization edges of H and He, respectively (Fig. 8). The resulting X+EUV (5–920 Å) flux at 1 au is 3.98 erg s^{-1} cm^{-2}. Further details of the coronal model will be given elsewhere (Sanz-Forcada et al., in prep.). The observed X-ray emission is rather low for a K4V star (Pizzolato et al. 2003), which implies that WASP-29 is an aged star with a low state of activity.

Using the energy-limited approximation (Salz et al. 2016b), we estimate a total mass loss rate of WASP-29 b at 4×10^9 g s^{-1} for 15% escape efficiency. This value is intermediate when compared to the rates inferred from observations of the hot Jupiters HD 209458 b and HD 189733 b, and the warm Neptunes GJ 436 b and GJ 3470 b, which range from 10^8 to 10^{11} g s^{-1} (Lecavelier des Etangs et al. 2010; Bourrier & Lecavelier des Etangs 2013; Bourrier et al. 2016, 2018b).

Similarly to Bourrier et al. (2017c), we estimate the photoionization rate and lifetime of atomic H around WASP-29 b based on the synthetic spectrum up to the ionization threshold of 911.8 Å (13.6 eV). We found that the H I photoionization rate is 11.8×10^{-5} s^{-1}, yielding a photoionization lifetime of 2.35 h. For comparison, the H I lifetimes around the warm Neptunes with detected exospheres GJ 436 b and GJ 3470 b are ∼12 h and 55 min, respectively (Bourrier et al. 2016, 2018b); in the case of the hot Jupiters with detected exospheres HD 209458 b and HD 189733 b, the photoionization lifetimes are ∼8 h and ∼3.5 h, respectively (Bourrier & Lecavelier des Etangs 2013). The most likely explanation for the non-detection of exospheric H I in WASP-29 b is a combination of the short photoionization lifetime, the fast acceleration of H atoms away from the planet by radiation pressure (also known as a "blow-out" regime), the low signal-to-noise ratio (S/N) in the Lyman-α blue wing and the strong ISM absorption precluding access to velocities between [−84, +35] km s^{-1}. Thus, it is possible that WASP-29 b is, in fact, currently losing its atmosphere, but the high-energy environment around the planet and the distance of the system in relation to Earth are not conducive to produce detectable signals in FUV transmission spectroscopy.

One possible alternative to search for atmospheric escape signals in WASP-29 b is through the metastable He I triplet near

1.083 μm (Seager & Sasselov 2000; Oklopčić & Hirata 2018) in transmission. This technique has been successfully applied in both space- and ground-based spectroscopy (e.g., Spake et al. 2018; Allart et al. 2018; Mansfield et al. 2018; Nortmann et al. 2018; Alonso-Floriano et al. 2019; Kirk et al. 2020). We computed the He I ionizing irradiation (up to 504 Å) level of WASP-29 b using the synthetic spectrum, and found a value of 0.44 W m^{-2} at the planet's orbit (440 erg s^{-1} cm^{-2}). For comparison, the hot Jupiter HD 209458 b receives an irradiation of approximately 1 W m^{-2}, and its He I signal was challenging to measure (Alonso-Floriano et al. 2019); it is possible that a significant amount of observational effort may be required to measure He I in the extended atmosphere of WASP-29 b, since the intensity of the planetary signal in this line depends on the level of ionizing XUV irradiation received (Nortmann et al. 2018). The planets GJ 436 b, KELT-9 b (Nortmann et al. 2018), and WASP-127 b (dos Santos et al. 2020a), which possess lower EUV irradiation levels than WASP-29 b, exhibit non-detections.

6. Conclusions

We observed six transits of WASP-29 b using the STIS and COS spectrographs installed on HST to search for signals of atmospheric escape in transmission. We did not find evidence for the presence of a H I exosphere around WASP-29 b, likely due to a combination of factors: short H I photoionization lifetime, a fast acceleration of H atoms away from the planet, and the low S/N in the Lyman-α emission between Doppler velocities [−100, +100] km s^{-1}, which is the range where we expect such signal to appear.

An analysis of the stellar flux time series from COS spectra did not reveal significant, repeatable evidence for escaping metallic species in the atmosphere of WASP-29 b. The stellar line fluxes remain mostly stable over the three observing epochs. We found only a tentative in-transit absorption in the ground-state C II emission near 1334.5 Å, but we were unable to disentangle it from stellar activity effects. This result reinforces the requirement of repeatability for FUV atmospheric signals since this in-transit absorption is dominated by only one of the three visits. One way to assess if the observed signal comes from planetary absorption is to search for atmospheric escape using the 1.083 μm metastable He triplet. If He is detected at high-altitudes around WASP-29 b, it is likely the planet is undergoing active atmospheric escape and thus would give support to the hypothesis of an atmospheric C II signal.

Despite these non-detections, our observations allowed us to constrain the high-energy spectrum of WASP-29, as well as the environment around WASP-29 b. We reconstructed the intrinsic Lyman-α spectrum of WASP-29 using the STIS observations, and found that the Lyman-α flux is stable when we compare the three different epochs of observation spanning a baseline of 12 days. Furthermore, this results suggests that the level of Lyman-α radiation pressure efficiently overcomes gravity by a factor of seven, which is higher than those observed for other G- and K-type exoplanet hosts, such as HD 189733, HD 97658, and HD 209458. This puts the planet WASP-29 b in a regime of faster radiative acceleration of H atoms compared to other hot giant exoplanets for which we have observed signals of H I escape. Future observations of He I escape in the 1.083 μm triplet may be able to provide better atmospheric escape constraints for WASP-29 b. We also used *XMM-Newton* observations to constrain its EUV spectrum using a coronal model. The low levels of stellar activity in FUV, lack of stellar flares (in contrast to, for example, GJ 436), and the inferred low X-ray luminosity strongly suggest that WASP-29 is an old star. Based on the reconstructed EUV spectrum, we estimate that WASP-29 b is currently losing its atmosphere at a total rate of 4×10^9 g s^{-1}, assuming a heating efficiency of 15%. This mass loss rate is intermediate between the rates observed in hot Jupiters and warm Neptunes through Lyman-α spectroscopy.

Acknowledgements. L.d.S. thanks the valuable discussions with P. Wheatley on the results of this manuscript. G.W.H. acknowledges long-term support from NASA, NSF, Tennessee State University, and the State of Tennessee through its Centers of Excellence program. A.L.d.E. acknowledges the CNES for financial support. J.S.F. acknowledges support from the Spanish State Research Agency projects AYA2016-79425-C3-2-P and PID2019-109522GB-C51. We are grateful for the helpful feedback provided by the anonymous referee. This project has received funding from the European Research Council (ERC) under the European Union's Horizon 2020 research and innovation programme (project FOUR ACES grant agreement No 724427; project SPICE DUNE grant agreement No 947634), and it has been carried out in the frame of the National Centre for Competence in Research PlanetS supported by the Swiss National Science Foundation (SNSF). This research is based on observations made with the NASA/ESA *Hubble* Space Telescope. The data are openly available in the Mikulski Archive for Space Telescopes (MAST), which is maintained by the Space Telescope Science Institute (STScI). STScI is operated by the Association of Universities for Research in Astronomy, Inc. under NASA contract NAS 5-26555. This research made use of the NASA Exoplanet Archive, which is operated by the California Institute of Technology, under contract with the National Aeronautics and Space Administration under the Exoplanet Exploration Program. We used the open source software SciPy (Jones et al. 2001), Jupyter (Kluyver et al. 2016), Astropy (Astropy Collaboration 2013), Matplotlib (Hunter 2007), `batman` (Kreidberg 2015), and `emcee` (Foreman-Mackey et al. 2013).

References

Allan, A., & Vidotto, A. A. 2019, MNRAS, 490, 3760
Allart, R., Bourrier, V., Lovis, C., et al. 2018, Science, 362, 1384
Alonso-Floriano, F. J., Snellen, I. A. G., Czesla, S., et al. 2019, A&A, 629, A110
Armstrong, D. J., Lopez, T. A., Adibekyan, V., et al. 2020, Nature, 583, 39
Astropy Collaboration (Robitaille, T. P., et al.) 2013, A&A, 558, A33
Beaugé, C., & Nesvorný, D. 2013, ApJ, 763, 12
Ben-Jaffel, L., & Ballester, G. E. 2013, A&A, 553, A52
Bonomo, A. S., Desidera, S., Benatti, S., et al. 2017, A&A, 602, A107
Bourrier, V., & Lecavelier des Etangs, A. 2013, A&A, 557, A124
Bourrier, V., Lecavelier des Etangs, A., Dupuy, H., et al. 2013, A&A, 551, A63
Bourrier, V., Lecavelier des Etangs, A., Ehrenreich, D., Tanaka, Y. A., & Vidotto, A. A. 2016, A&A, 591, A121
Bourrier, V., de Wit, J., Bolmont, E., et al. 2017a, AJ, 154, 121
Bourrier, V., Ehrenreich, D., Allart, R., et al. 2017b, A&A, 602, A106
Bourrier, V., Ehrenreich, D., King, G., et al. 2017c, A&A, 597, A26
Bourrier, V., Ehrenreich, D., Lecavelier des Etangs, A., et al. 2018a, A&A, 615, A117
Bourrier, V., Lecavelier des Etangs, A., Ehrenreich, D., et al. 2018b, A&A, 620, A147
Cubillos, P., Erkaev, N. V., Juvan, I., et al. 2017, MNRAS, 466, 1868
dos Santos, L. A., Ehrenreich, D., Bourrier, V., et al. 2019, A&A, 629, A47
dos Santos, L. A., Ehrenreich, D., Bourrier, V., et al. 2020a, A&A, 640, A29
dos Santos, L. A., Ehrenreich, D., Bourrier, V., et al. 2020b, A&A, 634, L4
Ehrenreich, D., & Désert, J.-M. 2011, A&A, 529, A136
Ehrenreich, D., Lecavelier Des Etangs, A., Hébrard, G., et al. 2008, A&A, 483, 933
Ehrenreich, D., Bourrier, V., Wheatley, P. J., et al. 2015, Nature, 522, 459
Foreman-Mackey, D., Hogg, D. W., Lang, D., & Goodman, J. 2013, PASP, 125, 306
Fossati, L., Haswell, C. A., Froning, C. S., et al. 2010, ApJ, 714, L222
Gaia Collaboration (Brown, A. G. A., et al.) 2018, A&A, 616, A1
García Muñoz A. 2007, Planet. Space Sci., 55, 1426
García Muñoz, A., & Schneider, P. C. 2019, ApJ, 884, L43
García Muñoz, A., Fossati, L., Youngblood, A., et al. 2021, ApJ, 907, L36
Gehrels, N. 1986, ApJ, 303, 336
Gibson, N. P., Aigrain, S., Barstow, J. K., et al. 2013, MNRAS, 428, 3680
Hébrard, G., & Moos, H. W. 2003, ApJ, 599, 297
Helled, R., Lozovsky, M., & Zucker, S. 2016, MNRAS, 455, L96
Hellier, C., Anderson, D. R., Collier Cameron, A., et al. 2010, ApJ, 723, L60
Hubbard, W. B., Hattori, M. F., Burrows, A., Hubeny, I., & Sudarsky, D. 2007, Icarus, 187, 358
Hunter, J. D. 2007, Comput. Sci. Eng., 9, 90

Jin, S., Mordasini, C., Parmentier, V., et al. 2014, ApJ, 795, 65
Jones, E., Oliphant, T., Peterson, P., et al. 2001, SciPy: Open source scientific tools for Python
Kirk, J., Alam, M. K., López-Morales, M., & Zeng, L. 2020, AJ, 159, 115
Kite, E. S., Fegley, Bruce, J., Schaefer, L., & Ford, E. B. 2019, ApJ, 887, L33
Kluyver, T., Ragan-Kelley, B., Pérez, F., et al. 2016, in Positioning and Power in Academic Publishing: Players, Agents and Agendas, eds. F. Loizides, & B. Schmid (Amsterdam: IOS Press), 87
Kreidberg, L. 2015, PASP, 127, 1161
Kulow, J. R., France, K., Linsky, J., & Loyd, R. O. P. 2014, ApJ, 786, 132
Kurokawa, H., & Nakamoto, T. 2014, ApJ, 783, 54
Lavie, B., Ehrenreich, D., Bourrier, V., et al. 2017, A&A, 605, L7
Lecavelier Des Etangs, A. 2007, A&A, 461, 1185
Lecavelier des Etangs, A., Ehrenreich, D., Vidal-Madjar, A., et al. 2010, A&A, 514, A72
Lecavelier des Etangs, A., Bourrier, V., Wheatley, P. J., et al. 2012, A&A, 543, L4
Linsky, J. L. 2017, ARA&A, 55, 159
Linsky, J. L., Draine, B. T., Moos, H. W., et al. 2006, ApJ, 647, 1106
Linsky, J. L., Yang, H., France, K., et al. 2010, ApJ, 717, 1291
Loyd, R. O. P., Koskinen, T. T., France, K., Schneider, C., & Redfield, S. 2017, ApJ, 834, L17
Mansfield, M., Bean, J. L., Oklopčić, A., et al. 2018, ApJ, 868, L34
Matsakos, T., & Königl, A. 2016, ApJ, 820, L8
Mazeh, T., Holczer, T., & Faigler, S. 2016, A&A, 589, A75
McDonald, G. D., Kreidberg, L., & Lopez, E. 2019, ApJ, 876, 22
Minnis, C. M. 1955, Nature, 176, 652
Nortmann, L., Pallé, E., Salz, M., et al. 2018, Science, 362, 1388
Oklopčić, A., & Hirata, C. M. 2018, ApJ, 855, L11
Owen, J. E. 2019, Ann. Rev. Earth Planet. Sci., 47, 67
Owen, J. E., & Lai, D. 2018, MNRAS, 479, 5012
Pizzolato, N., Maggio, A., Micela, G., Sciortino, S., & Ventura, P. 2003, A&A, 397, 147
Redfield, S., & Linsky, J. L. 2008, ApJ, 673, 283
Rogers, L. A., Bodenheimer, P., Lissauer, J. J., & Seager, S. 2011, ApJ, 738, 59
Salz, M., Czesla, S., Schneider, P. C., & Schmitt, J. H. M. M. 2016a, A&A, 586, A75
Salz, M., Schneider, P. C., Czesla, S., & Schmitt, J. H. M. M. 2016b, A&A, 585, L2
Sanz-Forcada, J., Micela, G., Ribas, I., et al. 2011, A&A, 532, A6
Seager, S., & Sasselov, D. D. 2000, ApJ, 537, 916
Segura, A., Kasting, J. F., Meadows, V., et al. 2005, Astrobiology, 5, 706
Sing, D. K., Lavvas, P., Ballester, G. E., et al. 2019, AJ, 158, 91
Spake, J. J., Sing, D. K., Evans, T. M., et al. 2018, Nature, 557, 68
Spearman, C. 1904, Am. J. Psychol., 15, 72
Szabó, G. M., & Kiss, L. L. 2011, ApJ, 727, L44
Tian, F. 2015, Ann. Rev. Earth Planet. Sci., 43, 459
Vidal-Madjar, A., Lecavelier des Etangs, A., Désert, J.-M., et al. 2003, Nature, 422, 143
Vidal-Madjar, A., Désert, J.-M., Lecavelier des Etangs, A., et al. 2004, ApJ, 604, L69
Vidal-Madjar, A., Huitson, C. M., Bourrier, V., et al. 2013, A&A, 560, A54
Vidotto, A. A., & Cleary, A. 2020, MNRAS, 494, 2417
Warren, H. P., Mariska, J. T., & Wilhelm, K. 1998, ApJS, 119, 105
Wilson, P. A., Lecavelier des Etangs, A., Vidal-Madjar, A., et al. 2017, A&A, 599, A75
Wood, B. E., Redfield, S., Linsky, J. L., Müller, H.-R., & Zank, G. P. 2005, ApJS, 159, 118
Youngblood, A., France, K., Loyd, R. O. P., et al. 2016, ApJ, 824, 101

Chapter 3

Are Neptunes and sub-Neptunes in a regime of hydrodynamic escape?

> *“ A cactus doesn’t live in the desert because it likes the desert; it lives there because the desert hasn’t killed it yet. ”*
>
> *Hope Jahren*

Since the discovery of evaporating exoplanets, many studies have assessed the impact of high-energy irradiation into their evaporative status [e.g., 110, 41, 52, 90, 119, 55]. Due to limited availability of high-energy spectra for most planet-hosting stars, some of the studies cited above were either focused on case-by-case planets, or were completely theoretical. Nowadays, with a large sample of detected exoplanets, studies of evaporation focus on its effect at the demographic level, where it is possible to marginalize over some of the unknowns [e.g., 95, 142, 172, 99]. In this context, with a total of 106 known transiting exoplanets by 2011, a curious trend started to emerge: Szabó and Kiss [173] reported that sub-Jovian planets with low density were statistically unlikely to be found orbiting at short periods. The authors further proposed that photoevaporation was one of the causes of this hot-Neptune desert. Later, several studies would expand on this idea by showing that this demographic feature was a result of a combination of planet formation, dynamical history, and atmospheric evolution [e.g., 84, 9, 125, 129, see Fig. 3.1].

The *Kepler* satellite was instrumental to gather a sample of thousands of transiting exoplanets that would allow us to study them at the demographic level. Based on this survey, Owen and Wu [143] used photoevaporation models to simulate a population of rocky exoplanets, and they showed that: i) there is a dearth of planets with radius $R_{\rm p} = 2\ {\rm R}_{\oplus}$, and ii) those with radii above $2\ {\rm R}_{\oplus}$ would be able to retain a significant fraction of their primordial atmospheres, while those below this threshold could be completely stripped off into naked

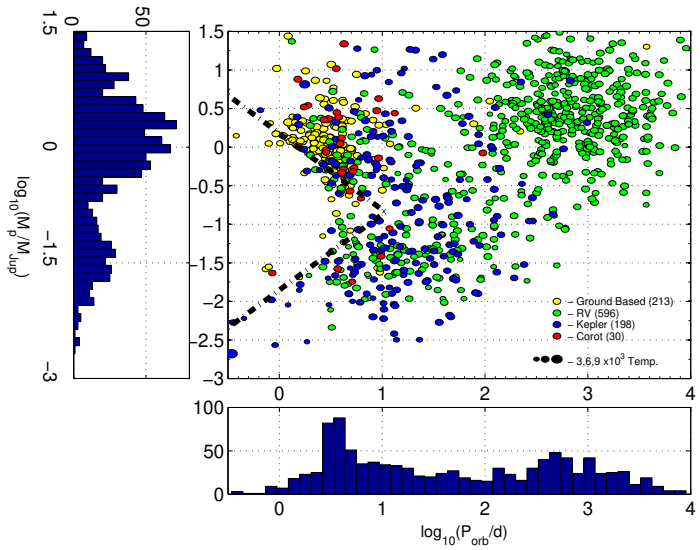

Fig. 3.1 Planetary mass versus orbital period diagram of gas giants. The hot-Neptune desert is delimited by the dashed lines. Symbols depict planets detected by ground-based transit surveys (yellow), radial velocities (green), the *Kepler* satellite (blue), and the *CoRoT* mission (red). Adapted from Mazeh et al. [129].

cores. This feature, now known as the radius gap, was later confirmed with the results of the California-Kepler survey [65] (see Fig. 3.2), precise asteroseismic radii of Sun-like hosts [177], and the *K2* survey [85].

The state-of-the-art demography of rocky exoplanets has two theories to explain their atmospheric evolution: photoevaporation [144, 151] and core-powered mass loss [73, 80]. The latter consists on the onset of atmospheric escape triggered by the internal heat of the planet remaining from its formation. Whether either one of them is the main driver of atmospheric evolution, or if it is a combination of both is still under investigation. The first is supposed to occur in the first $\sim$100 Myr of a planet's lifetime, while the second occurs at Gyr timescales. One observational evidence in favor of photoevaporation is the dependence of the position of the radius valley on stellar host properties [64], since core-powered mass loss in principle does not depend on that; but this observation does not completely rule out the latter. King and Wheatley [99] argue that, due to the Gyr timescale of evolution of extreme-ultraviolet (EUV) irradiation of stars, it may be difficult to discern these two processes. Misener and Schlichting [131] proposed a list of well-characterized exoplanets that could be observed to assess the role of core-powered mass loss in atmospheric evolution; two of them, GJ 9827 d and π Men c, were already observed and showed non-detections of H and He escape [69, 25], but these negative results still allow an undetectable, yet present escape due to the planetary internal energy. A very recent, third possibility to explain the

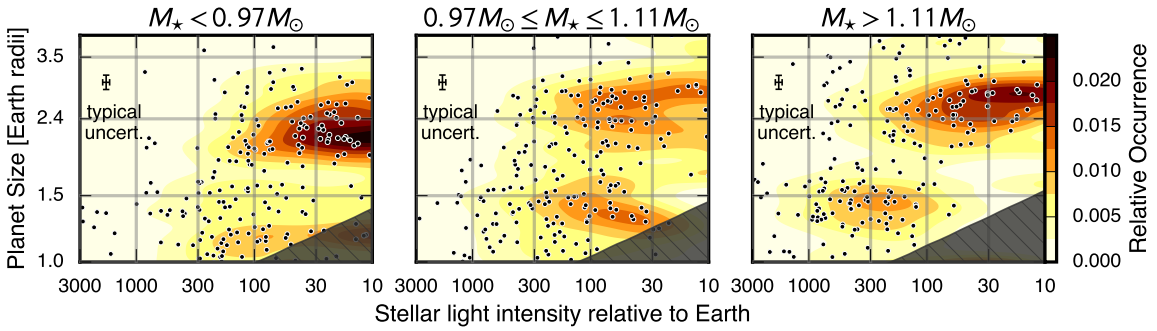

Fig. 3.2 Irradiation versus planet radius diagram of super-Earths for three bins of stellar host mass. The dependence of the position and shape of the radius valley near $\sim$2 $R_\oplus$ with host mass is considered evidence for the role of photoevaporation in shaping the demography of exoplanets. Adapted from Fulton and Petigura [64].

radius valley states that it is primordial [114], and that a more filled gap after $\sim$2 Gyr supports this hypothesis [39], but more theoretical and observational development is needed.

3.1 An extensive search for metallic ions in the exosphere of GJ 436 b

Not long after the first deliberations about evaporating gas giants and how they would evolve, the discovery of the first short-period Neptune would pave the way towards the obtaining evidence for evolution in exoplanets. Initially discovered with the radial veloticies method [24], and later found to be transiting [72], GJ 436 b rapidly became a community favorite to attempt studying atmospheres of exoplanets smaller than hot Jupiters. The first transmission spectroscopy studies with *HST* yielded only flat spectra characteristic of a cloudy atmosphere [148, 101, 100]. But despite these first disappointing results, a relatively low-mass planet orbiting so close to its host star posed an interesting untapped potential: Ehrenreich et al. [53] predicted that it was evaporating at a steady rate of 10^{10} g s^{-1}, similarly to HD 209458 b, but curiously still surviving this process despite an orbital semi-major axis shorter than 0.03 au. This hypothesis was then confirmed with *HST* observations, and led to the seminal publication of the Lyman-α transit of GJ 436 b [51], which is still largely used to date as a testbed case of atmospheric loss in an exoplanet. Later, Bourrier et al. [20] would infer an escape rate in the order of 10^8 g s^{-1} for GJ 436 b, but the question of it being a regime of hydrodynamic escape or not was still open.

As we discussed in Sections 1.2.1 and 1.3.2, hydrodynamic escape is characterized by a supersonic or near-transonic motion of gas through the upper atmosphere of a given planet.

In this regime, the motion of H particles can drag heavier species to the upper atmosphere, populating the exosphere with metals. Ultra-hot Jupiters (UHJ) have been shown to be the best targets to observe escaping metals because they are inflated and near tidal disruption due to their very short orbital periods around relatively massive F-type host stars [183, 106]. To date, no such detection has been done for a Neptune-size planet, and GJ 436 b stands as one of the best candidates to this end. The planet also benefits from an extensive coverage of observations with *HST*, a result of several campaigns led by different investigators since the discovery that it transits.

Our analysis of this extensive dataset for GJ 436 b shows that there are no detectable signals of metals escaping the planet and populating its exosphere. This result rules out the tentative detection of Si reported by Lavie et al. [109], and supports the conclusions of Loyd et al. [123], whose modeling determined that the exospheric densities of metals in GJ 436 b should be undetectable. We do, however, reproduce the Lyman-α transit absorption, which was previously detected with STIS, using the COS spectrograph on *HST*. We conclude that the escape of H in GJ 436 b is stable across several years.

This Section has previously been published in dos Santos et al. [47], and is reproduced with permission © ESO.

A&A 629, A47 (2019)
https://doi.org/10.1051/0004-6361/201935663

Astronomy & Astrophysics

The *Hubble* PanCET program: an extensive search for metallic ions in the exosphere of GJ 436 b

L. A. dos Santos[1], D. Ehrenreich[1], V. Bourrier[1], A. Lecavelier des Etangs[2], M. López-Morales[3], D. K. Sing[4,5], G. Ballester[6], L. Ben-Jaffel[2], L. A. Buchhave[7], A. García Muñoz[8], G. W. Henry[9], T. Kataria[10], B. Lavie[1], P. Lavvas[11], N. K. Lewis[12], T. Mikal-Evans[13], J. Sanz-Forcada[14], and H. Wakeford[15]

[1] Observatoire astronomique de l'Université de Genève, 51 chemin des Maillettes, 1290 Versoix, Switzerland
e-mail: leonardo.dossantos@unige.ch
[2] Institut d'Astrophysique de Paris, CNRS, UMR 7095 & Sorbonne Universités UPMC Paris 6, 98bis bd Arago, 75014 Paris, France
[3] Center for Astrophysics, Harvard & Smithsonian, 60 Garden Street, Cambridge, MA 02138, USA
[4] Department of Earth & Planetary Sciences, Johns Hopkins University, Baltimore, MD, USA
[5] Department of Physics & Astronomy, Johns Hopkins University, Baltimore, MD, USA
[6] Lunar and Planetary Laboratory, University of Arizona, Tucson, AZ 85721, USA
[7] DTU Space, National Space Institute, Technical University of Denmark, Elektrovej 328, 2800 Kgs. Lyngby, Denmark
[8] Zentrum für Astronomie und Astrophysik, Technische Universität Berlin, Hardenbergstrasse 36, 10623 Berlin, Germany
[9] Center of Excellence in Information Systems, Tennessee State University, Nashville, TN 37209, USA
[10] NASA Jet Propulsion Laboratory, 4800 Oak Grove Drive, Pasadena, CA 91109, USA
[11] Groupe de Spectrométrie Moléculaire et Atmosphérique, Université de Reims, CNRS UMR, Champagne-Ardenne 7331, Reims, France
[12] Department of Astronomy and Carl Sagan Institute, Cornell University, 122 Sciences Drive, 14853 Ithaca, NY, USA
[13] Kavli Institute for Astrophysics and Space Research, Massachusetts Institute of Technology, 77 Massachusetts Avenue, 37-241, Cambridge, MA 02139, USA
[14] Centro de Astrobiología (CSIC-INTA), 28692 Villanueva de la Cañada, Madrid, Spain
[15] Space Telescope Science Institute, 3700 San Martin Drive, Baltimore, MD 21218, USA

Received 11 April 2019 / Accepted 10 July 2019

ABSTRACT

Context. The quiet M2.5 star GJ 436 hosts a warm Neptune that displays an extended atmosphere that dwarfs its own host star. Predictions of atmospheric escape in such planets state that H atoms escape from the upper atmosphere in a collisional regime and that the flow can drag heavier atoms to the upper atmosphere. It is unclear, however, what astrophysical mechanisms drive the process.
Aims. Our objective is to leverage the extensive coverage of observations of the far-ultraviolet (FUV) spectrum of GJ 436 obtained with the Cosmic Origins Spectrograph (COS) to search for signals of metallic ions in the upper atmosphere of GJ 436 b, as well as study the activity-induced variability of the star.
Methods. We analyzed flux time-series of species present in the FUV spectrum of GJ 436 and successfully performed geocoronal contamination removal in the COS Lyman-α profiles obtained near the Earth's night-side.
Results. GJ 436 displays flaring events with a rate of ~10 d^{-1}. There is evidence for a possibly long-lived active region or longitude that modulates the FUV metallic lines of the star with amplitudes up to 20%. Despite the strong geocoronal contamination in the COS spectra, we detected in-transit excess absorption signals of ~50 and ~30% in the blue and red wings, respectively, of the Lyman-α line. We rule out a wide range of excess absorption levels in the metallic lines of the star during transit.
Conclusions. The large atmospheric loss of GJ 436 b observed in Lyman-α transmission spectra is stable over the timescale of a few years, and the red wing signal supports the presence of a variable hydrogen absorption source besides the stable exosphere. The previously claimed in-transit absorption in the Si III line is likely an artifact resulting from the stellar magnetic cycle. The non-detection of metallic ions in absorption could indicate that the escape is not hydrodynamic or that the atmospheric mixing is not efficient in dragging metals high enough for sublimation to produce a detectable escape rate of ions to the exosphere.

Key words. stars: individual: GJ 436 – stars: activity – stars: chromospheres – planets and satellites: atmospheres

1. Introduction

Atmospheric escape is an important process that dictates planetary evolution and habitability in the Solar System (e.g., Pollack et al. 1987; Lammer et al. 2003a; Kulikov et al. 2006) and extrasolar systems (e.g., Sanz-Forcada et al. 2011; Chadney et al. 2015; Dong et al. 2017; Bolmont et al. 2017). Hydrodynamic escape in strongly irradiated planets is driven by extreme ultraviolet (XUV) irradiation from their host stars (Vidal-Madjar et al. 2003; Lammer et al. 2003b; García Muñoz 2007; Owen & Jackson 2012), which is presumed to be strongest in the early history of a given planetary system (Ribas et al. 2005; Güdel 2007). Further evidence for the importance of atmospheric escape in planetary evolution comes from studies of transiting exoplanet populations, which brought our attention to a dearth of short-period ($P < 10$ d) planets with masses between 0.01 and 1 M_J (the hot Neptune desert; Lecavelier Des Etangs 2007; Davis & Wheatley 2009; Ehrenreich & Désert 2011; Szabó & Kiss 2011;

Table 1. Stellar and planetary parameters of GJ 436 and GJ 436 b.

Stellar parameters of GJ 436		Ref.
Radius	$0.449 \pm 0.019\ R_\odot$	(a)
Mass	$0.445 \pm 0.044\ M_\odot$	(a)
Eff. temperature	3479 ± 60 K	(a)
Proj. rot. velocity	$0.330^{+0.091}_{-0.066}$ km s^{-1}	(b)
Rotational period	44.09 ± 0.08 d	(b)
Inclination rot. axis	39^{+13}_{-9} deg	(b)
Distance	9.756 ± 0.009 pc	(c)
$\log R'_{\rm HK}$	-5.32 ± 0.07	(d)
$L_{\rm X}/L_{\rm Bol}$	1.950×10^{-6}	(e)
Planetary parameters of GJ 436 b		**Ref.**
Radius	$4.04 \pm 0.85\ R_\oplus$	(f)
Mass	$25.4^{+2.1}_{-2.0}\ M_\oplus$	(f)
Orbital period	$2.64389803 \pm 0.00000026$ d	(f)
Semi-major axis	$14.54 \pm 0.14\ R_\star$	(f)
Ref. time (BJD)	$2454865.084034 \pm 0.000035$	(f)
Orbital inclination	$88.858^{+0.049}_{-0.052}$ deg	(b)
Eccentricity	0.1616 ± 0.004	(f)
Arg. periastron	$327.2^{+1.8}_{-2.2}$ deg	(f)

References. (a) Mann et al. (2015), (b) Bourrier et al. (2018c), (c) Gaia Collaboration (2018), (d) Suárez Mascareño et al. (2015), (e) Sanz-Forcada et al. (2011), (f) Lanotte et al. (2014).

Lopez et al. 2012; Mazeh et al. 2016; Ionov et al. 2018). Despite the detection of many ultra short-period small (presumably rocky) planets, the *Kepler* satellite found almost no strongly irradiated Neptune-size planets, even though the survey was much more sensitive to larger planets (Howard et al. 2012).

Transiting exoplanets amenable to atmospheric characterization offer one of the most compelling opportunities to study planetary evolution. The first observation of Na in the optical transmission spectrum of the giant exoplanet HD 209458 b (Charbonneau et al. 2002) was a crucial milestone toward this goal, generating several theoretical and experimental efforts to probe exoplanetary atmospheres. In particular, the first direct evidence of atmospheric escape in exoplanets was reported for the hot Jupiters HD 209458 b (Vidal-Madjar et al. 2003, 2004; Ehrenreich et al. 2008; Ballester & Ben-Jaffel 2015) and HD 189733 b (Lecavelier des Etangs et al. 2010, 2012; Bourrier et al. 2013; Ben-Jaffel & Ballester 2013), using far-ultraviolet (FUV) transit spectroscopy with the *Hubble* Space Telescope (HST). However, to this date, the most spectacular observation of atmospheric escape remains that of GJ 436 b. It displays a transit depth of 56% and a long egress in the blue wing of the Lyman-α line caused by the extended tail of neutral hydrogen that escapes vigorously from the planet (Kulow et al. 2014; Ehrenreich et al. 2015; Bourrier et al. 2015, 2016; Lavie et al. 2017).

GJ 436 b is a warm Neptune exoplanet orbiting a nearby and relatively quiet M2.5 dwarf (Butler et al. 2004; Gillon et al. 2007). The planet lies in the lower-mass edge of the hot Neptune desert (see the stellar and planetary parameters in Table 1). One of the most important mechanisms to explain the hot Neptune desert is the erosion of inflated envelopes rich in H and He, and the observation of large-scale atmospheric escape from GJ 436 b seems to corroborate this hypothesis. According to Bourrier et al. (2016), the current atmospheric loss rate of GJ 436 b is $\sim$1/18 000 Gyr^{-1} in planetary mass fraction, which is not large enough to carve the hot Neptune desert. Moreover, the eccentricity and orbital misalignment of the planet with the spin of the star suggests that it may have recently migrated inward due to an undetected outer companion as of yet (Beust et al. 2012; Stevenson et al. 2014; Bourrier et al. 2018c). In contrast, Bourrier et al. (2018b) showed that the warm Neptune GJ 3470 b displays a large mass loss rate comparable to that of hot Jupiters, rendering it the most extreme case of mass loss observed to date. GJ 3470 b could already have lost up to 40% of its mass over its 2 Gyr lifetime, suggesting that planetary mass loss has the potential to change the population of close-in giant exoplanets.

Several questions about the GJ 436 system remain unanswered, such as: how stellar activity affects the stellar FUV energy output, whether the planet loses other species besides hydrogen, and whether we should expect other warm Neptunes around M dwarfs to display similar escape rates (e.g., Bourrier et al. 2018b). We note that FUV transit spectra with HST will help answer these questions, but several datasets may be necessary since the stellar lines of GJ 436 are weak when compared to solar-type stars. In particular, the Cosmic Origins Spectrograph (COS; Green et al. 2012) has a wider wavelength range and is more sensitive than the Space Telescope Imaging Spectrograph (STIS; Woodgate et al. 1998) in the FUV, giving us access to several metallic stellar lines.

Lavie et al. (2017) reported a tentative absorption signal in the Si III stellar line (1206.5 Å) of GJ 436 that could be of a planetary nature. If proven to be accurate, this signal would suggest that Si atoms are hydrodynamically dragged from the lower atmosphere of the planet by the H atoms (similarly to HD 209458 b; Vidal-Madjar et al. 2003; Koskinen et al. 2010), indicating the presence of atmospheric mixing and clouds in the lower atmosphere (Visscher et al. 2010), which is consistent with the flat infrared-optical transit spectrum of the planet (Knutson et al. 2014; Lothringer et al. 2018). In contrast, Loyd et al. (2017) reported a non-detection of C II and Si III in-transit absorption signals in two HST visits during the transit of GJ 436 b, assuming a large asymmetric transit light curve as seen in Lyman-α. Their simulations predict C II transit depths of 2 and 19% in the full line passband and line center, respectively.

We report here on the analysis of several HST-COS observations covering different phases of the planetary transit in four epochs, aiming to resolve the questions about GJ 436 b and the hydrodynamical nature of the atmospheric escape process. This manuscript has the following structure: in Sect. 2 we describe the observations and the post-processing necessary after data reduction; in Sects. 3 and 4 we examine the impact of activity (flares and rotational modulation) in the FUV fluxes of GJ 436; in Sect. 5 we present the first detection of the deep Lyman-α transit of GJ 436 b using HST-COS; in Sect. 6 we discuss the results of the search for metallic ions in the exosphere of GJ 436 b; and in Sect. 7 we summarize our conclusions and present future research perspectives for GJ 436 b.

2. Observations and data reduction

GJ 436 b is one of the targets of the *Hubble* Panchromatic Comparative Exoplanet Treasury (PanCET) program GO-14767 (PIs: D. Sing and M. López-Morales; see Wakeford et al. 2017; Evans et al. 2017; Nikolov et al. 2018; Alam et al. 2018; Bourrier et al. 2018b). GJ 436 was observed during four visits using the Cosmic Origins Spectrograph (COS) fed by the *Hubble* Space Telescope, using the grating G130M centered on 1291 Å. These visits were planned to include at least one orbit during the optical primary transit of the planet GJ 436 b, according to the ephemeris of Lanotte et al. (2014). In total, two orbits, one of them while

Table 2. Observations log of GJ 436 with HST-COS centered at 1291 Å.

Visit	Orbit	Start time (UT)	Exp. time (s)	Phase (h)
		Hubble PanCET program		
A	1	2017-11-19 20:30:21	1881.184	−1.32
	2 (†)	2017-11-19 21:49:34	2702.08	···
	3	2017-11-19 23:24:55	2702.176	+1.71
	4	2017-11-20 01:00:15	2702.112	+3.30
	5	2017-11-20 02:36:06	2702.176	+4.89
B	1	2017-12-21 12:17:30	1881.152	−2.97
	2	2017-12-21 13:34:53	2702.144	−1.57
	3	2017-12-21 15:10:16	2702.144	+0.02
	4	2017-12-21 16:45:38	2702.144	+1.61
	5	2017-12-21 18:21:00	2702.144	+3.20
C	1	2018-01-24 21:02:28	1688.192	−3.15
	2	2018-01-24 22:17:19	2702.176	−1.76
	3	2018-01-24 23:52:39	2702.176	−0.17
	4	2018-01-25 01:27:59	2702.176	+1.42
	5	2018-01-25 03:03:19	2702.176	+3.01
D	1	2018-02-28 07:32:12	1688.096	−1.55
	2	2018-02-28 08:48:36	2702.176	−0.13
	3	2018-02-28 10:23:56	2702.176	+1.46
	4 (†)	2018-02-28 11:59:18	2702.176	···
	5	2018-02-28 13:34:39	2702.176	+4.64
		MUSCLES program		
E	1	2012-06-23 07:22:56	980.192	−14.76
	2	2012-06-23 07:41:15	1191.168	−14.43
	3	2012-06-23 08:47:20	1200.192	−13.32
F	1	2015-06-25 23:37:36	1243.168	−3.68
	2	2015-06-26 00:43:54	2713.184	−2.37
	3	2015-06-26 02:19:20	2713.216	−0.80
	4	2015-06-26 03:54:46	2713.184	+0.79
	5	2015-06-26 05:30:12	2713.216	+2.38
		Program GO-15174		
···	1	2017-12-22 21:35:19	1957.152	+30.34
	2	2017-12-23 21:25:43	1957.184	−9.28
	3	2017-12-24 09:55:32	1957.152	+3.22
	4	2017-12-24 16:29:58	1957.152	+9.79
	5	2018-01-19 10:24:56	1850.176	−6.84
	6	2018-01-19 15:27:48	1850.144	−1.79
	7	2018-02-08 13:52:25	1850.144	−31.01
	8	2018-02-23 08:19:12	1850.144	+6.17

Notes. Phases are in relation to the orbit of GJ 436 b. Orbits marked with (†) had a pointing failure and did not register counts; these orbits were discarded from our analysis. Observations of program GO-15174 were performed with single-orbit visits.

in-transit, were affected by technical failures and did not register counts since the shutter of the instrument was closed; these orbits are discarded from the analysis. In this study we also made use of HST-COS archival observations obtained during programs GO-15174 (PI: R. O. Loyd) and GO-13650 (MUSCLES Treasury Survey; PI: K. France). The following observations log is located in Table 2: for visits A–D (PanCET program), we have a total of 18 usable orbits of which three are in transit; in visits E and F (MUSCLES program) there are eight orbits and none of them are in-transit; the eight single-orbit visits of program GO-15174 were meant to cover a wide swath of phases of the orbit of GJ 436 b and do not cover the transit.

Table 3. Spectral line list used in this work.

Ion	Central wavelength (Å)	Integration range (km s^{-1})
C III	1175.59	[−240, +230] (multiplet)
Si III	1206.5	[−50, +50]
H I	1215.6702	See Fig. 9
O V	1218.344	[−50, +50]
Si II	1264.738	[−50, +100] (doublet)
N V	1238.821	[−80, +80]
	1242.804	[−70, +70]
C II	1334.532	[−50, +50]
	1335.708	[−60, +60]
Si IV	1393.755	[−50, +50]
	1402.77	[−40, +40]

Notes. More information about the formation of FUV lines can be found in, e.g., Avrett & Loeser (2008).

The raw spectra were processed automatically by the instrument's pipeline. Since the observations were performed in time-tag mode, we were able to split the data in sub-exposures using the `calcos` package from the AstroConda software stack[1]. We performed our analysis using the same FUV line list as in Table 3. For a reference, we combined all the HST-COS observations of GJ 436 that are publicly available and produced a high signal-to-noise FUV spectrum, which we reproduce in Fig. 1.

We found that the spectral lines of GJ 436 are systematically shifted from the stellar rest frame in our datasets, displaying excess Doppler shifts from −6 to 20 km s^{-1} over the systemic velocity of the star (v_R = 9.61 km s^{-1}; Nidever et al. 2002). The variation occurs at different levels depending on the position of the line in the detector and the time of the observation. However, orbits from the same visit tend to display similar line-to-line Doppler shifts. This wavelength calibration issue has been previously observed with COS (e.g., Linsky et al. 2012; Loyd et al. 2017; Bourrier et al. 2018a).

In order to correct for these systematic Doppler shifts, we measured them in a line-by-line and visit-by-visit fashion for all lines in the spectra, except for the lines contaminated by airglow (see Sect. 5.1) and those that are too faint. In the latter case, we consider that Doppler shifts changed by the same value as the closest line that we could measure. The Doppler shifts are quantified as an average per visit by fitting Gaussian profiles (whose parameters are fit at the position of the Gaussian and its amplitude) to the stellar lines. The correction for Doppler velocity shifts is applied during the computation of fluxes for each line in each spectrum. For each spectral line, the fluxes are computed by integrating the flux densities in their corresponding passbands (see Table 3). When applicable, we accumulated the fluxes of multiplets to improve the signal-to-noise ratio of the emission for each species. In addition, we removed the subexposures with possible flaring activity (Sect. 3).

Wilson et al. (2017) found that the uncertainties of the spectra processed by the instrument's pipeline are overestimated, especially for fluxes above 10^{-14} erg s^{-1} cm^{-2} Å^{-1}. For our analysis, we defined the uncertainties of the spectra according to Eqs. (1)

[1] Available at `http://astroconda.readthedocs.io`.

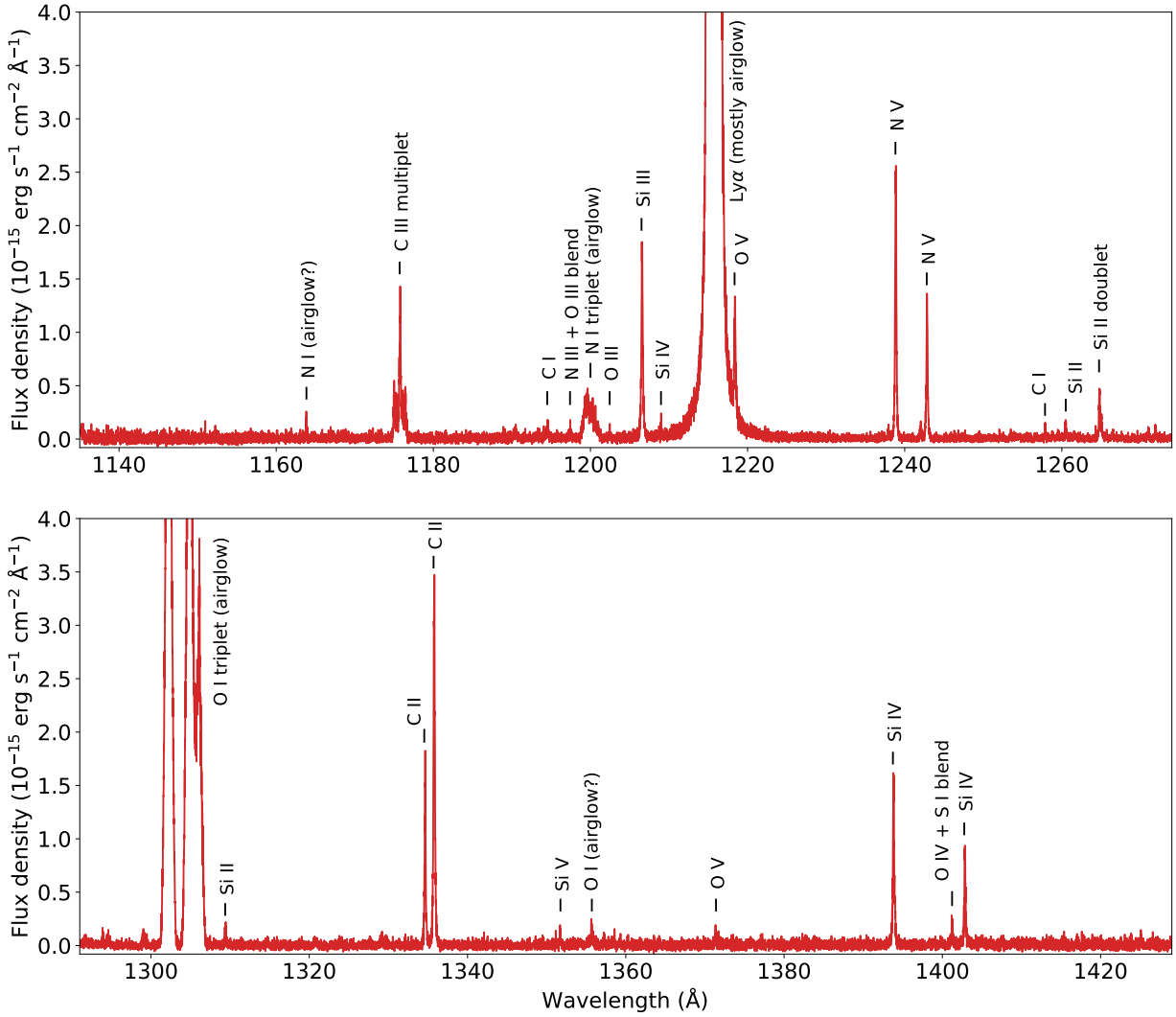

Fig. 1. Combined FUV spectrum of GJ 436 measured with HST-COS using G130M grating centered on 1291 Å.

and (2) of Wilson et al. (2017). Furthermore, errors in measuring stellar spectra affect how accurately we measured the flux. In theory, it should be possible to correct these errors if we know their sources and how they affect the data. In particular, systematic instrumental effects of HST observations, such errors in flux calibration, and the thermal "breathing" effect (e.g., Ehrenreich et al. 2012; Lavie et al. 2017) can occur as flux variations resulting from changes in focus that correlate with the orbit of the telescope. We searched for such correlations in the available datasets for GJ 436 and for 55 Cnc e (V. Bourrier, priv. comm.), but we did not find evidence for significant thermal breathing with HST-COS. This is likely because COS has a circular aperture and is thus less sensitive to losses due to focus variations when compared to slit or grism spectrographs, such as STIS and WFC3.

Effects intrinsic to the target being observed that are not known or not taken into account are another important source of errors. One example is the Lyman-α transit of GJ 436 b in which the duration of the transit in optical wavelengths is only one hour (Lanotte et al. 2014). However, in Lyman-α the transit event lasts more than 20 h, owing to the large size and shape of the planet's exosphere (Lavie et al. 2017). Were this not known, then we would have erroneously measured the baseline Lyman-α flux of the star during the long transit of the planet's exosphere. Another example of measurement error occurs when stellar activity effects, such as modulation by active regions in the stellar surface, are not taken into account.

3. Flares of GJ 436

In this section we mainly discuss the results obtained during Program GO-15174, which were measured more than five hours away from the optical transit in order to avoid any possible planetary signal. Although GJ 436 is a quiet star compared to other M dwarfs (e.g., Suárez Mascareño et al. 2015), we observed strong levels of stellar variability in some of the lines in its FUV spectrum.

3.1. Identification of flares during exposures

We used the time-tag information from the raw data to divide each HST-COS exposure in four subexposures. We found strong correlations (Pearson-$r > 0.7$) between the out-of-transit fluxes of the lines Si III, Si IV, C II, and C III. If the spread in fluxes was only due to stochastic uncertainties, then there would not be a correlation between line-by-line flux comparisons. Such flux correlations observed in the out-of-transit spectra only appear when systematics are present, so they must be either of instrumental (see Sect. 2) or astrophysical origin. The spectral lines

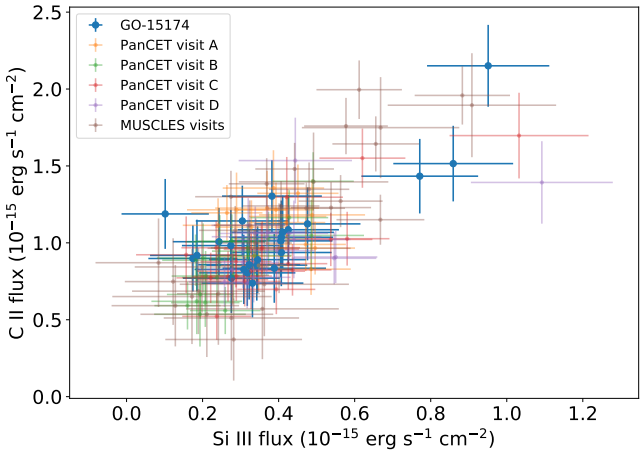

Fig. 2. Fluxes of Si III versus C II lines in spectra of GJ 436. The strong correlation (Pearson-$r > 0.7$) between these fluxes leads us to conclude that the higher flux end of the plot corresponds to stellar flares, while the lower flux end corresponds to the quiescent state of the star.

with the lowest level of intrinsic variability are the N V lines at 1239 and 1243 Å.

Since these flux correlations are wavelength-dependent and being that we did not find evidence for instrumental systematics with HST-COS, a sensible first approach is to assume the effect is astrophysical. Following an inspection of the time-tag split light curve of the Si III and C II fluxes, we found a statistically significant ($\gtrsim 5\sigma$) increase in fluxes by 100% during the first quarter of orbit 2 of program GO-15174; this variation is not seen in the N V lines. The second half of orbit 8 also displays a similar increase, but with a lower significance. The first quarter of orbit 6 shows an increase in the fluxes of Si lines by 100% in relation to the average flux of the remaining subexposures, but the same is not seen at high significance in the other lines. We reproduce the Si III versus C II line fluxes dispersion map in Fig. 2, in which each point corresponds to a sub-exposure with HST-COS during the out-of-transit program. There are the following two noticeable features in this plot: first, the low fluxes cluster around each other and have a dispersion that is consistent with a weak correlation (probably related to rotational modulation, see Sect. 4); and second, the higher fluxes are less common and show an apparent correlation. One interpretation for the observed large fluxes is that they result from transient brightenings, while the low-flux end corresponds to the stellar quiescent state. Further, we overplotted the sub-exposure fluxes of the PanCET and MUSCLES visits in Fig. 2 and identified flares in their data as well; these sub-exposures were excised from the data. Orbit 6 of the MUSCLES observations is completely contaminated by a flare, which was originally reported by Loyd et al. (2017). The flare events in the datasets we analyzed are not limited to a specific phase of the orbit of GJ 436 b. We also observed flares in GJ 436 in X-rays, as well as several other targets in the PanCET survey. The results will be published in a a following article (Sanz-Forcada et al., in prep.); the X-ray light curves of GJ 436 are available publicly in the `X-exoplanets` database[2].

3.2. Discussion

As an M2.5-type dwarf, GJ 436 is near the limit where stars become fully convective (Wright et al. 2011) and start to display strong activity signals. According to Yang et al. (2017), 10–15% of stars of this spectral type display flare behavior; moreover, M dwarfs with a rotational period similar to GJ 436 (44.09 d; Bourrier et al. 2018c) tend to have flare activity levels near 6×10^{-6} $L_{\rm flare}/L_{\rm bol}$ (two orders of magnitude lower than the fastest-rotating M dwarfs in the Kepler field). It is not completely clear, however, if these results can accurately be applied to flaring activity in FUV wavelengths. Previous observations of GJ 436 for the MUSCLES Treasury Survey have also resulted in the detection of flares in C II and Si III lines, although they are less frequent and weaker than in other M dwarfs in the program (Youngblood et al. 2017; Loyd et al. 2017). Flares with similar levels of brightening are also observed in X-ray light curves of the Sun and have durations between 1 and 20 min (Shimizu 1995).

A comparison between the quiescent and flare spectra of GJ 436 is shown in Fig. 3 and Table 4; these spectra were derived by combining all of the out-of-transit, time-tag split subexposures in the quiescent and flare state. The flare spectrum seems to be blueshifted in relation to the quiescent spectrum for both spectral lines shown, which is unexpected given that other M dwarfs and the Sun exhibit a redshifted flare excess instead (Hawley et al. 2003; Loyd et al. 2018). We presume this blueshift is physical, since we applied wavelength shift corrections for systematic errors uniformly across visits before combining the flare and quiescent spectra; these correction factors are estimated using exposures from which the flare subexposure was eliminated. Stellar lines can show physical redshifts (or even slight blueshifts) because of the chromospheric structure (see, e.g., Linsky et al. 2012; Bourrier et al. 2018a). We cannot measure the absolute position of a given line relatively to the stellar photosphere, but we can measure relative shifts of a flaring line relatively to its quiescent state. The fact that these transition region lines exhibit slightly blueshifted excess is indicative of material flowing upward from the stellar surface.

In order to avoid contamination by flares in our results, we removed the subexposures affected by flares from the analysis. The Si III and C II lines are the ones that more clearly show these features. In the case of GJ 436, we deem subexposures to be contaminated with flares when the combined fluxes of the Si III line and the C II doublet exceed 2.4×10^{-15} erg s^{-1} cm^{-2}. Discerning the quiescent flux level from flare-contaminated subexposures from faint emission lines by eye or by analyzing light curves is neither straightforward or reliable. However, we were able to take advantage of a large number of measurements to average out stochastic variations from the baseline flux.

4. Rotational modulation of FUV fluxes

Bourrier et al. (2018c) and Lothringer et al. (2018) used photometric observations acquired from 2003 to 2017 with the T12 0.80 m automatic photoelectric telescope (APT) at the Fairborn Observatory (Henry 1999). They found evidence for rotational modulation with a period of 44.09 days and a peak-to-peak amplitude of 0.0032 mag. In this section we quantify the potential modulation of the stellar FUV fluxes due to the presence of active regions on the stellar surface of GJ 436.

4.1. Assessing the presence of a long-lived active region or an active longitude

In order to verify the presence of rotational modulation of the fluxes in the FUV lines of GJ 436, we phase-folded the data to the rotational period of the star and fit the fluxes with the following two different models: a sinusoid and a constant. Further, we used

[2] http://sdc.cab.inta-csic.es/xexoplanets/

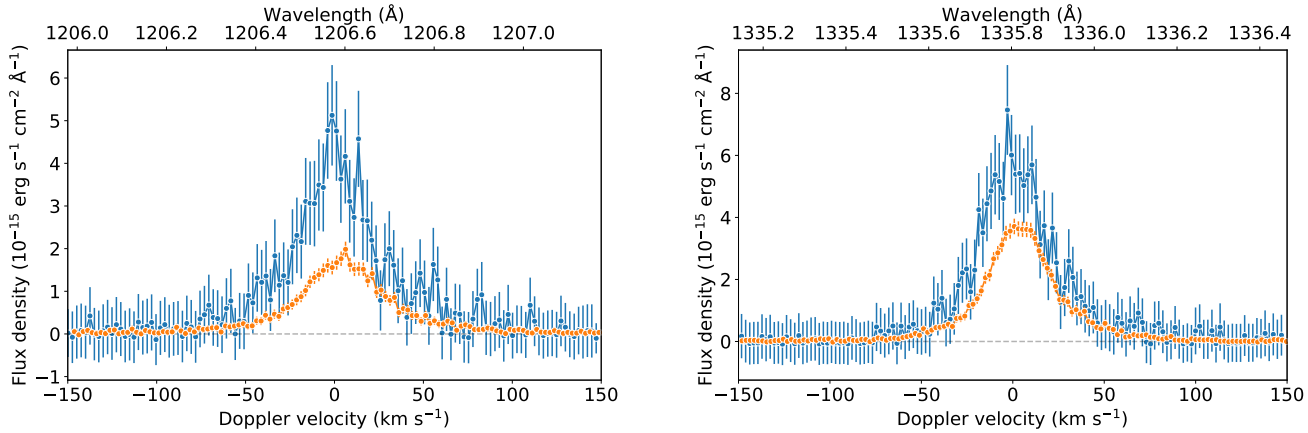

Fig. 3. Comparison between flare spectrum (blue) of GJ 436 against its quiescent spectrum (orange) near the Si III (*left panel*) and C II (*right panel*) emission lines. These spectra are computed by combining several HST-COS exposures. Absolute velocities are in the stellar rest frame but may be affected by biases resulting from the instrument and post-processing; however, the relative Doppler shift between the flare and quiescent spectra is physical.

Table 4. Quiescent and flare fluxes of GJ 436 in lines most sensitive to stellar activity.

Ion	Central wavelength (Å)	Quiescent flux ($\times 10^{-16}$ erg s^{-1} cm^{-2})	Flare flux
C II	1334.532	2.99 ± 0.10	4.91 ± 0.72
C II	1335.708	7.99 ± 0.13	13.5 ± 0.8
Si III	1206.5	4.33 ± 0.10	10.2 ± 0.7

the Bayesian Information Criterion (BIC; Schwarz 1978) to evaluate which of these two models best describe the overall behavior of the fluxes when phase-folded to the rotational period of the star.

We fit the flux modulation by maximizing the likelihood function

$$\ln\left[p\left(F_{\rm obs}|\mathcal{M}\right)\right] = -\frac{1}{2}\sum_k \left[\frac{\left(F_{{\rm obs},k} - F_{\mathcal{M},k}\right)^2}{\sigma_k^2} + \ln\left(2\pi\sigma_k^2\right)\right], \quad (1)$$

where F is the flux, $\mathcal{M}$ is the model, and σ is the uncertainty of the flux. The best fit was calculated using the truncated Newton algorithm implementation of SciPy (Jones et al. 2001). The fit parameters are the amplitude, reference phase, and flux baseline for the sinusoidal model; the flux baseline was the only parameter used for the constant model (the amplitude and baseline were measured as a fraction of the mean observed flux). The rotational period was fixed at 44.09 d. We did not use in-transit fluxes in this analysis to avoid contamination by possible transit signals. We performed the fits for the combined flux of multiplets where applicable in order to have the highest signal-to-noise ratio (S/N) possible for each species. We evaluated the hypothesis of sinusoidal modulation using the Bayesian Information Criterion (BIC).

M dwarfs can display long-lived active regions that modulate their fluxes over several rotations. It is not clear, however, how long-lived they are on GJ 436; the extended data in Fig. 7 from Bourrier et al. (2018c) show that the low-amplitude rotational modulation of GJ 436 stays coherent over 14 consecutive years in optical wavelengths. On visual inspection, the rotationally phase-folded fluxes of Si III, C II, and N V seem to modulate with a sinusoidal behavior, except for measurements during the mid-2012 epoch. Although the measurements from the mid-2015 epoch follow the trend, it is also plausible that they are coincidentally higher near a magnetic cycle maximum and are not necessarily related to an active region being observed in the late-2017 to early-2018 epoch. We thus propose the following two hypotheses to be assessed: (a) the measurements during epochs mid-2012 and mid-2015 are not coherent with the latest epoch and should not be included in the rotational modulation analysis; (b) the mid-2015 epoch is coherent with the latest epoch, either by an active longitude (as seen in the Sun and in GJ 1214; Berdyugina & Usoskin 2003; Kitchatinov & Olemskoi 2005; Weber et al. 2013; Mallonn et al. 2018) or the same long-lived active region, and it should be included in the rotational modulation analysis.

Assuming hypothesis (b), we found that the fluxes of the C II doublet, the N V doublet, and the Si III line in the COS data seem to display rotational modulation with a sinusoidal model favored by ΔBIC > 10 in relation to the constant model (see Fig. 4 and Table 5). The flux time series of the individual species with weaker lines are not as well described by sinusoids but, when their fluxes are combined, the modulation is clear (lower right panel of Fig. 4). We used a Markov-chain Monte Carlo (MCMC) algorithm to evaluate the uncertainties of the sinusoidal fit and verified that it displays reference phases that are similar within 1σ given the uncertainties of the fit.

Assuming hypothesis (a), we found that the sinusoidal rotational modulation model is not significantly favored over a constant flux model (ΔBIC < 10). In this case, it would not be necessary to correct for rotational modulation during the light curve analysis. On the other hand, the epochs from mid-2012 and mid-2015 cannot be included in the light curve analysis because we are not able to accurately assess the effects of activity in the flux measurements during these earlier epochs. A visual inspection of the S-index of activity (Vaughan et al. 1978) of GJ 436 measured with the HIRES spectrograph (Butler et al. 2017) suggests that the star was at a minimum of its activity cycle around 2012, and that the activity started to increase again around 2014. A consistent behavior is also seen in optical photometric monitoring of GJ 436; based on Fig. 1 of Lothringer et al. (2018), the epoch when the star becomes the brightest in optical, which represents the minimum spot coverage, roughly corresponds to the minimum of S-index around 2012 (see Fig. 5). Furthermore, the

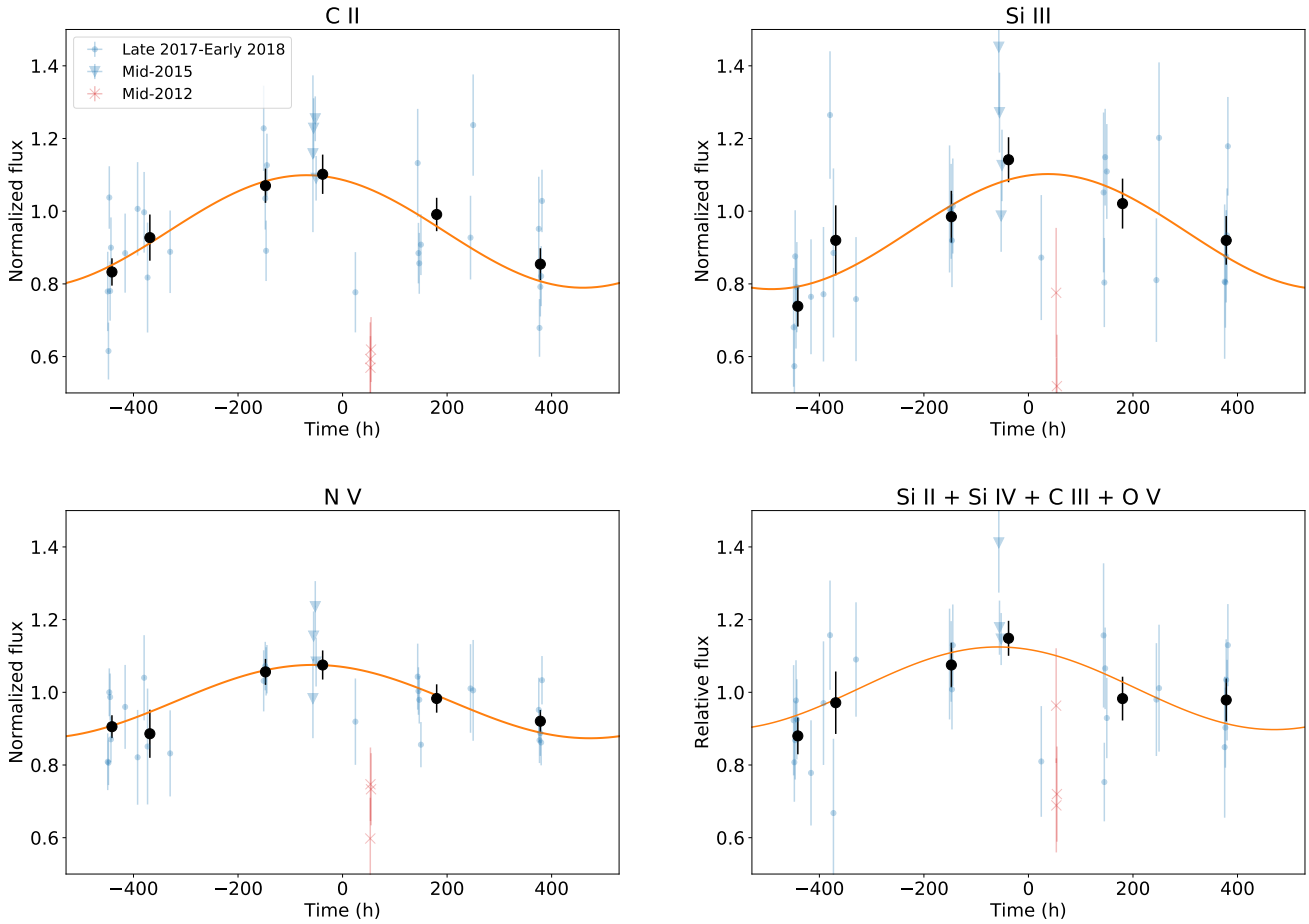

Fig. 4. Rotational modulation of fluxes of C II doublet, Si III line, N V doublet, and combined fluxes of Si II, Si IV, C III, and O V lines in the COS spectra, assuming that epoch mid-2015 is affected by the same active region or longitude. The light curves were phase-folded to the rotational period of the star GJ 436 (44.09 d); the amplitude and baseline are measured in fraction of the mean average flux. The black data points are bins of groups of observations near the same phase. The fits were performed to the orbit-to-orbit data and not to the binned data.

Table 5. Bayesian information criterion (BIC) and deviance (χ^2) values of models for stellar flux variation.

Species	Epochs	Sinusoidal		Constant	
		BIC	χ^2	BIC	χ^2
C II	2015–2018	−65.5	63.3	−25.2	110
	2017–2018	−56.9	49.1	−51.8	60.8
Si III	2015–2018	−69.8	35.1	−54.8	57.0
	2017–2018	−58.5	25.4	−55.8	34.5
N V	2015–2018	−107	32.6	−84.9	61.8
	2017–2018	−93.8	23.5	−88.9	34.9
All weaker lines	2015–2018	−81.6	32.7	−71.7	49.3
	2017–2018	−71.1	22.0	−76.4	23.2
Lyman-α	2010–2016	−78.3	42.1	−71.5	55.4

epoch of lowest optical flux (between 2014 and 2016), representing maximum spot coverage, corresponds to the epochs when we see the highest UV fluxes in the HST data. The stellar magnetic cycle modulation[3] can explain the variation seen between the observations in epochs in mid-2012 and mid-2015.

[3] Lothringer et al. (2018) found that the magnetic cycle of GJ 436 is roughly 7.4 yr.

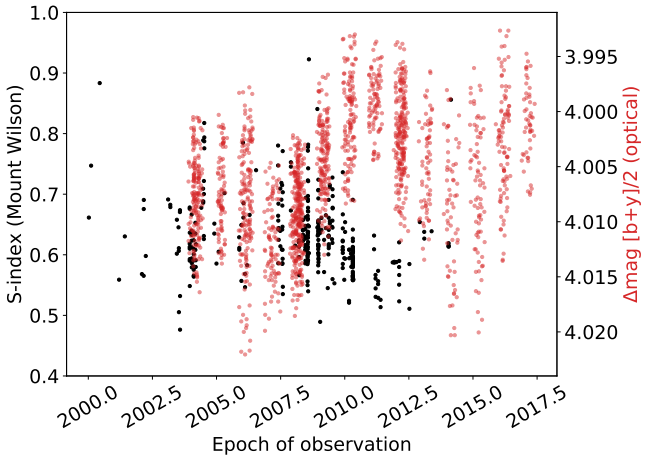

Fig. 5. Long-term activity modulation of GJ 436 seen in optical photometry (red) and S-index (black).

As the strongest emission line in the FUV spectra of M dwarfs, the Lyman-α line is also susceptible to rotational modulation in its flux. In the case of GJ 436, the blue wing of the line (Doppler velocities range [−120, +50] km s^{-1}) is affected by a strong and long-lasting planetary absorption when near or in-transit. However, the atmospheric escape models of Bourrier et al. (2016) suggest that the far blue wing ([−250,

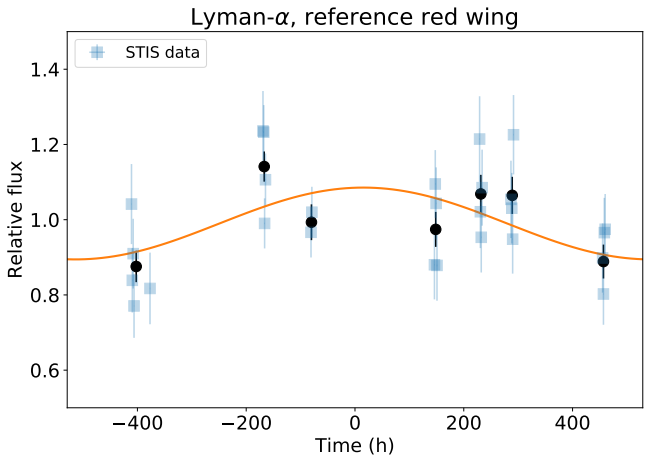

Fig. 6. Same as Fig. 4, but for fluxes in Lyman-α reference red wing [120, 250] km s^{-1} as observed with STIS spectrograph. The epoch of observations span from 2010 to 2016.

−120] km s^{-1}) and the reference red wing ([+120, +250] km s^{-1}) of the Lyman-α line of GJ 436 should be free of planetary signals (see Sect. 5).

We re-analyzed the STIS data obtained in previous programs (Kulow et al. 2014; Ehrenreich et al. 2015; Lavie et al. 2017) to check for rotational modulation in the reference red wing of the Lyman-α line of GJ 436 (Doppler velocities range [120, 250] km s^{-1}). The epochs of observation with the STIS spectrograph range from mid-2010 to early-2016, which encompasses the supposed activity minimum around 2012 and the increase in activity starting in 2014. In this case, we found that the sinusoidal fit is not significantly favored against the constant flux model (ΔBIC ≈ 7; see Fig. 6).

4.2. Discussion

To the best of our knowledge, the potential modulation of FUV fluxes that we found for GJ 436 has not been previously reported for another quiet M dwarf in the literature. Using optical photometric data obtained with the *Kepler* mission, Giles et al. (2017) concluded that M dwarfs with rotational periods of 10 or 20 d can have active regions with lifetimes varying from a few tens to 430 days, depending on the size of the active region (in general, larger regions should last longer than smaller ones). Furthermore, Robertson et al. (2015) reported on the presence of a large active region or complex of spots in GJ 176, an M2 dwarf with a rotational period of 39 d, and this region remained stable for at least six years (the photometric variability remained in phase during the span of observations, unlike the other activity indices). Another example is Proxima Cen, which possesses a longer rotational period and similar activity index as GJ 436 ($P_{\rm rot}$ = 83.2 d and $\log R'_{\rm HK} = -5.65$) but exhibits rotational modulation that is stable for more than eight years (Suárez Mascareño et al. 2015, 2016).

If hypothesis (b) is correct, then our results indicate that GJ 436 possessed either a stable active region or an active longitude that modulated the FUV fluxes for more than 45 rotations since the mid-2015 epoch. In principle, we do not expect the rotational modulation in FUV spectra to be in phase with optical broadband photometry since they trace different regions of the stellar atmosphere. In fact, we expect them to be out of phase by $\pi/2$ since active regions usually display bright features in the ultraviolet (e.g., Dupree et al. 1973; Brosius et al. 2000) and dark spots in broadband optical wavelengths (e.g., Hook 1671; Collier Cameron 1997; Özavcı et al. 2018).

If hypothesis (a) is correct, then the flux modulations seen in epochs in mid-2012 and mid-2015 are not related to a putative active region observed in the later epochs (late-2017 to early-2018), and they are more likely related to the longer magnetic cycle of the star instead of rotation. In addition, the observations from the later epochs do not display significant rotational modulation by themselves. It is difficult to disentangle hypotheses (a) and (b) because similar observations have not been performed between mid-2015 and late-2017, and both of them have observational evidences in their favor. Youngblood et al. (2016) also investigated the variability of the Lyman-α of several M dwarfs and found no significant variability for GJ 436; other, more active M dwarfs did exhibit variations in their Lyman-α flux in the order of 10–20%.

5. The planetary Lyman-α absorption

Previous observations with HST-STIS showed that GJ 436 b possesses an extended H-rich exosphere, which is readily detectable in Lyman-α transit spectroscopy (Kulow et al. 2014; Ehrenreich et al. 2015; Bourrier et al. 2015, 2016; Lavie et al. 2017). In this section we analyze the Lyman-α time-series of GJ 436 b obtained during several transits with HST-COS in order to reproduce this previous detection and verify the suitability of geocoronal emission correction for faint FUV targets.

5.1. Airglow contamination correction

The FUV spectra obtained with HST are contaminated by geocoronal emission (also known as airglow) in the Lyman-α (1215.6702 Å) and O I lines (1302.168, 1304.858, and 1306.029 Å). The level of contamination is variable and tends to either increase (decrease) during an orbit depending on whether the telescope is moving from the Earth's night(day)-side to day(night)-side. This variation is visible when the time-tag data are split in subsequent subexposures. The level of contamination also varies from orbit to orbit and, in our data, the first orbit of a given visit tends to be more severely contaminated; this is because the first orbit usually started closer to the Earth's dayside than the other orbits.

When using STIS, the instrument pipeline automatically removes the geocoronal contamination by taking advantage of the fact that it is a slit spectrograph; in the case of COS, which has a circular aperture, it is impossible to measure the airglow independently from the stellar spectra, so a simple automatic subtraction of contamination is not possible. However, Bourrier et al. (2018a) showed that it is possible to correct the Lyman-α emission of 55 Cnc on HST-COS spectra and remove the geocoronal contamination by using airglow templates[4] accumulated from previous programs (see also Ben-Jaffel & Ballester 2013; Wilson et al. 2017). Here, we applied the same technique to the GJ 436 spectra. Since the O I lines of GJ 436 are too faint to be discerned from the airglow emission, we decided to perform the correction only for the Lyman-α line and discard the O I lines analysis.

The geocoronal airglow spectra have an approximately constant shape. In order to subtract the airglow from the observations, we needed to fit the amplitude and Doppler shift of the template to the observed emission line since the observed spectra have systematic Doppler shifts that we needed to correct for.

[4] Airglow templates for HST-COS are available at http://www.stsci.edu/hst/cos/calibration/airglow.html.

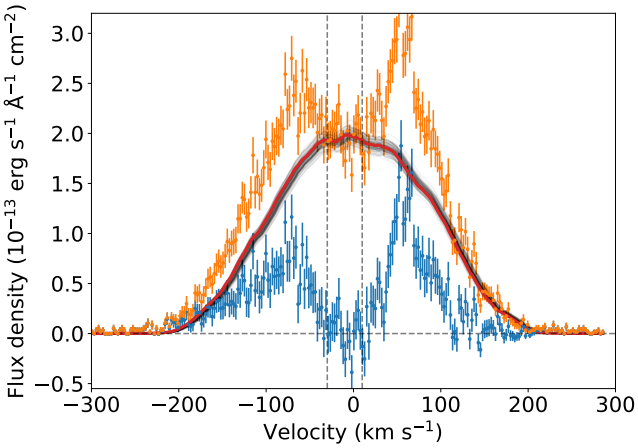

Fig. 7. Airglow contamination removal in Lyman-α profile of GJ 436 measured during orbit 1 of Visit D. The cleaned (contaminated) spectrum is shown in blue (orange), the best fit airglow template is shown in red, and the MCMC posterior sample is shown as a family of gray airglow templates.

Following the procedure outlined in Bourrier et al. (2018a), we fit the core of the airglow template to a region of the observed Lyman-α profile where we did not expect any emission from the star. The wavelength range where the interstellar medium (ISM) completely absorbs the stellar emission line[5] is suitable to fit the amplitude of the airglow; in our data set, this spectral range is located between −10 and 30 km s^{-1} in the rest frame of the star (Bourrier et al. 2015). The best fit is obtained by minimizing an objective function, namely the difference between the observed spectrum and the template in the aforementioned range using a truncated Newton algorithm. The objective function also includes a term that penalizes airglow templates that produce negative fluxes when subtracted from the observed spectra. The fit parameters are the Doppler shift of the airglow in relation to the stellar spectra and the amplitude of the airglow in each exposure. We estimated the uncertainties of the fit by performing a MCMC simulation; an example of the airglow removal results is shown in Fig. 7.

Since the data were obtained in time-tag mode, each exposure was divided in four in order to select the subexposures with the least geocoronal contamination (i.e., near the Earth's night side). As long as the wings of the stellar Lyman-α emission can be visually distinguished from the geocoronal emission, then the subexposure is suitable for airglow removal. The datasets that could be corrected are listed in Table 6.

We measured the out-of-transit spectrum of GJ 436 with HST-COS observations from orbits 5 and 7 of program GO-15174 (see Fig. 8; the other orbits were either too close to the planetary transit or too contaminated by airglow). The COS exposures of the MUSCLES dataset were not used in the Lyman-α analysis because part of the airglow profile falls inside the region with shadows caused by the wire grid of COS (the shadows produce a 15% depression in the continuum). The pipeline normally calibrates these regions as point sources during the flat-field correction; however, the Earth's airglow is not a point source, so this correction is not perfect if the emission falls in this region, resulting in spurious emissions on top of the airglow.

[5] See estimates for the H I column density in the line of sight of GJ 436 in Bourrier et al. (2015).

Table 6. Summary of suitability of COS subexposures for Lyman-α recovery.

Visit	Orbit	Subexposures			
A	1				
	3	✓			
	4	✓			
	5				✓
B	1				
	2	✓			
	3				✓
	4	✓			
	5	✓			
C	1	×	✓		
	2		✓	✓	✓
	3		✓	✓	✓
	4		✓	✓	✓
	5	✓	✓	✓	
D	1		×		✓
	2	✓		✓	✓
	3		✓	✓	✓
	5	✓		✓	✓

Notes. Each subexposure corresponds to a quarter of the total exposure in the orbit. Subexposures marked with ✓are suitable for Lyman-α recovery; those marked with × are contaminated by flares.

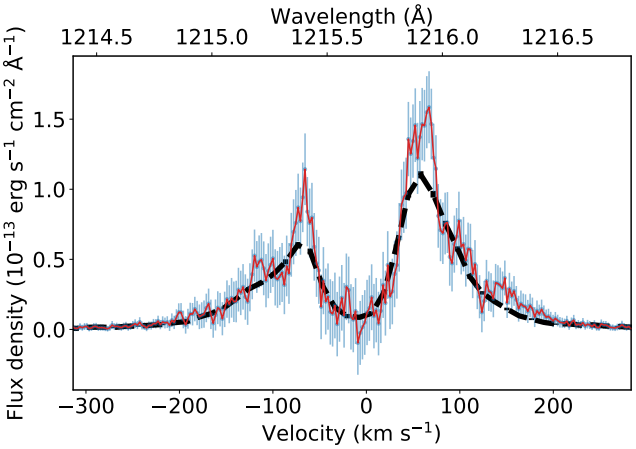

Fig. 8. Mean out-of-transit Lyman-α spectrum of GJ 436 measured with HST-COS observations from program GO-15174 (red spectrum with blue uncertainty bars). For comparison, we plot the mean out-of-transit spectrum measured with HST-STIS in black. The spectra are centered in the stellar rest frame. The intrinsic Lyman-α emission line of GJ 436 likely possesses a single-peaked Voigt shape (Bourrier et al. 2015), but the core of the line is absorbed by the ISM, producing a double-peaked feature when observed from the Earth.

5.2. Stable absorption in the blue wing

After applying the geocoronal contamination removal described in Sect. 5.1 to the spectra, we obtained the clean Lyman-α profile of GJ 436 during the four visits (see the cleaned spectra from Visit D in Fig. 9). More information about the observed and intrinsic shape of the Lyman-α line for a range of stellar types can be found in Wood et al. (2005), for example. The variability seen in the line is partly due to photon noise, imperfections in the airglow decontamination, and potential astrophysical signals. The blue wing of the line, inside the Doppler velocity interval [−120, −40] km s^{-1} (region II in Fig. 9), is known to display

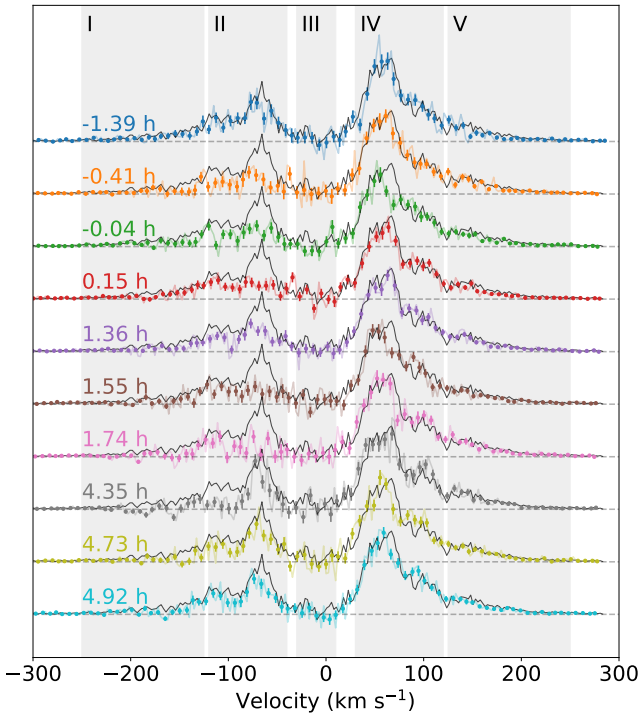

Fig. 9. HST-COS Lyman-α profiles of GJ 436 observed during Visit D after airglow decontamination (color spectra), binned to Doppler velocity intervals of 7 km s^{-1}. The reference out-of-transit spectrum is plotted for comparison as a black spectrum against each exposure of Visit D. The regions shaded in gray correspond to: I) the reference far blue wing [−250, −120] km s^{-1}; II) the blue wing [−120, −40] km s^{-1}; III) the line core absorbed by the ISM [−30, +10] km s^{-1}; IV) the red wing [+30, +120] km s^{-1}; V) the reference far red wing [+120, +250] km s^{-1}. We do not expect planetary signals in regions I and V, so they can be used to estimate the stability of the Lyman-α emission. The timestamps correspond to the phases in relation to the orbital motion of the planet.

a periodic absorption due to the transit of GJ 436 b and its extended exosphere.

We reproduced the light curve of the Lyman-α blue wing obtained with the COS spectrograph and plotted the previous STIS results in Fig. 10 for a comparison of the shape of the light curve. Even though we analyzed the same passbands, there may be an offset between COS and STIS passband fluxes due to their different instrumental profiles. The spectral resolving power of STIS/G140M and COS/G130M are, respectively, ∼12 000 and ∼14 000 near the Lyman-α wavelength. Although the full-line Lyman-α fluxes are expected to be equal, independent of the instrumental profiles, narrower passbands in this line are expected to produce different fluxes between different instruments. In order to avoid these offsets, we show the Lyman-α light curves normalized in relation to the baseline fluxes measured outside the phase range [−3, +24] h.

The planetary absorption in the blue wing of the Lyman-α line of GJ 436 shows that the signal is also present in the COS data, and it remains repeatable over several epochs during our observations (Fig. 10). The signal at mid-transit displays a decrease of ∼50% in flux in relation to the baseline, which is consistent with previous results obtained with HST-STIS (Ehrenreich et al. 2015; Lavie et al. 2017). These results indicate that the large atmospheric loss rate of GJ 436 b is stable on a timescale of a few years; however, it is difficult to evaluate the effects of stellar activity in the escape rate because of the large uncertainties and spread in the Lyman-α light curves obtained with COS. In addition to the uncertainties of the spectra calculated by the pipeline, the uncertainties shown in Fig. 10 also include those of the airglow removal procedure; the latter were estimated by computing the flux for each airglow template from the MCMC simulation, and adding the spread in quadrature to the original uncertainty. In general, the uncertainties of the fit increase those of the resulting cleaned spectra by ∼10%.

5.3. Deep absorption event seen in the red wing

We also analyzed the red wing of the Lyman-α line of GJ 436 in the wavelength region where Lavie et al. (2017) had previously suggested an absorption signal at +5.75 h after mid-transit (region IV in Fig. 11). We found that the observed Lyman-α red wing fluxes during Visit C are ∼30% lower than the other visits and the out-of-transit exposures (see the time series in Figs. 11 and 12). We do not expect the intrinsic stellar Lyman-α to decrease by ∼30% in flux by chance or stellar activity alone, and the uncertainties in the airglow removal procedure do not account for this lower resulting flux. Even though our observations with COS have a similar precision as the STIS data, they do not cover the phase +5.75 h. Therefore, we were unable to reproduce an absorption signal similar to what is seen with STIS. The COS and STIS signals seem to have a similar shape, but they are shifted in phase space and are deeper with COS.

This excess absorption seen in the red wing indicates the presence of H I atoms inflowing to the host star at speeds varying from 30 to 120 km s^{-1}. As pointed out by Lavie et al. (2017), the exospheric model of GJ 436 b produced by EVE (Bourrier & Lecavelier des Etangs 2013; Bourrier et al. 2015, 2016) predicts that the population of H I atoms moving toward the star is localized in the coma of the planet, producing potential signatures of up to 50 km s^{-1} only. Furthermore, Lavie et al. (2017) suggests that star–planet interactions (SPIs) could explain redshifted signatures (as in Matsakos et al. 2015; Strugarek 2016). It is unclear, however, how stable SPI signatures are in orbital phase space.

Similar redshifted in-transit excess absorption signals were marginally detected for HD 189733 b (Lecavelier des Etangs et al. 2012) and HD 209458 b (Vidal-Madjar et al. 2003). A persistent and significant signal was observed in the stellar Lyman-α red wing during the transit of GJ 3470 b (Bourrier et al. 2018b). In order to explain this feature, Bourrier et al. (2018b) argues that the excess redshifted absorption is caused by the damping wings of dense layers of neutral hydrogen that extend beyond the planetary Roche lobe and are elongated in the direction of the orbital motion (see, e.g., Tian et al. 2005; Ben-Jaffel 2008). These observations do not constrain the line-of-sight position of this layer of H I atoms, but Bourrier et al. (2018b) suggest that they could be located in the shock interface between the planetary thermosphere and the stellar wind. A direct comparison with the episodic redshifted signal observed in GJ 436 b is not straightforward since the orbital configuration and systemic properties are different. However, detailed modeling of the interaction between the upper atmosphere of GJ 436 b and the stellar wind, particularly during and after flares, could provide an explanation for the observed redshifted signal.

6. Searching for planet-induced variability signals in metallic lines

Loyd et al. (2017) reported on observations performed for the MUSCLES program and concluded that there was no absorption signal in the Si III line and, with 95% confidence, ruled out signals with depths larger than 49% (in the case of a highly

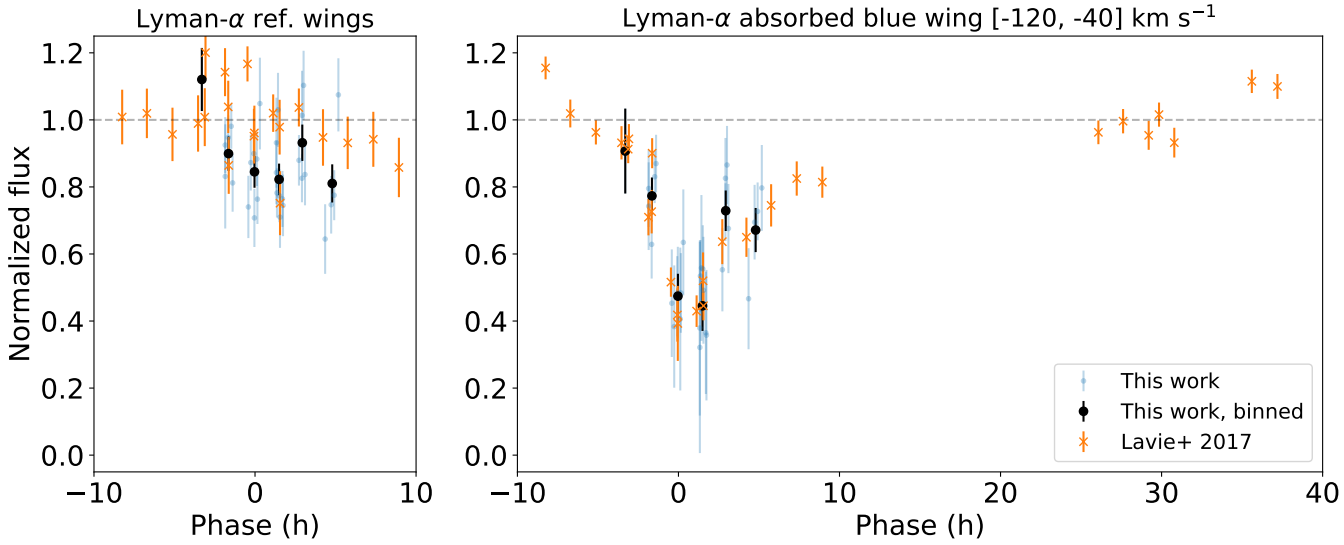

Fig. 10. Normalized Lyman-α light curves of GJ 436 from COS (this work) and STIS (Lavie et al. 2017) observations. The baseline fluxes used for normalization were measured in phases outside the [−3, +24] h range. In the case of COS spectra, we measured the baseline flux from the out-of-transit exposures from program GO-15174. The uncertainties of the baseline flux were propagated to the final uncertainties of the normalized fluxes. *Left panel*: light curve of the Lyman-α reference far wing fluxes, measured in the passbands I and V from Fig. 9.

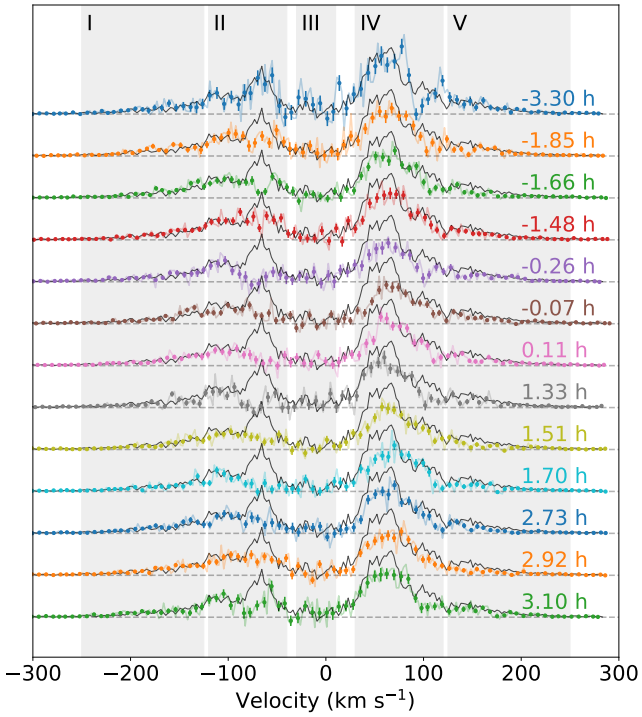

Fig. 11. Same as Fig. 9, but for subexposures of Visit C. In addition to the persistent in-transit absorption seen in the blue wing (region II), this visit also displays a 30%-deep excess absorption signal in the Lyman-α red wing (region IV).

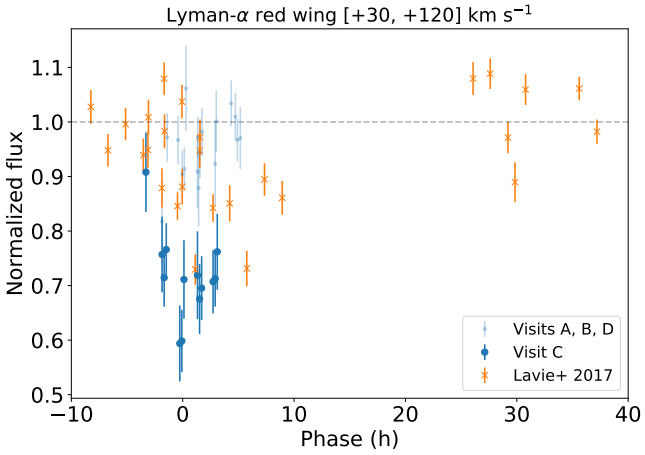

Fig. 12. Normalized light curve of red wing (region IV) fluxes during transit of GJ 436 b. The baseline flux used for normalization was computed in the same way as in Fig. 10. Visits A, B, and D display fluxes similar to the baseline value, while Visit C displays a decrease in flux by ∼30% in relation to the baseline. The excess absorption in Visit C is likely physical and traces possible inflow of material to the host star.

asymmetrical transit similar to what is observed in Lyman-α). Furthermore, Loyd et al. (2017) reported a non-detection of C II absorption in the transmission spectrum of GJ 436 b. Lavie et al. (2017) obtained a tentative detection of absorption during transit in the Si III line using HST-STIS; they reported a transit depth of $47 \pm 10\%$ for the line flux in the interval $[-50, 50]$ km s^{-1}. However, Lavie et al. (2017) also cautioned that they could not rule out possible stellar variability on the line, similarly for the red wing of the Lyman-α line. Aiming to reproduce and improve upon these previous results, we searched for possible exospheric absorption signals in the metallic FUV lines of GJ 436 in several datasets available to us.

In order to increase the S/Ns of the phase-folded light curves, we binned the fluxes in phase space (black circles in Fig. 13). We included the visits from programs previous to the 2017–2018 epoch in our plots for comparison purposes only, but they are not to be taken into account when computing baseline fluxes and detection levels. As discussed in Sect. 4, the exposures taken during the epochs in 2012 and 2015 may correspond to different phases of the magnetic cycle of GJ 436, so it is difficult to correct for activity effects in them without continuously monitoring them. Thus, we did not apply rotational modulation correction to the 2017–2018 epoch since the effect is not significant in this period alone (it is only significant if we assume that the activity modulation in mid-2015 is coherent with the most recent epoch).

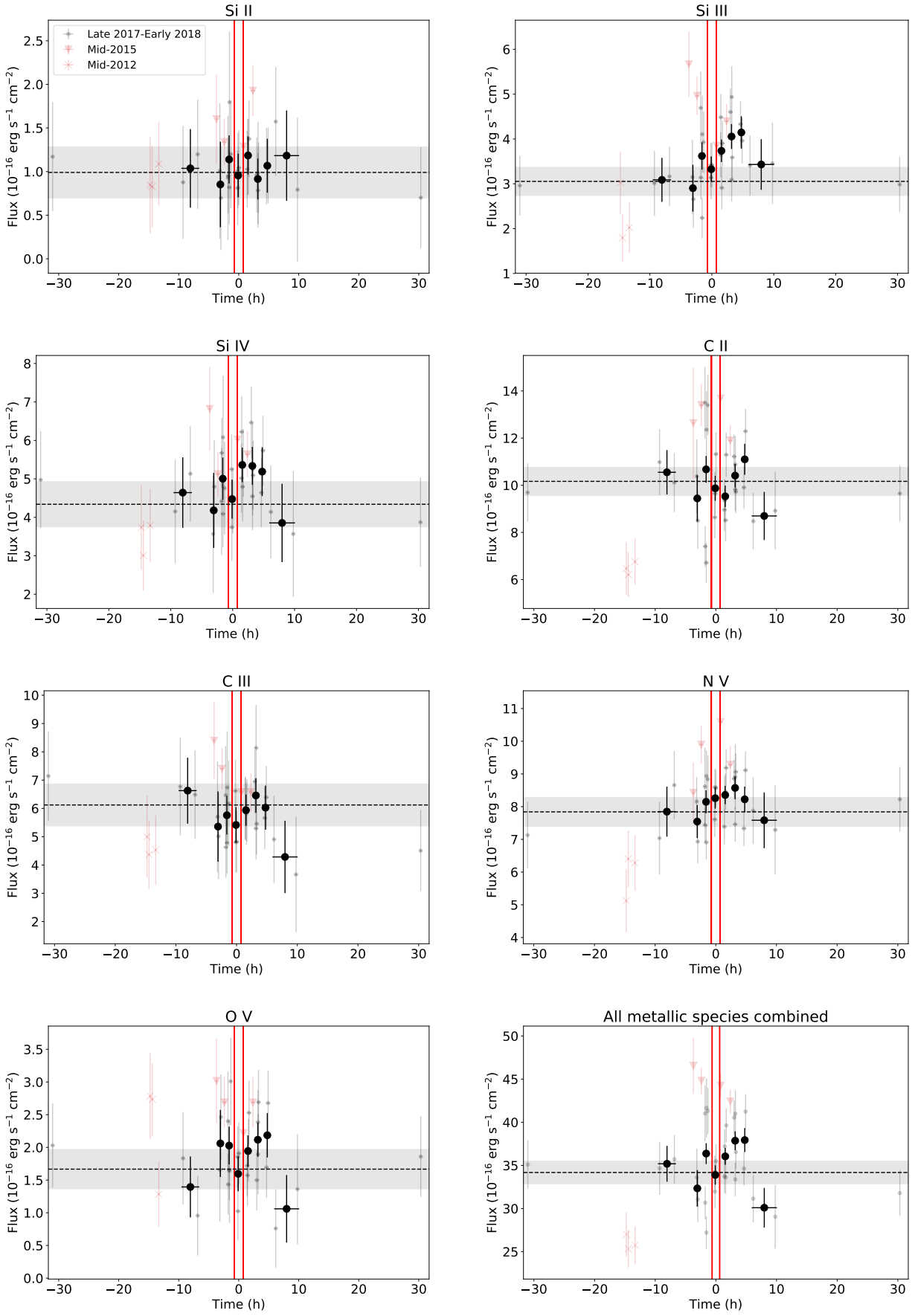

Fig. 13. Light curves of FUV stellar lines during transit of GJ 436 b. The larger circular symbols represent the late 2017-early 2018 data binned in phase. The red vertical lines represent the ingress and egress of the optical transit. The vertical dashed line and the gray region represent, respectively, the mean and 1σ uncertainty of the baseline measured asymmetrically, similarly to the Lyman-α baseline.

Table 7. Minimum levels of planet-induced variability signals in metallic lines of GJ 436 that we can rule out at 95% confidence (2σ).

Species	Absorption depth		
	(Opt. transit)	(Long transit)	(Asym. transit)
C II	4.8%	11%	12%
C III	10%	24%	24%
Si II	23%	51%	59%
Si III	7.4%	18%	21%
Si IV	9.8%	25%	27%
N V	4.2%	12%	11%
O V	7.8%	20%	20%

Notes. The minimum detectable signals of variability depend on how the baseline is defined. The different baseline definitions we adopted are outlined in Sect. 6.

It is not straightforward to interpret the flux time series for each species due to the strong variability. If we fix the confidence level at 95% (which corresponds to 2σ), we could rule out different levels of mid-transit absorption signals depending on the precision with which we can measure the baseline stellar flux for each species. The baseline flux itself is uncertain for the metallic lines; we adopted the following three different definitions of baseline for the purpose of determining the non-detection levels of absorption: (i) one similar to the optical transit (based on the parameters in Table 1) in which the baseline is measured in phases outside the optical transit; (ii) a long symmetric transit, for which the baseline is measured with every data point outside the phase range [−5, 5] h; and (iii) an asymmetric transit, for which the baseline is measured in the same way as the Lyman-α flux, namely outside the phase range [−3, +24] h. These non-detection levels are summarized in Table 7, and they represent the minimum levels of excess absorption or emission that can be detected if such signals were present in the data.

Since we were unable to reproduce the result over several visits with HST-COS, it is likely that the Si III absorption signal reported by Lavie et al. (2017) is related to stellar variability instead of absorption by the exosphere of GJ 436 b. As discussed in Sect. 4, approximately half of the STIS observations were obtained in 2016 when the star was coming out of an activity maximum and the Si III fluxes, which are very sensitive to stellar activity, increased in variability and average flux (see Fig. 14). The previous observations were obtained between 2013 and 2015, the epochs when GJ 436 was coming out of an activity minimum. The STIS observations after 2015 were specifically performed to cover orbital phase ranges farther from mid-transit, so that explains the higher Si III baseline inferred by Lavie et al. (2017) in relation to the exposures near mid-transit, which were executed before the increase in activity.

Our results do not, however, rule out the 2% absorption depth in the C II lines predicted by Loyd et al. (2017), and more observations would in principle be necessary to confirm their prediction. Our analysis indicates that the C II lines are particularly sensitive to stellar activity, so the detection of such a shallow signal may be very challenging using the current FUV instrumentation. In the future, more sensitive instruments, such as the Large Ultraviolet/Optical/Infrared Surveyor (LUVOIR; Bolcar et al. 2017), the LUVOIR Ultraviolet Multi-Object Spectrograph (LUMOS; France et al. 2017), and the Habitable Planet Explorer (HabEx; Mennesson et al. 2016) will be able to measure FUV fluxes with several times better precision than HST-COS.

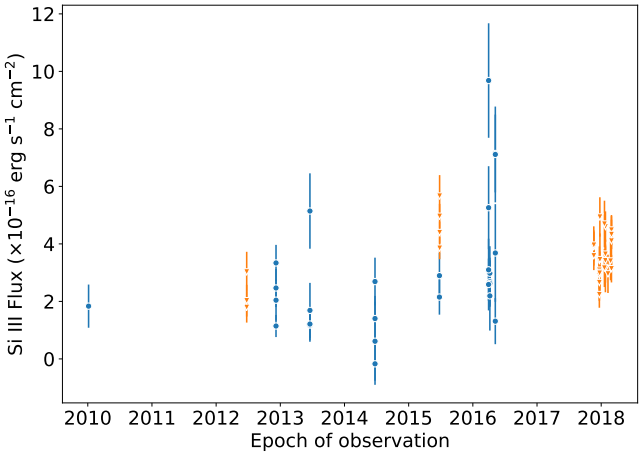

Fig. 14. Stellar Si III fluxes of GJ 436 measured with STIS and COS spectrographs on HST across different epochs. The average flux and variability of the line seem to have increased since 2015, which can be related to the stellar activity cycle.

Neptune-sized planets have a lower surface gravity than Jupiter-sized ones, so in principle we would expect the first to lose heavier atoms more easily than the second. However, it is likely that these atoms condense into clouds more easily in warm Neptunes and, therefore, they cannot be carried upward to the exosphere as easily (Loyd et al. 2017). In the particular case of GJ 436 b, the planet is relatively cool ($T_{\rm eq} \sim 600$ K; Turner et al. 2016) when compared to hot Jupiters ($T_{\rm eq} > 1000$ K) where heavier elements have been detected in their extended atmospheres. The upper limits of absorption levels of metallic ions during the transit of GJ 436 b are similar to the absorption signals detected for the hot Jupiters HD 209458 b (Vidal-Madjar et al. 2004) and HD 189733 b (Ben-Jaffel & Ballester 2013). Our results could indicate that either: first, the escape process in GJ 436 b is not hydrodynamic, but hydrostatic; or second, by assuming hydrodynamic escape, mixing in the lower atmosphere is not efficient in dragging the metal-rich clouds high enough for sublimation and allow for a significant escape rate of metallic ions.

7. Conclusions

We reported on the analysis of HST-COS observations of the stellar FUV spectra during four transits of the planet GJ 436 b obtained for the PanCET program, as well as archival HST data from the MUSCLES and GO-15174 programs. Even though GJ 436 is considered a quiet M dwarf when compared to other similar stars, it displays flaring activity such as the events reported by Loyd et al. (2017). Our analysis revealed that GJ 436 also displays flare activity that increases the fluxes of C II and Si III by ∼50 and ∼200%, respectively, and returns to quiescent levels in 20 min or less – such a behavior is also observed in X-ray light curves of the Sun and GJ 436 (Sanz-Forcada et al., in prep.). In total, we found seven events with flux brightenings in the FUV spectra of GJ 436 in the PanCET and the archival data, resulting in a flaring rate of 10.1 d^{-1}. Some of these brightening events are not apparent in other FUV spectral lines that are less sensitive to activity, such as Lyman-α.

The FUV fluxes of GJ 436 taken in the 2017–2018 epoch do not display significant rotational modulation if analyzed alone. However, if we assume that the mid-2015 traces the same, long-lived activity region or the same active longitude, then the strongest metallic lines, namely C II, Si III, and N V display

significant rotational modulation. In the latter case, the amplitudes of the modulation would be approximately 20% for the first two and 10% for the last, and they would all appear to be in phase. Slowly-rotating M dwarfs similar to GJ 436 have long-lived activity regions that can last for many years (such as GJ 176 and Proxima Centauri; Robertson et al. 2015; Suárez Mascareño et al. 2016). Analysis of the STIS data also suggests a marginal rotational modulation of the Lyman-α line of GJ 436 with a ~10% amplitude in phase with the COS fluxes of the stellar metallic lines. Future observations of stars like GJ 436 in short wavelengths require carefully planned monitoring to cover the entire rotational phase of the star in order to remove effects of rotational modulation and variability.

The HST-COS observations centered at 1291 Å include the stellar Lyman-α emission, but it is severely contaminated by the Earth's geocoronal emission in comparison to STIS exposures because COS possesses a circular aperture. Removing the airglow contamination in this case is not a trivial process, especially when the stellar emission is fainter than the airglow, which is the case for GJ 436. We performed the same Lyman-α correction procedure as in Bourrier et al. (2018a) to estimate the stellar emission from the COS observations and to recover the stellar Lyman-α emission for the subexposures that were performed near the Earth's shadow (namely when the airglow and stellar emission levels were comparable).

We searched for potential atmospheric signals caused by the planet GJ 436 b transiting its host star. We were able to reproduce the Lyman-α blue wing light curve during the transit of GJ 436 b that had previously revealed that the planet possesses a large exosphere that produces a ~50% decrease in the stellar emission between [−120, −40] km s^{-1} in Doppler velocities. We conclude that the excess absorption in the Lyman-α blue wing is stable for several years. In addition, one of the PanCET visits, more specifically the one obtained in late January 2018, displays a significant excess absorption of ~30% in the Lyman-α red wing (between [+30, +120] km s^{-1} in Doppler velocities). This potential in-transit signal in the red wing occurs during the whole visit, and it is deeper and shifted in phase when compared to the ones reported by Lavie et al. (2017). However, it is not reproduced in the other PanCET visits, indicating a temporary and possibly stochastic event.

Several metallic lines of ions in the transition region of GJ 436 are present in our datasets, with the brightest being C II, C III, Si II, Si III, Si IV, N V, and O V. The in-transit light curves of the combined fluxes for each species do not reveal any evidence that leads us to conclude that such ions are present in the exosphere of the planet. In particular, assuming an asymmetrical transit similar to Lyman-α, we can rule out an absorption depth of 12 and 11% for the C II and N V fluxes, respectively, with 95% confidence during the transit of GJ 436 b, which is consistent with the results of Loyd et al. (2017). On the other hand, we were not able to reproduce the in-transit absorption signal in Si III that was suggested by (Lavie et al. 2017); it is likely that this signal was caused by the increased Si III fluxes of GJ 436 after 2015, which is when the observations of the baseline flux were made and coincidentally the star was coming out of a maximum in its activity cycle. A large observational effort may be necessary to put stricter constraints on the presence of Si ions in the upper atmosphere GJ 436 b.

We are still trying to better understand the atmosphere of GJ 436 b. The FUV transmission spectrum gives us access to the upper atmopshere, while optical and infrared spectra trace the lower atmopshere. Given its featureless optical transmission spectrum, it is still not completely clear if it has a high metallicity or a cloudy atmosphere (Lothringer et al. 2018). Using *Spitzer* photometry at 3.6, 4.5, and 8 μm, Lanotte et al. (2014) concluded that their results are consistent with a metal-rich atmosphere depleted in methane and enhanced in CO and CO_2. The non-detection of metallic species in its exosphere, in particular Si, suggests that if GJ 436 b possesses a cloudy atmosphere and if the escape is hydrodynamic, then mixing is not efficient in dragging the Si-rich clouds high enough for sublimation which would allow for a significant escape rate of metallic ions. On the other hand, non-detection cannot rule out a hydrostatic escape process instead.

Acknowledgements. L.A.d.S. warmly thanks A. Suárez Mascareño, H. Cegla, H. Giles, J. Seidel, N. Hara, and K. France for the fruitful discussions about stellar activity and modeling during the preparation of this manuscript. We are also grateful for the valuable feedback from the anonymous referee and support provided by the Help Desk of STScI. This project has received funding from the European Research Council (ERC) under the European Union's Horizon 2020 research and innovation programme (project FOUR ACES; grant agreement No 724427), and it has been carried out in the frame of the National Centre for Competence in Research PlanetS supported by the Swiss National Science Foundation (SNSF). This research is based on observations made with the NASA/ESA *Hubble* Space Telescope. The data were obtained for the *Hubble* Panchromatic Comparative Exoplanet Treasury program and is openly available in the Mikulski Archive for Space Telescopes (MAST), which is maintained by the Space Telescope Science Institute (STScI). STScI is operated by the Association of Universities for Research in Astronomy, Inc. under NASA contract NAS 5-26555. This research made use of the NASA Exoplanet Archive, which is operated by the California Institute of Technology, under contract with the National Aeronautics and Space Administration under the Exoplanet Exploration Program. We used the open source software SciPy (Jones et al. 2001), Jupyter (Kluyver et al. 2016), Astropy (Astropy Collaboration 2013), Matplotlib (Hunter 2007), `emcee` (Foreman-Mackey et al. 2013) and `batman` (Kreidberg 2015).

References

Alam, M. K., Nikolov, N., López-Morales, M., et al. 2018, AJ, 156, 298
Astropy Collaboration (Robitaille, T. P., et al.) 2013, A&A, 558, A33
Avrett, E. H., & Loeser, R. 2008, ApJS, 175, 229
Ballester, G. E., & Ben-Jaffel, L. 2015, ApJ, 804, 116
Ben-Jaffel, L. 2008, ApJ, 688, 1352
Ben-Jaffel, L., & Ballester, G. E. 2013, A&A, 553, A52
Berdyugina, S. V., & Usoskin, I. G. 2003, A&A, 405, 1121
Beust, H., Bonfils, X., Montagnier, G., Delfosse, X., & Forveille, T. 2012, A&A, 545, A88
Bolcar, M. R., Aloezos, S., Bly, V. T., et al. 2017, SPIE Conf. Ser., 10398, 1039809
Bolmont, E., Selsis, F., Owen, J. E., et al. 2017, MNRAS, 464, 3728
Bourrier, V., & Lecavelier des Etangs, A. 2013, A&A, 557, A124
Bourrier, V., Lecavelier des Etangs, A., Dupuy, H., et al. 2013, A&A, 551, A63
Bourrier, V., Ehrenreich, D., & Lecavelier des Etangs, A. 2015, A&A, 582, A65
Bourrier, V., Lecavelier des Etangs, A., Ehrenreich, D., Tanaka, Y. A., & Vidotto, A. A. 2016, A&A, 591, A121
Bourrier, V., Ehrenreich, D., Lecavelier des Etangs, A., et al. 2018a, A&A, 615, A117
Bourrier, V., Lecavelier des Etangs, A., Ehrenreich, D., et al. 2018b, A&A, 620, A147
Bourrier, V., Lovis, C., Beust, H., et al. 2018c, Nature, 553, 477
Brosius, J. W., Thomas, R. J., Davila, J. M., & Landi, E. 2000, ApJ, 543, 1016
Butler, R. P., Vogt, S. S., Marcy, G. W., et al. 2004, ApJ, 617, 580
Butler, R. P., Vogt, S. S., Laughlin, G., et al. 2017, AJ, 153, 208
Chadney, J. M., Galand, M., Unruh, Y. C., Koskinen, T. T., & Sanz-Forcada, J. 2015, Icarus, 250, 357
Charbonneau, D., Brown, T. M., Noyes, R. W., & Gilliland, R. L. 2002, ApJ, 568, 377
Collier Cameron A. 1997, MNRAS, 287, 556
Davis, T. A., & Wheatley, P. J. 2009, MNRAS, 396, 1012
Dong, C., Huang, Z., Lingam, M., et al. 2017, ApJ, 847, L4
Dupree, A. K., Huher, M. C. E., Noyes, R. W., et al. 1973, ApJ, 182, 321
Ehrenreich, D., & Désert, J.-M. 2011, A&A, 529, A136
Ehrenreich, D., Lecavelier Des Etangs, A., Hébrard, G., et al. 2008, A&A, 483, 933
Ehrenreich, D., Bourrier, V., Bonfils, X., et al. 2012, A&A, 547, A18
Ehrenreich, D., Bourrier, V., Wheatley, P. J., et al. 2015, Nature, 522, 459

Evans, T. M., Sing, D. K., Kataria, T., et al. 2017, Nature, 548, 58
Foreman-Mackey, D., Hogg, D. W., Lang, D., & Goodman, J. 2013, PASP, 125, 306
France, K., Fleming, B., West, G., et al. 2017, SPIE Conf. Ser., 10397, 1039713
Gaia Collaboration (Brown, A. G. A., et al.) 2018, A&A, 616, A1
García Muñoz, A. 2007, Planet. Space Sci., 55, 1426
Giles, H. A. C., Collier Cameron, A., & Haywood, R. D. 2017, MNRAS, 472, 1618
Gillon, M., Pont, F., Demory, B.-O., et al. 2007, A&A, 472, L13
Green, J. C., Froning, C. S., Osterman, S., et al. 2012, ApJ, 744, 60
Güdel, M. 2007, Liv. Rev. Sol. Phys., 4, 3
Hawley, S. L., Allred, J. C., Johns-Krull, C. M., et al. 2003, ApJ, 597, 535
Henry, G. W. 1999, PASP, 111, 845
Hook, M. 1671, Phil. Trans. R. Soc. London, Ser. I, 6, 2295
Howard, A. W., Marcy, G. W., Bryson, S. T., et al. 2012, ApJS, 201, 15
Hunter, J. D. 2007, Comput. Sci. Eng., 9, 90
Ionov, D. E., Pavlyuchenkov, Y. N., & Shematovich, V. I. 2018, MNRAS, 476, 5639
Jones, E., Oliphant, T., Peterson, P., et al. 2001, SciPy: Open source scientific tools for Python
Kitchatinov, L. L., & Olemskoi, S. V. 2005, Astron. Lett., 31, 280
Kluyver, T., Ragan-Kelley, B., Pérez, F., et al. 2016, in Positioning and Power in Academic Publishing: Players, Agents and Agendas, eds. F. Loizides & B. Schmidt (Amsterdam: IOS Press), 87
Knutson, H. A., Benneke, B., Deming, D., & Homeier, D. 2014, Nature, 505, 66
Koskinen, T. T., Yelle, R. V., Lavvas, P., & Lewis, N. K. 2010, ApJ, 723, 116
Kreidberg, L. 2015, PASP, 127, 1161
Kulikov, Y. N., Lammer, H., Lichtenegger, H. I. M., et al. 2006, Planet. Space Sci., 54, 1425
Kulow, J. R., France, K., Linsky, J., & Loyd, R. O. P. 2014, ApJ, 786, 132
Lammer, H., Lichtenegger, H. I. M., Kolb, C., et al. 2003a, Icarus, 165, 9
Lammer, H., Selsis, F., Ribas, I., et al. 2003b, ApJ, 598, L121
Lanotte, A. A., Gillon, M., Demory, B.-O., et al. 2014, A&A, 572, A73
Lavie, B., Ehrenreich, D., Bourrier, V., et al. 2017, A&A, 605, L7
Lecavelier Des Etangs, A. 2007, A&A, 461, 1185
Lecavelier des Etangs, A., Ehrenreich, D., Vidal-Madjar, A., et al. 2010, A&A, 514, A72
Lecavelier des Etangs, A., Bourrier, V., Wheatley, P. J., et al. 2012, A&A, 543, L4
Linsky, J. L., Bushinsky, R., Ayres, T., & France, K. 2012, ApJ, 754, 69
Lopez, E. D., Fortney, J. J., & Miller, N. 2012, ApJ, 761, 59
Lothringer, J. D., Benneke, B., Crossfield, I. J. M., et al. 2018, AJ, 155, 66
Loyd, R. O. P., Koskinen, T. T., France, K., Schneider, C., & Redfield, S. 2017, ApJ, 834, L17
Loyd, R. O. P., France, K., Youngblood, A., et al. 2018, ApJ, 867, 71
Mallonn, M., Herrero, E., Juvan, I. G., et al. 2018, A&A, 614, A35
Mann, A. W., Feiden, G. A., Gaidos, E., Boyajian, T., & von Braun K. 2015, ApJ, 804, 64
Matsakos, T., Uribe, A., & Königl, A. 2015, A&A, 578, A6
Mazeh, T., Holczer, T., & Faigler, S. 2016, A&A, 589, A75
Mennesson, B., Gaudi, S., Seager, S., et al. 2016, Proc. SPIE, 9904, 99040L
Nidever, D. L., Marcy, G. W., Butler, R. P., Fischer, D. A., & Vogt, S. S. 2002, ApJS, 141, 503
Nikolov, N., Sing, D. K., Goyal, J., et al. 2018, MNRAS, 474, 1705
Owen, J. E., & Jackson, A. P. 2012, MNRAS, 425, 2931
Özavcı, I., Şenavcı, H. V., Işık, E., et al. 2018, MNRAS, 474, 5534
Pollack, J. B., Kasting, J. F., Richardson, S. M., & Poliakoff, K. 1987, Icarus, 71, 203
Ribas, I., Guinan, E. F., Güdel, M., & Audard, M. 2005, ApJ, 622, 680
Robertson, P., Endl, M., Henry, G. W., et al. 2015, ApJ, 801, 79
Sanz-Forcada, J., Micela, G., Ribas, I., et al. 2011, A&A, 532, A6
Schwarz, G. 1978, Ann. Stat., 6, 461
Shimizu, T. 1995, PASJ, 47, 251
Stevenson, K. B., Bean, J. L., Fabrycky, D., & Kreidberg, L. 2014, ApJ, 796, 32
Strugarek, A. 2016, ApJ, 833, 140
Suárez Mascareño, A., Rebolo, R., González Hernández, J. I., & Esposito, M. 2015, MNRAS, 452, 2745
Suárez Mascareño, A., Rebolo, R., & González Hernández, J. I. 2016, A&A, 595, A12
Szabó, G. M., & Kiss, L. L. 2011, ApJ, 727, L44
Tian, F., Toon, O. B., Pavlov, A. A., & De Sterck, H. 2005, ApJ, 621, 1049
Turner, J. D., Pearson, K. A., Biddle, L. I., et al. 2016, MNRAS, 459, 789
Vaughan, A. H., Preston, G. W., & Wilson, O. C. 1978, PASP, 90, 267
Vidal-Madjar, A., Lecavelier des Etangs, A., Désert, J.-M., et al. 2003, Nature, 422, 143
Vidal-Madjar, A., Désert, J.-M., Lecavelier des Etangs, A., et al. 2004, ApJ, 604, L69
Visscher, C., Lodders, K., & Fegley, Jr. B. 2010, ApJ, 716, 1060
Wakeford, H. R., Stevenson, K. B., Lewis, N. K., et al. 2017, ApJ, 835, L12
Weber, M. A., Fan, Y., & Miesch, M. S. 2013, ApJ, 770, 149
Wilson, P. A., Lecavelier des Etangs, A., Vidal-Madjar, A., et al. 2017, A&A, 599, A75
Wood, B. E., Redfield, S., Linsky, J. L., Müller, H.-R., & Zank, G. P. 2005, ApJS, 159, 118
Woodgate, B. E., Kimble, R. A., Bowers, C. W., et al. 1998, PASP, 110, 1183
Wright, N. J., Drake, J. J., Mamajek, E. E., & Henry, G. W. 2011, ApJ, 743, 48
Yang, H., Liu, J., Gao, Q., et al. 2017, ApJ, 849, 36
Youngblood, A., France, K., Loyd, R. O. P., et al. 2016, ApJ, 824, 101
Youngblood, A., France, K., Loyd, R. O. P., et al. 2017, ApJ, 843, 31

3.2 The high-energy environment and atmospheric escape of the mini-Neptune K2-18 b

As the interest to search for atmospheres on ever smaller planets has grown, K2-18 b stands out as one of the best targets to efficiently study atmospheres of sub-Neptune sized planets and is an important benchmark for future observations. Owing to its readily detectable water vapor signal observed by *HST*/WFC3 in transmission [175, 12], there is a growing interest of the community to thoroughly characterize the atmosphere of K2-18 b and its host star.

Several possible solutions could explain the observed WFC3 transmission spectrum and density of K2-18 b: they range from high metallicity cloud-free atmospheres (with water vapour abundance as large as several tens of percent) to low metallicity atmospheres with clouds [with water vapor abundance as little as a few hundredths of a percent 175, 12, 124, 34]. All scenarios require the presence of a H-rich atmosphere. However, little is currently known about the best conditions to sustain extended, H-rich atmospheres around sub-Neptune exoplanets, and for the onset of hydrodynamic escape in smaller planets. Previous attempts to detect atmospheric escape in planets with similar sizes and lower densities, but more irradiated, such as π Men c and GJ 1132 b, have resulted in non-detections [186, 69].

One transit of K2-18 b was observed by *HST*/STIS aiming to detect a H-rich exosphere using Lyman-α transmission spectroscopy. Our analysis of this dataset shows tentative evidence favoring the presence of a H-rich exosphere around the planet, which attenuates the blue wing of the stellar Lyman-α average emission by $67\% \pm 18\%$ during the transit. Surprisingly, this in-transit feature is similar to previous detections in GJ 436 b and GJ 3470 b. However, due to the low observable far-ultraviolet fluxes, the fact that only one transit was observed, and the variable nature of M dwarfs in the FUV, this feature can only be confirmed if observed again.

This Section has previously been published in dos Santos et al. [46], and is reproduced with permission © ESO.

A&A 634, L4 (2020)
https://doi.org/10.1051/0004-6361/201937327

Astronomy & Astrophysics

LETTER TO THE EDITOR

The high-energy environment and atmospheric escape of the mini-Neptune K2-18 b⋆

Leonardo A. dos Santos[1], David Ehrenreich[1], Vincent Bourrier[1], Nicola Astudillo-Defru[2], Xavier Bonfils[3], François Forget[4], Christophe Lovis[1], Francesco Pepe[1], and Stéphane Udry[1]

[1] Observatoire Astronomique de l'Université de Genève, 51 Chemin des Maillettes, 1290 Versoix, Switzerland
e-mail: Leonardo.dosSantos@unige.ch
[2] Departamento de Matemática y Física Aplicadas, Universidad Católica de la Santísima Concepción, Alonso de Rivera, 2850 Concepción, Chile
[3] Université Grenoble Alpes, CNRS, IPAG, 38000 Grenoble, France
[4] Laboratoire de Météorologie Dynamique, Institut Pierre Simon Laplace, Université Paris 6 Boite Postale 99, 75252 Paris Cedex 05, France

Received 16 December 2019 / Accepted 13 January 2020

ABSTRACT

K2-18 b is a transiting mini-Neptune that orbits a nearby (38 pc), cool M3 dwarf and is located inside its region of temperate irradiation. We report on the search for hydrogen escape from the atmosphere K2-18 b using Lyman-α transit spectroscopy with the Space Telescope Imaging Spectrograph instrument installed on the *Hubble* Space Telescope. We analyzed the time-series of fluxes of the stellar Lyman-α emission of K2-18 in both its blue- and redshifted wings. We found that the average blueshifted emission of K2-18 decreases by 67% ± 18% during the transit of the planet compared to the pre-transit emission, tentatively indicating the presence of H atoms escaping vigorously and being blown away by radiation pressure. This interpretation is not definitive because it relies on one partial transit. Based on the reconstructed Lyman-α emission of K2-18, we estimate an EUV irradiation in the range $10^1 - 10^2$ erg s^{-1} cm^{-2} and a total escape rate on the order of 10^8 g s^{-1}. The inferred escape rate suggests that the planet will lose only a small fraction (< 1%) of its mass and retain its volatile-rich atmosphere during its lifetime. More observations are needed to rule out stellar variability effects, confirm the in-transit absorption, and better assess the atmospheric escape and high-energy environment of K2-18 b.

Key words. stars: individual: K2-18 – stars: chromospheres – planets and satellites: atmospheres – ISM: kinematics and dynamics

1. Introduction

Short-period exoplanets orbiting nearby, cool M dwarfs are prime targets for the search and characterization of atmospheres of low-mass, sub-Neptune-sized worlds. One particular target that falls in this category is K2-18 b, which was first pointed out as a transiting planet candidate by Montet et al. (2015) and later confirmed with *Spitzer* photometry (Benneke et al. 2017) and Doppler velocity measurements (Cloutier et al. 2017). This planet has a radius of $R_\mathrm{P} = 2.711 \pm 0.065\,R_\oplus$, a mass of $M_\mathrm{P} = 8.64 \pm 1.35\,M_\oplus$ and an orbital period of $T_\mathrm{orb} = 32.9$ d (Cloutier et al. 2019). At an average distance of 0.14 au from its host star, K2-18 b receives a similar amount of bolometric irradiation to that received by the Earth from the Sun. Nevertheless, its high-energy environment is unconstrained, and its density is consistent with either a significant H_2/He envelope or a 100% H_2O composition (Sarkis et al. 2018; Cloutier et al. 2019). The host star is a nearby M2.8-type dwarf located at 38 pc (Gaia Collaboration 2018), rendering K2-18 b one of the best mini-Neptunes suitable for atmospheric follow-up using the *Hubble* Space Telescope (HST), the *James Webb* Space Telescope (JWST), and high-resolution infrared spectrographs.

The 0.4–5.0 μm transmission spectrum of K2-18 b measured with data from the *Kepler* satellite (K2 mission), the Wide-Field Camera 3 (WFC3/HST), and the Infrared Array Camera (IRAC/*Spitzer*) revealed the presence of water vapor in its lower atmosphere (Benneke et al. 2019; Tsiaras et al. 2019). By comparing atmospheric models with the data, Benneke et al. (2019) concludes that the best match is a H_2-dominated atmosphere with water vapor absorbing above the cloud deck below the 10−1000 mbar pressure level. While these observations provided us with some initial information regarding the composition of its lower atmosphere, they do not constrain the abundances of molecular species.

Models predict that the deposition of high-energy photons (X-rays and far-ultraviolet-FUV) produced by the host star leads to an expansion of the planetary upper atmosphere, as well as the production of H atoms due to photodissociation of H_2O (e.g., Ip 1983; Wu & Chen 1993). This expansion populates the outer layers of the planetary atmosphere where the gas is collisionless, also known as the exosphere. It is therefore likely that the atmosphere of K2-18 b, which is rich in H_2 and H_2O, possesses a H-rich exosphere. Previous HST observations have shown evidence for the presence of large-scale,

⋆ The HST Lyman-α spectra are only available at the CDS via anonymous ftp to cdsarc.u-strasbg.fr (130.79.128.5) or via http://cdsarc.u-strasbg.fr/viz-bin/cat/J/A+A/634/L4

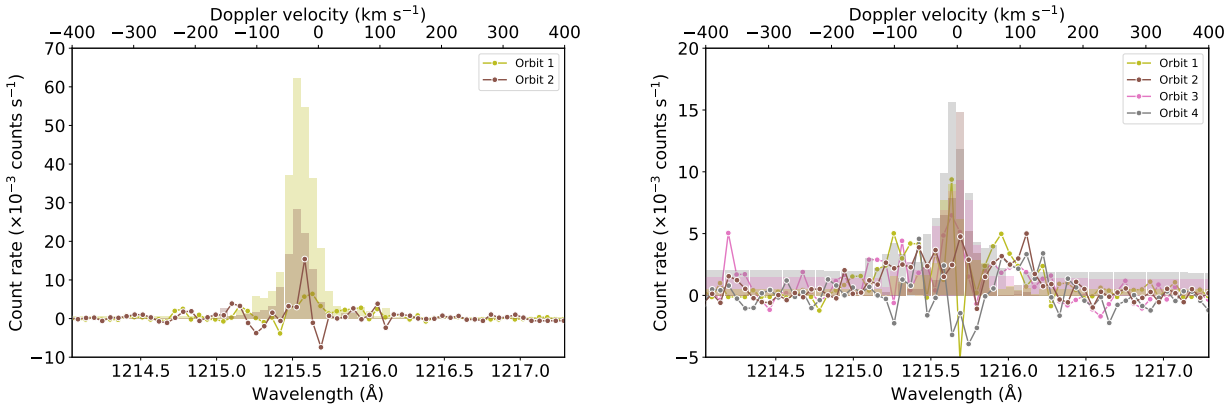

Fig. 1. HST/STIS spectra of K2-18 in Visits A (*left panel*) and B (*right panel*) obtained after data reduction (lines). The geocoronal and background contamination is shown as vertical bars; in Visit A, the geocoronal emission overwhelms the stellar fluxes, preventing us from reliably measuring the latter. The Doppler velocities are in the stellar rest frame.

H-rich exospheres around the warm Neptunes GJ 436 b (Ehrenreich et al. 2015; Lavie et al. 2017; dos Santos et al. 2019) and GJ 3470 b (Bourrier et al. 2018). However, to date, no evidence for extended atmospheres has been found for planets smaller than Neptune, as non-detections were reported for the super-Earths 55 Cnc e (Ehrenreich et al. 2012), HD 97658 b (Bourrier et al. 2017a), GJ 1132 b (Waalkes et al. 2019), and π Men c (García Muñoz et al. 2020), and marginal detections were reported for the small rocky-planet systems in TRAPPIST-1 (Bourrier et al. 2017b) and Kepler-444 (Bourrier et al. 2017c).

In this Letter, we report the results of a series of FUV observations of two transits of K2-18 b using the Space Telescope Imaging Spectrograph (STIS) installed on HST. The aim of these observations was to perform Lyman-α transmission spectroscopy of K2-18 b in order to detect its H-rich exosphere, which should produce an excess absorption in the stellar Lyman-α emission during the transit of the planet.

2. Observations and data reduction

K2-18 was observed with HST/STIS and the grating G140M (resolving power $R \approx 10\,000$) during two transits on June 18 2017 and March 9 2018 (Program GO-14221, PI: D. Ehrenreich). The first visit (A) allowed five exposures, of which only the first two were successful but were severely contaminated by strong geocoronal emission; this contamination completely swamped the stellar Lyman-α emission and rendered this visit unsuitable for analysis (see Fig. 1). The second visit (B) contained four successful exposures, of which two were performed before the transit ingress and the other two in-transit.

The data were reduced using the standard STIS pipeline, except for the spectral extraction. Since the star is faint, the automated extraction is unable to accurately find the stellar spectrum in the flat-fielded frames. Furthermore, the dark current background of the FUV-MAMA detector of STIS reaches levels high enough to be comparable with the stellar spectrum. In order to correctly extract the spectrum and remove the dark current background, we use the `x1d` method of `stistools`[1] with user-defined values for the location of: (i) the spectrum in the cross-dispersion direction, and (ii) the regions where the dark current background near the spectrum can be accurately estimated.

[1] Software freely available at `https://stistools.readthedocs.io/en/latest/`

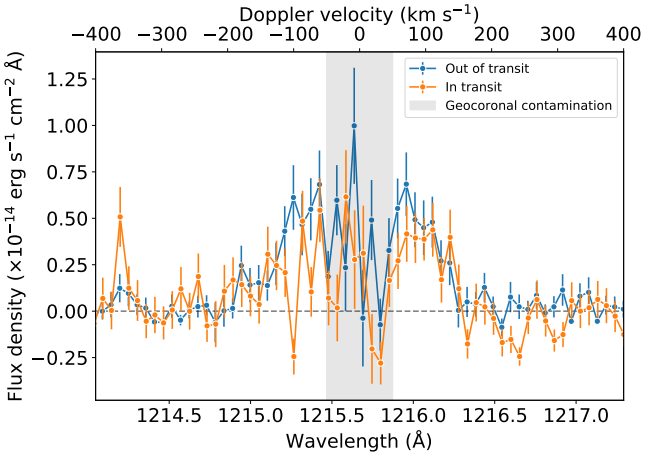

Fig. 2. HST/STIS spectra of K2-18 in Visit B. The Doppler velocities are in the stellar rest frame. The shaded interval is the region with geocoronal contamination.

Using visual inspection, we determined the location of the spectrum in the cross-dispersion direction to be $y = 389$ px (parameter `a2center` in the pipeline). Determining the best location of the background is not as straightforward; normally, the pipeline extracts the background from regions far from the spectrum, but these regions have discrepant levels of dark current compared to the region of the spectrum. Therefore, we chose to use regions immediately near the location of the spectrum to determine the background (parameters `bk1offst` and `bk2offst` in the pipeline), namely at a distance of $\Delta = 20$ px from `a2center`. We combine the two out-of-transit spectra and the two in-transit spectra separately in order to isolate potential signals of an atmospheric signal of K2-18 b, and the resulting spectra are shown in Fig. 2.

3. Tentative detection of a H-rich exosphere in K2-18 b

Since the interstellar medium (ISM) absorbs the core of the Lyman-α emission line, we can only observe the attenuated fluxes in the blue and red wings of the stellar line. We integrated the flux densities in wavelength space between Doppler velocities $[-160, -50]$ km s^{-1} and $[+50, +160]$ km s^{-1}, respectively, to produce the Lyman-α light curves in the blue and red wings.

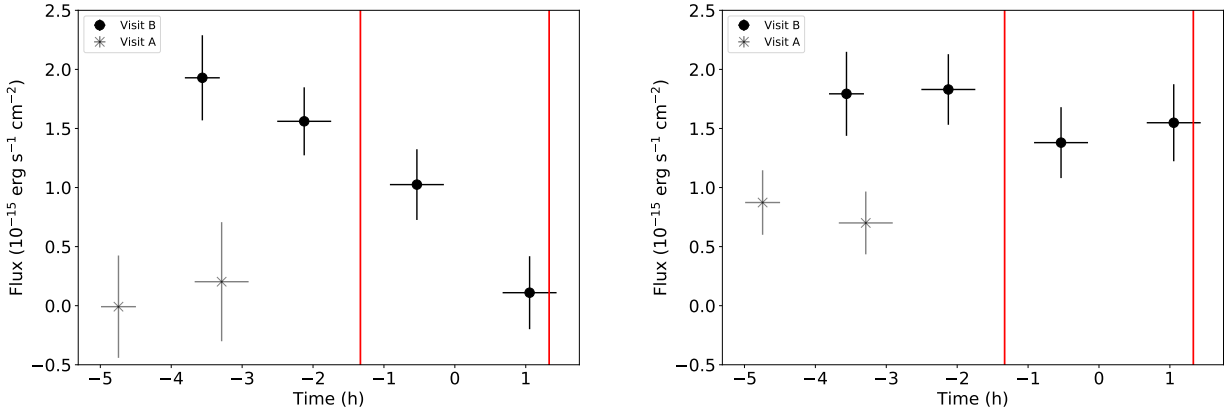

Fig. 3. Light curves of the blue (*left panel*) and red (*right panel*) wings of the Lyman-α emission of K2-18 during the transit of planet b. Time = 0 corresponds to the transit center according to the ephemeris of Benneke et al. (2019). The vertical red lines represent the ingress and egress of K2-18 b. Visit A was affected by strong geocoronal contamination, and therefore the measured stellar fluxes are likely inaccurate.

During Visit B, we observe a steep decrease in the blueshifted Lyman-α fluxes during the transit of K2-18 b (left panel in Fig. 3), reaching almost zero emission near the planetary egress. This decrease in flux is also seen when we compare the combined out-of-transit and in-transit spectra (see Fig. 2). The redshifted Lyman-α emission of the combined in-transit orbits varies by $14\% \pm 23\%$, which is consistent with a stable redshifted flux during the visit; this indicates that the variation in the blue wing is likely to be astrophysical in nature. Similar results are obtained even when we extract the background emission at different positions in the detector.

The blue wing flux measured in the combined in-transit spectra decreases by 67% ± 18% in relation to the combined out-of-transit spectra; in particular, the last orbit displays an absorption of 93% ± 18% in relation to the combined out-of-transit spectra. Although statistically significant, we conservatively deem this result tentative until it is repeated in future observations; for a reference, the intrinsic stellar variability of the Lyman-α emission of HD 97658 b is on the order of a few tens of percent at $\sim 2\sigma$ confidence (Bourrier et al. 2017a). If confirmed to be linked to the transit of K2-18 b, the variation in Lyman-α flux can be interpreted as the absorption caused by an extended, H-rich exosphere of the planet. Such a large absorption signal can be explained by a combination of large atmospheric escape rate and long photoionization lifetime of the H atoms in the exosphere. This result gives further support to the hypothesis that K2-18 b possesses a H_2-dominated envelope (as in the conclusions of Benneke et al. 2019), unlike the super-Earths 55 Cnc e and HD 219134 b. Previous results for the super-Earths HD 97658 b and GJ 1132 b were inconclusive due to stellar variability for the first (Bourrier et al. 2017a) and lack of stellar blue wing emission in the second (Waalkes et al. 2019).

4. The high-energy environment of K2-18 b

Determining the high-energy environment of K2-18 b provides a critical piece of information to interpret the evolution and current state of its atmosphere. To that end, we used the STIS observations of K2-18 to reconstruct its intrinsic Lyman-α spectrum and estimate the high-energy irradiation received by planet b. The reconstruction process follows the standard method used in, for example, Bourrier et al. (2017b, 2018). In short, we fit the observed spectrum to a model of the intrinsic emission line attenuated by ISM absorption, scaled for distance and convolved with the instrumental response; the fit yields an estimate of the intrinsic emission and certain properties of the ISM in the line of sight. In this process, we assume that the intrinsic Lyman-α emission of K2-18 possesses a Gaussian profile (applicable for M dwarfs and for the quality of the available spectra; see Bourrier et al. 2017c, 2018), and fix the temperature and turbulent velocity of the ISM to 8000 K and 1.23 km s^{-1} (for the NGP cloud, as estimated by the LISM calculator Redfield & Linsky 2008), respectively. We also set the deuterium-to-hydrogen ratio (D I/H I) to 1.5×10^{-5} and the systemic velocity to 0.6537 km s^{-1} (measured with high-resolution spectra by Cloutier et al. 2017).

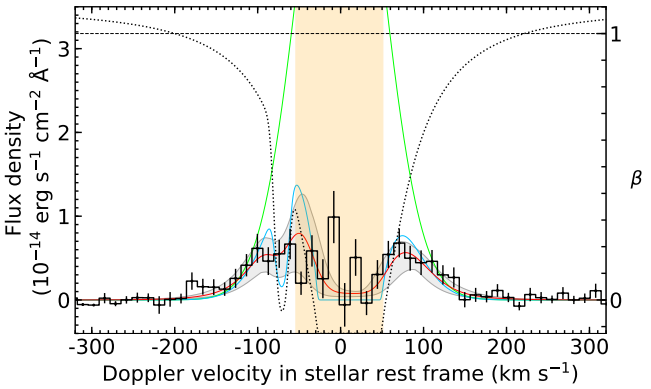

Fig. 4. Reconstructed intrinsic Lyman-α spectrum of K2-18 (green) and the average Lyman-α profile as observed with HST/STIS (black bars). The red (blue) curve shows the inferred observable spectrum with (without) instrumental convolution and the shaded region represents the 1σ uncertainty for the red curve. The dotted curve shows the inferred ISM absorption profile.

The result of the Lyman-α line reconstruction is shown in Fig. 4. We simultaneously fit each exposure to a global Lyman-α line model within ±300 km s^{-1} in the stellar rest frame, excluding the band that corresponds to significant airglow contamination (approximately the range ±50 km s^{-1}, shown in orange in Fig. 4). When fitting the in-transit orbits we excluded the pixels corresponding to the range potentially absorbed by the planet. We explore the parameter space using the Markov chain Monte Carlo ensemble sampler implementation of `emcee` (Foreman-Mackey et al. 2013); in addition, we report the uncertainties based on the highest density interval (HDI), which contains 68.3% of the distribution mass such that no point outside the interval has a higher density than any point within it. We

Table 1. Properties of the high-energy environment of K2-18 b.

Lyman-α flux (erg s^{-1} cm^{-2})	$100.7^{+96.1}_{-82.4}$
EUV 10–91.2 nm flux (erg s^{-1} cm^{-2})	$107.9^{+124.7}_{-90.8}$
Photoionization rate ($\times 10^{-6}$ s^{-1})	$3.7^{+7.5}_{-3.5}$
Photoionization lifetime (h)	3600^{+49900}_{-2400}
Escape rate at 100% efficiency ($\times 10^{8}$ g s^{-1})	$3.5^{+4.0}_{-2.9}$

fit for four free parameters in total: the temperature (assuming a Gaussian thermal broadening) and amplitude of the intrinsic stellar Lyman-α line, and the radial velocity and H I density of the ISM. We estimated the EUV flux in K2-18 b using the relation from Linsky et al. (2014).

We determined that the heliocentric radial velocity of the ISM is $V_R = 11.39^{+4.04}_{-4.73}$ km s^{-1}, and the H I column density in the line of sight is $\log_{10}\eta = 18.16^{+0.44}_{-0.34}$ cm^{-2}. While η is consistent with the results from Wood et al. (2005), the value we determined for V_R differs by 2σ with the value predicted by LISM calculator (Redfield & Linsky 2008).

We estimated the properties of the high-energy environment of K2-18 b based on the reconstructed Lyman-α emission and the results are shown in Table 1; the large uncertainties in these estimates are due to the low signal-to-noise ratio (S/N) of the spectra and the uncertainties in the semi-empirical relations used to estimate the EUV flux. The best fit model of the intrinsic Lyman-α emission of K2-18 results in a β (ratio between radiation pressure and stellar gravity; see right axis of Fig. 4) of about 2.2. Although more data would be necessary to confirm this line shape, and the corresponding high β, it nonetheless suggests that radiation pressure could blow away the escaping hydrogen atoms more strongly in K2-18 b than in GJ 436 b (Bourrier et al. 2016) or the TRAPPIST-1 planets (Bourrier et al. 2017b). This value of β is similar to that inferred for GJ 3470 b (Bourrier et al. 2018), which could indicate that the exosphere of K2-18 b possesses a similar shape. Using the energy-limited escape (e.g., Salz et al. 2015) as an initial estimate, we predict that the total escape rate in K2-18 b is two orders of magnitude lower when compared to the values inferred for GJ 436 b ($\sim 2.2 \times 10^{10}$ g s^{-1}; Bourrier et al. 2016) and GJ 3470 b ($\sim 8.5 \times 10^{10}$ g s^{-1}; Bourrier et al. 2018). We estimated the photoionization rate and lifetime as in Bourrier et al. (2017a), which yields a value likely above 1200 h for the latter; this long lifetime means that the H atoms in the exosphere of K2-18 b could stay neutral for much longer than in GJ 436 (12 h) and GJ 3470 b (3.5 h). These results are not surprising because K2-18 b is subject to lower irradiation levels than the aforementioned warm Neptunes.

The inferred escape rate of K2-18 b is likely underestimated because we do not take into account the stellar X-ray flux, which is currently unknown. For a similar star like GJ 436, the ratio between X-ray and EUV emission is ~0.23 (Bourrier et al. 2016), which provides an upper limit on the level of underestimation contained in our calculation; however, the contribution of X-ray flux may be less important for the ionization conditions because of the smaller ionization cross-section when compared to EUV wavelengths.

5. Conclusions

K2-18 b is currently one of the best targets for transit spectroscopy among sub-Neptune planets due to its large scale height, its short distance from the Sun, and the infrared brightness of the host star. Previous results have shown evidence that the atmosphere of the planet is dominated by H_2/He and contains water vapor. In these atmospheric conditions and under the expected high levels of EUV irradiation, K2-18 b is prone to efficiently losing its atmosphere and producing a detectable excess absorption of H in Lyman-α caused by a H-rich exosphere during transit. In this study we analyzed four HST orbits before and during the transit of K2-18 b with the STIS instrument to search for this feature.

We analyzed the flux time series of both the blue- and redshifted wings of the stellar Lyman-α emission. The blue wing displays a significant excess absorption during the transit; in particular, near the egress of K2-18 b, the flux in the blue wing is consistent with 100% absorption. The in-transit red wing fluxes vary by 14% ± 23% and are significantly more stable than the blue wing fluxes. A blueshifted absorption could indicate the presence of a H-rich exosphere around K2-18 b being swept away by radiation pressure from its host star towards the direction of the observer, similar to the exospheres of GJ 436 b and GJ 3470 b.

Despite the low S/N of the observed spectra, we were able to reconstruct the intrinsic stellar emission (without the ISM absorption) to assess the high-energy environment of K2-18 b. Our first estimate for the expected total escape rate of K2-18 b leads to a value on the order of 10^8 g s^{-1}. The ratio between radiation pressure and gravity (β) suggests that the exosphere of K2-18 b is in a similar state to that observed for GJ 3470 b. We estimate that the EUV (10–91.2 nm) flux in the planet is on the order of 10^1–10^2 erg s^{-1} cm^{-2}. At the estimated escape rate, it is likely that the planet will lose only a small fraction (1% or less) of its mass during its remaining lifetime, and therefore it is probably not an archetypal planet crossing the radius valley to become a bare rock (Fulton et al. 2017; Van Eylen et al. 2018; Fulton & Petigura 2018); as such, the planet will likely retain its volatile-rich atmosphere due to the more amenable EUV irradiation flux than for example GJ 3470 b, which is at least ten times more EUV irradiated than K2-18 b.

Since we observed only one partial transit of K2-18 b, we conclude that the H-rich exosphere detection is only tentative for now, and more observations are needed to rule out stellar activity effects and confirm the reported feature. Furthermore, additional observations of the Lyman-α spectrum of K2-18 will help in better constraining the high-energy environment of the planet and its atmospheric escape history.

Acknowledgements. LAdS thanks M. Turbet and M. López-Morales for the insightful discussions about K2-18 b. This project has received funding from the European Research Council (ERC) under the European Union's Horizon 2020 research and innovation programme (project FOUR ACES; grant agreement No 724427), and it has been carried out in the frame of the National Centre for Competence in Research PlanetS supported by the Swiss National Science Foundation (SNSF). This research is based on observations made with the NASA/ESA *Hubble* Space Telescope. NA-D acknowledges the support of FONDECYT project 3180063. The authors are grateful to the anonymous referee for the quick and helpful review. The data are openly available in the Mikulski Archive for Space Telescopes (MAST), which is maintained by the Space Telescope Science Institute (STScI). STScI is operated by the Association of Universities for Research in Astronomy, Inc. under NASA contract NAS 5-26555. This research made use of the NASA Exoplanet Archive, which is operated by the California Institute of Technology, under contract with the National Aeronautics and Space Administration under the Exoplanet Exploration Program. We used the open source software SciPy (Jones et al. 2001), Jupyter (Kluyver et al. 2016), Astropy (Astropy Collaboration 2013), Matplotlib (Hunter 2007) and `emcee` (Foreman-Mackey et al. 2013).

References

Astropy Collaboration (Robitaille, T. P., et al.) 2013, A&A, 558, A33
Benneke, B., Werner, M., Petigura, E., et al. 2017, ApJ, 834, 187
Benneke, B., Wong, I., Piaulet, C., et al. 2019, ApJ, 887, L14
Bourrier, V., Lecavelier des Etangs, A., Ehrenreich, D., Tanaka, Y. A., & Vidotto, A. A. 2016, A&A, 591, A121
Bourrier, V., Ehrenreich, D., King, G., et al. 2017a, A&A, 597, A26
Bourrier, V., de Wit, J., Bolmont, E., et al. 2017b, AJ, 154, 121
Bourrier, V., Ehrenreich, D., Allart, R., et al. 2017c, A&A, 602, A106
Bourrier, V., Lecavelier des Etangs, A., Ehrenreich, D., et al. 2018, A&A, 620, A147
Cloutier, R., Astudillo-Defru, N., Doyon, R., et al. 2017, A&A, 608, A35
Cloutier, R., Astudillo-Defru, N., Doyon, R., et al. 2019, A&A, 621, A49
dos Santos, L. A., Ehrenreich, D., Bourrier, V., et al. 2019, A&A, 629, A47
Ehrenreich, D., Bourrier, V., Bonfils, X., et al. 2012, A&A, 547, A18
Ehrenreich, D., Bourrier, V., Wheatley, P. J., et al. 2015, Nature, 522, 459
Foreman-Mackey, D., Hogg, D. W., Lang, D., & Goodman, J. 2013, PASP, 125, 306
Fulton, B. J., & Petigura, E. A. 2018, AJ, 156, 264
Fulton, B. J., Petigura, E. A., Howard, A. W., et al. 2017, AJ, 154, 109
Gaia Collaboration (Brown, A. G. A., et al.) 2018, A&A, 616, A1
García Muñoz, A., Youngblood, A., Fossati, L., et al. 2020, ApJ, 888, L21
Hunter, J. D. 2007, Comput. Sci. Eng., 9, 90
Ip, W. H. 1983, ApJ, 264, 726
Jones, E., Oliphant, T., Peterson, P., et al. 2001, SciPy: Open Source Scientific Tools for Python
Kluyver, T., Ragan-Kelley, B., Pérez, F., et al. 2016, in Positioning and Power in Academic Publishing: Players, Agents and Agendas, eds. F. Loizides, & B. Schmidt (IOS Press), 87
Lavie, B., Ehrenreich, D., Bourrier, V., et al. 2017, A&A, 605, L7
Linsky, J. L., Fontenla, J., & France, K. 2014, ApJ, 780, 61
Montet, B. T., Morton, T. D., Foreman-Mackey, D., et al. 2015, ApJ, 809, 25
Redfield, S., & Linsky, J. L. 2008, ApJ, 673, 283
Salz, M., Schneider, P. C., Czesla, S., & Schmitt, J. H. M. M. 2015, A&A, 576, A42
Sarkis, P., Henning, T., Kürster, M., et al. 2018, AJ, 155, 257
Tsiaras, A., Waldmann, I. P., Tinetti, G., Tennyson, J., & Yurchenko, S. N. 2019, Nat. Astron., 3, 1086
Van Eylen, V., Agentoft, C., Lundkvist, M. S., et al. 2018, MNRAS, 479, 4786
Waalkes, W. C., Berta-Thompson, Z., Bourrier, V., et al. 2019, AJ, 158, 50
Wood, B. E., Redfield, S., Linsky, J. L., Müller, H.-R., & Zank, G. P. 2005, ApJS, 159, 118
Wu, C. Y. R., & Chen, F. Z. 1993, J. Geophys. Res., 98, 7415

Chapter 4

Observability of hydrogen-rich exospheres in Earth-like exoplanets

> *“ Look again at that dot. That’s here. That’s home. That’s us. On it, everyone you love, everyone you know, everyone you ever heard of, every human being who ever was, lived out their lives [...] – on a mote of dust suspended in a sunbeam. ”*
>
> *Carl Sagan*

It is safe to say that one of the biggest goals of exoplanetary science is to find another planet similar to the Earth, one that could potentially sustain life and be habitable. So far, this goal has been elusive, and will likely remain so for the next few decades. The reason is two-fold: rocky planets are small, so their signals are difficult to disentangle from the light of the host star; and even if we are able to detect a signal, there are confounding factors related to habitability, making the endeavor prone to false positives. However, there are a few unique aspects that make our own Earth stand out among the other rocky planets of the Solar System, among them the 1% water vapor content of our atmosphere, as well as the presence of a H-rich extended atmosphere.

Ironically, we routinely detect the Earth’s geocorona when we observe in Lyman-α with the *Hubble Space Telescope*. This "contaminant" is precisely what we want to detect in other exoplanets. As we briefly discussed in Sect. 1.2.1, the Earth’s H-rich exosphere that we observe today is fundamentally different from those that we observe in hot gas giants, and also from the early Earth: it is fed by Jeans escape of H atoms, which in turn are produced by photodissociation of water molecules from an atmosphere rich in water vapor. Thus, if we are able to detect a similar tenuous exosphere around a rocky exoplanet at amenable temperatures, that can be used as an additional diagnostic in our toolkit to search for Earth-like planets.

We end our journey across evaporating exoplanets with the first project realized in my doctorate. Interesting enough, we come full circle, as this is precisely where Waterston and Rayleigh [188] first wondered about atmospheres evaporating from planets. Here, we sought to quantify how well we can detect signs of an Earth-like exosphere as if it were an exoplanet orbiting a nearby M dwarf. Our findings show that the excess absorption for such an exoplanet varies from 50 to 600 ppm, which is a level of precision that *HST* is not capable of yielding in Lyman-α wavelengths. However, our research also shows that a *LUVOIR*-class telescope [15] coupled with the LUMOS spectrograph [60] will be able to achieve such a precision.

This chapter has previously been published in dos Santos et al. [43], and is reproduced with permission © ESO.

A&A 622, A46 (2019)
https://doi.org/10.1051/0004-6361/201833392

Astronomy & Astrophysics

Observability of hydrogen-rich exospheres in Earth-like exoplanets

Leonardo A. dos Santos[1], Vincent Bourrier[1], David Ehrenreich[1], and Shingo Kameda[2]

[1] Observatoire astronomique de l'Université de Genève, 51 chemin des Maillettes, 1290 Versoix, Switzerland
e-mail: leonardo.dossantos@unige.ch
[2] Department of Physics, College of Science, Rikkyo University, 3 Chome-34-1 Nishiikebukuro, Tokyo 171-8501, Japan

Received 8 May 2018 / Accepted 28 November 2018

ABSTRACT

Context. The existence of an extended neutral hydrogen exosphere around small planets can be used as evidence of the presence of water in their lower atmosphere, but, to date, such a feature has not been securely detected in rocky exoplanets. Planetary exospheres can be observed using transit spectroscopy of the Lyman-α line, which is limited mainly by interstellar medium absorption in the core of the line, and airglow contamination from the geocorona when using low-orbit space telescopes.
Aims. Our objective is to assess the detectability of the neutral hydrogen exosphere of an Earth-like planet transiting a nearby M dwarf using Lyman-α spectroscopy and provide the necessary strategies to inform future observations.
Methods. Our tests require spatial and velocity information of the neutral hydrogen particles in the upper atmosphere. The spatial distribution is provided by an empirical model of the geocorona, and we assume a velocity distribution based on radiative pressure as the main driver in shaping the exosphere. We compute the excess absorption in the stellar Lyman-α line while in transit, and use realistic estimates of the uncertainties involved in observations to determine the observability of the signal.
Results. We found that the signal in Lyman-α of the exosphere of an Earth-like exoplanet transiting M dwarfs with radii between 0.1 and 0.6 $R_\odot$ produces an excess absorption between 50 and 600 ppm. The Lyman-α flux of stars decays exponentially with distance because of interstellar medium absorption, which is the main observability limitation. Other limits are related to the stellar radial velocity and instrumental setup.
Conclusions. The excess absorption in Lyman-α is observable using LUVOIR/LUMOS in M dwarfs up to a distance of ~15 pc. The analysis of noise-injected data suggests that it would be possible to detect the exosphere of an Earth-like planet transiting TRAPPIST-1 within 20 transits.

Key words. planets and satellites: atmospheres – techniques: spectroscopic – ultraviolet: stars – ultraviolet: planetary systems

1. Introduction

The exosphere of a planet is defined as the region where the gas becomes collisionless, or more formally the region where the Knudsen number (the ratio of the mean free path to the scale height) is higher than one. This region is predominantly sustained by atmospheric escape from the planet, driven mainly by nonthermal processes (Shizgal & Arkos 1996; Volkov et al. 2011) for planets like the Earth, and thermal hydrodynamic escape for strongly irradiated giant planets (e.g., Lammer et al. 2003; Lecavelier Des Etangs et al. 2004).

The first observations of evaporating atmospheres of exoplanets were performed for hot Jupiters such as HD 209458 b (Vidal-Madjar et al. 2003; Ehrenreich et al. 2008; Linsky et al. 2010) and HD 189733 b (Lecavelier Des Etangs et al. 2010, 2012; Poppenhaeger et al. 2013). The process of evaporation is facilitated in such close-in inflated planets because, in the energy-limited regime, the mass loss rate is proportional to the high-energy flux received from the host star and inversely proportional to the bulk density of the planet (Lecavelier Des Etangs 2007). Atmospheric escape has also been observed in the warm Neptune exoplanet GJ 436 b (Kulow et al. 2014; Ehrenreich et al. 2015), in which the conditions are favorable to produce a comet-like tail of neutral hydrogen (Bourrier et al. 2015, 2016; Lavie et al. 2017).

An exospheric cloud such as that around GJ 436 b produces extremely large transit absorption signatures in Lyman-α (56% ±3%; Ehrenreich et al. 2015) compared to what is measured in the optical transmission spectrum of this planet (250 ppm; Lothringer et al. 2018). It is not known how small a planet can be and still exhibit a readily detectable exospheric cloud. The Earth itself is surrounded by a neutral hydrogen exosphere, which produces the geocorona[1] (Wallace et al. 1970; Carruthers & Page 1972). A recent Lyman-α (hereafter Lyα) image of the Earth taken from 0.1 au showed that the geocorona spans more than 38 Earth radii (Kameda et al. 2017). The hydrogen density is approximately 20 atoms cm^{-3} at a height of 600 000 km in the Earth's exosphere. Venus and Mars also have H-rich exospheres, but they are far less extended and less dense because these planets have atmospheres rich in CO_2 and possess lower exospheric temperatures (Kulikov et al. 2007).

Detecting an extended hydrogen exosphere around a rocky exoplanet would be compelling evidence for the presence of water in the lower atmosphere of the planet, since the atomic H is a product of photodissociation of water. Jura (2004) indeed proposed that evaporating exoplanetary oceans could fuel H-rich

[1] The traditional definition of geocorona is the light emitted by the Earth's exosphere. In this manuscript, however, we use the terms "Earth's exosphere" and "geocorona" interchangeably.

exospheres (see also Selsis et al. 2007; Bolmont et al. 2017). This could be a new path to characterize habitability-zone (HZ) exoplanets and trace their water content[2]. This is especially relevant for planets around M dwarfs, which are targets of intense searches for rocky planets because their HZ is closer to the star and transiting planets produce large signals. Much speculation has been done, for instance, for the water content of the TRAPPIST-1 planets (Gillon et al. 2016; Bourrier et al. 2017a,b; Bolmont et al. 2017).

Far-extended exospheres are easier to analyze in Lyα than the compact lower atmospheres at longer wavelengths. Moreover, the velocity field in the exosphere can reach more than 100 km s^{-1}, spreading the atmospheric absorption signal over a large range of wavelengths and increasing its detectability. Currently, the only telescope that has access to the Lyα line is the *Hubble* Space Telescope (HST), and the instrument usually employed for these observations is the Space Telescope Imaging Spectrograph (STIS). In the future, projects such as the Large Ultraviolet/Optical/Infrared Surveyor (LUVOIR; Bolcar et al. 2017) and the Habitable Planet Explorer (HabEx; Gaudi et al. 2018) will build upon on the FUV (far-ultraviolet) capabilities of HST in several aspects. Using a theoretical model of the Earth's exosphere and several simplifications, Gómez de Castro et al. (2018) calculated that the detection of an Earth-like exosphere is possible for the nearest stars, provided that the mirror size is larger than 4 m. In this work, we perform a more detailed and extensive assessment of this prospect based on observational constraints of the geocorona (Kameda et al. 2017) and provide scaling relations for the stellar radius, distance (considering interstellar medium (ISM) absorption), exospheric density, and instrumental setup. Further, this study aims at informing the community about the capabilities of future UV telescopes to characterize HZ exoplanets.

This manuscript has the following structure: in Sect. 2 we present the observation and models of the Earth's exosphere; in Sect. 3 we describe how the Lyα profile of different targets and conditions is computed and estimate the excess absorption signal in Lyα transmission spectroscopy for an Earth-like planet transiting a M dwarf; in Sect. 4 we extensively discuss the observation strategies and limitation on performing such a detection; in Sect. 5 we briefly present the best targets on which to conduct intensive searches; in Sect. 6 we present the main conclusions obtained in this research.

2. Observation and model of the Earth's hydrogen exosphere

2.1. The neutral hydrogen geocorona

The Earth's exosphere was observed using the Lyman Alpha Imaging Camera (LAICA) on board the Proximate Object Close Flyby with Optical Navigation (PROCYON) on 9 January 2015, when the spacecraft was at a distance of 2348 $R_\oplus$ (0.1 au) from the Earth and at coordinates 74.09° and −23.94° in right ascension and declination (see Fig. 1 in Kameda et al. 2017). The LAICA instrumentation consists of a 41 mm diameter Cassegrain-type telescope and a detector unit equipped with a 122 ± 10 nm bandpass wavelength filter. The total exposure time of the observation was 300 s, spatial resolution was 1.34 and 0.98 $R_\oplus$/pixel in the horizontal and vertical directions, respectively, and the effective field of view of LAICA is 2° × 2°. This observation revealed that the geocorona spans more than 38 $R_\oplus$, a value that exceeds the previously determined lower limit of 16 $R_\oplus$ (Wallace et al. 1970; Carruthers & Page 1972). According to Kameda et al. (2017), the geocorona possesses north-south symmetry, indicating that magnetic fields are not dominant in shaping the geocorona under moderate solar activity; the asymmetry in the horizontal direction is inconclusive, since it could be simply explained by the viewing geometry of the observations. These observations did not include high-resolution spectroscopy, thus they do not provide direct dynamical information about the geocorona.

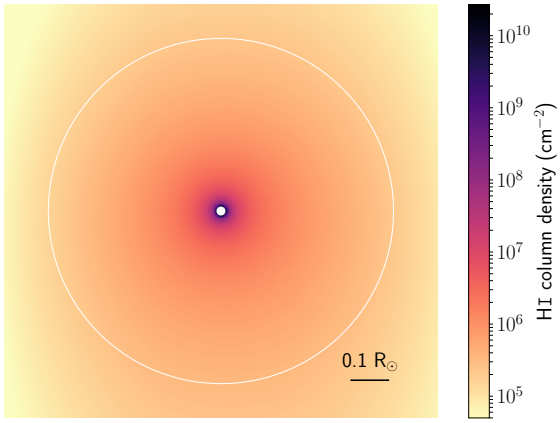

Fig. 1. Column density map of the model of the geocorona obtained by Kameda et al. (2017). The Earth's transiting disk is shown as a small white circle. The large white circle represents the size of the M dwarf GJ 436. Asymmetries near the borders are artificial because of the rotation of a box-shaped model.

Based on this observation, Kameda et al. (2017) reconstructed the geocorona using a modified Chamberlain model (Chamberlain 1963) with three parameters: the exobase temperature, exobase density, and solar radiation pressure. The force of the solar radiation was determined using the local photon scattering rate; assuming an exobase temperature of 1000 K (as in Picone et al. 2002), the exobase density was derived from the fit to the emission data using a simple χ^2 minimization.

2.2. Densities and velocity field

To verify if an Earth-like exosphere around a rocky extrasolar planet is observable with current instrumentation in transit at Lyα, we start from the analytical model of the neutral hydrogen geocorona produced by Kameda et al. (2017). We calculated the three-dimensional density distribution using the model and computed the column densities by integrating the volumetric densities in the line of sight (see Fig. 1).

The geocorona model yields the densities of neutral hydrogen, but not their velocities distribution, which is necessary to compute the Lyα absorption profile. In order to estimate this distribution, we assume that there are two competing forces dictating the dynamics of the neutral hydrogen particles in the exosphere: gravity and radiation pressure. The second can either overturn stellar gravity and move particles away from the star ("radiative blow-out," Bourrier & Lecavelier des Etangs 2013) or slow down the infall of matter toward the star ("radiative braking"; see the case of GJ 436 b, a moderately irradiated warm Neptune in Figs. 1 and 2 in Bourrier et al. 2015). Effectively, the line-of-sight velocities of the particles are limited in the

[2] The direct detection of water in the atmosphere of water-rich planets will be challenging, even with future infrared spectrographs such as JWST (see, e.g., Deming & Seager 2017).

bluer end by the orbital velocity of the planet and in the redder end by the mode of a thermal distribution of particles with a kinetic temperature of 1000 K (mean temperature at the exobase; Kameda et al. 2017), since the line-of-sight component of the orbital velocity at transit center is null for circular orbits. Using this temperature, we obtain that the upper limit of velocities of particles in Earth's exosphere is approximately 4 km s^{-1}.

In the reference frame of the host star, particles escaping from an exoplanet atmosphere have an initial velocity that combines the orbital velocity of the planet and the velocity of the planetary wind. Assuming nearly circular orbits, the orbital speed of a planet in relation to the host star is

$$v_{\rm orb} = \sqrt{\frac{GM_\star}{a}}, \quad (1)$$

where $M_\star$ is the stellar mass and a is the orbital semimajor axis of the planet. Assuming that a planet orbits in the inner edge of the HZ of its host star (similarly to the Earth; Kopparapu et al. 2013), the orbital speeds of the hypothetical planet in the range 30–50 km s^{-1}, respectively for $M_\star$ varying from 0.1 $M_\odot$ to 1 $M_\odot$; for reference, Earth's orbital speed in relation to the Sun is 29.8 km s^{-1}. In addition, the planetary wind of the Earth is well inside the Jeans escape regime, which means that particles escaping from the atmosphere are in the high-velocity tail of the Maxwell-Boltzmann distribution. The introduction of other mechanisms such as stellar wind and bow shocks, although they could play a role in determining the distribution of positions and velocities of particles, would add too many free parameters to our model and is not justified at this point. Thus, as a first approximation, and based on the results for the Earth (e.g., Kameda et al. 2017) and evaporating planets (e.g., Bourrier & Lecavelier des Etangs 2013; Bourrier et al. 2015), we consider radiation pressure to be the main driver of the dynamics of neutral hydrogen atoms escaping from Earth-like planets.

3. Signature of transiting exospheres in Lyman-α emission of quiet M dwarfs

In general, the Lyα emission line of M dwarfs possesses a nearly Gaussian shape (Wood et al. 2005; Youngblood et al. 2016; Wheatley et al. 2017). The MUSCLES survey[3] obtained the Lyα reconstructed flux for 12 inactive early- to mid-M dwarfs using HST (Youngblood et al. 2017), and these survey results show that the Lyα luminosity among the sample varies by two orders of magnitude and correlate with the rotational period of the star; the Lyα luminosity of GJ 436 is representative of the mean in their sample (see Fig. 2).

3.1. Interstellar medium absorption

Except for the Sun, we do not have access to the intrinsic Lyα emission of stars due to absorption by the neutral hydrogen atoms present in the ISM between the target and the Earth. If the ISM clouds in the line of sight have radial velocities close to the radial velocity of the target star, the core of the stellar Lyα emission line is completely absorbed. Thus, in such cases, only the wings of the Lyα line contain information about the system. For distant targets, not only their faintness is a limitation in UV observations, but their distances also increase the column densities of ISM neutral hydrogen in the line of sight, as well as the range of ISM radial velocities; for these reasons, we can only study escaping atmospheres in Lyα for the closest ($d \lesssim 60$ pc) exoplanetary systems, or for host stars with large radial velocity (such as Kepler-444, Bourrier et al. 2017c). There is also absorption by deuterium at the rest wavelength 1215.25 Å, although less pronounced than the absorption by H I atoms. The radial velocity of the local interstellar cloud (LIC) varies between −25 km s^{-1} and 25 km s^{-1}, approximately, depending on the direction of sight (Wood et al. 2005).

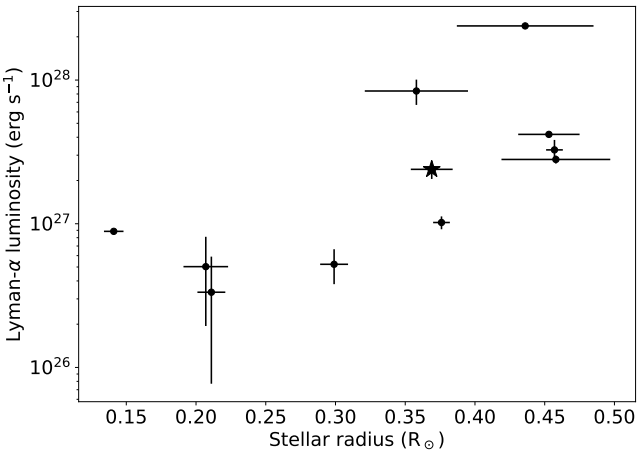

Fig. 2. Lyα luminosity of quiet M dwarfs in the MUSCLES sample (based on GAIA DR2 distances). The Lyα fluxes and stellar radii were reported in Youngblood et al. (2017). The star symbol denotes the position of GJ 436.

In order to estimate how the ISM absorption affects the observable Lyα fluxes of M dwarfs with different distances, we simulated the total attenuation of the flux caused by ISM absorption. We set the physical properties of the ISM to be isotropic, namely the temperature to 8000 K (similar to the what is measured in the solar neighborhood), the radial velocity to zero, and turbulence velocity to zero; other values of turbulence do not significantly affect our results and conclusions. We assumed the minimum and maximum densities of neutral H in the solar neighborhood (0.01 and 0.1 cm^{-3}), and adopted the fraction between the densities of deuterium and H $N_{\rm D}/N_{\rm H} = 1.5 \times 10^{-5}$ (Bourrier & Lecavelier des Etangs 2013). The ISM absorption profiles are computed as in Bourrier et al. (2017d).

We found that the Lyα line fluxes of M dwarfs decrease approximately exponentially with the distance in the range from 2 to 20 pc, where the flux is attenuated to less than 10% of the intrinsic emission in case we observe in a direction with high H column density. However, we reiterate that this is an approximation, since it is well known that the ISM in the solar neighborhood is patchy (Redfield & Linsky 2008) and its physical properties vary, so in reality the attenuation depends on the direction of observation.

3.2. Estimating the excess absorption

When a planet with a H-rich exosphere transits its host star, the opaque disk of the planet blocks part of the Lyα flux (i.e., baseline continuum absorption) and its exosphere absorbs part of the flux in addition (i.e., excess absorption).

The absorption profile caused by the passage of a cloud of neutral hydrogen in front of a stellar disk is computed following

[3] The Measurements of the Ultraviolet Spectral Characteristics of Low-mass Exoplanetary Systems (MUSCLES) was a HST Treasury Survey aimed at measuring the ultraviolet flux distribution of nearby planet-hosting M dwarfs (France et al. 2016a).

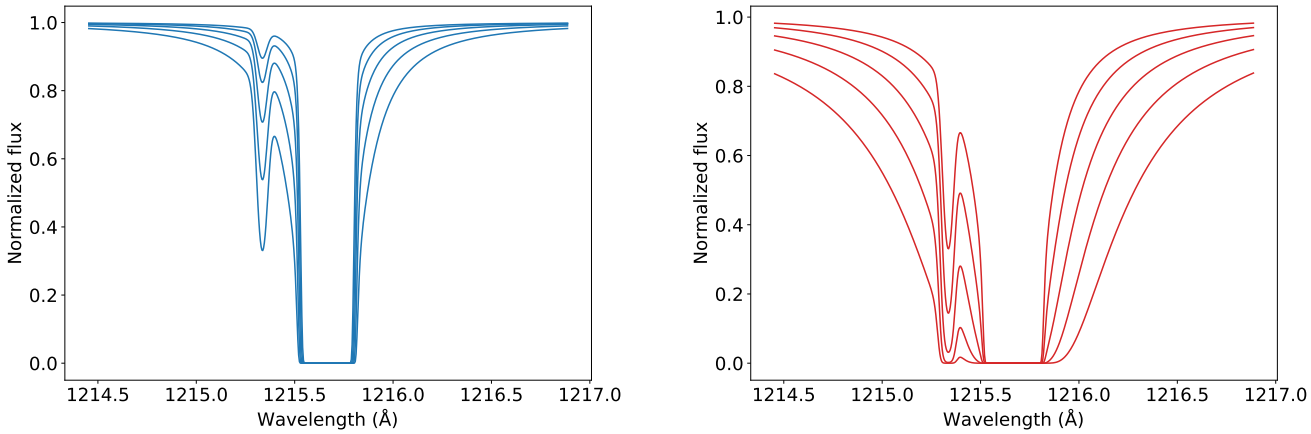

Fig. 3. *Left panel*: expected ISM absorption profiles for distances 2.0, 3.6, 6.3, 11.2, and 20.0 pc and for the minimum column density of the LIC (radial velocity of the cloud is fixed at zero). *Right panel*: same as left panel, but for the maximum column density of the LIC.

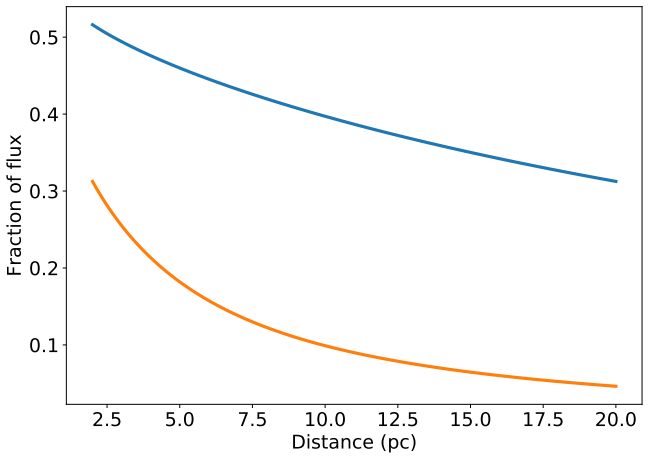

Fig. 4. Observed fraction of the intrinsic Lyman-α flux as a function of distance after ISM absorption. The blue (orange) curve represents the attenuation in the lowest (highest) density of the LIC.

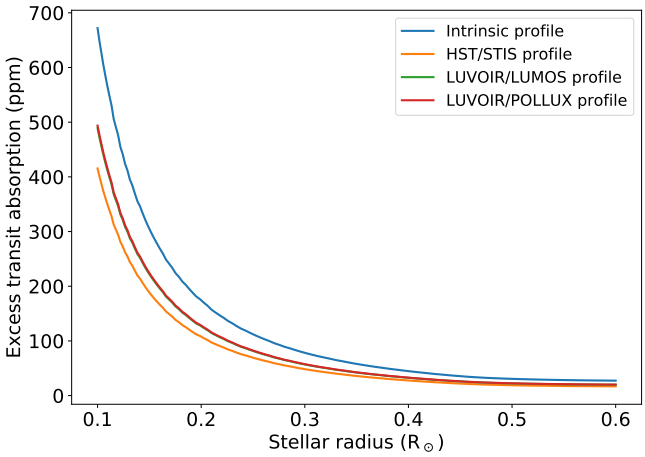

Fig. 5. Mean excess transit absorption in Lyα caused by an Earth-like exosphere as a function of the stellar radius. In the case of absorption profiles convolved with an instrumental profile, we considered the signal located inside the Doppler velocity range -50 km s^{-1} to 10 km s^{-1}.

the equations in Sect. 2.4 of Bourrier & Lecavelier des Etangs (2013) applied to the model proposed by Kameda et al. (2017). The absorption profile depends mainly on the spatial and velocity distributions of neutral hydrogen atoms (see Sect. 2.2). In order to assess the excess absorption by a transiting exosphere, we use synthetic Lyα profiles based on the observed emission line of the quiet M dwarf GJ 436.

To obtain the in-transit spectrum, we position an Earth-sized planet and its exosphere in the center of the disk of the star at mid-transit (impact parameter $b = 0$), compute its absorption profile, and multiply this profile by the out-of-transit intrinsic stellar spectrum. Both in- and out-of-transit spectra are then absorbed by a realistic ISM model. When measured through a telescope, the observable spectra are convolved with the instrumental response; furthermore, during the analysis we need to avoid using wavelength ranges where the signal-to-noise ratio is too low – we describe practical aspects of observations in Sect. 4.

The exospheric excess absorption per unit wavelength S_λ in the Lyα line is measured by the ratio of the in- ($F_{\lambda,\mathrm{in}}$) and out-of-transit flux densities ($F_{\lambda,\mathrm{out}}$). We have, thus,

$$S_\lambda = 1 - \frac{F_{\lambda,\mathrm{in}}}{F_{\lambda,\mathrm{out}}} - a_{\mathrm{pl}}, \tag{2}$$

where a_{pl} is the baseline absorption caused by the opaque disk of the planet. The value S_λ does not depend on the distance of the target since the fraction $F_{\lambda,\mathrm{in}}/F_{\lambda,\mathrm{out}}$ cancels out this dependence. The mean excess absorption depth S is measured by taking the mean of S_λ between a given range of Doppler velocities.

We simulated a grid of models of transiting events as described above around stars of radii varying between 0.1 $R_\odot$ and 0.6 $R_\odot$, which is our adopted definition of a M dwarf. Since we assumed a flat distribution of velocities for the particles in the exosphere of the planet, the intrinsic excess transit profile is constant in wavelength. If we take into account the instrumental profile of a spectrograph, this signal is diluted. The resulting relation between stellar size and excess transit absorption is shown in Fig. 5. Similar to optical transits, it is clear that excess transit depths are deeper the smaller the host star is, which results from simple geometry.

We expect S_λ to depend on the distribution of velocities of H atoms in the exosphere and on the radial velocity of the target star because the ISM absorption quickly saturates with distance and can partially or completely erase the signal we want to observe. Considering our assumptions in Sect. 2.2, the radial velocity range where $S_\lambda < 10$ ppm depends mainly on the spectral resolution of the spectrograph: for HST/STIS, this range

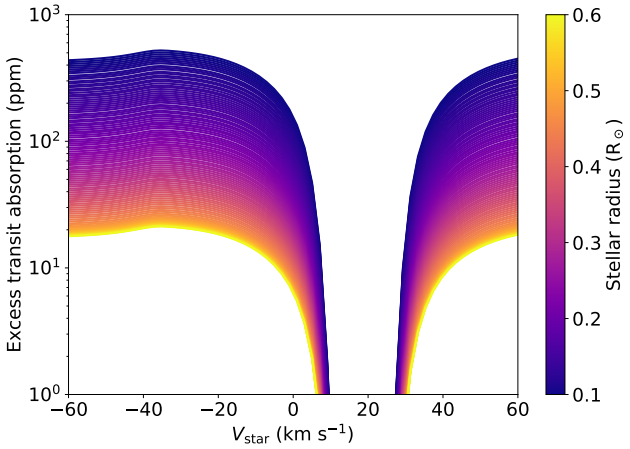

Fig. 6. Mean excess transit absorption in Lyα caused by an Earth-like exosphere as a function of systemic radial velocity as observed with HST/STIS. For spectrographs with higher resolution, the range at which the signal is lost is narrower than the range of STIS (R = 10 000).

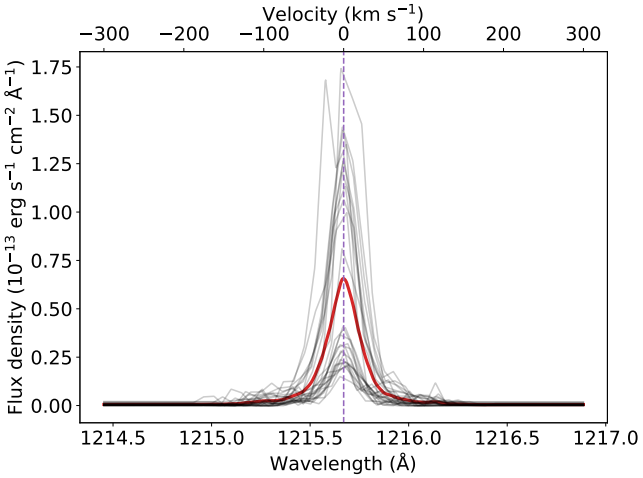

Fig. 7. Mean geocoronal emission of the Earth as measured with HST/STIS during 27 observations (red spectrum). The gray spectra correspond to the different exposures. The emission lines were aligned to the rest frame of the telescope by fitting Gaussians to each exposure.

is located approximately between [0, 40] km s^{-1} (see Fig. 6); the approximate ranges for the LUVOIR planned spectrographs LUMOS and POLLUX are 5–30 km s^{-1} and 10–25 km s^{-1}, respectively. Outside these ranges, the expected signal should follow the relations seen in Fig. 5.

4. Practical and observational aspects

Currently, the only instruments capable of performing FUV spectroscopy of exoplanetary atmospheres are the STIS and the Cosmic Origins Spectrograph (COS) aboard the HST. Several projects of large-aperture telescopes equipped with FUV instruments are currently being studied. In particular, the World Space Observatory (WSO-UV; Sachkov et al. 2016) is even partially built. In the following sections we are going to consider HST/STIS and two potential instruments with known specifications for the LUVOIR telescope: LUMOS (France et al. 2016b, 2017) and POLLUX (Muslimov et al. 2018). We discuss how these instruments can overcome the current limitations that make it challenging to detect the excess absorption signal of exospheres around Earth-like planets in Sect. 3.

4.1. Geocoronal contamination

Far-ultraviolet observations can only be performed from space, and low-orbit telescopes (such as the HST) contain contamination from geocoronal emission produced by the Earth's exosphere (see Fig. 7). In general, the geocoronal contamination is variable (stronger on the dayside of the Earth and weaker in the nightside), but it can be removed in a straightforward fashion, provided that the observations are performed with a slit spectrograph: the sky spectrum is measured away from the target, and then it is simply subtracted from the spectrum of the target. According to the manual of HST/STIS, during an exposure with high geocoronal contamination, the fluxes are ∼1.98 times larger than the average, and they are ∼0.20 times lower when in the shadow of the Earth. In the case of spectrographs with a circular aperture, such as the COS on HST, the removal of geocoronal contamination is not straightforward, but it can be performed using airglow templates[4] (see, e.g., Wilson et al. 2017; Bourrier et al. 2018).

[4] Airglow templates for HST/COS are available at http://www.stsci.edu/hst/cos/calibration/airglow.html

In any case, even after the removal of the geocoronal contamination, the additional photon noise remains in the spectra obtained with low-orbit telescopes. The increased noise affects how well we can measure the excess absorption signal by the exosphere of a hypothetical Earth-like exoplanet. This issue can be alleviated by observing near the nightside of the Earth, but such a measure results in shorter exposures: in the case of HST, opting for observations in the Earth's shadow reduces the exposure time by approximately 50%. It is also more difficult to allocate time for such a proposal that is already time-constrained in the first place.

4.2. Measurement uncertainties

The uncertainties σ of the flux density F_λ measured in a spectrograph are a combination of the nonphotonic background term $\sigma_{\rm offset}$ and the photon noise that scales linearly with the square root of F_λ as follows:

$$\sigma^2 = \sigma_{\rm offset}^2 + \left(G\sqrt{F_\lambda}\right)^2 . \quad (3)$$

These parameters can vary broadly between different instruments. Based on the observations of GJ 436 reported by Lavie et al. (2017), we found that for HST/STIS $\sigma_{\rm offset} \approx 4.15 \times 10^{-16}$ erg s^{-1} cm^{-2} Å^{-1} and $G \approx 3.74 \times 10^{-8}$ (erg s^{-1} cm^{-2} Å^{-1})$^{1/2}$ for one exposure of 50 minutes using the grating G140M. With these numbers, we estimate that the mean uncertainty added by geocoronal photon noise in a 50-minute-long exposure of HST/STIS amounts to 4.7×10^{-15} erg s^{-1} cm^{-2}.

The factor G in Eq. (3) depends on the exposure time and several instrumental properties, such as mirror size and the efficiencies of the optics and the detector. To realistically compute the expected uncertainties of the observable Lyα spectrum measured with HST/STIS and other instruments, we consider that

$$G \propto \frac{1}{A_{\rm eff}\sqrt{t_{\rm exp}}} , \quad (4)$$

where $A_{\rm eff}$ is the effective area of the instrument (which is the end-to-end throughput multiplied by the geometric area of an unobstructed circular aperture with the size of the mirror) and $t_{\rm exp}$ is the exposure time.

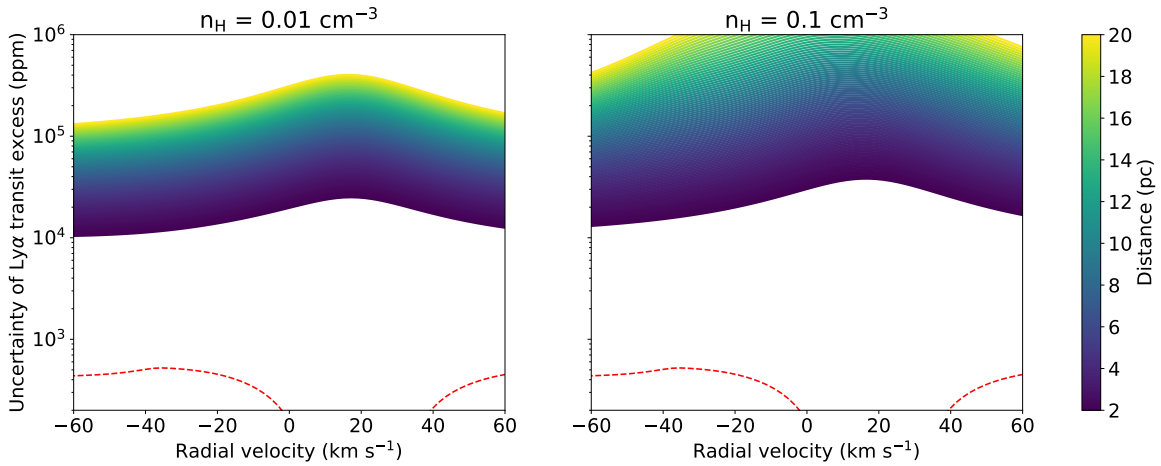

Fig. 8. Expected uncertainty of the Lyman-α flux of M dwarfs as a function of their distance in a single exposure of HST/STIS using the G140M grating and for two different densities of H I in the ISM. The flux was computed in the Doppler velocity range −50 km s^{-1} to 10 km s^{-1} and we assumed the radial velocity of the ISM to be null in the rest frame of the telescope. The dashed line represents the excess transit absorption level in a 0.1 $R_\odot$ M dwarf.

The uncertainty σ_S of the mean excess absorption depth S is obtained by propagating the uncertainties of $F_{\rm in}$, $F_{\rm out}$ and $a_{\rm pl}$, i.e.,

$$\sigma_S^2 = \left(\frac{F_{\rm in}}{F_{\rm out}}\right)^2 \left[\left(\frac{\sigma_{\rm in}}{F_{\rm in}}\right)^2 + \left(\frac{\sigma_{\rm out}}{F_{\rm out}}\right)^2\right] + \sigma_a^2. \quad (5)$$

If we assume that $F_{\rm in} \approx F_{\rm out}$ and ignoring the uncertainty σ_a of $a_{\rm pl}$ for now, then σ_S simplifies to

$$\sigma_S = \frac{\sigma}{F}\sqrt{2}. \quad (6)$$

4.2.1. HST/STIS

According to the manual of HST/STIS[5], the throughput of the instrument using the grating G140M (the standard used to perform Lyα spectroscopy of M dwarfs) is ∼1.5%, resulting in an effective area of 680 cm^2 around 1216 Å.

In the regime where radiation pressure dominates the dynamics of an exosphere, we expect the velocities of the H particles in the upper atmosphere of the planet to be between the limits we described in Sect. 2.2 (usually between −40 km s^{-1} and 0 km s^{-1} in the rest frame of the star). Thus, depending on the difference between the radial velocity of the host star and that of the ISM cloud in the line of sight, the exospheric absorption signal may fall inside (totally or partially) or outside of the wavelength region where there is no flux to be measured (i.e., no information can be obtained).

Assuming no slit losses, we used Eqs. (3), (4), and (6) to estimate the uncertainty of the mean excess absorption in Lyα flux of M dwarfs between −50 km s^{-1} and 10 km s^{-1} in the stellar rest frame (the range where we expect the exospheric absorption signal to be located). The estimates were performed for a range of stellar stellar radial velocities and distances, assuming the Lyα profile to be similar to GJ 436, and we plot the results in Fig. 8.

For a small M dwarf with $R = 0.1\ R_\odot$, the expected excess transit depth between Doppler velocities −50 km s^{-1} and 10 km s^{-1} is approximately 400 ppm for HST/STIS (dashed line in Fig. 8), and such a precision is beyond the capabilities of the instrument. The increase in flux uncertainty between radial velocities 0 and 40 km s^{-1} is due to the ISM absorption. Furthermore, we note that, in the case of a large density of H I in the line of sight (as seen in the right panel of Fig. 8), little to no information about the flux can be measured for M dwarfs beyond ∼16 pc and radial velocities between −20 km s^{-1} and 30 km s^{-1} if we use HST/STIS. These results are compatible with the precision obtained for the Lyα flux of TRAPPIST-1 using HST/STIS data (Bourrier et al. 2017a).

4.2.2. LUVOIR/LUMOS and LUVOIR/POLLUX

The detection of an exosphere around an Earth-like planet may require the use of a larger telescope and improved efficiencies to decrease the uncertainties of the Lyα flux. For comparison, the expected effective areas of LUVOIR using the spectrographs POLLUX and LUMOS are 2000 (1100) and 130 000 (73 100) cm^2, respectively, assuming the design with a diameter of 12 (9) m (K. France, priv. comm.; see a summary of instrumental properties in Table 1).

We performed the same tests with LUVOIR/LUMOS and LUVOIR/POLLUX[6] to estimate the uncertainties they yield when observing M dwarfs at different distances; the results are summarized in Figs. 9 and 10. It is important to note that LUVOIR will reside at the Earth-Sun L2 point, thus avoiding contamination by geocoronal emission. It will, however, still contain astrophysical background contamination; based on the value ∼710 R reported by Kameda et al. (2017), we estimate that the astrophysical background in Lyα to be $\sim 2 \times 10^{-14}$ erg s^{-1} cm^{-2} arcsec^{-2}.

Our estimates show that, in a 50-minute[7] exposure with LUVOIR, the uncertainties of the Lyα flux of M dwarfs up to a distance of 20 pc and up to radius 0.6 $R_\odot$ are always limited by the photon noise of the source and well above the limit set by the photon noise of background astrophysical sources. The LUMOS spectrograph will have uncertainties two orders of magnitude lower than POLLUX owing to its larger effective area. On the

[5] Available at http://www.stsci.edu/hst/stis/performance/throughput

[6] For POLLUX we assumed the same instrumental background as LUMOS.

[7] We chose 50 minutes so that the results are comparable to HST/STIS. The duration of an HZ exoplanet transit around an M dwarf is on this order of magnitude.

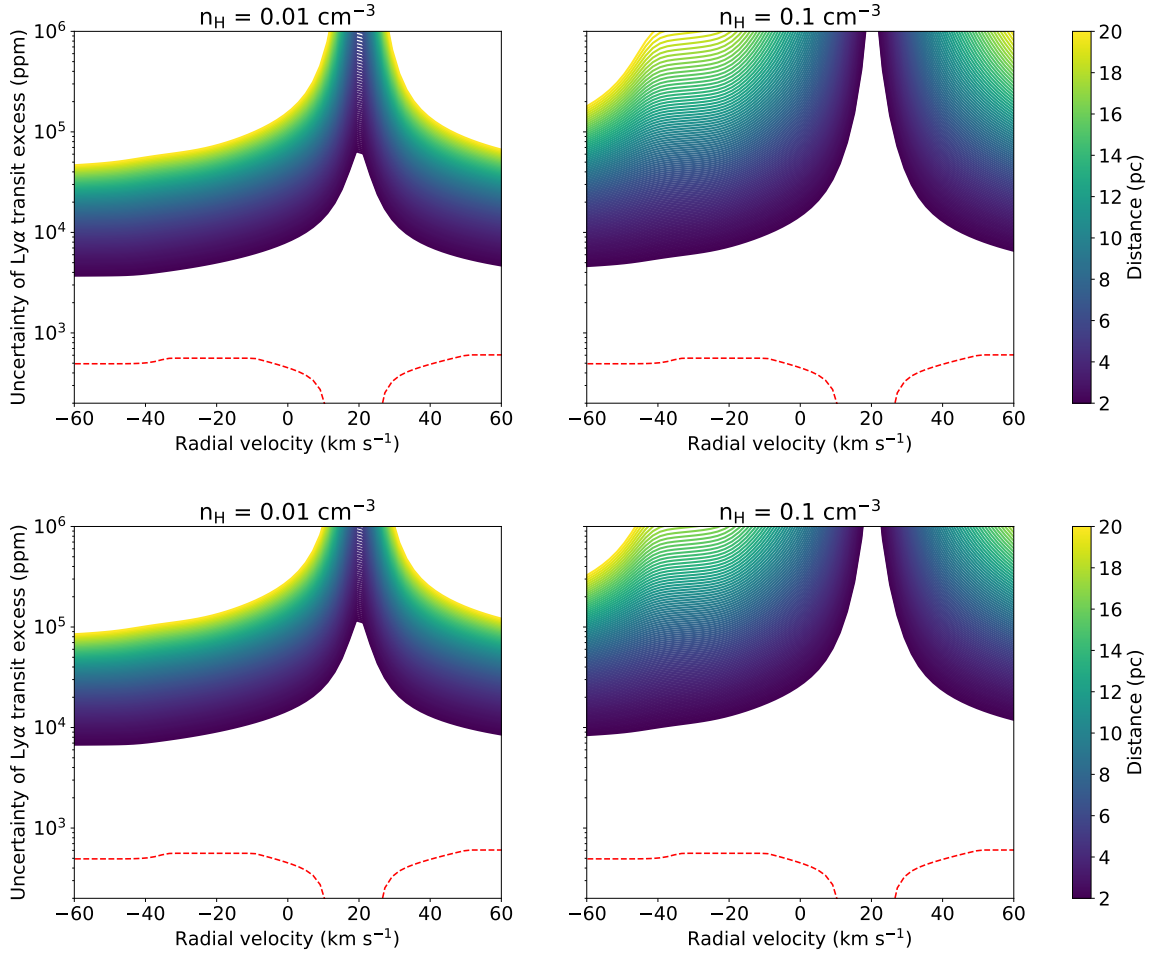

Fig. 9. Same as Fig. 8, but for LUVOIR/POLLUX. The top (bottom) row corresponds to LUVOIR-A (-B).

Table 1. Properties of the instruments.

Properties near Lyα	HST/STIS G140M	LUVOIR-A(B)/LUMOS G120M	LUVOIR-A(B)/POLLUX
Resolving power	10 000	44 000	120 000
Effective area (cm^2)	680	130 000 (73 100)	2000 (1100)
Background rate (erg cm^{-2} s^{-1} Å^{-1})	7×10^{-17}	2×10^{-20}	...
Aperture size (arcsec)	52×0.1 [slit]	0.136×0.068 [shutter]	0.03 [pinhole]

other hand, the POLLUX instrument provides an improvement of one order of magnitude in the flux precision when compared to HST/STIS.

By comparing the estimated uncertainty levels with the expected signal in Fig. 5, we can conclude that LUVOIR/LUMOS will be better suited to perform the detection of an Earth-like exosphere transiting an M dwarf in Lyα. Such a detection will, nonetheless, be limited to a certain distance, which will vary depending on the time we are willing to invest. If we consider that 30 transits is a reasonable time investment for a single target, then this distance limit should be 15–20 pc in the most favorable scenarios.

4.3. Analysis of a synthetic dataset with injected noise

To illustrate the point of this manuscript, we analyze two test cases with synthetic datasets and a well-established analysis strategy used in previous studies of FUV transmission spectroscopy. In case 1, we produce the Lyα spectrum of a M dwarf with $R = 0.2\,R_\odot$, $V_{\rm star} = -30$ km s^{-1}, $d = 5$ pc, and simulate the observable spectra with realistic injected noise based on the instrumental design of LUVOIR/LUMOS. In case 2, to simulate a case similar to TRAPPIST-1, we change the stellar radius to $0.12\,R_\odot$, distance to $d = 12$ pc, and $V_{\rm star} = -55$ km s^{-1}. The Lyα synthetic spectra of the test cases are shown in Fig. 11.

We produce light curves of the Lyα flux of the star by integrating its flux density between the Doppler velocities -50 km s^{-1} and 10 km s^{-1} in the stellar reference frame, assuming that all transit exposures happened at roughly the same phases of the planetary orbit. The exposure time is set by the duration of the optical transit, which should be around 100 (60) minutes in the case of an Earth-sized planet orbiting in the inner edge of the HZ of a $R = 0.20$ (0.12) $R_\odot$ M dwarf. The resulting light curves are shown in Fig. 12.

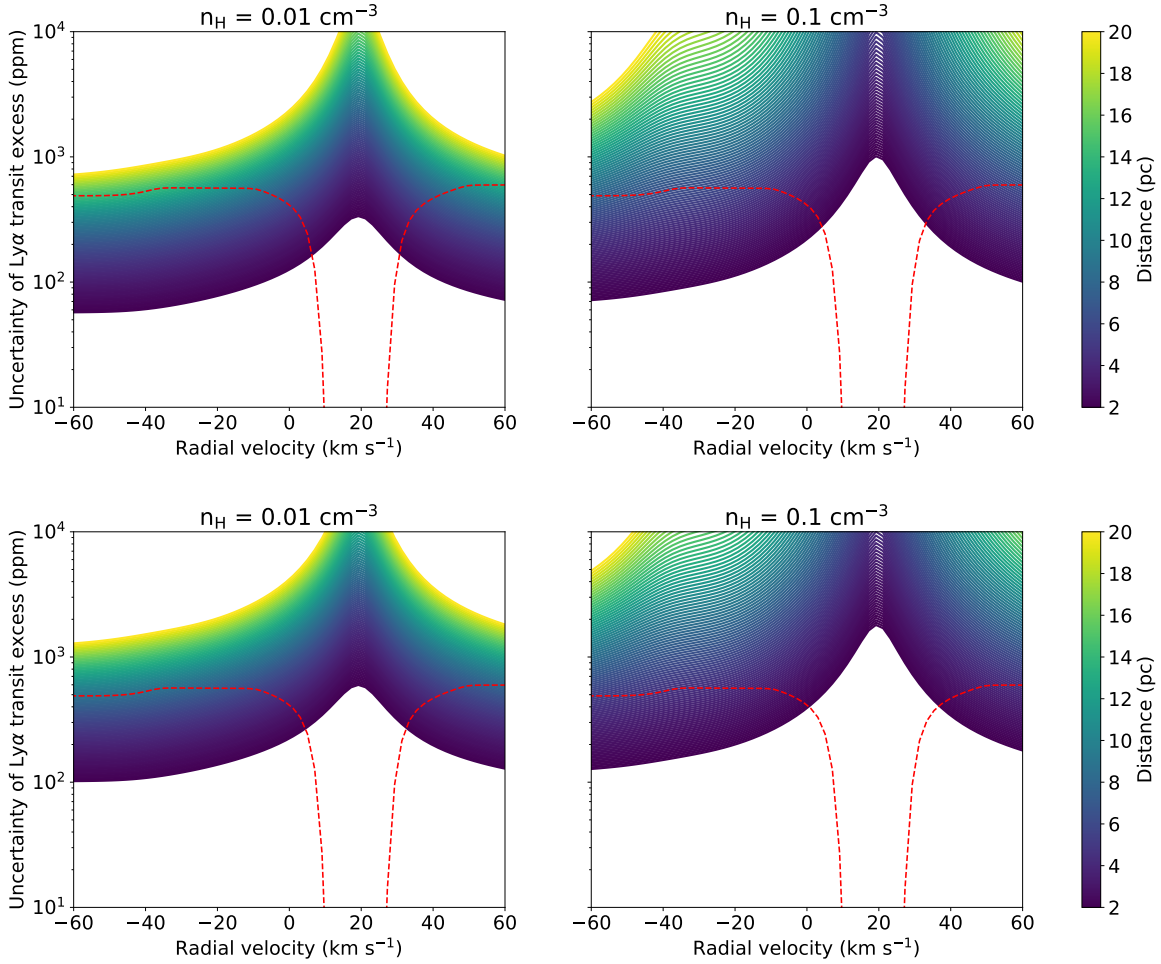

Fig. 10. Same as Fig. 8, but for LUVOIR/LUMOS and with a different scale in the *y*-axis.

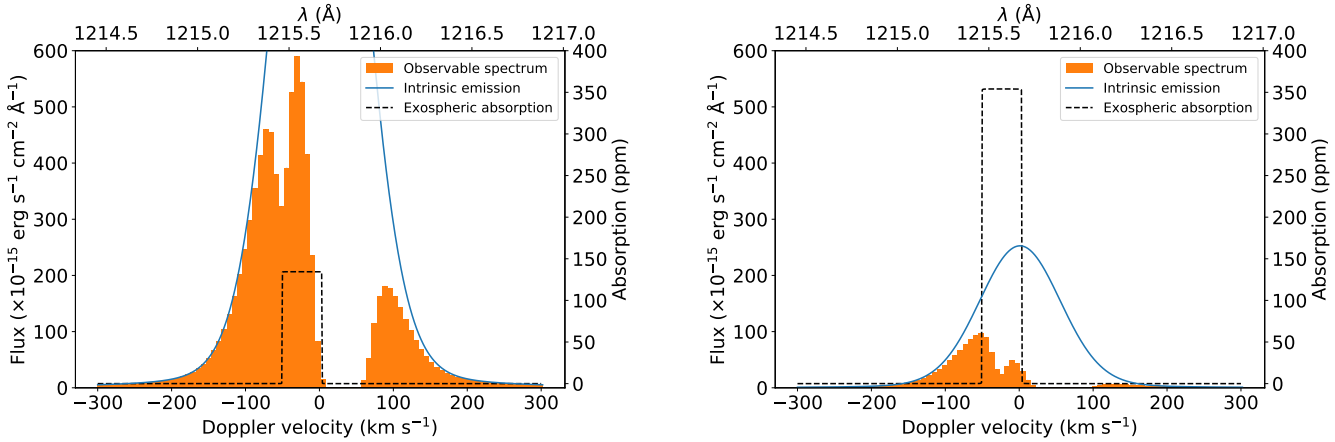

Fig. 11. Synthetic spectra used in the test case 1 (*left panel*) and 2 (*right panel*). The scales in the *y*-axes are kept the same to highlight the difference between the observable fluxes.

The white-light absorption dominates the total Lyα occultation for an Earth-like exoplanet transiting a M dwarf, as expected. However, with the accumulation of several transit light curves with LUVOIR/LUMOS, there is a visible excess absorption in the mid-transit exposures assuming that the white-light radius of the transiting exoplanet is known perfectly; this exposures are ∼200 ppm for case 1 and 500 ppm for case 2, whose values are comparable to the expected transit depth excess seen in Fig. 5. For a reference, the precision of TESS light curves for bright targets ($T_{mag} < 8$) is on the order of 100 ppm (Sullivan et al. 2015; Oelkers & Stassun 2018), which is similar to the signal we are trying to detect; thus, an extensive photometric follow-up on Earth-sized candidates from TESS may be necessary to obtain a precise white-light radius before attempting a Lyα transmission spectrum; the satellite CHEOPS (Broeg et al. 2013) will be a crucial instrument to obtain precise radii of exoplanets.

The Lyα transit excess absorption obtained in the noise-injected test cases is shown in Table 2. In general, we show that

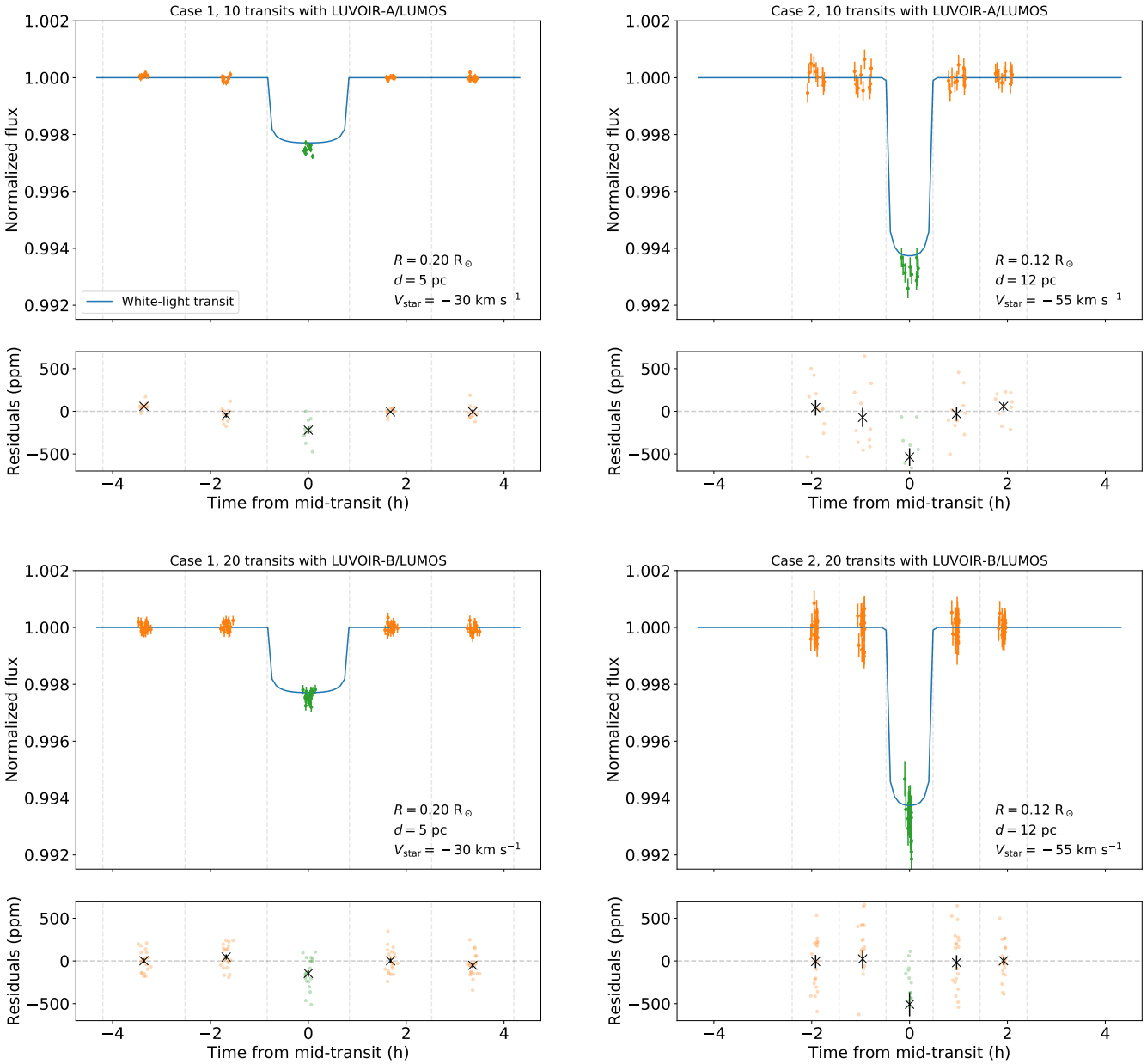

Fig. 12. Transit light curves of our test cases. The vertical dashed lines separate the different exposures (5 in total for each transit; the exposure time for each data point is equal to the transit duration).

Table 2. Mid-transit excess absorption obtained for cases 1 and 2 using noise-injected data based on the specifications of LUVOIR/LUMOS.

	Transit excess (ppm)		# of transits
	Case 1	Case 2	
LUVOIR-A	220 ± 42	535 ± 103	10
LUVOIR-B	145 ± 39	507 ± 142	20

it is possible to perform the detections within a resonable time investment (10–20 transits) using LUVOIR/LUMOS and obtain a significance of 5σ for a targets at 5 pc or 12 pc.

4.4. Comparison with previous studies

A recent report by Gómez de Castro et al. (2018) showed that detecting exospheric hydrogen in terrestrial planets is feasible for nearby M dwarf targets, provided that the telescope is large enough (4–8 m primary mirror). Our results corroborate this conclusion of Gómez de Castro et al. (2018), but we found that the detectability depends not only on the telescope size and it is also highly dependent on the intrinsic properties of the host star, such as radius and the radial velocity difference of the system. In fact, stars with favorable properties may allow us to search for H-rich exospheres in a range of distances up to 20 pc (see Sect. 5).

There are other, more direct but not necessarily more efficient, ways to search for evidence of atmospheric water in Earth-sized planets. Transmission spectroscopy using JWST[8] (Greene et al. 2016) offers the most obvious choice. In particular,

[8] The *James Webb* Space Telescope (JWST) is planned to be launched in the early 2020s and will perform imaging and spectroscopic observations between wavelengths 0.6 μm and 30 μm during a lifetime of 5–10 years.

Barstow & Irwin (2016) showed that it is possible to detect water in the atmospheres of some planets in the TRAPPIST-1 system using JWST, but it would require 60 transits for a clear detection. Another strategy that may become available in the future is high-dispersion spectroscopy coupled with high-resolution imaging (e.g., Snellen et al. 2015; Lovis et al. 2017), but such techniques may be limited to very nearby systems (up to only a few pc, such as Proxima b). In addition, high-dispersion spectroscopy with the extremely large telescopes may provide a window to search for biosignatures, such as oxygen, in rocky nearby planets up to several parsecs in distance (Snellen et al. 2013).

5. Targets of interest

Our results from Sects. 3 and 4 show that the best targets to search for the signal of exospheric absorption in an Earth-like exoplanet are small M dwarfs within ∼15 pc. These limits can be stretched or shrunk depending on the radial velocity of the star and the H I density of the ISM in the line of sight. To date, the nearest M dwarfs with known Earth-sized transiting planets are LHS 1140 (Dittmann et al. 2017; Ment et al. 2019) and TRAPPIST-1 (Gillon et al. 2016, 2017). We were able to obtain a detection in simulated data for a TRAPPIST-1-like system, but the distance and radial velocity of LHS 1140 (15 pc and -13.2 km s^{-1}, respectively) may render the latter a difficult target for the search of an Earth-like exosphere.

In the case of nearby solar-type stars, such as α Cen AB and 18 Sco, the most significant barrier to perform this search is that the inner edge of their HZ sits too far from the host star, rendering orbital periods in the order of several months (Kasting et al. 1993) and severely decreasing the transit probability of a potential exoplanet.

More Earth-sized planets amenable to exospheric characterization are likely going to be discovered by TESS (Ricker et al. 2014). The mission will detect several new transiting exoplanets in the solar neighborhood, particularly around M dwarfs in a brighter regime than the *Kepler* and K2 missions. Based on the Catalogue of Simulated TESS Detections (Sullivan et al. 2015), we estimate that planets amenable to atmospheric escape detection – namely those around stars within 50 pc – will amount to a sample of ∼130 planets. Of these, ∼30 will have radii between 0.7 and 1.5 $R_\oplus$, of which ∼10 will have a similar level of irradiation as the Earth. A final cut to a distance of 15 pc results that only ∼4 of these predicted transiting planets will be similar to Earth in size and irradiation level, and viably be amenable to exospheric characterization using LUVOIR.

In this article, we limited ourselves to consider only quiet M dwarfs and exoplanets with an exosphere similar to the Earth's, which do not provide the most favorable conditions to produce evidence for water in the lower atmosphere of a rocky exoplanet. Other targets that can potentially be of interest are active M dwarfs that host transiting exoplanets, which are known to display strong Lyα emission and thus would likely produce stronger exospheric absorption signal.

Exoplanets with denser exospheres produce a stronger absorption signal in Lyα, and our simulations indicate that the signal is proportional to the overall density of the exosphere, as long as it remains optically thin. Although simulating atmospheric escape in water-rich planets is not in the scope of our study, we expect that such planets could have exospheres orders of magnitude more dense than the Earth, and could be potentially detectable with HST/STIS. We computed the synthetic spectrum of the star from case 1 (see Sect. 4.3) as if observed with HST/STIS, and produced an exosphere model with densities

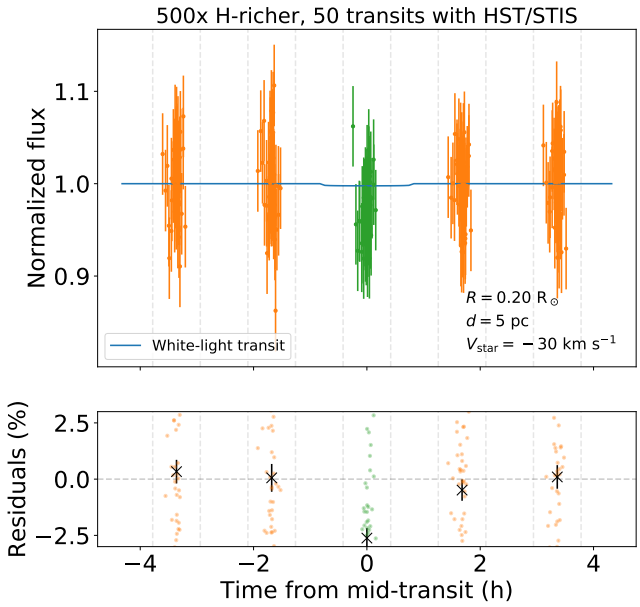

Fig. 13. Transit light curves of test case 1 with an exosphere 500 times denser than the Earth's. The Lyα transit excess is detected reliably within 50 transits with HST/STIS.

500 times larger than the Earth's to test the limit we can observe with this instrument: our simulation indicates that a signal can be detected with significance 4σ during 50 transits with HST/STIS, assuming that the exosphere has the same shape as the Earth's (see Fig. 13).

Theoretical models of planet formation predict a pathway to form deep ocean planets, in which a significant part of their mass (up to ∼50%) is composed of water (e.g., Léger et al. 2004). Furthermore, based on demographics of exoplanets observed with *Kepler*, it is also possible that many small planets are dense enough to be rocky, but may harbor thick envelopes rich in volatiles (Rogers 2015). Such water- and volatile-rich planets are prime targets for the search of H-rich exospheres using the UV capabilities of HST.

6. Conclusions

Studying the upper atmospheres of extrasolar planets will be an important tool to move forward toward understanding habitability and planetary evolution. The region of the upper atmosphere known as exosphere is mainly composed of neutral hydrogen that escapes from the planet driven by the high-energy irradiation from the host star and, for an Earth-like planet, it can be a product of the presence of water in the lower atmosphere. In extrasolar planets, this feature has only been confirmed for giant planets thus far, but the Earth is known to possess its own exosphere. In this work, we sought to investigate if it is possible to observe the exosphere of an Earth-like planet orbiting nearby M dwarfs using transit spectroscopy with the Lyα line. To perform such tests, we employ realistic constraints in the instrumental limitations of current and future space missions, namely the HST and LUVOIR, and the empirical model of the geocorona proposed by Kameda et al. (2017).

The observable Lyα flux of stars scales most strongly with their distance, owing to ISM absorption in the line of sight. We found that the intrinsic Lyα flux attenuation as a function of distance follows an exponential relation, and also depends on the density of H I atoms in the line of sight. This relation is useful not only to achieve our particular objectives, but also to

estimate the observed Lyα flux in any star in the solar neighborhood. Further, we obtained several relations between the excess absorption caused by a transiting exosphere during the mid-transit of an Earth-like planet. These relations are complex because they depend on the difference between the radial velocity of the star and that of the ISM in the line of sight, and also on the instrumental setup.

We presented an extensive and detailed discussion on the observational strategies necessary to perform the above-mentioned detection in Sect. 4, which we summarize below:

- The space telescope LUVOIR will be able to characterize exospheres in Earth-like planets using the LUMOS spectrograph. The number of transits necessary to obtain a reliable detection varies strongly depending on the target, but we can set a flexible limit at distances up to 15 pc for 30 transits. The astrophysical background contamination will not be a limitation for nearby targets, neither will the Earth's own exosphere.
- We analyzed two test cases with noise-injected, simulated data: case 1 had $R = 0.20\ R_\odot$, $d = 5$ pc and $\Delta V = -30$ km s^{-1}; for case 2, we used a system similar to TRAPPIST-1, in which $R = 0.12\ R_\odot$, $d = 10$ pc and $\Delta V = -55$ km s^{-1}. In both cases, even though they did not involve the most favorable conditions, we obtained reliable detections within 10 (20) transits with LUVOIR-A (-B).
- Although an Earth-like exosphere is not observable in Lyα spectroscopy with HST/STIS, we were able to obtain a reliable detection using noise-injected data in the case of an exosphere 500 times more dense in 50 transits with this instrument, for a target at a distance of 5 pc.

The nearest M dwarf with transiting planets is TRAPPIST-1, and its distance of 12 pc renders it a clear target for Lyα transmission spectroscopy with LUVOIR/LUMOS. LHS 1140, another nearby M dwarf that hosts transiting planets is a more challenging target owing to its unfavorable radial velocity. We did not consider active M dwarfs in this study but, owing to their stronger Lyα emission than inactive M dwarfs, they likely have more extended limits in distance than inactive M dwarfs. The TESS mission will expand the search for transiting planets around nearby M dwarfs to the whole sky, which will likely yield more viable targets for atmospheric escape characterization. Future studies in this direction will benefit from performing simulations of neutral hydrogen exospheres (e.g., using the EVE models; Bourrier & Lecavelier des Etangs 2013; Bourrier et al. 2016) around rocky planets with denser atmospheres (such as ocean or steam worlds) orbiting M dwarfs; these stars have a more intense high-energy output than Sun-like stars and likely produce denser exospheres and are shaped into comet-like tails by radiation pressure, increasing detectability.

Acknowledgements. This project has received funding from the European Research Council (ERC) under the European Union's Horizon 2020 research and innovation program (project FOUR ACES; grant agreement No 724427), and it has been carried out in the frame of the National Centre for Competence in Research PlanetS supported by the Swiss National Science Foundation (SNSF). The authors thank B. Wood for providing us the intrinsic Lyα profile of Proxima Centauri that was used in a previous version of this manuscript, and acknowledge the information about the LUMOS and POLLUX spectrographs kindly provided by K. France and C. Neiner, respectively. We also thank A. Suárez Mascareño, J. Seidel, C. Lovis, and the anonymous referee for providing valuable input that helped improve the manuscript. This research made use of the software SciPy (Jones et al. 2001), Astropy (Astropy Collaboration 2013), Matplotlib (Hunter 2007), Jupyter (Kluyver et al. 2016), `emcee` (Foreman-Mackey et al. 2013), `batman` (Kreidberg 2015), and the online databases SIMBAD and VizieR (Wenger et al. 2000; Ochsenbein et al. 2000), operated at CDS, Strasbourg, France.

References

Astropy Collaboration (Robitaille, T. P., et al.) 2013, A&A, 558, A33
Barstow, J. K., & Irwin, P. G. J. 2016, MNRAS, 461, L92
Bolcar, M. R., Aloezos, S., Bly, V. T., et al. 2017, SPIE Conf. Ser. 10398, 1039809
Bolmont, E., Selsis, F., Owen, J. E., et al. 2017, MNRAS, 464, 3728
Bourrier, V., & Lecavelier des Etangs, A. 2013, A&A, 557, A124
Bourrier, V., Ehrenreich, D., & Lecavelier des Etangs, A. 2015, A&A, 582, A65
Bourrier, V., Lecavelier des Etangs, A., Ehrenreich, D., Tanaka, Y. A., & Vidotto, A. A. 2016, A&A, 591, A121
Bourrier, V., de Wit, J., Bolmont, E., et al. 2017a, AJ, 154, 121
Bourrier, V., Ehrenreich, D., Wheatley, P. J., et al. 2017b, A&A, 599, L3
Bourrier, V., Ehrenreich, D., Allart, R., et al. 2017c, A&A, 602, A106
Bourrier, V., Ehrenreich, D., King, G., et al. 2017d, A&A, 597, A26
Bourrier, V., Ehrenreich, D., Lecavelier des Etangs, A., et al. 2018, A&A, 615, A117
Broeg, C., Fortier, A., Ehrenreich, D., et al. 2013, Eur. Phys. J. Web Conf., 47, 03005
Carruthers, G. R., & Page, T. 1972, Science, 177, 788
Chamberlain, J. W. 1963, Planet. Space Sci., 11, 901
Deming, L. D., & Seager, S. 2017, J. Geophys. Res. (Planets), 122, 53
Dittmann, J. A., Irwin, J. M., Charbonneau, D., et al. 2017, Nature, 544, 333
Ehrenreich, D., Lecavelier Des Etangs, A., Hébrard, G., et al. 2008, A&A, 483, 933
Ehrenreich, D., Bourrier, V., Wheatley, P. J., et al. 2015, Nature, 522, 459
Foreman-Mackey, D., Hogg, D. W., Lang, D., & Goodman, J. 2013, PASP, 125, 306
France, K., Fleming, B., & Hoadley, K. 2016a, J. Astron. Telesc. Instr. Syst., 2, 041203
France, K., Parke Loyd, R. O., Youngblood, A., et al. 2016b, ApJ, 820, 89
France, K., Fleming, B., West, G., et al. 2017, SPIE Conf. Ser., 10397, 1039713
Gaudi, B. S., Seager, S., Mennesson, B., et al. 2018, Nat. Astron., 2, 600
Gillon, M., Jehin, E., Lederer, S. M., et al. 2016, Nature, 533, 221
Gillon, M., Triaud, A. H. M. J., Demory, B.-O., et al. 2017, Nature, 542, 456
Gómez de Castro, A. I., Beitia-Antero, L., & Ustamujic, S. 2018, Exp. Astron., 45, 147
Greene, T. P., Line, M. R., Montero, C., et al. 2016, ApJ, 817, 17
Hunter, J. D. 2007, Comput. Sci. Eng., 9, 90
Jones, E., Oliphant, T., Peterson, P., et al. 2001, SciPy: Open source scientific tools for Python
Jura, M. 2004, ApJ, 605, L65
Kameda, S., Ikezawa, S., Sato, M., et al. 2017, Geophys. Res. Lett., 44, 11
Kasting, J. F., Whitmire, D. P., & Reynolds, R. T. 1993, Icarus, 101, 108
Kluyver, T., Ragan-Kelley, B., Pérez, F., et al. 2016, in Positioning and Power in Academic Publishing: Players, Agents and Agendas, eds. F. Loizides, & B. Schmidt (Amsterdam: IOS Press) 87
Kopparapu, R. K., Ramirez, R., Kasting, J. F., et al. 2013, ApJ, 765, 131
Kreidberg, L. 2015, PASP, 127, 1161
Kulikov, Y. N., Lammer, H., Lichtenegger, H. I. M., et al. 2007, Space Sci. Rev., 129, 207
Kulow, J. R., France, K., Linsky, J., & Loyd, R. O. P. 2014, ApJ, 786, 132
Lammer, H., Selsis, F., Ribas, I., et al. 2003, ApJ, 598, L121
Lavie, B., Ehrenreich, D., Bourrier, V., et al. 2017, A&A, 605, L7
Lecavelier Des Etangs, A. 2007, A&A, 461, 1185
Lecavelier Des Etangs, A., Vidal-Madjar, A., McConnell, J. C., & Hébrard, G. 2004, A&A, 418, L1
Lecavelier Des Etangs, A., Ehrenreich, D., Vidal-Madjar, A., et al. 2010, A&A, 514, A72
Lecavelier Des Etangs, A., Bourrier, V., Wheatley, P. J., et al. 2012, A&A, 543, L4
Léger, A., Selsis, F., Sotin, C., et al. 2004, Icarus, 169, 499
Linsky, J. L., Yang, H., France, K., et al. 2010, ApJ, 717, 1291
Lothringer, J. D., Benneke, B., Crossfield, I. J. M., et al. 2018, AJ, 155, 66
Lovis, C., Snellen, I., Mouillet, D., et al. 2017, A&A, 599, A16
Ment, K., Dittmann, J. A., Astudillo-Defru, N., et al. 2019, AJ, 157, 32
Muslimov, E., Bouret, J.-C., Neiner, C., et al. 2018, Proc. SPIE, 10699, 1069906
Ochsenbein, F., Bauer, P., & Marcout, J. 2000, A&AS, 143, 23
Oelkers, R. J., & Stassun, K. G. 2018, AJ, 156, 132

Picone, J. M., Hedin, A. E., Drob, D. P., & Aikin, A. C. 2002, J. Geophys. Res. Space Phys., 107, 1468
Poppenhaeger, K., Schmitt, J. H. M. M., & Wolk, S. J. 2013, ApJ, 773, 62
Redfield, S., & Linsky, J. L. 2008, ApJ, 673, 283
Ricker, G. R., Winn, J. N., Vanderspek, R., et al. 2014, Proc. SPIE, 9143, 914320
Rogers, L. A. 2015, ApJ, 801, 41
Sachkov, M., Shustov, B., & Gómez de Castro, A. I. 2016, Proc. SPIE, 9905, 990504
Selsis, F., Chazelas, B., Bordé, P., et al. 2007, Icarus, 191, 453
Shizgal, B. D., & Arkos, G. G. 1996, Rev. Geophys., 34, 483
Snellen, I. A. G., de Kok, R. J., le Poole, R., Brogi, M., & Birkby, J. 2013, ApJ, 764, 182
Snellen, I., de Kok, R., Birkby, J. L., et al. 2015, A&A, 576, A59
Sullivan, P. W., Winn, J. N., Berta-Thompson, Z. K., et al. 2015, ApJ, 809, 77
Vidal-Madjar, A., Lecavelier des Etangs, A., Désert, J.-M., et al. 2003, Nature, 422, 143
Volkov, A. N., Johnson, R. E., Tucker, O. J., & Erwin, J. T. 2011, ApJ, 729, L24
Wallace, L., Barth, C. A., Pearce, J. B., et al. 1970, J. Geophys. Res., 75, 3769
Wenger, M., Ochsenbein, F., Egret, D., et al. 2000, A&AS, 143, 9
Wheatley, P. J., Louden, T., Bourrier, V., Ehrenreich, D., & Gillon, M. 2017, MNRAS, 465, L74
Wilson, P. A., Lecavelier des Etangs, A., Vidal-Madjar, A., et al. 2017, A&A, 599, A75
Wood, B. E., Redfield, S., Linsky, J. L., Müller, H.-R., & Zank, G. P. 2005, ApJS, 159, 118
Youngblood, A., France, K., Parke Loyd, R. O., et al. 2016, ApJ, 824, 101
Youngblood, A., France, K., Loyd, R. O. P., et al. 2017, ApJ, 843, 31

Chapter 5

Conclusions

> *“ The mind is a strange and wonderful thing. I’m not sure it’ll ever be able to figure itself out. Everything else maybe, from the atom to the universe, everything except itself. ”*
>
> *Daniel Mainwaring*

The idea of a planet losing its atmosphere to space started as a proposal that had fallen between the cracks in the archives of the Royal Society of London, only to be published in late 19th Century [188]. What started as a modest hypothesis based on the kinetic theory of gas is today on the bleeding edge of our understanding of how extra-solar planets evolve [e.g., 141, 10]. Some of the most capable instruments available to astronomers today are used to measure atmospheric escape and put our hypotheses to test. And yet, we have just barely started uncovering the physics behind the evolution of exoplanets, their atmospheres, and their habitability.

5.1 Summary

There are many challenges involved in studies of atmospheric escape. On the observational side, exoplanetary atmospheres absorb a vanishingly small fraction of stellar light when they pass in front of their host stars, limiting transmission spectroscopy feasible to only the most sensitive instruments. In the ultraviolet, our instruments are only capable to reach precisions in the order of a few percent, so we can only observe atmospheric signatures stronger than this limit. Due to many favorable conditions, warm Neptunes are likely to remain a sweet spot for atmospheric escape observations. However, our observations of hot gas giants and sub-Neptunes has yielded non-detections and a tentative detection. If anything,

we demonstrate that even with the most capable instruments currently available to us, and coupled with our most well-crafted data reduction and analysis pipelines, the detection of atmospheric escape is still a challenging feat.

We attempted to detect the escape of metals in the hot Saturn WASP-29 b and the warm Neptune GJ 436 b in the *HST* PanCET program. Such a detection of exospheric metals would be the smoking-gun evidence for hydrodynamic escape in sub-Jovian planets. In the case of WASP-29 b, the distance of the host star (88 pc) is the main limitation to UV observations, since the stellar flux decreases with the square of distance. We were only able to put upper limits of planetary absorption due to exospheric metals. Furthermore, the faint UV fluxes indicate that WASP-29 is a likely a quiet, old star. Using an energy-limited approach, we estimate that the total mass-loss rate of WASP-29 b is 4×10^9 g s^{-1}. The non-detection of atomic H absorption coupled with the reconstructed Lyman-α profile of the host star suggests that WASP-29 b is in a regime of strong radiative blow-out, which quickly accelerate atomic H particles away from the planet.

Despite being the most extensively observed warm Neptune with *HST*, GJ 436 b does not display significant in-transit absorption by metallic ions in its exosphere. It is possible that either this planet is not in a regime of hydrodynamic escape, that the rate of escape of metallic ions is not large enough to produce detectable signatures, or that the structure of the exosphere make the signal undetectable. On the other hand, this extensive campaign did allow us to observe, for the first time, the UV activity modulations and cycles of a quiet M dwarf.

We utilized, for the first time, the Phoenix spectrograph installed in the Gemini South telescope to search for He in the upper atmosphere of the inflated hot Jupiter WASP-127 b. At the time of publication, Phoenix was the only spectrograph in the Southern Hemisphere capable of such a measurement; however, the instrument has recently been retired. We found that the transmission spectrum of WASP-127 b rules out a signal as strong as that observed for WASP-107 b. The host, WASP-127, is an old, inactive G-type star, which explains the non-detection: we showed in this manuscript that this host's radiation cannot populate the upper atmosphere of WASP-127 b with metastable He using a Parker wind model.

Finally, we reported on the Lyman-α transmission spectrum of the temperate mini-Neptune K2-18 b. This is a challenging dataset to analyze, due to the low fluxes of the M dwarf host star and the strong instrumental contamination by background counts. Despite this challenge, we obtained a promising tentative detection of planetary absorption, further pushing the idea that mildly irradiated planets with H-He atmospheres are the best targets for atmospheric escape observations in Lyman-α.

The challenge does not end there. For Earth-like planets, we have shown that detecting their H-rich exospheres is going to take more than the *HST* and its UV instruments are capable of performing currently. A *LUVOIR*-class telescope with updated instruments and higher collecting area will be necessary to measure their upper atmospheres. But such a detection is one of the tools available to infer about the habitability of an exoplanet, since the Earth has a unique exosphere compared to other planets in the Solar System.

5.2 Future prospects

From a pragmatic point of view, the *Hubble Space Telescope* remains the only instrument currently available to observe the Lyman-α line in the ultraviolet, but it is also one of the most oversubscribed telescopes and it has a limited lifetime. Since observing exoplanetary transits involve long time series and ideally multiple epochs, availability of telescope time has been the main bottleneck to test hypothesis about atmospheric escape. The most promising avenue to guarantee our ability to study the evolution of atmospheres in exoplanets is to have dedicated missions and instruments that are capable of minimally-interrupted observations. Similar endeavors, such as the ESPRESSO and CARMENES spectrographs, and the *CHEOPS* satellite, have already been extremely fruitful in yielding discoveries that further our understanding of atmospheres in distant worlds. Fortunately, there are a few UV-dedicated missions that make a crucial promise, such as the *CUTE* satellite [57] and the *UV-Scope* concept [164].

As for my next steps, I intend on conducting large-scale surveys on the high-energy environment of planet-hosting stars aiming to understand the role of this aspect in the evolution of planets young and old. In 2020, we observed one transit of the 45 Myr-old Neptune DS Tuc A b with *HST* to measure its Lyman-α transit spectrum. Our objective is to put constraints on the atmospheric escape rate of this planet at the earliest stages of its life, which will be informative to understand how it evolves. Recently, we obtained another program with *HST* to observe two more visits of DS Tuc A b to provide a better coverage of the transit. Furthermore, I am part of a collaboration to observe escape of He in young planets using the Keck/NIRSPEC instrument (PIs: M. Alam, L. A. Dos Santos, J. Kirk). This dataset is currently being analyzed, and we plan on publishing our results soon. Finally, I am also the PI of a new observing program with *HST* to observe hydrodynamic escape in the ultra-hot Jupiter WASP-76 b.

I also plan on continuing the campaign to measure the H-rich exosphere of K2-18 b and to confirm (or demote) the tentative signal we have recently detected. I will propose further observations of ultrahot Jupiters using the UV capabilities of *HST* to detect and study the

escape of metals in these planets. I will expand my research to understand the impact of high-energy irradiation in the optical and IR transmission spectra of exoplanets using the *James Webb Space Telescope*. On the theoretical front, I intend on further developing the `p-winds` code to implement a tridimensional treatment of escape of He, as well as using it to interpret archived and future observations of upper atmospheres. Finally, I will also implement the escape of metals in the code to allow us to interpret observations of such species using *HST*.

All of these projects will pave the way towards the ultimate goal of my research: to use our most advanced space-based facility, *LUVOIR*, to observe the atmosphere of an Earth-like exoplanet from ultraviolet to infrared, and understand its evolution.

References

[1] Adams, F. C. (2011). Magnetically Controlled Outflows from Hot Jupiters. *ApJ*, 730(1):27.

[2] Afrin Badhan, M., Wolf, E. T., Kopparapu, R. K., Arney, G., Kempton, E. M. R., Deming, D., and Domagal-Goldman, S. D. (2019). Stellar Activity Effects on Moist Habitable Terrestrial Atmospheres around M Dwarfs. *ApJ*, 887(1):34.

[3] Allan, A. and Vidotto, A. A. (2019). Evolution of atmospheric escape in close-in giant planets and their associated Ly α and H α transit predictions. *MNRAS*, 490(3):3760–3771.

[4] Allart, R., Bourrier, V., Lovis, C., Ehrenreich, D., Spake, J. J., Wyttenbach, A., Pino, L., Pepe, F., Sing, D. K., and Lecavelier des Etangs, A. (2018). Spectrally resolved helium absorption from the extended atmosphere of a warm Neptune-mass exoplanet. *Science*, 362(6421):1384–1387.

[5] Alonso-Floriano, F. J., Snellen, I. A. G., Czesla, S., Bauer, F. F., Salz, M., Lampón, M., Lara, L. M., Nagel, E., López-Puertas, M., Nortmann, L., Sánchez-López, A., Sanz-Forcada, J., Caballero, J. A., Reiners, A., Ribas, I., Quirrenbach, A., Amado, P. J., Aceituno, J., Anglada-Escudé, G., Béjar, V. J. S., Brinkmöller, M., Hatzes, A. P., Henning, T., Kaminski, A., Kürster, M., Labarga, F., Montes, D., Pallé, E., Schmitt, J. H. M. M., and Zapatero Osorio, M. R. (2019). He I λ 10 830 Å in the transmission spectrum of HD209458 b. *A&A*, 629:A110.

[6] Baker, D. N. (2013). The Major Solar Eruptive Event in July 2012: Defining Extreme Space Weather Scenarios (Invited). In *AGU Fall Meeting Abstracts*, volume 2013, pages SM13C–04.

[7] Ballester, G. E., Sing, D. K., and Herbert, F. (2007). The signature of hot hydrogen in the atmosphere of the extrasolar planet HD 209458b. *Nature*, 445(7127):511–514.

[8] Baraffe, I., Selsis, F., Chabrier, G., Barman, T. S., Allard, F., Hauschildt, P. H., and Lammer, H. (2004). The effect of evaporation on the evolution of close-in giant planets. *A&A*, 419:L13–L16.

[9] Batygin, K., Bodenheimer, P. H., and Laughlin, G. P. (2016). In Situ Formation and Dynamical Evolution of Hot Jupiter Systems. *ApJ*, 829(2):114.

[10] Bean, J. L., Raymond, S. N., and Owen, J. E. (2021). The Nature and Origins of Sub-Neptune Size Planets. *Journal of Geophysical Research (Planets)*, 126(1):e06639.

[11] Ben-Jaffel, L. and Ballester, G. E. (2013). Hubble Space Telescope detection of oxygen in the atmosphere of exoplanet HD 189733b. *A&A*, 553:A52.

[12] Benneke, B., Wong, I., Piaulet, C., Knutson, H. A., Lothringer, J., Morley, C. V., Crossfield, I. J. M., Gao, P., Greene, T. P., Dressing, C., Dragomir, D., Howard, A. W., McCullough, P. R., Kempton, E. M. R., Fortney, J. J., and Fraine, J. (2019). Water Vapor and Clouds on the Habitable-zone Sub-Neptune Exoplanet K2-18b. *ApJ*, 887(1):L14.

[13] Bisikalo, D., Kaygorodov, P., Ionov, D., Shematovich, V., Lammer, H., and Fossati, L. (2013). Three-dimensional Gas Dynamic Simulation of the Interaction between the Exoplanet WASP-12b and its Host Star. *ApJ*, 764(1):19.

[14] Bisikalo, D. V., Cherenkov, A. A., Shematovich, V. I., Fossati, L., and Möstl, C. (2018). The Influence of a Stellar Flare on the Dynamical State of the Atmosphere of the Exoplanet HD 209458b. *Astronomy Reports*, 62(10):648–653.

[15] Bolcar, M. R., Aloezos, S., Bly, V. T., Collins, C., Crooke, J., Dressing, C. D., Fantano, L., Feinberg, L. D., France, K., Gochar, G., Gong, Q., Hylan, J. E., Jones, A., Linares, I., Postman, M., Pueyo, L., Roberge, A., Sacks, L., Tompkins, S., and West, G. (2017). The Large UV/Optical/Infrared Surveyor (LUVOIR): Decadal Mission concept design update. In *Society of Photo-Optical Instrumentation Engineers (SPIE) Conference Series*, volume 10398 of *Society of Photo-Optical Instrumentation Engineers (SPIE) Conference Series*, page 1039809.

[16] Bourrier, V., dos Santos, L. A., Sanz-Forcada, J., García Muñoz, A., Henry, G. W., Lavvas, P., Lecavelier, A., López-Morales, M., Mikal-Evans, T., Sing, D. K., Wakeford, H. R., and Ehrenreich, D. (2021). The Hubble PanCET program: long-term chromospheric evolution and flaring activity of the M dwarf host GJ 3470. *A&A*, 650:A73.

[17] Bourrier, V., Ehrenreich, D., Allart, R., Wyttenbach, A., Semaan, T., Astudillo-Defru, N., Gracia-Berná, A., Lovis, C., Pepe, F., Thomas, N., and Udry, S. (2017). Strong H I Lyman-α variations from an 11 Gyr-old host star: a planetary origin? *A&A*, 602:A106.

[18] Bourrier, V. and Lecavelier des Etangs, A. (2013). 3D model of hydrogen atmospheric escape from HD 209458b and HD 189733b: radiative blow-out and stellar wind interactions. *A&A*, 557:A124.

[19] Bourrier, V., Lecavelier des Etangs, A., Ehrenreich, D., Sanz-Forcada, J., Allart, R., Ballester, G. E., Buchhave, L. A., Cohen, O., Deming, D., Evans, T. M., García Muñoz, A., Henry, G. W., Kataria, T., Lavvas, P., Lewis, N., López-Morales, M., Marley, M., Sing, D. K., and Wakeford, H. R. (2018). Hubble PanCET: an extended upper atmosphere of neutral hydrogen around the warm Neptune GJ 3470b. *A&A*, 620:A147.

[20] Bourrier, V., Lecavelier des Etangs, A., Ehrenreich, D., Tanaka, Y. A., and Vidotto, A. A. (2016). An evaporating planet in the wind: stellar wind interactions with the radiatively braked exosphere of GJ 436 b. *A&A*, 591:A121.

[21] Bourrier, V., Wheatley, P. J., Lecavelier des Etangs, A., King, G., Louden, T., Ehrenreich, D., Fares, R., Helling, C., Llama, J., Jardine, M. M., and Vidotto, A. A. (2020). MOVES III. Simultaneous X-ray and ultraviolet observations unveiling the variable environment of the hot Jupiter HD 189733b. *MNRAS*, 493(1):559–579.

[22] Burrows, A., Hubbard, W. B., Saumon, D., and Lunine, J. I. (1993). An Expanded Set of Brown Dwarf and Very Low Mass Star Models. *ApJ*, 406:158.

[23] Burrows, A. and Orton, G. (2009). Giant Planet Atmospheres and Spectra. *arXiv e-prints*, page arXiv:0910.0248.

[24] Butler, R. P., Vogt, S. S., Marcy, G. W., Fischer, D. A., Wright, J. T., Henry, G. W., Laughlin, G., and Lissauer, J. J. (2004). A Neptune-Mass Planet Orbiting the Nearby M Dwarf GJ 436. *ApJ*, 617:580–588.

[25] Carleo, I., Youngblood, A., Redfield, S., Casasayas Barris, N., Ayres, T. R., Vannier, H., Fossati, L., Palle, E., Livingston, J. H., Lanza, A. F., Niraula, P., Alvarado-Gómez, J. D., Chen, G., Gandolfi, D., Guenther, E. W., Linsky, J. L., Nagel, E., Narita, N., Nortmann, L., Shkolnik, E. L., and Stangret, M. (2021). A Multiwavelength Look at the GJ 9827 System: No Evidence of Extended Atmospheres in GJ 9827b and d from HST and CARMENES Data. *AJ*, 161(3):136.

[26] Carolan, S., Vidotto, A. A., Plavchan, P., Villarreal D'Angelo, C., and Hazra, G. (2020). The dichotomy of atmospheric escape in AU Mic b. *MNRAS*, 498(1):L53–L57.

[27] Carrington, R. C. (1859). Description of a Singular Appearance seen in the Sun on September 1, 1859. *MNRAS*, 20:13–15.

[28] Casasayas-Barris, N., Palle, E., Stangret, M., Bourrier, V., Tabernero, H. M., Yan, F., Borsa, F., Allart, R., Zapatero Osorio, M. R., Lovis, C., Sousa, S. G., Chen, G., Oshagh, M., Santos, N. C., Pepe, F., Rebolo, R., Molaro, P., Cristiani, S., Adibekyan, V., Alibert, Y., Allende Prieto, C., Bouchy, F., Demangeon, O. D. S., Di Marcantonio, P., D'Odorico, V., Ehrenreich, D., Figueira, P., Génova Santos, R., González Hernández, J. I., Lavie, B., Lillo-Box, J., Lo Curto, G., Martins, C. J. A. P., Mehner, A., Micela, G., Nunes, N. J., Poretti, E., Sozzetti, A., Suárez Mascareño, A., and Udry, S. (2021). The atmosphere of HD 209458b seen with ESPRESSO. No detectable planetary absorptions at high resolution. *A&A*, 647:A26.

[29] Catling, D. C. and Kasting, J. F. (2017). *Atmospheric Evolution on Inhabited and Lifeless Worlds*.

[30] Cauley, P. W., Redfield, S., and Jensen, A. G. (2017). A Decade of Hα Transits for HD 189733 b: Stellar Activity versus Absorption in the Extended Atmosphere. *AJ*, 153(5):217.

[31] Chadney, J. M., Koskinen, T. T., Galand, M., Unruh, Y. C., and Sanz-Forcada, J. (2017). Effect of stellar flares on the upper atmospheres of HD 189733b and HD 209458b. *A&A*, 608:A75.

[32] Chamberlain, J. W. (1963). Planetary coronae and atmospheric evaporation. *Planet. Space Sci.*, 11(8):901–960.

[33] Charbonneau, D., Brown, T. M., Noyes, R. W., and Gilliland, R. L. (2002). Detection of an Extrasolar Planet Atmosphere. *ApJ*, 568:377–384.

[34] Charnay, B., Blain, D., Bézard, B., Leconte, J., Turbet, M., and Falco, A. (2021). Formation and dynamics of water clouds on temperate sub-Neptunes: the example of K2-18b. *A&A*, 646:A171.

[35] Chassefière, E. (1996). Hydrodynamic escape of hydrogen from a hot water-rich atmosphere: The case of Venus. *J. Geophys. Res.*, 101(E11):26039–26056.

[36] Cincunegui, C., Díaz, R. F., and Mauas, P. J. D. (2007). A possible activity cycle in <ASTROBJ>Proxima Centauri</ASTROBJ>. *A&A*, 461(3):1107–1113.

[37] Coustenis, A., Schneider, J., Wittemberg, R., Chazsefiere, E., Guillot, T., Penny, A., Greene, T., Rauer, H., and Bockelee-Morvan, D. (1998). High Resolution Ground-Based Spectroscopy of 51 Peg b: Search for Atmospheric Signatures. In Rebolo, R., Martin, E. L., and Zapatero Osorio, M. R., editors, *Brown Dwarfs and Extrasolar Planets*, volume 134 of *Astronomical Society of the Pacific Conference Series*, page 296.

[38] Curry, S. M., Liemohn, M., Fang, X., Ma, Y., and Espley, J. (2013). The influence of production mechanisms on pick-up ion loss at Mars. *Journal of Geophysical Research (Space Physics)*, 118(1):554–569.

[39] David, T. J., Contardo, G., Sandoval, A., Angus, R., Yuxi, Lu, Bedell, M., Curtis, J. L., Foreman-Mackey, D., Fulton, B. J., Grunblatt, S. K., and Petigura, E. A. (2020). Evolution of the Exoplanet Size Distribution: Forming Large Super-Earths Over Billions of Years. *arXiv e-prints*, page arXiv:2011.09894.

[40] David, T. J., Petigura, E. A., Luger, R., Foreman-Mackey, D., Livingston, J. H., Mamajek, E. E., and Hillenbrand, L. A. (2019). Four Newborn Planets Transiting the Young Solar Analog V1298 Tau. *ApJ*, 885(1):L12.

[41] Davis, T. A. and Wheatley, P. J. (2009). Evidence for a lost population of close-in exoplanets. *MNRAS*, 396:1012–1017.

[42] Debrecht, A., Carroll-Nellenback, J., Frank, A., Blackman, E. G., Fossati, L., McCann, J., and Murray-Clay, R. (2020). Effects of radiation pressure on the evaporative wind of HD 209458b. *MNRAS*, 493(1):1292–1305.

[43] dos Santos, L. A., Bourrier, V., Ehrenreich, D., and Kameda, S. (2019a). Observability of hydrogen-rich exospheres in Earth-like exoplanets. *A&A*, 622:A46.

[44] dos Santos, L. A., Bourrier, V., Ehrenreich, D., Sanz-Forcada, J., López-Morales, M., Sing, D. K., García Muñoz, A., Henry, G. W., Lavvas, P., Lecavelier des Etangs, A., Mikal-Evans, T., Vidal-Madjar, A., and Wakeford, H. R. (2021). HST PanCET program: Non-detection of atmospheric escape in the warm Saturn-sized planet WASP-29 b. *A&A*, 649:A40.

[45] dos Santos, L. A., Ehrenreich, D., Bourrier, V., Allart, R., King, G., Lendl, M., Lovis, C., Margheim, S., Meléndez, J., Seidel, J. V., and Sousa, S. G. (2020a). Search for helium in the upper atmosphere of the hot Jupiter WASP-127 b using Gemini/Phoenix. *A&A*, 640:A29.

[46] dos Santos, L. A., Ehrenreich, D., Bourrier, V., Astudillo-Defru, N., Bonfils, X., Forget, F., Lovis, C., Pepe, F., and Udry, S. (2020b). The high-energy environment and atmospheric escape of the mini-Neptune K2-18 b. *A&A*, 634:L4.

[47] dos Santos, L. A., Ehrenreich, D., Bourrier, V., Lecavelier des Etangs, A., López-Morales, M., Sing, D. K., Ballester, G., Ben-Jaffel, L., Buchhave, L. A., García Muñoz, A., Henry, G. W., Kataria, T., Lavie, B., Lavvas, P., Lewis, N. K., Mikal-Evans, T., Sanz-Forcada, J., and Wakeford, H. (2019b). The Hubble PanCET program: an extensive search for metallic ions in the exosphere of GJ 436 b. *A&A*, 629:A47.

[48] dos Santos, L. A., Meléndez, J., do Nascimento, J.-D., Bedell, M., Ramírez, I., Bean, J. L., Asplund, M., Spina, L., Dreizler, S., Alves-Brito, A., and Casagrande, L. (2016). The Solar Twin Planet Search. IV. The Sun as a typical rotator and evidence for a new rotational braking law for Sun-like stars. *A&A*, 592:A156.

[49] Duvvuri, G. M., Sebastian Pineda, J., Berta-Thompson, Z. K., Brown, A., France, K., Kowalski, A. F., Redfield, S., Tilipman, D., Vieytes, M. C., Wilson, D. J., Youngblood, A., Froning, C. S., Linsky, J., Parke Loyd, R. O., Mauas, P., Miguel, Y., Newton, E. R., Rugheimer, S., and Christian Schneider, P. (2021). Reconstructing the Extreme Ultraviolet Emission of Cool Dwarfs Using Differential Emission Measure Polynomials. *ApJ*, 913(1):40.

[50] Edwards, S., Fischer, W., Kwan, J., Hillenbrand, L., and Dupree, A. K. (2003). He I λ10830 as a Probe of Winds in Accreting Young Stars. *ApJ*, 599(1):L41–L44.

[51] Ehrenreich, D., Bourrier, V., Wheatley, P. J., Lecavelier des Etangs, A., Hébrard, G., Udry, S., Bonfils, X., Delfosse, X., Désert, J.-M., Sing, D. K., and Vidal-Madjar, A. (2015). A giant comet-like cloud of hydrogen escaping the warm Neptune-mass exoplanet GJ 436b. *Nature*, 522:459–461.

[52] Ehrenreich, D. and Désert, J.-M. (2011). Mass-loss rates for transiting exoplanets. *A&A*, 529:A136.

[53] Ehrenreich, D., Lecavelier Des Etangs, A., and Delfosse, X. (2011). HST/STIS Lyman-α observations of the quiet M dwarf GJ 436. Predictions for the exospheric transit signature of the hot Neptune GJ 436b. *A&A*, 529:A80.

[54] Ehrenreich, D., Lecavelier Des Etangs, A., Hébrard, G., Désert, J.-M., Vidal-Madjar, A., McConnell, J. C., Parkinson, C. D., Ballester, G. E., and Ferlet, R. (2008). New observations of the extended hydrogen exosphere of the extrasolar planet HD 209458b. *A&A*, 483:933–937.

[55] Erkaev, N. V., Lammer, H., Odert, P., Kislyakova, K. G., Johnstone, C. P., Güdel, M., and Khodachenko, M. L. (2016). EUV-driven mass-loss of protoplanetary cores with hydrogen-dominated atmospheres: the influences of ionization and orbital distance. *MNRAS*, 460(2):1300–1309.

[56] Evans, T. M., Aigrain, S., Gibson, N., Barstow, J. K., Amundsen, D. S., Tremblin, P., and Mourier, P. (2015). A uniform analysis of HD 209458b Spitzer/IRAC light curves with Gaussian process models. *MNRAS*, 451(1):680–694.

[57] Fleming, B. T., France, K., Nell, N., Kohnert, R., Pool, K., Egan, A., Fossati, L., Koskinen, T., Vidotto, A. A., Hoadley, K., Desert, J.-M., Beasley, M., and Petit, P. M. (2018). Colorado Ultraviolet Transit Experiment: a dedicated CubeSat mission to study exoplanetary mass loss and magnetic fields. *Journal of Astronomical Telescopes, Instruments, and Systems*, 4:014004.

[58] Fossati, L., Haswell, C. A., Froning, C. S., Hebb, L., Holmes, S., Kolb, U., Helling, C., Carter, A., Wheatley, P., Collier Cameron, A., Loeillet, B., Pollacco, D., Street, R., Stempels, H. C., Simpson, E., Udry, S., Joshi, Y. C., West, R. G., Skillen, I., and Wilson, D. (2010). Metals in the Exosphere of the Highly Irradiated Planet WASP-12b. *ApJ*, 714(2):L222–L227.

[59] France, K., Duvvuri, G., Egan, H., Koskinen, T., Wilson, D. J., Youngblood, A., Froning, C. S., Brown, A., Alvarado-Gómez, J. D., Berta-Thompson, Z. K., Drake, J. J., Garraffo, C., Kaltenegger, L., Kowalski, A. F., Linsky, J. L., Loyd, R. O. P., Mauas, P. J. D., Miguel, Y., Pineda, J. S., Rugheimer, S., Schneider, P. C., Tian, F., and Vieytes, M. (2020). The High-energy Radiation Environment around a 10 Gyr M Dwarf: Habitable at Last? *AJ*, 160(5):237.

[60] France, K., Fleming, B., West, G., McCandliss, S. R., Bolcar, M. R., Harris, W., Moustakas, L., O'Meara, J. M., Pascucci, I., Rigby, J., Schiminovich, D., and Tumlinson, J. (2017). The LUVOIR Ultraviolet Multi-Object Spectrograph (LUMOS): instrument definition and design. In *Society of Photo-Optical Instrumentation Engineers (SPIE) Conference Series*, volume 10397 of *Society of Photo-Optical Instrumentation Engineers (SPIE) Conference Series*, page 1039713.

[61] France, K., Linsky, J. L., Tian, F., Froning, C. S., and Roberge, A. (2012). Time-resolved Ultraviolet Spectroscopy of the M-dwarf GJ 876 Exoplanetary System. *ApJ*, 750(2):L32.

[62] France, K., Loyd, R. O. P., Youngblood, A., Brown, A., Schneider, P. C., Hawley, S. L., Froning, C. S., Linsky, J. L., Roberge, A., Buccino, A. P., Davenport, J. R. A., Fontenla, J. M., Kaltenegger, L., Kowalski, A. F., Mauas, P. J. D., Miguel, Y., Redfield, S., Rugheimer, S., Tian, F., Vieytes, M. C., Walkowicz, L. M., and Weisenburger, K. L. (2016). The MUSCLES Treasury Survey. I. Motivation and Overview. *ApJ*, 820(2):89.

[63] Fuhrmeister, B., Czesla, S., Hildebrandt, L., Nagel, E., Schmitt, J. H. M. M., Hintz, D., Johnson, E. N., Sanz-Forcada, J., Schöfer, P., Jeffers, S. V., Caballero, J. A., Zechmeister, M., Reiners, A., Ribas, I., Amado, P. J., Quirrenbach, A., Bauer, F. F., Béjar, V. J. S., Cortés-Contreras, M., Díez-Alonso, E., Dreizler, S., Galadí-Enríquez, D., Guenther, E. W., Kaminski, A., Kürster, M., Lafarga, M., and Montes, D. (2019). The CARMENES search for exoplanets around M dwarfs. The He I triplet at 10830 Å across the M dwarf sequence. *A&A*, 632:A24.

[64] Fulton, B. J. and Petigura, E. A. (2018). The California-Kepler Survey. VII. Precise Planet Radii Leveraging Gaia DR2 Reveal the Stellar Mass Dependence of the Planet Radius Gap. *AJ*, 156:264.

[65] Fulton, B. J., Petigura, E. A., Howard, A. W., Isaacson, H., Marcy, G. W., Cargile, P. A., Hebb, L., Weiss, L. M., Johnson, J. A., Morton, T. D., Sinukoff, E., Crossfield, I. J. M., and Hirsch, L. A. (2017). The California-Kepler Survey. III. A Gap in the Radius Distribution of Small Planets. *AJ*, 154:109.

[66] Gaidos, E., Hirano, T., Mann, A. W., Owens, D. A., Berger, T. A., France, K., Vanderburg, A., Harakawa, H., Hodapp, K. W., Ishizuka, M., Jacobson, S., Konishi, M., Kotani, T., Kudo, T., Kurokawa, T., Kuzuhara, M., Nishikawa, J., Omiya, M., Serizawa, T., Tamura,

M., and Ueda, A. (2020). Zodiacal exoplanets in time - X. The orbit and atmosphere of the young 'neptune desert'-dwelling planet K2-100b. *MNRAS*, 495(1):650–662.

[67] García Muñoz, A. (2007). Physical and chemical aeronomy of HD 209458b. *Planet. Space Sci.*, 55:1426–1455.

[68] García Muñoz, A., Fossati, L., Youngblood, A., Nettelmann, N., Gandolfi, D., Cabrera, J., and Rauer, H. (2021). A Heavy Molecular Weight Atmosphere for the Super-Earth π Men c. *ApJ*, 907(2):L36.

[69] García Muñoz, A., Youngblood, A., Fossati, L., Gandolfi, D., Cabrera, J., and Rauer, H. (2020). Is π Men c's Atmosphere Hydrogen-dominated? Insights from a Non-detection of H I Lyα Absorption. *ApJ*, 888(2):L21.

[70] Garcia-Sage, K., Glocer, A., Drake, J. J., Gronoff, G., and Cohen, O. (2017). On the Magnetic Protection of the Atmosphere of Proxima Centauri b. *ApJ*, 844(1):L13.

[71] Gaudi, B. S., Stassun, K. G., Collins, K. A., Beatty, T. G., Zhou, G., Latham, D. W., Bieryla, A., Eastman, J. D., Siverd, R. J., Crepp, J. R., Gonzales, E. J., Stevens, D. J., Buchhave, L. A., Pepper, J., Johnson, M. C., Colon, K. D., Jensen, E. L. N., Rodriguez, J. E., Bozza, V., Novati, S. C., D'Ago, G., Dumont, M. T., Ellis, T., Gaillard, C., Jang-Condell, H., Kasper, D. H., Fukui, A., Gregorio, J., Ito, A., Kielkopf, J. F., Manner, M., Matt, K., Narita, N., Oberst, T. E., Reed, P. A., Scarpetta, G., Stephens, D. C., Yeigh, R. R., Zambelli, R., Fulton, B. J., Howard, A. W., James, D. J., Penny, M., Bayliss, D., Curtis, I. A., Depoy, D. L., Esquerdo, G. A., Gould, A., Joner, M. D., Kuhn, R. B., Labadie-Bartz, J., Lund, M. B., Marshall, J. L., McLeod, K. K., Pogge, R. W., Relles, H., Stockdale, C., Tan, T. G., Trueblood, M., and Trueblood, P. (2017). A giant planet undergoing extreme-ultraviolet irradiation by its hot massive-star host. *Nature*, 546(7659):514–518.

[72] Gillon, M., Pont, F., Demory, B.-O., Mallmann, F., Mayor, M., Mazeh, T., Queloz, D., Shporer, A., Udry, S., and Vuissoz, C. (2007). Detection of transits of the nearby hot Neptune GJ 436 b. *A&A*, 472:L13–L16.

[73] Ginzburg, S., Schlichting, H. E., and Sari, R. (2018). Core-powered mass-loss and the radius distribution of small exoplanets. *MNRAS*, 476(1):759–765.

[74] Gronoff, G., Arras, P., Baraka, S., Bell, J. M., Cessateur, G., Cohen, O., Curry, S. M., Drake, J. J., Elrod, M., Erwin, J., Garcia-Sage, K., Garraffo, C., Glocer, A., Heavens, N. G., Lovato, K., Maggiolo, R., Parkinson, C. D., Simon Wedlund, C., Weimer, D. R., and Moore, W. B. (2020). Atmospheric Escape Processes and Planetary Atmospheric Evolution. *Journal of Geophysical Research (Space Physics)*, 125(8):e27639.

[75] Gross, S. H. (1972). On the exospheric temperature of hydrogen-dominated planetary atmospheres. *Journal of Atmospheric Sciences*, 29:214–218.

[76] Gryciuk, M., Siarkowski, M., Gburek, S., Podgorski, P., Sylwester, J., Kepa, A., and Mrozek, T. (2016). Model of flare lightcurve profile observed in soft X-rays. In Kosovichev, A. G., Hawley, S. L., and Heinzel, P., editors, *Solar and Stellar Flares and their Effects on Planets*, volume 320, pages 89–94.

[77] Guillot, T., Burrows, A., Hubbard, W. B., Lunine, J. I., and Saumon, D. (1996). Giant Planets at Small Orbital Distances. *ApJ*, 459:L35.

[78] Guilluy, G., Andretta, V., Borsa, F., Giacobbe, P., Sozzetti, A., Covino, E., Bourrier, V., Fossati, L., Bonomo, A. S., Esposito, M., Giampapa, M. S., Harutyunyan, A., Rainer, M., Brogi, M., Bruno, G., Claudi, R., Frustagli, G., Lanza, A. F., Mancini, L., Pino, L., Poretti, E., Scandariato, G., Affer, L., Baffa, C., Baruffolo, A., Benatti, S., Biazzo, K., Bignamini, A., Boschin, W., Carleo, I., Cecconi, M., Cosentino, R., Damasso, M., Desidera, S., Falcini, G., Martinez Fiorenzano, A. F., Ghedina, A., González-Álvarez, E., Guerra, J., Hernandez, N., Leto, G., Maggio, A., Malavolta, L., Maldonado, J., Micela, G., Molinari, E., Nascimbeni, V., Pagano, I., Pedani, M., Piotto, G., and Reiners, A. (2020). The GAPS programme at TNG. XXII. The GIARPS view of the extended helium atmosphere of HD 189733 b accounting for stellar activity. *A&A*, 639:A49.

[79] Gunell, H., Maggiolo, R., Nilsson, H., Stenberg Wieser, G., Slapak, R., Lindkvist, J., Hamrin, M., and De Keyser, J. (2018). Why an intrinsic magnetic field does not protect a planet against atmospheric escape. *A&A*, 614:L3.

[80] Gupta, A. and Schlichting, H. E. (2021). Caught in the act: core-powered mass-loss predictions for observing atmospheric escape. *MNRAS*, 504(3):4634–4648.

[81] Haff, P. K., Watson, C. C., and Yung, Y. L. (1981). Sputter ejection of matter from Io. *J. Geophys. Res.*, 86(A8):6933–6938.

[82] Hall, J. C. (2008). Stellar Chromospheric Activity. *Living Reviews in Solar Physics*, 5(1):2.

[83] Hall, J. C., Lockwood, G. W., and Gibb, E. L. (1995). Activity Cycles in Cool Stars. I. Observation and Analysis Methods and Case Studies of Four Well-observed Examples. *ApJ*, 442:778.

[84] Hansen, B. M. S. and Murray, N. (2012). Migration Then Assembly: Formation of Neptune-mass Planets inside 1 AU. *ApJ*, 751(2):158.

[85] Hardegree-Ullman, K. K., Zink, J. K., Christiansen, J. L., Dressing, C. D., Ciardi, D. R., and Schlieder, J. E. (2020). Scaling K2. I. Revised Parameters for 222,088 K2 Stars and a K2 Planet Radius Valley at 1.9 $R_{\oplus}$. *ApJS*, 247(1):28.

[86] Hodgson, R. (1859). On a curious Appearance seen in the Sun. *MNRAS*, 20:15–16.

[87] Holmström, M., Ekenbäck, A., Selsis, F., Penz, T., Lammer, H., and Wurz, P. (2008a). Energetic neutral atoms as the explanation for the high-velocity hydrogen around HD 209458b. *Nature*, 451(7181):970–972.

[88] Holmström, M., Ekenbäck, A., Selsis, F., Penz, T., Lammer, H., and Wurz, P. (2008b). Holmström et al. reply. *Nature*, 456(7219):E1–2.

[89] Howard, A. W., Marcy, G. W., Bryson, S. T., Jenkins, J. M., Rowe, J. F., Batalha, N. M., Borucki, W. J., Koch, D. G., Dunham, E. W., Gautier, III, T. N., Van Cleve, J., Cochran, W. D., Latham, D. W., Lissauer, J. J., Torres, G., Brown, T. M., Gilliland, R. L., Buchhave, L. A., Caldwell, D. A., Christensen-Dalsgaard, J., Ciardi, D., Fressin, F., Haas, M. R., Howell, S. B., Kjeldsen, H., Seager, S., Rogers, L., Sasselov, D. D., Steffen, J. H., Basri, G. S., Charbonneau, D., Christiansen, J., Clarke, B., Dupree, A., Fabrycky, D. C., Fischer, D. A., Ford, E. B., Fortney, J. J., Tarter, J., Girouard, F. R., Holman, M. J., Johnson, J. A.,

Klaus, T. C., Machalek, P., Moorhead, A. V., Morehead, R. C., Ragozzine, D., Tenenbaum, P., Twicken, J. D., Quinn, S. N., Isaacson, H., Shporer, A., Lucas, P. W., Walkowicz, L. M., Welsh, W. F., Boss, A., Devore, E., Gould, A., Smith, J. C., Morris, R. L., Prsa, A., Morton, T. D., Still, M., Thompson, S. E., Mullally, F., Endl, M., and MacQueen, P. J. (2012). Planet Occurrence within 0.25 AU of Solar-type Stars from Kepler. *ApJS*, 201:15.

[90] Jackson, A. P., Davis, T. A., and Wheatley, P. J. (2012). The coronal X-ray-age relation and its implications for the evaporation of exoplanets. *MNRAS*, 422(3):2024–2043.

[91] Jakosky, B. M., Brain, D., Chaffin, M., Curry, S., Deighan, J., Grebowsky, J., Halekas, J., Leblanc, F., Lillis, R., Luhmann, J. G., Andersson, L., Andre, N., Andrews, D., Baird, D., Baker, D., Bell, J., Benna, M., Bhattacharyya, D., Bougher, S., Bowers, C., Chamberlin, P., Chaufray, J. Y., Clarke, J., Collinson, G., Combi, M., Connerney, J., Connour, K., Correira, J., Crabb, K., Crary, F., Cravens, T., Crismani, M., Delory, G., Dewey, R., DiBraccio, G., Dong, C., Dong, Y., Dunn, P., Egan, H., Elrod, M., England, S., Eparvier, F., Ergun, R., Eriksson, A., Esman, T., Espley, J., Evans, S., Fallows, K., Fang, X., Fillingim, M., Flynn, C., Fogle, A., Fowler, C., Fox, J., Fujimoto, M., Garnier, P., Girazian, Z., Groeller, H., Gruesbeck, J., Hamil, O., Hanley, K. G., Hara, T., Harada, Y., Hermann, J., Holmberg, M., Holsclaw, G., Houston, S., Inui, S., Jain, S., Jolitz, R., Kotova, A., Kuroda, T., Larson, D., Lee, Y., Lee, C., Lefevre, F., Lentz, C., Lo, D., Lugo, R., Ma, Y. J., Mahaffy, P., Marquette, M. L., Matsumoto, Y., Mayyasi, M., Mazelle, C., McClintock, W., McFadden, J., Medvedev, A., Mendillo, M., Meziane, K., Milby, Z., Mitchell, D., Modolo, R., Montmessin, F., Nagy, A., Nakagawa, H., Narvaez, C., Olsen, K., Pawlowski, D., Peterson, W., Rahmati, A., Roeten, K., Romanelli, N., Ruhunusiri, S., Russell, C., Sakai, S., Schneider, N., Seki, K., Sharrar, R., Shaver, S., Siskind, D. E., Slipski, M., Soobiah, Y., Steckiewicz, M., Stevens, M. H., Stewart, I., Stiepen, A., Stone, S., Tenishev, V., Terada, N., Terada, K., Thiemann, E., Tolson, R., Toth, G., Trovato, J., Vogt, M., Weber, T., Withers, P., Xu, S., Yelle, R., Yiğit, E., and Zurek, R. (2018). Loss of the Martian atmosphere to space: Present-day loss rates determined from MAVEN observations and integrated loss through time. *Icarus*, 315:146–157.

[92] Jakosky, B. M., Slipski, M., Benna, M., Mahaffy, P., Elrod, M., Yelle, R., Stone, S., and Alsaeed, N. (2017). Mars' atmospheric history derived from upper-atmosphere measurements of ^{38}Ar/^{36}Ar. *Science*, 355(6332):1408–1410.

[93] Jeans, J. H. (1925). *The Dynamical Theory of Gases*. Cambridge University Press, 3 edition.

[94] Jensen, A. G., Redfield, S., Endl, M., Cochran, W. D., Koesterke, L., and Barman, T. (2012). A Detection of Hα in an Exoplanetary Exosphere. *ApJ*, 751(2):86.

[95] Jin, S., Mordasini, C., Parmentier, V., van Boekel, R., Henning, T., and Ji, J. (2014). Planetary Population Synthesis Coupled with Atmospheric Escape: A Statistical View of Evaporation. *ApJ*, 795(1):65.

[96] Kaltenegger, L. (2017). How to Characterize Habitable Worlds and Signs of Life. *ARA&A*, 55(1):433–485.

[97] Kameda, S., Ikezawa, S., Sato, M., Kuwabara, M., Osada, N., Murakami, G., Yoshioka, K., Yoshikawa, I., Taguchi, M., Funase, R., Sugita, S., Miyoshi, Y., and Fujimoto, M.

(2017). Ecliptic North-South Symmetry of Hydrogen Geocorona. *Geophys. Res. Lett.*, 44(23):11,706–11,712.

[98] Kasper, D., Bean, J. L., Oklopčić, A., Malsky, I., Kempton, E. M. R., Désert, J.-M., Rogers, L. A., and Mansfield, M. (2020). Nondetection of Helium in the Upper Atmospheres of Three Sub-Neptune Exoplanets. *AJ*, 160(6):258.

[99] King, G. W. and Wheatley, P. J. (2021). EUV irradiation of exoplanet atmospheres occurs on Gyr time-scales. *MNRAS*, 501(1):L28–L32.

[100] Knutson, H. A., Benneke, B., Deming, D., and Homeier, D. (2014). A featureless transmission spectrum for the Neptune-mass exoplanet GJ436b. *Nature*, 505:66–68.

[101] Knutson, H. A., Madhusudhan, N., Cowan, N. B., Christiansen, J. L., Agol, E., Deming, D., Désert, J.-M., Charbonneau, D., Henry, G. W., Homeier, D., Langton, J., Laughlin, G., and Seager, S. (2011). A Spitzer Transmission Spectrum for the Exoplanet GJ 436b, Evidence for Stellar Variability, and Constraints on Dayside Flux Variations. *ApJ*, 735(1):27.

[102] Kopp, G. (2016). Magnitudes and timescales of total solar irradiance variability. *Journal of Space Weather and Space Climate*, 6:A30.

[103] Kubyshkina, D., Fossati, L., Erkaev, N. V., Cubillos, P. E., Johnstone, C. P., Kislyakova, K. G., Lammer, H., Lendl, M., and Odert, P. (2018a). Overcoming the Limitations of the Energy-limited Approximation for Planet Atmospheric Escape. *ApJ*, 866(2):L18.

[104] Kubyshkina, D., Fossati, L., Erkaev, N. V., Johnstone, C. P., Cubillos, P. E., Kislyakova, K. G., Lammer, H., Lendl, M., and Odert, P. (2018b). Grid of upper atmosphere models for 1-40 $M_\oplus$ planets: application to CoRoT-7 b and HD 219134 b,c. *A&A*, 619:A151.

[105] Kubyshkina, D. and Vidotto, A. A. (2021). How does the mass and activity history of the host star affect the population of low-mass planets? *MNRAS*, 504(2):2034–2050.

[106] Lai, D., Helling, C., and van den Heuvel, E. P. J. (2010). Mass Transfer, Transiting Stream, and Magnetopause in Close-in Exoplanetary Systems with Applications to WASP-12. *ApJ*, 721(2):923–928.

[107] Lammer, H., Kasting, J. F., Chassefière, E., Johnson, R. E., Kulikov, Y. N., and Tian, F. (2008). Atmospheric Escape and Evolution of Terrestrial Planets and Satellites. *Space Sci. Rev.*, 139(1-4):399–436.

[108] Lammer, H., Selsis, F., Ribas, I., Guinan, E. F., Bauer, S. J., and Weiss, W. W. (2003). Atmospheric Loss of Exoplanets Resulting from Stellar X-Ray and Extreme-Ultraviolet Heating. *ApJ*, 598:L121–L124.

[109] Lavie, B., Ehrenreich, D., Bourrier, V., Lecavelier des Etangs, A., Vidal-Madjar, A., Delfosse, X., Gracia Berna, A., Heng, K., Thomas, N., Udry, S., and Wheatley, P. J. (2017). The long egress of GJ 436b's giant exosphere. *A&A*, 605:L7.

[110] Lecavelier Des Etangs, A. (2007). A diagram to determine the evaporation status of extrasolar planets. *A&A*, 461:1185–1193.

[111] Lecavelier des Etangs, A., Bourrier, V., Wheatley, P. J., Dupuy, H., Ehrenreich, D., Vidal-Madjar, A., Hébrard, G., Ballester, G. E., Désert, J.-M., Ferlet, R., and Sing, D. K. (2012). Temporal variations in the evaporating atmosphere of the exoplanet HD 189733b. *A&A*, 543:L4.

[112] Lecavelier Des Etangs, A., Vidal-Madjar, A., and Desert, J. M. (2008). The origin of hydrogen around HD 209458b. *Nature*, 456:E1.

[113] Lecavelier des Etangs, A., Vidal-Madjar, A., McConnell, J. C., and Hébrard, G. (2004). Atmospheric escape from hot Jupiters. *A&A*, 418:L1–L4.

[114] Lee, E. J. and Connors, N. J. (2021). Primordial Radius Gap and Potentially Broad Core Mass Distributions of Super-Earths and Sub-Neptunes. *ApJ*, 908(1):32.

[115] Leighly, K. M., Dietrich, M., and Barber, S. (2011). The Discovery of the First He Iλ10830 Broad Absorption Line Quasar. *ApJ*, 728(2):94.

[116] Li, S.-L., Miller, N., Lin, D. N. C., and Fortney, J. J. (2010). WASP-12b as a prolate, inflated and disrupting planet from tidal dissipation. *Nature*, 463(7284):1054–1056.

[117] Linsky, J. L., Yang, H., France, K., Froning, C. S., Green, J. C., Stocke, J. T., and Osterman, S. N. (2010). Observations of Mass Loss from the Transiting Exoplanet HD 209458b. *ApJ*, 717(2):1291–1299.

[118] Livingston, J. H., Dai, F., Hirano, T., Gandolfi, D., Nowak, G., Endl, M., Velasco, S., Fukui, A., Narita, N., Prieto-Arranz, J., Barragan, O., Cusano, F., Albrecht, S., Cabrera, J., Cochran, W. D., Csizmadia, S., Deeg, H. J., Eigmüller, P., Erikson, A., Fridlund, M., Grziwa, S., Guenther, E. W., Hatzes, A. P., Kawauchi, K., Korth, J., Nespral, D., Palle, E., Pätzold, M., Persson, C. M., Rauer, H., Smith, A. M. S., Tamura, M., Tanaka, Y., Van Eylen, V., Watanabe, N., and Winn, J. N. (2018). Three Small Planets Transiting a Hyades Star. *AJ*, 155(3):115.

[119] Lopez, E. D., Fortney, J. J., and Miller, N. (2012). How Thermal Evolution and Mass-loss Sculpt Populations of Super-Earths and Sub-Neptunes: Application to the Kepler-11 System and Beyond. *ApJ*, 761:59.

[120] Lothringer, J. D., Fu, G., Sing, D. K., and Barman, T. S. (2020). UV Exoplanet Transmission Spectral Features as Probes of Metals and Rainout. *ApJ*, 898(1):L14.

[121] Louden, T., Wheatley, P. J., and Briggs, K. (2017). Reconstructing the high-energy irradiation of the evaporating hot Jupiter HD 209458b. *MNRAS*, 464(2):2396–2402.

[122] Loyd, R. O. P., France, K., Youngblood, A., Schneider, C., Brown, A., Hu, R., Segura, A., Linsky, J., Redfield, S., Tian, F., Rugheimer, S., Miguel, Y., and Froning, C. S. (2018). The MUSCLES Treasury Survey. V. FUV Flares on Active and Inactive M Dwarfs. *ApJ*, 867(1):71.

[123] Loyd, R. O. P., Koskinen, T. T., France, K., Schneider, C., and Redfield, S. (2017). Ultraviolet C II and Si III Transit Spectroscopy and Modeling of the Evaporating Atmosphere of GJ436b. *ApJ*, 834:L17.

[124] Madhusudhan, N., Nixon, M. C., Welbanks, L., Piette, A. A. A., and Booth, R. A. (2020). The Interior and Atmosphere of the Habitable-zone Exoplanet K2-18b. *ApJ*, 891(1):L7.

[125] Matsakos, T. and Königl, A. (2016). On the Origin of the Sub-Jovian Desert in the Orbital-period-Planetary-mass Plane. *ApJ*, 820(1):L8.

[126] Mauerhofer, V., Verhamme, A., Blaizot, J., Garel, T., Kimm, T., Michel-Dansac, L., and Rosdahl, J. (2021). UV absorption lines and their potential for tracing the Lyman continuum escape fraction. *A&A*, 646:A80.

[127] Maxwell, J. C. (1877). A Treatise on the Kinetic Theory of Gases. *Nature*, 16(404):242–246.

[128] Mayor, M. and Queloz, D. (1995). A Jupiter-mass companion to a solar-type star. *Nature*, 378:355–359.

[129] Mazeh, T., Holczer, T., and Faigler, S. (2016). Dearth of short-period Neptunian exoplanets: A desert in period-mass and period-radius planes. *A&A*, 589:A75.

[130] Miguel, Y., Kaltenegger, L., Linsky, J. L., and Rugheimer, S. (2015). The effect of Lyman α radiation on mini-Neptune atmospheres around M stars: application to GJ 436b. *MNRAS*, 446(1):345–353.

[131] Misener, W. and Schlichting, H. E. (2021). To cool is to keep: residual H/He atmospheres of super-Earths and sub-Neptunes. *MNRAS*, 503(4):5658–5674.

[132] Moutou, C., Coustenis, A., Schneider, J., St Gilles, R., Mayor, M., Queloz, D., and Kaufer, A. (2001). Search for spectroscopical signatures of transiting HD 209458b's exosphere. *A&A*, 371:260–266.

[133] Murray, C. D. and Correia, A. C. M. (2010). *Keplerian Orbits and Dynamics of Exoplanets*, pages 15–23.

[134] Murray-Clay, R. A., Chiang, E. I., and Murray, N. (2009). Atmospheric Escape From Hot Jupiters. *ApJ*, 693(1):23–42.

[135] Newton, E. R., Mann, A. W., Tofflemire, B. M., Pearce, L., Rizzuto, A. C., Vanderburg, A., Martinez, R. A., Wang, J. J., Ruffio, J.-B., Kraus, A. L., Johnson, M. C., Thao, P. C., Wood, M. L., Rampalli, R., Nielsen, E. L., Collins, K. A., Dragomir, D., Hellier, C., Anderson, D. R., Barclay, T., Brown, C., Feiden, G., Hart, R., Isopi, G., Kielkopf, J. F., Mallia, F., Nelson, P., Rodriguez, J. E., Stockdale, C., Waite, I. A., Wright, D. J., Lissauer, J. J., Ricker, G. R., Vanderspek, R., Latham, D. W., Seager, S., Winn, J. N., Jenkins, J. M., Bouma, L. G., Burke, C. J., Davies, M., Fausnaugh, M., Li, J., Morris, R. L., Mukai, K., Villaseñor, J., Villeneuva, S., De Rosa, R. J., Macintosh, B., Mengel, M. W., Okumura, J., and Wittenmyer, R. A. (2019). TESS Hunt for Young and Maturing Exoplanets (THYME): A Planet in the 45 Myr Tucana-Horologium Association. *ApJ*, 880(1):L17.

[136] Nichols, J. D., Wynn, G. A., Goad, M., Alexander, R. D., Casewell, S. L., Cowley, S. W. H., Burleigh, M. R., Clarke, J. T., and Bisikalo, D. (2015). Hubble Space Telescope Observations of the NUV Transit of WASP-12b. *ApJ*, 803(1):9.

[137] Odert, P., Erkaev, N. V., Kislyakova, K. G., Lammer, H., Mezentsev, A. V., Ivanov, V. A., Fossati, L., Leitzinger, M., Kubyshkina, D., and Holmström, M. (2020). Modeling the Lyα transit absorption of the hot Jupiter HD 189733b. *A&A*, 638:A49.

[138] Oklopčić, A. (2019). Helium Absorption at 1083 nm from Extended Exoplanet Atmospheres: Dependence on Stellar Radiation. *ApJ*, 881(2):133.

[139] Oklopčić, A. and Hirata, C. M. (2018). A New Window into Escaping Exoplanet Atmospheres: 10830 Å Line of Helium. *ApJ*, 855(1):L11.

[140] Öpik, E. J. (1963). Selective Escape of Gases. *Geophysical Journal*, 7(4):490–506.

[141] Owen, J. E. (2019). Atmospheric Escape and the Evolution of Close-In Exoplanets. *Annual Review of Earth and Planetary Sciences*, 47:67–90.

[142] Owen, J. E. and Lai, D. (2018). Photoevaporation and high-eccentricity migration created the sub-Jovian desert. *MNRAS*, 479(4):5012–5021.

[143] Owen, J. E. and Wu, Y. (2013). Kepler Planets: A Tale of Evaporation. *ApJ*, 775(2):105.

[144] Owen, J. E. and Wu, Y. (2017). The Evaporation Valley in the Kepler Planets. *ApJ*, 847:29.

[145] Palle, E., Nortmann, L., Casasayas-Barris, N., Lampón, M., López-Puertas, M., Caballero, J. A., Sanz-Forcada, J., Lara, L. M., Nagel, E., Yan, F., Alonso-Floriano, F. J., Amado, P. J., Chen, G., Cifuentes, C., Cortés-Contreras, M., Czesla, S., Molaverdikhani, K., Montes, D., Passegger, V. M., Quirrenbach, A., Reiners, A., Ribas, I., Sánchez-López, A., Schweitzer, A., Stangret, M., Zapatero Osorio, M. R., and Zechmeister, M. (2020). A He I upper atmosphere around the warm Neptune GJ 3470 b. *A&A*, 638:A61.

[146] Parker, E. N. (1958). Dynamics of the Interplanetary Gas and Magnetic Fields. *ApJ*, 128:664.

[147] Plavchan, P., Barclay, T., Gagné, J., Gao, P., Cale, B., Matzko, W., Dragomir, D., Quinn, S., Feliz, D., Stassun, K., Crossfield, I. J. M., Berardo, D. A., Latham, D. W., Tieu, B., Anglada-Escudé, G., Ricker, G., Vanderspek, R., Seager, S., Winn, J. N., Jenkins, J. M., Rinehart, S., Krishnamurthy, A., Dynes, S., Doty, J., Adams, F., Afanasev, D. A., Beichman, C., Bottom, M., Bowler, B. P., Brinkworth, C., Brown, C. J., Cancino, A., Ciardi, D. R., Clampin, M., Clark, J. T., Collins, K., Davison, C., Foreman-Mackey, D., Furlan, E., Gaidos, E. J., Geneser, C., Giddens, F., Gilbert, E., Hall, R., Hellier, C., Henry, T., Horner, J., Howard, A. W., Huang, C., Huber, J., Kane, S. R., Kenworthy, M., Kielkopf, J., Kipping, D., Klenke, C., Kruse, E., Latouf, N., Lowrance, P., Mennesson, B., Mengel, M., Mills, S. M., Morton, T., Narita, N., Newton, E., Nishimoto, A., Okumura, J., Palle, E., Pepper, J., Quintana, E. V., Roberge, A., Roccatagliata, V., Schlieder, J. E., Tanner, A., Teske, J., Tinney, C. G., Vanderburg, A., von Braun, K., Walp, B., Wang, J., Wang, S. X., Weigand, D., White, R., Wittenmyer, R. A., Wright, D. J., Youngblood, A., Zhang, H., and Zilberman, P. (2020). A planet within the debris disk around the pre-main-sequence star AU Microscopii. *Nature*, 582(7813):497–500.

[148] Pont, F., Gilliland, R. L., Knutson, H., Holman, M., and Charbonneau, D. (2009). Transit infrared spectroscopy of the hot Neptune around GJ 436 with the Hubble Space Telescope. *MNRAS*, 393(1):L6–L10.

[149] Ribas, I., Guinan, E. F., Güdel, M., and Audard, M. (2005). Evolution of the Solar Activity over Time and Effects on Planetary Atmospheres. I. High-Energy Irradiances (1-1700 Å). *ApJ*, 622:680–694.

[150] Ringwood, A. E. (1966). Chemical evolution of the terrestrial planets. *Geochim. Cosmochim. Acta*, 30(1):41–104.

[151] Rogers, J. G. and Owen, J. E. (2021). Unveiling the planet population at birth. *MNRAS*, 503(1):1526–1542.

[152] Salz, M., Czesla, S., Schneider, P. C., and Schmitt, J. H. M. M. (2016). Simulating the escaping atmospheres of hot gas planets in the solar neighborhood. *A&A*, 586:A75.

[153] Sanz-Forcada, J., Micela, G., Ribas, I., Pollock, A. M. T., Eiroa, C., Velasco, A., Solano, E., and García-Álvarez, D. (2011). Estimation of the XUV radiation onto close planets and their evaporation. *A&A*, 532:A6.

[154] Sarkis, P., Henning, T., Kürster, M., Trifonov, T., Zechmeister, M., Tal-Or, L., Angladа-Escudé, G., Hatzes, A. P., Lafarga, M., Dreizler, S., Ribas, I., Caballero, J. A., Reiners, A., Mallonn, M., Morales, J. C., Kaminski, A., Aceituno, J., Amado, P. J., Béjar, V. J. S., Hagen, H.-J., Jeffers, S., Quirrenbach, A., Launhardt, R., Marvin, C., and Montes, D. (2018). The CARMENES Search for Exoplanets around M Dwarfs: A Low-mass Planet in the Temperate Zone of the Nearby K2-18. *AJ*, 155(6):257.

[155] Saumon, D., Hubbard, W. B., Burrows, A., Guillot, T., Lunine, J. I., and Chabrier, G. (1996). A Theory of Extrasolar Giant Planets. *ApJ*, 460:993.

[156] Schilling, G. (1996). 'Hot Jupiters' Leave Theorists in the Cold. *Science*, 273(5274):429.

[157] Schlichting, H. E., Sari, R., and Yalinewich, A. (2015). Atmospheric mass loss during planet formation: The importance of planetesimal impacts. *Icarus*, 247:81–94.

[158] Seager, S. and Sasselov, D. D. (1998). Extrasolar Giant Planets under Strong Stellar Irradiation. *ApJ*, 502(2):L157–L161.

[159] Seager, S. and Sasselov, D. D. (2000). Theoretical Transmission Spectra during Extrasolar Giant Planet Transits. *ApJ*, 537(2):916–921.

[160] Segura, A., Walkowicz, L. M., Meadows, V., Kasting, J., and Hawley, S. (2010). The Effect of a Strong Stellar Flare on the Atmospheric Chemistry of an Earth-like Planet Orbiting an M Dwarf. *Astrobiology*, 10(7):751–771.

[161] Shematovich, V. I., Bisikalo, D. V., and Gerard, J. C. (1994). A kinetic model of the formation of the hot oxygen geocorona 1. quiet geomagnetic conditions. *J. Geophys. Res.*, 99(A12):23217–23228.

[162] Shematovich, V. I., Ionov, D. E., and Lammer, H. (2014). Heating efficiency in hydrogen-dominated upper atmospheres. *A&A*, 571:A94.

[163] Shizgal, B. D. and Arkos, G. G. (1996). Nonthermal escape of the atmospheres of Venus, Earth, and Mars. *Reviews of Geophysics*, 34(4):483–505.

[164] Shkolnik, E. L., Ardila, D. R., Barman, T., Dressing, C., Line, M., Lothringer, J., Loyd, P., Meadows, V., Murray-Clay, R., Nikzad, S., Owen, J., Peacock, S., Sing, D., Stevenson, K., Swain, M., Davis, C., and Lincowski, A. (2021). UV-SCOPE: A MidEx Mission Concept for the Ultraviolet Spectroscopic Characterization Of Planets and their Environments. In *American Astronomical Society Meeting Abstracts*, volume 53 of *American Astronomical Society Meeting Abstracts*, page 231.02.

[165] Sing, D. K., Fortney, J. J., Nikolov, N., Wakeford, H. R., Kataria, T., Evans, T. M., Aigrain, S., Ballester, G. E., Burrows, A. S., Deming, D., Désert, J.-M., Gibson, N. P., Henry, G. W., Huitson, C. M., Knutson, H. A., Lecavelier Des Etangs, A., Pont, F., Showman, A. P., Vidal-Madjar, A., Williamson, M. H., and Wilson, P. A. (2016). A continuum from clear to cloudy hot-Jupiter exoplanets without primordial water depletion. *Nature*, 529(7584):59–62.

[166] Sing, D. K., Lavvas, P., Ballester, G. E., Lecavelier des Etangs, A., Marley, M. S., Nikolov, N., Ben-Jaffel, L., Bourrier, V., Buchhave, L. A., Deming, D. L., Ehrenreich, D., Mikal-Evans, T., Kataria, T., Lewis, N. K., López-Morales, M., García Muñoz, A., Henry, G. W., Sanz-Forcada, J., Spake, J. J., Wakeford, H. R., and PanCET Collaboration (2019). The Hubble Space Telescope PanCET Program: Exospheric Mg II and Fe II in the Near-ultraviolet Transmission Spectrum of WASP-121b Using Jitter Decorrelation. *AJ*, 158(2):91.

[167] Skumanich, A. (1972). Time Scales for Ca II Emission Decay, Rotational Braking, and Lithium Depletion. *ApJ*, 171:565.

[168] Soderblom, D. R. (1983). Rotational studies of late-type stars. II. Ages of solar-type stars and the rotational history of the Sun. *ApJS*, 53:1–15.

[169] Sousa-Silva, C., Seager, S., Ranjan, S., Petkowski, J. J., Zhan, Z., Hu, R., and Bains, W. (2020). Phosphine as a Biosignature Gas in Exoplanet Atmospheres. *Astrobiology*, 20(2):235–268.

[170] Spake, J. J., Sing, D. K., Evans, T. M., Oklopčić, , A., Bourrier, V., Kreidberg, L., Rackham, B. V., Irwin, J., Ehrenreich, D., Wyttenbach, A., Wakeford, H. R., Zhou, Y., Chubb, K. L., Nikolov, N., Goyal, J. M., Henry, G. W., Williamson, M. H., Blumenthal, S., Anderson, D. R., Hellier, C., Charbonneau, D., Udry, S., and Madhusudhan, N. (2018). Helium in the eroding atmosphere of an exoplanet. *Nature*, 557(7703):68–70.

[171] Spitzer, Lyman, J. (1949). The Terrestrial Atmosphere above 300 KM. In Kuiper, G. P., editor, *The Atmospheres of the Earth and Planets*, page 211.

[172] Szabó, G. M. and Kálmán, S. (2019). The sub-Jupiter/Neptune desert of exoplanets: parameter dependent boundaries and implications on planet formation. *MNRAS*, 485(1):L116–L120.

[173] Szabó, G. M. and Kiss, L. L. (2011). A Short-period Censor of Sub-Jupiter Mass Exoplanets with Low Density. *ApJ*, 727:L44.

[174] Tian, F., Chassefière, E., Leblanc, F., and Brain, D. (2013). *Atmospheric Escape and Climate Evolution of Terrestrial Planets*, page 567.

[175] Tsiaras, A., Waldmann, I. P., Tinetti, G., Tennyson, J., and Yurchenko, S. N. (2019). Water vapour in the atmosphere of the habitable-zone eight-Earth-mass planet K2-18 b. *Nature Astronomy*, 3:1086–1091.

[176] Valsecchi, F., Rappaport, S., Rasio, F. A., Marchant, P., and Rogers, L. A. (2015). Tidally-driven Roche-lobe Overflow of Hot Jupiters with MESA. *ApJ*, 813(2):101.

[177] Van Eylen, V., Agentoft, C., Lundkvist, M. S., Kjeldsen, H., Owen, J. E., Fulton, B. J., Petigura, E., and Snellen, I. (2018). An asteroseismic view of the radius valley: stripped cores, not born rocky. *MNRAS*, 479:4786–4795.

[178] van Saders, J. L., Ceillier, T., Metcalfe, T. S., Silva Aguirre, V., Pinsonneault, M. H., García, R. A., Mathur, S., and Davies, G. R. (2016). Weakened magnetic braking as the origin of anomalously rapid rotation in old field stars. *Nature*, 529(7585):181–184.

[179] Vaughan, A. H., Preston, G. W., and Wilson, O. C. (1978). Flux measurements of CA II H and K emission. *PASP*, 90:267–274.

[180] Vidal-Madjar, A., Désert, J.-M., Lecavelier des Etangs, A., Hébrard, G., Ballester, G. E., Ehrenreich, D., Ferlet, R., McConnell, J. C., Mayor, M., and Parkinson, C. D. (2004). Detection of Oxygen and Carbon in the Hydrodynamically Escaping Atmosphere of the Extrasolar Planet HD 209458b. *ApJ*, 604:L69–L72.

[181] Vidal-Madjar, A., Huitson, C. M., Bourrier, V., Désert, J. M., Ballester, G., Lecavelier des Etangs, A., Sing, D. K., Ehrenreich, D., Ferlet, R., Hébrard, G., and McConnell, J. C. (2013). Magnesium in the atmosphere of the planet HD 209458 b: observations of the thermosphere-exosphere transition region. *A&A*, 560:A54.

[182] Vidal-Madjar, A., Lecavelier des Etangs, A., Désert, J.-M., Ballester, G. E., Ferlet, R., Hébrard, G., and Mayor, M. (2003). An extended upper atmosphere around the extrasolar planet HD209458b. *Nature*, 422:143–146.

[183] Vidal-Madjar, A., Lecavelier des Etangs, A., Désert, J. M., Ballester, G. E., Ferlet, R., Hébrard, G., and Mayor, M. (2008). Exoplanet HD 209458b (Osiris): Evaporation Strengthened. *ApJ*, 676(1):L57.

[184] Vidotto, A. A., Jardine, M., and Helling, C. (2011). Transit variability in bow shock-hosting planets. *MNRAS*, 414(2):1573–1582.

[185] Villarreal D'Angelo, C., Vidotto, A. A., Esquivel, A., Hazra, G., and Youngblood, A. (2021). GJ 436b and the stellar wind interaction: simulations constraints using Ly α and H α transits. *MNRAS*, 501(3):4383–4395.

[186] Waalkes, W. C., Berta-Thompson, Z., Bourrier, V., Newton, E., Ehrenreich, D., Kempton, E. M. R., Charbonneau, D., Irwin, J., and Dittmann, J. (2019). Lyα in the GJ 1132 System: Stellar Emission and Planetary Atmospheric Evolution. *AJ*, 158(1):50.

[187] Waterston, J. J. (1843). On the Physics of Media That Are Composed of Free and Perfectly Elastic Molecules in a State of Motion. [Abstract]. *Proceedings of the Royal Society of London Series I*, 5:604.

[188] Waterston, J. J. and Rayleigh, L. (1892). On the Physics of Media that are Composed of Free and Perfectly Elastic Molecules in a State of Motion. *Philosophical Transactions of the Royal Society of London Series A*, 183:1–79.

[189] Watson, A. J., Donahue, T. M., and Walker, J. C. G. (1981). The dynamics of a rapidly escaping atmosphere: Applications to the evolution of Earth and Venus. *Icarus*, 48(2):150–166.

[190] Winn, J. N. (2010). *Exoplanet Transits and Occultations*, pages 55–77.

[191] Wood, B. E., Redfield, S., Linsky, J. L., Müller, H.-R., and Zank, G. P. (2005). Stellar Lyα Emission Lines in the Hubble Space Telescope Archive: Intrinsic Line Fluxes and Absorption from the Heliosphere and Astrospheres. *ApJS*, 159:118–140.

[192] Wyttenbach, A., Ehrenreich, D., Lovis, C., Udry, S., and Pepe, F. (2015). Spectrally resolved detection of sodium in the atmosphere of HD 189733b with the HARPS spectrograph. *A&A*, 577:A62.

[193] Wyttenbach, A., Mollière, P., Ehrenreich, D., Cegla, H. M., Bourrier, V., Lovis, C., Pino, L., Allart, R., Seidel, J. V., Hoeijmakers, H. J., Nielsen, L. D., Lavie, B., Pepe, F., Bonfils, X., and Snellen, I. A. G. (2020). Mass-loss rate and local thermodynamic state of the KELT-9 b thermosphere from the hydrogen Balmer series. *A&A*, 638:A87.

[194] Yan, F. and Henning, T. (2018). An extended hydrogen envelope of the extremely hot giant exoplanet KELT-9b. *Nature Astronomy*, 2:714–718.

[195] Youngblood, A., France, K., Loyd, R. O. P., Linsky, J. L., Redfield, S., Schneider, P. C., Wood, B. E., Brown, A., Froning, C., Miguel, Y., Rugheimer, S., and Walkowicz, L. (2016). The MUSCLES Treasury Survey. II. Intrinsic LYα and Extreme Ultraviolet Spectra of K and M Dwarfs with Exoplanets*. *ApJ*, 824(2):101.

[196] Zhang, M., Knutson, H. A., Wang, L., Dai, F., Oklopcic, A., and Hu, R. (2021). No Escaping Helium from 55 Cnc e. *AJ*, 161(4):181.

[197] Zhao, J. and Tian, F. (2015). Photochemical escape of oxygen from early Mars. *Icarus*, 250:477–481.

Appendix A

`p-winds`: An open-source tool to model upper atmospheres

I developed the open source Python code `p-winds` with the objective of supplying the community with an easy-to-use tool to predict and interpret signatures of atmospheric escape in transiting exoplanets. The following manuscript was submitted for publication to Astronomy & Astrophysics in August 2021.

Astronomy & Astrophysics manuscript no. aanda
August 17, 2021

p-winds: an open-source Python code to model planetary winds and upper atmospheres⋆

Leonardo A. Dos Santos[1], Aline A. Vidotto[2], Shreyas Vissapragada[3], Munazza K. Alam[4], Romain Allart[5], Vincent Bourrier[1], James Kirk[4], Julia V. Seidel[1], and David Ehrenreich[1]

[1] Observatoire astronomique de l'Université de Genève, Chemin Pegasi 51, 1290 Versoix, Switzerland
e-mail: Leonardo.dosSantos@unige.ch
[2] School of Physics, Trinity College Dublin, the University of Dublin, College Green, Dublin-2, Ireland
[3] Division of Geological and Planetary Sciences, California Institute of Technology, 1200 East California Blvd, Pasadena, CA 91125, USA
[4] Center for Astrophysics | Harvard & Smithsonian, 60 Garden Street, Cambridge, MA 02138, USA
[5] Department of Physics, and Institute for Research on Exoplanets, Université de Montréal, Montréal, H3T 1J4, Canada

Received day month year; accepted day month year

ABSTRACT

Atmospheric escape is considered to be one of the main channels for evolution in sub-Jovian planets, particularly in their early lives. While there are several hypotheses proposed to explain escape in exoplanets, testing them with atmospheric observations remains a challenge. In this context, high-resolution transmission spectroscopy of transiting exoplanets for the metastable helium triplet (He 2^3S) at 1 083 nm has emerged as a reliable technique to observe and measure escape. To aid in the prediction and interpretation of metastable He transmission spectroscopy observations, we developed the code `p-winds`. This is an open-source, fully documented, scalable Python implementation of the one-dimensional Parker wind model for upper atmospheres coupled with H and He ionization balance, ray-tracing, and radiative transfer routines. We demonstrate an atmospheric retrieval by fitting `p-winds` models to the observed metastable He transmission spectrum of the warm Neptune HAT-P-11 b, and take into account the variation of the in-transit absorption caused by transit geometry. For this planet, our best fit yields a total atmospheric escape rate of approximately 3.6×10^{10} g s^{-1} and wind temperature of 6600 K. The retrieved total escape rate is mostly insensitive to the H/He fraction when we allow the latter as a free parameter, but the resulting posterior of the fit shows a preference for H/He > 0.96. The stellar host limb darkening does not have a significant impact in the retrieved escape rate or wind temperature for HAT-P-11 b. Based on the non-detection of escaping He for GJ 436 b, we are able to rule out total escape rates higher than 8.9×10^9 g s^{-1} at 99.7% (3σ) confidence, and show that the retrieval favors high values of H/He.

Key words. Methods: numerical – Planets and satellites: atmospheres

1. Introduction and motivation

The evolution of short-period exoplanets is thought to be dictated by atmospheric escape. This conclusion is supported by two different approaches: i) the detection of planetary winds and large escape rates in hot exoplanets (e.g., Vidal-Madjar et al. 2003; Ehrenreich et al. 2015; Bourrier et al. 2018), and ii) the observation of demographic features possibly carved by atmospheric escape in the population of Neptunes and super-Earths (Beaugé & Nesvorný 2013; Owen & Wu 2013; Mazeh et al. 2016; Fulton et al. 2017; Fulton & Petigura 2018; Hardegree-Ullman et al. 2020). These discoveries have led the community to attempt combining the theoretical descriptions of escape based on demographic features to predict observable atmospheric signatures in transiting exoplanets (e.g., Lecavelier Des Etangs 2007; Salz et al. 2016; King et al. 2019; Carolan et al. 2020). This experiment has been challenging, mainly because of limitations in our instruments and our theories (e.g., Cubillos et al. 2017; Kasper et al. 2020; Gaidos et al. 2020; Bean et al. 2021).

There are four known spectroscopic windows to observe atmospheric escape: the Lyman-α line at 121.57 nm (Vidal-Madjar et al. 2003), metallic chromospheric lines and continuum in the ultraviolet (Fossati et al. 2010; Sing et al. 2019), the metastable helium triplet at 1 083 nm (Seager & Sasselov 2000; Oklopčić & Hirata 2018), and the Balmer series of H lines in blue-optical (Jensen et al. 2012; Wyttenbach et al. 2020). Each one of them has its own set of challenges. While UV observations have classically been used to this end with a variable degree of success (e.g., Lecavelier des Etangs et al. 2010; Fossati et al. 2010; Vidal-Madjar et al. 2013; Waalkes et al. 2019; Dos Santos et al. 2020b, 2021; Bourrier et al. 2021; García Muñoz et al. 2021), they are particularly complicated because only the *Hubble Space Telescope* (*HST*) can access this wavelength range at high spectral resolution; in addition, cool stars usually do not have UV continuum, limiting transmission spectroscopy only to chromospheric or transition-region emission lines whose count rates are very low (Bourrier et al. 2017; Dos Santos et al. 2019).

Of these techniques, He transmission spectroscopy has been shown to be reliable and attainable using ground- and space-based instruments (Spake et al. 2018; Allart et al. 2018). This spectral channel is not photon-starved and is devoid of interstellar medium absorption (Indriolo et al. 2009), the main limitations

⋆ The source code can be freely obtained in `https://github.com/ladsantos/p-winds`. Documentation, installation instructions, and tutorials are available in `https://p-winds.readthedocs.io/`. Contributions to the project are welcome.

of Lyman-α spectroscopy. The disadvantage is that the formation of metastable He in the upper atmospheres of exoplanets depends on a specific level of irradiation arriving at the planet (e.g., Nortmann et al. 2018; Oklopčić 2019; Dos Santos et al. 2020a). Nevertheless, He spectroscopy has the potential to become the main technique of atmospheric escape observations (Allart et al. 2019; Alonso-Floriano et al. 2019; Kirk et al. 2020; Vissapragada et al. 2020; Lampón et al. 2021; Paragas et al. 2021).

Upper atmospheres extend to several planetary radii, and can dwarf the size of planet-hosting stars depending on the properties of the system (e.g., Chamberlain 1963; Chaffin et al. 2015; Lavie et al. 2017; Kameda et al. 2017; Bourrier et al. 2018). For this reason, when observing the upper atmospheres of exoplanets, the transit geometry can have important effects in the interpretation of the data. For example, if a transiting planet has a non-zero impact parameter, a large portion of its exosphere may not transit and does not contribute to the observed in-transit absorption. Furthermore, a more subtle effect in time-series analysis of transmission spectroscopy is the dilution of a planetary absorption signal when the data are co-added in phase space. Since upper atmospheres are extended, the in-transit absorption is variable with time. This variability dilutes the in-transit absorption because time-series of transmission spectra are co-added in phase space to improve the signal-to-noise ratio of the combined transmission spectrum (e.g., Wyttenbach et al. 2015).

There are currently no publicly available tools to predict and interpret metastable He transmission spectroscopy. Considering that there is a broad interest of the community in these observations, we developed `p-winds`, an open-source, fully-documented Python implementation of the one-dimensional, isothermal Parker wind description (Parker 1958) to model exoplanet atmospheres. This code is timely because many datasets used to study metastable He spectroscopy have recently become public. Furthermore, an open-source implementation allows for independent verification of results as well as community contributions to the code. `p-winds` implements limb-darkening and a ray-tracing algorithm that allows the user to change the transit geometry (namely the transit impact parameter and phase in relation to mid-transit).

In this manuscript we describe the overarching implementation of `p-winds`, discuss the design decisions, and illustrate the usage of the code. In Sect. 2 we describe the several modules implemented in the code to forward model the metastable He signature in a transiting exoplanet; in Sect. 3 we present case studies of the warm Neptunes HAT-P-11 b and GJ 436 b and their corresponding atmospheric escape rates retrieved by fitting `p-winds` models to observations; and in Sect. 4 we discuss the conclusions of this work.

2. Methods

The code `p-winds` is largely based on the formulations of Oklopčić & Hirata (2018) and Lampón et al. (2020). In its current version, the code has four core modules (and two support modules) to model the upper atmospheres and ionization balance of H and He around planetary bodies, which we describe below. In principle, these modules can be used independently of each other depending on the objective of the user. The code to reproduce the examples shown in this Section can be obtained via the `p-winds` documentation.

2.1. The `parker` module

The `parker` module calculates the structure of the upper atmosphere following the theoretical description of the solar wind by Parker (1958). In this model, a steady-state, spherically-symmetric wind follows the equation of mass conservation:

$$\dot{M} = 4\pi r^2 \rho(r) v(r), \tag{1}$$

where $\dot{M}$ is the mass loss rate, r is the radius, ρ is the gas density, and v is the wind velocity. This model also follows the steady-state momentum equation:

$$v\frac{dv}{dr} + \frac{1}{\rho}\frac{dp}{dr} + \frac{GM_{\rm pl}}{r^2} = 0, \tag{2}$$

where G is the gravitational constant, p is the thermal pressure and $M_{\rm pl}$ is the planetary mass. The isothermal Parker wind model assumes that the sound speed $v_{\rm s}$ is constant in the upper atmosphere, allowing for a significant simplification of the problem:

$$v_{\rm s} = \sqrt{\frac{kT_0}{\mu\, m_{\rm p}}}, \tag{3}$$

where T_0 is the gas temperature (assumed to be constant), $m_{\rm p}$ is the mass of a proton, and μ is the mean molecular weight. We calculate μ as:

$$\mu = \frac{1+4y}{1+y+f_{\rm ion}}, \text{with } y = \frac{n_{\rm He}}{n_{\rm H}}, \text{and } f_{\rm ion} = \frac{n_{\rm H^+}}{n_{\rm H}}, \tag{4}$$

where $n_{\rm X}$ is the number density of species X. For clarity, we note that $n_{\rm H} = n_{\rm H^0} + n_{\rm H^+}$ and $n_{\rm He} = n_{\rm He\ ^1S\ (singlet)} + n_{\rm He\ ^2{}^3S\ (triplet)} + n_{\rm He^+}$. We assume that the electrons coming from He ionization do not significantly contribute to changes in μ. According to Oklopčić & Hirata (2018), who also make this same assumption, including electrons from He ionization increases their number density by up to ~10%.

It is convenient to normalize the radii, velocities and densities to, respectively, the radius at the sonic point ($r_{\rm s}$), the constant speed of sound, and the density at the sonic point ($\rho_{\rm s}$). Based on the formulation of Lamers & Cassinelli (1999), the resulting equations describing the radial profiles of velocity and density are:

$$\tilde{v}(r)\exp\left[\frac{-\tilde{v}(r)^2}{2}\right] = \left(\frac{1}{\tilde{r}}\right)^2 \exp\left[-\frac{2}{\tilde{r}} + \frac{3}{2}\right] \text{ and} \tag{5}$$

$$\tilde{\rho}(r) = \exp\left[\frac{2}{\tilde{r}} - \frac{3}{2} - \frac{\tilde{v}^2}{2}\right], \tag{6}$$

where $\tilde{r}$, $\tilde{v}$, and $\tilde{\rho}$ are the normalized radial distance, velocity, and density, respectively.

Calculating the structure of the upper atmosphere requires the planetary parameters as input, as well as values for the atmospheric temperature and escape rate; the latter two are free parameters in the Parker wind model. Eq. 5 is transcendental, and requires a numerical approach to determine its solutions. To this end, we utilize a Newton-Raphson method implemented in `scipy.optimize`, which requires an initial guess for the optimization. Eq. 5 has many solutions, but we are only interested in

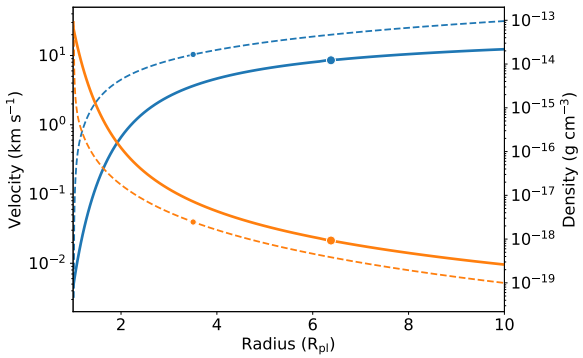

Fig. 1. One-dimensional structure of the upper atmosphere of the hot Jupiter HD 209458 b computed with `p-winds` (continuous curves). Velocities are shown in blue, and densities in orange. For comparison, we also plot a model for the same planet computed self-consistently using the formulation of Allan & Vidotto (2019) as dashed curves. The circles mark the sonic point.

the solution that represents an escaping atmosphere, i.e., a transonic solution. In order to guarantee we converge to the correct solution, we enforce that the initial guess is below (above) the speed of sound when calculating the velocities below (above) the sonic point. The end product of the `parker` module is the structure of the upper atmosphere from equations 5 and 6.

As an example, we calculated the structure of the upper atmosphere of the hot Jupiter HD 209458 b and the result is shown in Fig. 1. The ion fraction of H, which is important to determine the mean molecular weight and hence the location of the sonic point, was calculated self-consistently using the `hydrogen` module (Sect. 2.2). We compare the structure computed with `p-winds` (continuous curves) with a one-dimensional model of the same planet calculated self-consistently using the formulation of Allan & Vidotto (2019, dashed curves). In order to be comparable, the `p-winds` model was computed using the same mass loss rate, average wind temperature, and H/He fraction (which are free parameters in our model) as the self-consistent model. By a factor of a few, the isothermal Parker wind predicts densities larger than the self-consistent model, and lower velocities; furthermore, the former predicts a sonic point two times farther than the latter.

Naturally, a one-dimensional model does not capture outflow asymmetries that are sometimes observed in Lyman-α transit spectroscopy (e.g., Lecavelier des Etangs et al. 2010; Lavie et al. 2017; Bourrier et al. 2018). More complex, three-dimensional models are necessary to completely describe these features (e.g., Bourrier et al. 2016; Villarreal D'Angelo et al. 2021; Wang & Dai 2021a,b). Simple one-dimensional models are nevertheless able to retrieve atmospheric escape parameters when the outflow is mostly located along the line connecting the star to the planet (e.g., Lampón et al. 2020, 2021), beyond which the escaping material starts to become susceptible to acceleration by radiation pressure and interaction with the stellar wind. Models that are faster to calculate are also useful when there is a need to explore a large parameter space, which is what we discuss in Sect. 3 and in an upcoming manuscript (Vissapragada et al., in prep.).

2.2. The `hydrogen` module

The `hydrogen` module calculates the steady-state distribution of neutral and ionized H in the upper atmosphere. The quantity of interest here is $f_{\rm ion}$, whose radial profile is described by source and sink terms. In our case, the source of H ions is (photo-) ionization by high-energy photons, and the sink is recombination into neutral atoms. This radial distribution can be calculated with the following differential equation:

$$\frac{df_{\rm ion}}{dr} = \frac{1 - f_{\rm ion}}{v}\Phi e^{-\tau_0} - \frac{1}{(1+4y)m_{\rm p}y}\frac{\rho}{v}f_{\rm ion}^2\alpha_{\rm rec}. \quad (7)$$

The velocities v and densities ρ are calculated using the module `parker`. Eq. 7 has three factors that warrant an in-depth explanation:

- Φ is the hydrogen photoionization rate at null optical depth, calculated as:

$$\Phi = \int_0^{\lambda_0} \frac{\lambda}{hc} F_\lambda \sigma_\lambda d\lambda, \quad (8)$$

  where λ_0 is the wavelength corresponding to the ionization energy of H (911.65 Å) and f_λ is the flux density (in units of energy $\cdot$ time$^{-1}\cdot$ area$^{-1}\cdot$ wavelength^{-1}) arriving at the top of the atmosphere. σ_λ is the photoionization cross-section, which we calculate in the support module `microphysics`, following Eq. 10 in Oklopčić & Hirata (2018), which is based on Osterbrock & Ferland (2006).
- τ_0 is the optical depth due to neutral H (based on Eq. 11 of Oklopčić & Hirata 2018):

$$\tau_0 = \frac{1}{(1+4y)m_{\rm p}y}\sigma_0 \int_r^\infty (1 - f_{\rm ion})\rho(r)dr, \quad (9)$$

  where σ_0 is the flux-averaged photoionization cross-section of H:

$$\sigma_0 = \frac{\int_0^{\lambda_0} F_\lambda \sigma_\lambda d\lambda}{\int_0^{\lambda_0} F_\lambda d\lambda}, \quad (10)$$

- $\alpha_{\rm rec}$ is the case-B H recombination rate at a given temperature (Osterbrock & Ferland 2006; Tripathi et al. 2015), calculated as:

$$\alpha_{\rm rec} = 2.59 \times 10^{-13}\left(\frac{T_0}{10^4}\right)^{-0.7} \text{ cm}^3 \text{ s}^{-1}. \quad (11)$$

As seen in Eq. 9, τ_0 depends on $f_{\rm ion}$, which is what we want to calculate in the first place. However, the optical depth depends more strongly on the densities of H than the ion fraction. So instead of solving a system of coupled non-linear differential equations, a first solution can be achieved by assuming that the whole atmosphere is neutral at first. Later, we relax this assumption by recalculating the τ_0 and $f_{\rm ion}$ profiles iteratively until convergence is achieved (the user can define the convergence criterion).

We solve Eq. 7 using `solve_ivp`, an explicit Runge-Kutta integrator of hybrid 4th and 5th orders implemented in `scipy.integrate`. The user inputs an initial guess for $f_{\rm ion}$ at the innermost layer of the upper atmosphere. The code also takes as input the stellar host spectrum arriving at the planet, or the monochromatic flux between 0 and 911.65 Å, and the planetary parameters. The solution for the H distribution in 500 points including the relaxation takes approximately 400 ms on a CPU

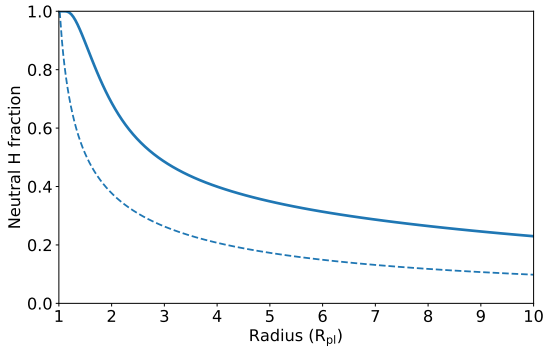

Fig. 2. Neutral H fraction in the upper atmosphere of the hot Jupiter HD 209458 b computed with `p-winds` for the same setup from Sect. 2.1 (continuous curve). We also show the neutral fraction calculated with a self-consistent escape model for comparison (dashed curve).

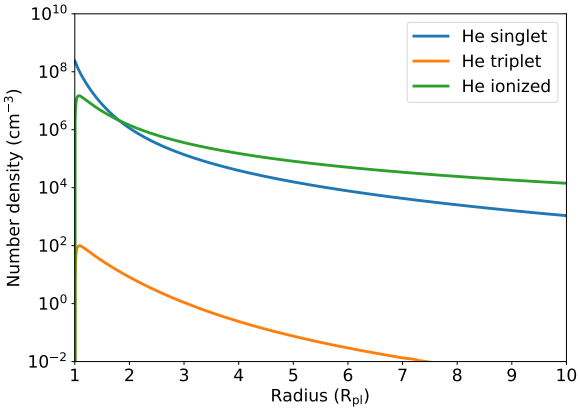

Fig. 3. Distribution of He in the upper atmosphere of HD 209458 b calculated with `p-winds` assuming the same input parameters as Oklopčić & Hirata (2018).

with frequency 3.1 GHz and four computing threads. Continuing the example for HD 209458 b from Sect. 2.1, we calculated the ion and neutral fraction of H in the upper atmosphere, and the resulting distribution is shown in Fig. 2 (continuous curve). We compare this result with the ion fraction calculated with the self-consistent escape model from Sect. 2.1 (dashed curve); in order to be comparable, both models are calculated assuming an impinging XUV monochromatic flux of 450 erg s^{-1} cm^{-2}. The `p-winds` model overpredicts the ion fraction by a factor of a few when compared to the self-consistent model, likely because of the larger densities (see Fig. 1), which increase the optical depth of the atmosphere to ionizing irradiation.

2.3. The `helium` module

The `helium` module calculates the steady-state distribution of neutral singlet, neutral triplet, and ionized He in the upper atmosphere. The quantities of interest here are $f_1 = n_{\mathrm{He}\,1^1\mathrm{S}}/n_{\mathrm{He}}$ and $f_3 = n_{\mathrm{He}\,2^3\mathrm{S}}/n_{\mathrm{He}}$. The radial profiles df_1/dr and df_3/dr are described by a coupled system of differential equations with source and sink terms:

$$\begin{cases} df_1/dr = \mathrm{sources}_1 + \mathrm{sinks}_1 \\ df_3/dr = \mathrm{sources}_3 + \mathrm{sinks}_3 \end{cases} . \tag{12}$$

We refer the reader to Oklopčić & Hirata (2018) and Table 2 of Lampón et al. (2020) for detailed equations of all the source and sink terms for He[1]. In our code we do include the He charge exchange terms pointed out by Lampón et al. (2020).

We assume that the distribution of He does not significantly change the structure of the upper atmosphere. This allows us to decouple the `helium` module from the `parker` and `hydrogen` modules. This is advantageous because the user can enter as input a H structure that was calculated by more complex and self-consistent models than the one of Parker (1958).

The procedure to solve the distribution of He (Eq. 12) is similar to that for H. The user inputs an initial guess for f_1 and f_3 at the innermost atmospheric layer, the stellar host spectrum from 0 to 2600 Å (or monochromatic fluxes in the bands 0-1200 Å and 1200-2600 Å), the structure of the upper atmosphere (profiles of density and velocity), and the planetary parameters. It is important to emphasize that neutral H also contributes to the optical depth between wavelengths 0-911 Å, attenuating the amount of high-energy flux that ionizes and populates the He levels. The code takes this contribution into account, as in Oklopčić & Hirata (2018).

Initially, the code assumes that the entire upper atmosphere has constant f_1 and f_3, and then a first solution is obtained using `odeint`[2], a Python wrapper for the `LSODA` solver from the Fortran library `odepack` implemented in `scipy.integrate`. This solution is then relaxed by updating the optical depths, f_1 and f_3 iteratively until convergence is achieved. The solution can, however, become numerically unstable for large density gradients, which can sometimes happen near the $R = 1$ R_{pl}. A practical workaround is to establish a cutoff near 1 R_{pl} that removes this large density gradient and ignore this layer of the atmosphere in the modeling.

We show the distribution of He in the upper atmosphere of HD 209458 b calculated as described above in Fig. 3. For comparison purposes, this time we assumed a model with the same input parameters as the one described in Oklopčić & Hirata (2018, namely an escape rate of 8×10^{10} g s^{-1}, a temperature of 9000 K, a H/He fraction of 0.9, and a solar irradiating spectrum). Our results match the models of Oklopčić & Hirata, as seen in Fig. 3 of their publication. The solution for the He distribution in 500 points including the relaxation takes approximately 2.5 s on a CPU with frequency 3.1 GHz and four computing threads. This is the main computational bottleneck of the `p-winds` code.

2.4. The `transit` module

The `transit` module has two independent functions that can be used to calculate the spectral signatures of the upper atmosphere in transmission. The first function, `draw_transit`, calculates two-dimensional intensity maps containing the host star and a transiting planet at a user-defined phase and impact parameter. The one-dimensional profiles of metastable He volumetric densities are required to calculate the two-dimensional array of column densities mapped to the same geometry as the transit.

[1] We note that, in Table 2 of Lampón et al. (2020), the units for the recombination and collisional processes is cm^3 s^{-1}, and not cm^{-3} s^{-1} as the authors list in their manuscript.

[2] When calculating the steady-state distribution of He, we opt to use `odeint` instead of `solve_ivp` in this case because the first is more stable and 2.6 times faster than the second. `solve_ivp` is faster than `odeint` when solving the distribution of H.

The output intensity map is normalized in a way that the disk-averaged stellar intensity is 1.0 when the planet is out of transit. Optionally, the user can also input a limb-darkening law.

The most important function in this module is `radiative_transfer_2d` which, as the name implies, calculates the in-transit absorption spectrum caused by the opaque disk of the planet and its upper atmosphere. In each cell of the 2-D transit mapped by the ij indexes, the resulting attenuated intensity $I_{ij}(\nu)$[3] of the stellar light caused by absorption of He in the upper atmosphere is given by:

$$I_{ij}(\nu) = I_{ij,0}(\nu) \exp\left(-\tau_{ij,\mathrm{He}}\right), \tag{13}$$

where $I_{ij,0}(\nu)$ is the intensity emerging from the host star before filtering through the atmosphere and $\tau_{ij,\mathrm{He}}$ is the optical depth due to metastable He. $I_{ij}(\nu)$ is set to zero in the cells corresponding to the opaque disk of the planet. From here onwards, we shall drop the ij indexes for the sake of brevity, but the reader should implicitly assume that the radiative transfer is carried out cell-by-cell in the transit map. Formally, the optical depth is given by:

$$\tau_{\mathrm{He}} = \int_{-R_{\mathrm{atm}}}^{R_{\mathrm{atm}}} \varphi_\nu(z)\, \sigma_{\mathrm{He}}\, n_{\mathrm{He}}(z)\, dz, \tag{14}$$

where φ_ν is the Voigt profile and σ_{He} is the cross-section of metastable helium lines near 1.083 μm. Following Oklopčić & Hirata (2018) (see also, e.g., Allan & Vidotto 2019), the He cross-section is calculated as:

$$\sigma_{\mathrm{He}} = \frac{\pi e^2}{m_e c} f, \tag{15}$$

where f is the oscillator strength of the transition, e is the electron charge, and m_e is the electron mass. This formula is only valid in the Gaussian-cgs unit system, where e is given in units of esu or statC; see, for example, Koskinen et al. (2010) for a formula that can be used in other unit systems.

The Voigt profile φ_ν is calculated using the `voigt_profile` implementation of `scipy.special`, which takes two parameters: the Gaussian (in our case Doppler) half-width at half maximum (HWHM) and the Lorentzian HWHM. Similar to Oklopčić & Hirata (2018), the Gaussian HWHM α is calculated as:

$$\alpha = \frac{\nu_0}{c} \sqrt{\frac{2 \ln(2)\, k_B T}{m_{\mathrm{He}}}}, \tag{16}$$

where m_{He} is the mass of a He atom, T is the temperature of the gas, ν_0 is the central frequency of the transition. The Lorenzian HWHM is $\gamma = A_{ij}/4\pi$, where A_{ij} is the Einstein coefficient of the transition. We took the properties of the metastable He transitions near 1.083 μm from the NIST database[4], and list them in Table 1.

In reality, φ_ν depends on the three-dimensional position in relation to the planet because each position has a different line-of-sight velocity, which broadens the absorption line. Thus, the formal calculation of the Voigt profile is performed for each pencil of light between the star and the observer. In a given position z along the pencil, the line-of-sight velocity v_{LOS} in function of distance r from the planet center is calculated using the formulation of Seidel et al. (2020):

$$|v_{\mathrm{LOS}}(r)| = |v_{\mathrm{ver}}| \frac{z^2}{\sqrt{r^2 + z^2}}, \tag{17}$$

where v_{ver} is the outflow velocity obtained from the Parker wind model.

This calculation has to be performed for three spectral lines, and it adds an extra dimension for wavelength. For these reasons, the formal calculation of φ_ν taking into account all the four dimensions is computationally costly. In order to accelerate the radiative transfer, instead of calculating the Parker wind broadening in full dimensionality, we can optionally assume that it contributes to the Gaussian broadening term of the Voigt profile uniformly through the line of sight. With the dependence on the z-axis dropped, we can remove φ_ν from the integrand in Eq. 14, yielding:

$$\tau_{\mathrm{He}} = \varphi_\nu\, \sigma_{\mathrm{He}} \int_{-R_{\mathrm{atm}}}^{R_{\mathrm{atm}}} n_{\mathrm{He}}(z)\, dz = \varphi_\nu\, \sigma_{\mathrm{He}}\, \eta_{\mathrm{He}}, \tag{18}$$

where η_{He} is the column density of He. In order to validate this approximation, we need to assume that the Gaussian wind broadening has a constant velocity v_w in the line of sight, and add it in quadrature to the square-velocity term of Eq. 16, yielding:

$$\alpha_{\mathrm{approx}} = \frac{\nu_0}{c} \sqrt{\frac{2 \ln(2)\, k_B T}{m_{\mathrm{He}}} + v_w^2}. \tag{19}$$

There are two ways to calculate v_w. The first option is to compute it as the density-weighted average of v_{LOS}:

$$v_w = \frac{\int_0^{R_{\mathrm{sim}}} v_{\mathrm{LOS}}(r)\, n_{\mathrm{He}}(r)\, dr}{\int_0^{R_{\mathrm{sim}}} n_{\mathrm{He}}(r)\, dr}. \tag{20}$$

The second option is to calculate it as the turbulent velocity, which is the strategy adopted by Lampón et al. (2020):

$$v_w = \sqrt{5 k_B T / (3 m_{\mathrm{He}})}. \tag{21}$$

We assess the validity of the assumption we made above in Fig. 4, where we calculated the metastable He transmission spectrum of HD 209458 b using the three different wind broadening implementations. The average velocity method produces the most accurate approximation to the formal calculation compared to the turbulent broadening and it is one order of magnitude

Table 1. Spectral line properties of the metastable He triplet in the near-infrared.

Upper level J	λ_0 (nm, in air)	A_{ij} (s^{-1})	f
0	1 082.909	1.0216×10^7	5.9902×10^{-2}
1	1 083.025	1.0216×10^7	1.7974×10^{-1}
2	1 083.034	1.0216×10^7	2.9958×10^{-1}

[3] The radiative transfer routine uses input in wavelength space, but the actual calculations are performed in frequency space for code clarity and brevity. The grid size is defined by the user.

[4] `https://www.nist.gov/pml/atomic-spectra-database`.

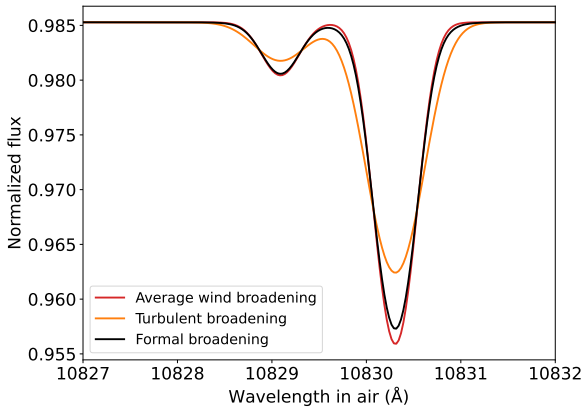

Fig. 4. Comparison of the spectral line broadening in the He triplet lines using three different methods: formal definition of the optical depth (black), density-weighted average velocity broadening (red), and turbulent broadening (orange).

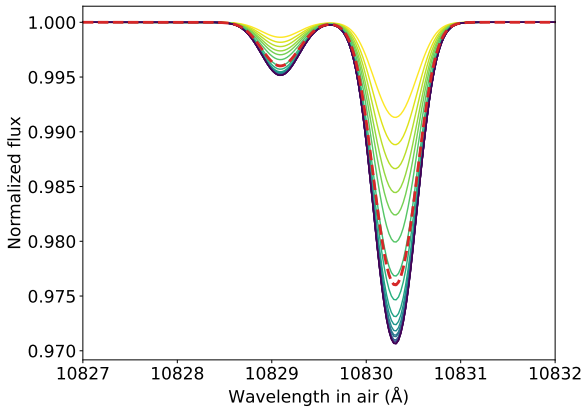

Fig. 5. Metastable He transmission spectrum of HD 209458 b for uniformly-sampled phases and transit impact parameter $b = 0.499$. The baseline $(R_p/R_s)^2$ was removed, as in actual ground-based observations. Lighter colors represent phases near the first/fourth contact, and darker colors represent phases near the transit center. The dashed red spectrum is the average of all phases.

faster in computation time than the formal method. `p-winds` allows the user to decide on which method to calculate the Voigt profile: the formal calculation (Eqs. 13 and 14), the density-weighted average broadening parameter (Eqs. 18, 19, and 20), and the turbulent broadening (Eqs. 18, 19, and 21). This is done with the optional parameter `wind_broadening_method` when calling the `radiative_transfer_2d` function; the default is the density-weighted average velocity implementation, which is a good compromise of speed and accuracy.

We emphasize that, at this point, we are only producing a forward model and not making an attempt to fit it to actual existing observations of this planet (e.g., Lampón et al. 2020). The results we obtain from the example of HD 209458 b throughout this Section, from the Parker wind structure to the predicted metastable He transmission spectrum, are consistent with those obtained by Oklopčić & Hirata (2018).

2.5. Dillution of the transit signature

Usually, the absorption of light by upper atmospheres in transiting exoplanets is in the order of several percent or less in a narrow bandpass. Thus, transmission spectroscopy observations sometimes rely on averaging time series in phase-space to build enough signal to noise and produce a detectable signal. However, upper atmospheres are so extended that the in-transit absorption signature is variable with phase, and phase-averaging them dilutes the observed signature (see Fig. 5). In addition, inhomogeneities in the stellar surface, such as limb darkening, may become important.

Previous 1-D descriptions of the metastable He transmission spectrum did not take into account the transit geometry, phase-averaging, and limb darkening. The `p-winds` code allows the user to set the transit impact parameter, phase in relation to the first and fourth contacts, and set a limb-darkening law. To this end, we utilize the auxiliary open-source code `flatstar`[5] to simulate transit grids (see a brief description in Appendix A). In the current implementation, this transit grid only allows for circular orbits and it neglects the curvature of the transit chord.

[5] The code is freely available in `https://flatstar.readthedocs.io`.

3. Atmospheric escape retrievals

We further benchmark the code `p-winds` by performing retrievals of the atmospheric escape rate, temperature, line-of-sight bulk velocity, and the H/He fraction of the warm Neptunes HAT-P-11 b and GJ 436 b. Both planets were observed in transmission spectroscopy by the CARMENES spectrograph, but only the first had a strong in-transit signal and the second had only a non-detection. For the latter, we attempt to fit upper/lower limits of the atmospheric escape rate and outflow temperature.

3.1. Fitting the He signature of HAT-P-11 b

The metastable He signature of HAT-P-11 b was measured with the CARMENES spectrograph installed in the 3.5 m telescope at the Calar Alto Observatory (Allart et al. 2018). The transmission spectrum is openly available in the DACE platform[6]. The central wavelengths of the metastable He transitions retrieved from the NIST database are listed as measured in air, but the wavelengths of the CARMENES spectrum are in vacuum. We convert the wavelengths of the latter to in-air using the following formula (Morton 2000, IAU standard):

$$\lambda_{\rm air} = \lambda_{\rm vacuum}/n \text{ with}$$
$$n = 1 + 0.0000834254 + \frac{0.02406147}{130 - s^2} + \frac{0.00015998}{38.9 - s^2} \text{ and}$$
$$s = 10^4/\lambda_{\rm vacuum}. \quad (22)$$

In general, we fit three free parameters: the atmospheric escape rate $\dot{m}$, the upper atmosphere temperature T, and the bulk line-of-sight velocity $v_{\rm bulk}$ of the upper atmosphere. It is also possible to run fits with additional parameters (such as the H/He fraction). The fit is performed by maximizing the likelihood $\mathcal{P}$ of a given transmission spectrum model $F_{\rm model}$ to represent the ob-

[6] `https://dace.unige.ch/openData/`

served transmission spectrum F. Such a log-likelihood is given by:

$$\ln \mathcal{P}(F|\lambda, \sigma, \boldsymbol{p}) = -\frac{1}{2}\sum_n \left[\frac{(F_n - F_{\rm model})^2}{\sigma_n^2} + \ln\left(2\pi\sigma_n^2\right)\right], \quad (23)$$

where n stands for a given bin of the spectrum, σ is the uncertainty of the measurement, and $\boldsymbol{p}$ is the vector containing the free parameters. To determine the uncertainties of the fit, we use the Markov chain Monte Carlo (MCMC) ensemble sampler `emcee` (Foreman-Mackey et al. 2013). The uncertainties we report here represent the confidence interval that encompasses the 16th to the 84th percentile of the posterior distribution of the free parameters.

For HAT-P-11 b, we ran in total four different models: (1) No limb darkening, H/He number fraction fixed to 0.90; (2) a quadratic limb-darkening law with coefficients $c_1 = 0.63$ and $c_2 = 0.09$ (Sing 2010), H/He number fraction fixed to 0.90; (3) no limb darkening, H/He as a free parameter with an uniform prior of [0.80, 0.99]; and (4) same as (1), but using the formal implementation of the radiative transfer instead of the average-velocity broadening approximation. For model (4), instead of a full MCMC, we perform only a maximum-likelihood (Eq. 23) using the Nelder-Mead algorithm implemented in `scipy.optimize.minimize`. The reason is because we simply want to assess the accuracy of the average-velocity broadening approximation for HAT-P-11 b in comparison to the formal, more computationally costly radiative transfer. HAT-P-11 does not have a full high-energy spectrum measurement, so we use the spectrum of a similar star from the MUSCLES Treasury Survey[7] (France et al. 2016; Youngblood et al. 2016; Loyd et al. 2016) as a proxy. We chose the star HD 40307, which has similar effective temperature, mass, radius, and surface gravity as HAT-P-11.

We ran the MCMC for 7000 steps and 10 walkers in 10 cores of a computer cluster with an average frequency of 3.0 GHz per core. The autocorrelation time t of the MCMC was, on average, 45 steps when we started from a first guess of 1×10^{10} g s^{-1}, 800 K, and -2.0 km s^{-1}, respectively for $\dot{m}$, T, and $v_{\rm bulk}$. We remove a total of $2t$ burn-in steps from the beginning of the MCMC and take a sample thinned by $t/2$, resulting in a flat chain of approximately 3600 samples. The computation of the MCMC chains took approximately 6.5 hours of computing time. Different planets will likely yield different computing times, because the numerical bottleneck (calculating the He distribution) is highly dependent on the input parameters. We show the posterior distributions of the fit parameters for Model 1 in Fig. 6 (see also Appendix B), and a sample of corresponding transmission spectrum models fit to the data in Fig. 7.

Table 2 contains the retrieved atmospheric escape parameters for HAT-P-11 b based on the CARMENES transmission spectrum. All models we tested yield results consistent with each other within their uncertainties, based on the marginalized posterior distribution of the retrieved parameters. In the case of Model 3, where we allowed the H/He fraction to vary between 0.80 and 0.99, the retrieval slightly favors fractions > 0.96, but the 3σ upper limit of > 0.80 is not constraining. We show the resulting posterior distributions of the fit to Model 3 in Fig. 9. Interestingly, the retrieved escape rate is mostly insensitive to the H/He fraction. However, for fractions above 0.92, the retrieved escape rate tends to increase by a factor of several percent. The retrieved

[7] Available at `https://archive.stsci.edu/prepds/muscles/`.

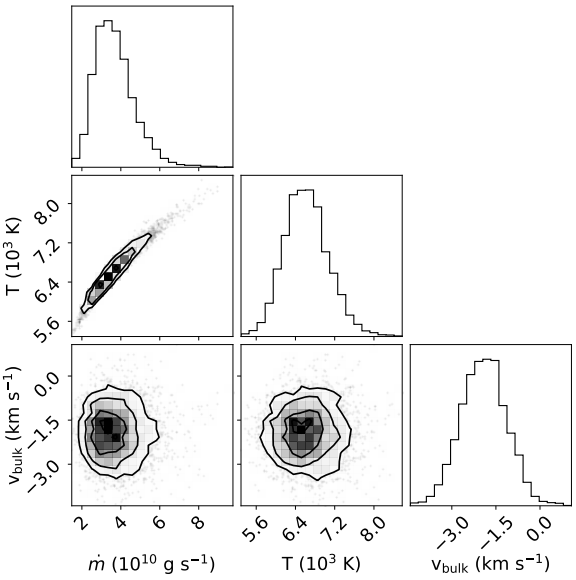

Fig. 6. Posterior distributions of mass loss rate, upper atmospheric temperature, and line-of-sight bulk velocity of HAT-P-11 b using `p-winds` models (no limb darkening included) as a retrieval tool against a CARMENES transmission spectrum.

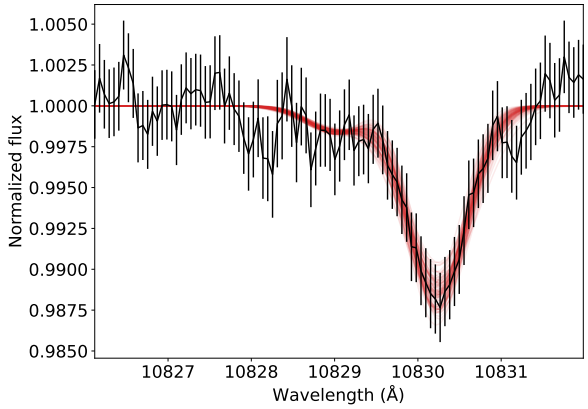

Fig. 7. Transmission spectrum of HAT-P-11 b measured with CARMENES (black) and a sample of 100 `p-winds` models fit to the data (red).

upper atmosphere temperature T is highly anti-correlated with the H/He fraction. This degeneracy increases the uncertainties of T by a factor of at least two. We show the resulting distribution of He in the upper atmosphere of HAT-P-11 b in Fig. 8 based on the best-fit model to the CARMENES data. Finally, we show that the retrieved escape parameters of models 1-3 (average-velocity approximation for the wind broadening) are fully consistent with that of model 4 (formal radiative transfer calculation). Hence, we demonstrate that this approximation, which saves an order of magnitude in computation time, does not significantly affect the retrieved escape parameters.

In order to compare our results with those obtained by the 3-d model EVE (Bourrier & Lecavelier des Etangs 2013) used by Allart et al. (2018), we need to calculate the escape of metastable He only instead of total mass loss. For a total escape rate of 3.6×10^{10} g s^{-1} and an upper atmosphere temperature of 6600 K obtained from the retrieval described above, we calculate an av-

Table 2. Upper atmosphere properties retrieved for HAT-P-11 b from the CARMENES transmission spectrum.

Model	$\dot{m}$ ($\times 10^{10}$ g s^{-1})	T ($\times 10^3$ K)	$v_{\rm bulk}$ (km s^{-1})	H/He
1	$3.6^{+1.1}_{-0.8}$	$6.6^{+0.5}_{-0.4}$	-1.9 ± 0.8	0.90 (fixed)
2	$3.6^{+1.1}_{-0.8}$	$6.6^{+0.5}_{-0.4}$	-1.9 ± 0.8	0.90 (fixed)
3	$4.1^{+3.8}_{-1.3}$	$6.4^{+1.1}_{-1.0}$	-1.9 ± 0.8	> 0.80 (3σ)
4	3.4	6.5	-1.9	0.90 (fixed)

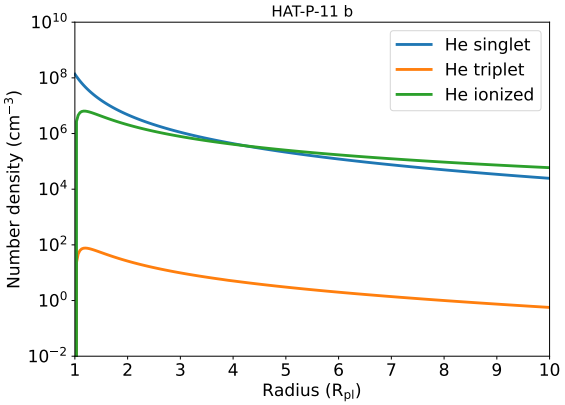

Fig. 8. Distribution of He in the upper atmosphere of HAT-P-11 b based on the best-fit solution obtained by fitting `p-winds` models (no limb darkening included) to the CARMENES transmission spectrum.

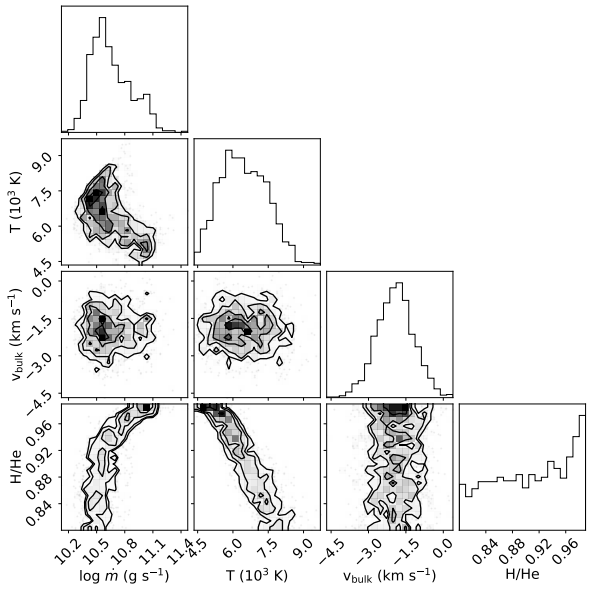

Fig. 9. Same as Fig. 6, but including H/He fraction as a free parameter to be fit.

erage metastable helium fraction of 5.0×10^{-6} and a T/μ fraction of 9000 K amu^{-1}. This result translates into a metastable-He escape rate of 1.8×10^5 g s^{-1}, which is compatible with the upper-limit rate of $\sim 3 \times 10^5$ g s^{-1} determined by Allart et al. (2018). Our retrieved T/μ fraction when assuming H/He of 0.9 is discrepant with the results of Allart et al. (2018), who found $T/\mu = 24\,000$ K amu^{-1}. Some of the solutions of our retrieval with H/He as a free parameter do allow for high values of T/μ up to 12 000, but they are nevertheless incompatible with Allart et al. (2018); the authors, however, do propose that a high T/μ may correspond to a low mean atomic weight, which can be obtained with a large fraction of ionized gas and free electrons. In an upcoming manuscript, Vissapragada et al. (in prep.) will discuss how solutions with high temperatures can be ruled out because they are not energetically self-consistent, assuming that the heating comes solely from the available high-energy irradiation budget.

The bulk velocity of -1.9 ± 0.8 km s^{-1} is consistent with the net blueshift of 3 km s^{-1} reported by Allart et al. (2018), which was previously interpreted as a high-altitude wind flowing from the day- to the night-side of the planet. This net blueshift is not predicted by the one-dimensional Parker wind model, which is the reason for fitting it as a free parameter in our models. More complex, tridimensional models that take into account other physical processes may be necessary to determine the exact mechanism that causes this bulk velocity shift in the metastable He absorption signature.

3.2. Fitting upper limits for a non-detection in GJ 436 b

GJ 436 b is a high-profile case of atmospheric escape because it possesses the deepest transmission spectrum feature detected to date: a repeatable 50% in-transit absorption in Lyman-α (Kulow et al. 2014; Ehrenreich et al. 2015; Lavie et al. 2017; Dos Santos et al. 2019) which is explained by a large volume of exospheric neutral H fed by escape (Bourrier et al. 2016; Villarreal D'Angelo et al. 2021). In fact, Oklopčić & Hirata (2018) predicted a metastable He signature as deep as 9% in the core of the strongest line of the triplet. However, when GJ 436 b was observed by CARMENES, the results yielded only a non-detection (Nortmann et al. 2018).

In this Sect. we attempt to fit an upper limit of atmospheric escape rate to the non-detection of He in GJ 436 b and compare it to the result derived from Lyman-α transmission spectroscopy and modeling. The metastable He transmission spectrum of GJ 436 b is rather unfortunately not publicly available, but the pipeline-reduced spectral time series from Nortmann et al. (2018) is available in the CARMENES data archive[8].

We ran an MCMC of 10 000 steps and 10 walkers with three free parameters: total escape rate, upper atmospheric temperature, and the H/He fraction. We increased the number of steps compared to the HAT-P-11 b retrieval in order to better explore the parameter space, since we are expecting to obtain only upper/lower limits. We did not include limb darkening. Based on previous theoretical predictions for GJ 436 b (e.g., Salz et al. 2016), we set uniform priors of $[10^7, 10^{12}]$ g s^{-1} for the mass loss and [1 000, 10 000] K for the temperature, and [0.40, 0.99] for the H/He fraction. We used the high-energy spectrum of GJ 436 measured in the MUSCLES Treasury Survey as a source of irradiation.

[8] `http://carmenes.cab.inta-csic.es/gto/jsp/nortmanneta l2018.jsp`

The resulting posterior distributions of the free parameters for GJ 436 b yield, at 99.7% (3σ) confidence, an upper limit of 8.9×10^9 g s^{-1} for the escape rate and a lower limit of 2100 K for the upper atmospheric temperature (given the uniform priors above). In broad terms, mass loss rates above this value or temperatures below the lower limit would yield a detectable metastable He signature. This result is fully consistent with the escape rate of $\sim 2.5\times10^8$ g s^{-1} inferred by Bourrier et al. (2016), and with the mass loss rate of $(6-10)\times10^9$ g s^{-1} inferred by Villarreal D'Angelo et al. (2021), both based on the same Lyman-α transmission spectroscopy dataset.

Given the flat prior of [0.40, 0.99] for the He abundance, the resulting posterior distribution of the H/He fraction is not constraining, however it seems to favor higher values and peaks near 0.99 (see Fig. B.3). Interestingly, this result is in slight disagreement with the prediction of a He-rich atmosphere for GJ 436 b (Hu et al. 2015), which states that such an enrichment is the outcome of a history of atmospheric escape. We cannot, however, draw strong conclusions on this matter because GJ 436 b had a non-detection of He. More detailed descriptions that fit both H and He simultaneously in the upper atmosphere of this planet are likely going to yield more definitive answers. For example, Lampón et al. (2021) used H densities derived from Lyman-α observations to inform metastable He models, and determined that the warm Neptune GJ 3470 b has H/He = $0.985^{+0.010}_{-0.015}$.

4. Conclusions

We demonstrate in this manuscript the usage of the open-source Python code `p-winds` to forward model the distribution of He atoms in the upper atmospheres of exoplanets, and their corresponding metastable He transmission spectra of exoplanets. The code also enables the retrieval of atmospheric escape rates and temperatures based on observations at high-resolution when coupled to an optimization algorithm, such as a maximum likelihood estimation or a Markov-Chain Monte Carlo sampler. A typical retrieval takes several hours to compute, depending on the setup. Example Python algorithms to perform such calculations are freely available online.

As an implementation of the method originally described by Oklopčić & Hirata (2018), the forward models produced by `p-winds` are fully compatible with that study. We also implement changes proposed by Lampón et al. (2020), such as the inclusion of charge exchange of He and H particles. Our implementation includes further improvements, such as the addition of transit geometry and limb darkening of the host star, as well as allowing the H/He fraction to vary in the retrieval.

We used `p-winds` to fit the escape rate, wind temperature, and the H/He fraction of the warm Naptune HAT-P-11 b based on CARMENES transmission spectroscopy previously reported in Allart et al. (2018). For a model without limb darkening and with H/He fixed at 0.90, we find that the escape rate of HAT-P-11 b is $(3.6^{+1.1}_{-0.8})\times10^{10}$ g s^{-1} and the planetary wind temperature is 6600^{+500}_{-400} K. Including limb darkening does not have a significant impact in the retrieved parameters of HAT-P-11 b. Allowing the H/He fraction to vary has a stronger impact, because it yields an anti-correlation with the retrieved wind temperature. It also increased the uncertainty of the retrieved atmospheric escape rate, but the most likely value does not change. We find that the H/He fraction is unconstrained, but with a preference for higher values. Finally, we also attempt to fit limits for the escape rate, wind temperature, and H/He fraction of GJ 436 b based on a non-detection with the CARMENES spectrograph reported by Nortmann et al. (2018). We find an upper limit of 8.9×10^9 g s^{-1} for the first and a lower limit of 2100 K for the second at 99.7% confidence. Our retrievals show a preference for high values of H/He, with the posterior distribution peaking near 0.99. These results are fully compatible with the escape rate of $\sim 2.5 \times 10^8$ g s^{-1} inferred by Bourrier et al. (2016) based on Lyman-α transmission spectroscopy.

The main limitations of a one-dimensional, isothermal Parker wind model are: 1) It does not capture the three-dimensional nature of very extended atmospheres, particularly when they have both a thermospheric and an exospheric contributions (see the case of WASP-107 b in Allart et al. 2019); 2) It does not take into account the variable profile of temperature with radial distance from the planet, which is seen in self-consistent models of escape (e.g., Salz et al. 2016; Allan & Vidotto 2019); and 3) it does not self-consistently consider the sources of heating and cooling that control the atmospheric escape process. The usefulness of simple models such as `p-winds` lies in an efficient exploration of the parameter space that defines atmospheric escape (scalability) and ease of use (open-source, fully-documented code) when more sophisticated models are not yet warranted.

As for the next steps, we aim to improve `p-winds` by including the escape of heavier atomic species, such as C, N, O, Mg, Si, and Fe. This will allow us to use the code to predict and interpret observations of metals escaping hot gas giants, such as the signatures reported by Vidal-Madjar et al. (2013) and Sing et al. (2019). We shall also add day-to-nightside winds to the atmospheric modeling, similar to Seidel et al. (2020). Another avenue to explore `p-winds` in the future consists in coupling it with more complex tridimensional hydrodynamic escape models.

Acknowledgements. LADS acknowledges the helpful input of A. Wyttenbach, M. Stalport, A. Oklopčić, J. Stürmer, and M. Zechmeister to the development of this project. SV is supported by an NSF Graduate Research Fellowship and the Paul & Daisy Soros Fellowship for New Americans. RA is a Trottier Postdoctoral Fellow and acknowledges support from the Trottier Family Foundation, and his contribution was supported in part through a grant from *Fonds de recherche du Québec – Nature et technologies*. This research was enabled by the financial support from the European Research Council (ERC) under the European Union's Horizon 2020 research and innovation programme (projects: Four Aces grant agreement No 724427; Spice Dune grant agreement No 947634; ASTROFLOW grant agreement No 817540), and it has been carried out in the frame of the National Centre for Competence in Research PlanetS supported by the Swiss National Science Foundation (SNSF). The `p-winds` code makes use of the open source software NumPy (Harris et al. 2020), SciPy (Virtanen et al. 2020), Pillow (`https://python-pillow.org`), and Astropy (Astropy Collaboration et al. 2018). The results of this manuscript were also made possible by the open source software Matplotlib (Hunter 2007), OpenMPI (`https://www.open-mpi.org`), Jupyter (Kluyver et al. 2016), MPI for Python (`mpi4py`; Dalcin et al. 2011), `emcee` (Foreman-Mackey et al. 2013), and `schwimmbad` (Price-Whelan & Foreman-Mackey 2017). Finally, the authors also extend a special thanks to the platforms GitHub, Conda-Forge, Read the Docs, and Travis.ci for the valuable support of open-source initiatives.

References

Allan, A. & Vidotto, A. A. 2019, MNRAS, 490, 3760
Allart, R., Bourrier, V., Lovis, C., et al. 2019, A&A, 623, A58
Allart, R., Bourrier, V., Lovis, C., et al. 2018, Science, 362, 1384
Alonso-Floriano, F. J., Snellen, I. A. G., Czesla, S., et al. 2019, A&A, 629, A110
Astropy Collaboration, Price-Whelan, A. M., Sipőcz, B. M., et al. 2018, AJ, 156, 123
Bean, J. L., Raymond, S. N., & Owen, J. E. 2021, Journal of Geophysical Research (Planets), 126, e06639
Beaugé, C. & Nesvorný, D. 2013, ApJ, 763, 12
Bourrier, V., dos Santos, L. A., Sanz-Forcada, J., et al. 2021, arXiv e-prints, arXiv:2103.09864
Bourrier, V., Ehrenreich, D., Wheatley, P. J., et al. 2017, A&A, 599, L3

Bourrier, V. & Lecavelier des Etangs, A. 2013, A&A, 557, A124
Bourrier, V., Lecavelier des Etangs, A., Ehrenreich, D., et al. 2018, A&A, 620, A147
Bourrier, V., Lecavelier des Etangs, A., Ehrenreich, D., Tanaka, Y. A., & Vidotto, A. A. 2016, A&A, 591, A121
Carolan, S., Vidotto, A. A., Plavchan, P., Villarreal D'Angelo, C., & Hazra, G. 2020, MNRAS, 498, L53
Chaffin, M. S., Chaufray, J. Y., Deighan, J., et al. 2015, Geophys. Res. Lett., 42, 9001
Chamberlain, J. W. 1963, Planet. Space Sci., 11, 901
Claret, A. 2000, A&A, 363, 1081
Claret, A. & Hauschildt, P. H. 2003, A&A, 412, 241
Cubillos, P., Erkaev, N. V., Juvan, I., et al. 2017, MNRAS, 466, 1868
Dalcin, L. D., Paz, R. R., Kler, P. A., & Cosimo, A. 2011, Advances in Water Resources, 34, 1124, new Computational Methods and Software Tools
Diaz-Cordoves, J. & Gimenez, A. 1992, A&A, 259, 227
Dos Santos, L. A., Bourrier, V., Ehrenreich, D., et al. 2021, arXiv e-prints, arXiv:2103.15688
Dos Santos, L. A., Ehrenreich, D., Bourrier, V., et al. 2020a, A&A, 640, A29
Dos Santos, L. A., Ehrenreich, D., Bourrier, V., et al. 2020b, A&A, 634, L4
Dos Santos, L. A., Ehrenreich, D., Bourrier, V., et al. 2019, A&A, 629, A47
Ehrenreich, D., Bourrier, V., Wheatley, P. J., et al. 2015, Nature, 522, 459
Foreman-Mackey, D., Hogg, D. W., Lang, D., & Goodman, J. 2013, PASP, 125, 306
Fossati, L., Haswell, C. A., Froning, C. S., et al. 2010, ApJ, 714, L222
France, K., Loyd, R. O. P., Youngblood, A., et al. 2016, ApJ, 820, 89
Fulton, B. J. & Petigura, E. A. 2018, AJ, 156, 264
Fulton, B. J., Petigura, E. A., Howard, A. W., et al. 2017, AJ, 154, 109
Gaidos, E., Hirano, T., Wilson, D. J., et al. 2020, MNRAS, 498, L119
García Muñoz, A., Fossati, L., Youngblood, A., et al. 2021, ApJ, 907, L36
Hardegree-Ullman, K. K., Zink, J. K., Christiansen, J. L., et al. 2020, ApJS, 247, 28
Harris, C. R., Millman, K. J., van der Walt, S. J., et al. 2020, Nature, 585, 357
Hu, R., Seager, S., & Yung, Y. L. 2015, ApJ, 807, 8
Hunter, J. D. 2007, Computing in Science & Engineering, 9, 90
Indriolo, N., Hobbs, L. M., Hinkle, K. H., & McCall, B. J. 2009, ApJ, 703, 2131
Jensen, A. G., Redfield, S., Endl, M., et al. 2012, ApJ, 751, 86
Kameda, S., Ikezawa, S., Sato, M., et al. 2017, Geophys. Res. Lett., 44, 11,706
Kasper, D., Bean, J. L., Oklopčić, A., et al. 2020, AJ, 160, 258
King, G. W., Wheatley, P. J., Bourrier, V., & Ehrenreich, D. 2019, MNRAS, 484, L49
Kirk, J., Alam, M. K., López-Morales, M., & Zeng, L. 2020, AJ, 159, 115
Klinglesmith, D. A. & Sobieski, S. 1970, AJ, 75, 175
Kluyver, T., Ragan-Kelley, B., Pérez, F., et al. 2016, in Positioning and Power in Academic Publishing: Players, Agents and Agendas, ed. F. Loizides & B. Scmidt (Netherlands: IOS Press), 87–90
Knutson, H. A., Charbonneau, D., Noyes, R. W., Brown, T. M., & Gilliland, R. L. 2007, ApJ, 655, 564
Kopal, Z. 1950, Harvard College Observatory Circular, 454, 1
Koskinen, T. T., Yelle, R. V., Lavvas, P., & Lewis, N. K. 2010, ApJ, 723, 116
Kreidberg, L. 2015, PASP, 127, 1161
Kulow, J. R., France, K., Linsky, J., & Loyd, R. O. P. 2014, ApJ, 786, 132
Lamers, H. J. G. L. M. & Cassinelli, J. P. 1999, Introduction to Stellar Winds
Lampón, M., López-Puertas, M., Lara, L. M., et al. 2020, A&A, 636, A13
Lampón, M., López-Puertas, M., Sanz-Forcada, J., et al. 2021, A&A, 647, A129
Lavie, B., Ehrenreich, D., Bourrier, V., et al. 2017, A&A, 605, L7
Lecavelier Des Etangs, A. 2007, A&A, 461, 1185
Lecavelier des Etangs, A., Ehrenreich, D., Vidal-Madjar, A., et al. 2010, A&A, 514, A72
Loyd, R. O. P., France, K., Youngblood, A., et al. 2016, ApJ, 824, 102
Mazeh, T., Holczer, T., & Faigler, S. 2016, A&A, 589, A75
Morton, D. C. 2000, ApJS, 130, 403
Nortmann, L., Pallé, E., Salz, M., et al. 2018, Science, 362, 1388
Oklopčić, A. 2019, ApJ, 881, 133
Oklopčić, A. & Hirata, C. M. 2018, ApJ, 855, L11
Osterbrock, D. E. & Ferland, G. J. 2006, Astrophysics of gaseous nebulae and active galactic nuclei
Owen, J. E. & Wu, Y. 2013, ApJ, 775, 105
Paragas, K., Vissapragada, S., Knutson, H. A., et al. 2021, ApJ, 909, L10
Parker, E. N. 1958, ApJ, 128, 664
Price-Whelan, A. M. & Foreman-Mackey, D. 2017, The Journal of Open Source Software, 2
Salz, M., Czesla, S., Schneider, P. C., & Schmitt, J. H. M. M. 2016, A&A, 586, A75
Seager, S. & Sasselov, D. D. 2000, ApJ, 537, 916
Seidel, J. V., Ehrenreich, D., Pino, L., et al. 2020, A&A, 633, A86
Sing, D. K. 2010, A&A, 510, A21
Sing, D. K., Désert, J. M., Lecavelier Des Etangs, A., et al. 2009, A&A, 505, 891
Sing, D. K., Lavvas, P., Ballester, G. E., et al. 2019, AJ, 158, 91
Spake, J. J., Sing, D. K., Evans, T. M., et al. 2018, Nature, 557, 68
Tripathi, A., Kratter, K. M., Murray-Clay, R. A., & Krumholz, M. R. 2015, ApJ, 808, 173
Vidal-Madjar, A., Huitson, C. M., Bourrier, V., et al. 2013, A&A, 560, A54
Vidal-Madjar, A., Lecavelier des Etangs, A., Désert, J.-M., et al. 2003, Nature, 422, 143
Villarreal D'Angelo, C., Vidotto, A. A., Esquivel, A., Hazra, G., & Youngblood, A. 2021, MNRAS, 501, 4383
Virtanen, P., Gommers, R., Oliphant, T. E., et al. 2020, Nature Methods, 17, 261
Vissapragada, S., Knutson, H. A., Jovanovic, N., et al. 2020, AJ, 159, 278
Waalkes, W. C., Berta-Thompson, Z., Bourrier, V., et al. 2019, AJ, 158, 50
Wang, L. & Dai, F. 2021a, ApJ, 914, 98
Wang, L. & Dai, F. 2021b, ApJ, 914, 99
Wyttenbach, A., Ehrenreich, D., Lovis, C., Udry, S., & Pepe, F. 2015, A&A, 577, A62
Wyttenbach, A., Mollière, P., Ehrenreich, D., et al. 2020, A&A, 638, A87
Youngblood, A., France, K., Loyd, R. O. P., et al. 2016, ApJ, 824, 101

Appendix A: The `flatstar` code

The code implemented in `flatstar` was originally written as a part of the `transit` module of `p-winds`. However, we decided to transform it into a separate package because this implementation can be useful for other astrophysical applications not necessarily related to transmission spectroscopy.

The typical usage of `flatstar` involves setting a grid shape (N_x, N_y) and stellar radius R_s in number of pixels, and optionally setting a limb-darkening (LD) law. The LD laws currently implemented in the code are: linear, quadratic (Kopal 1950), square-root (Diaz-Cordoves & Gimenez 1992), logarithmic (Klinglesmith & Sobieski 1970), exponential (Claret & Hauschildt 2003), the three-parameter law of Sing et al. (2009), and the four-parameter law of Claret (2000). Finally, the user can also set a custom LD law. The star is always centered to the grid.

In addition, `flatstar` can add a planetary transit with user-defined planet-to-star ratio R_p/R_s, transit impact parameter b, and phase ϕ. The first and fourth contact of the transit are defined as the phases -0.5 and $+0.5$, respectively, independent of b. The y-coordinate of the planetary center (y_p) in pixel space is calculated as:

$$y_p = (b \times R_s) + N_y/2. \tag{A.1}$$

The x-coordinate of the planetary center (x_p) is not as straightforward to calculate, since we define it based on ϕ and b. Let θ be the angle between the y-axis and the vector that connects the center of the star and the planet at first contact:

$$\cos\theta = \frac{b \times R_s}{R_p + R_s}. \tag{A.2}$$

The distance β from the planet center to the y-axis at first contact is given by:

$$\beta = \left(R_p + R_s\right)\sin\theta = \left(R_p + R_s\right)\sqrt{1 - \left(b \times \frac{R_s}{R_p + R_s}\right)^2}. \tag{A.3}$$

Thus, the distance x_0 of the planet center from the border of the simulation at first contact is:

$$x_0 = N_x/2 - \beta. \tag{A.4}$$

As the planet moves from the first contact to fourth contact, it covers a distance of 2β. For arbitrary phases between $\phi = -0.5$ (first contact) and $\phi = +0.5$ (fourth contact), the distance x_p of the planet from the border of the simulation is thus:

$$x_p = x_0 + 2\beta \times (\phi + 0.5). \tag{A.5}$$

This formulation assumes that the arc that the planet follows during the transit can be approximated to a chord.

The grid can be supersampled in order to avoid "hard" pixel edges when the grid size is coarse. This is useful to save computation time in cases where we need to mass produce grids while conserving the precision of intensities (which is the case of atmospheric retrievals with `p-winds`). By default, the resampling algorithm is the 'box' method, which takes the value of each pixel with fixed weights to compute the average flux of the resampled pixel. We do not recommend using `flatstar` to fit wide band photometric light curves, since the computation time is much longer than other codes that implement analytical equations to calculate light curves, such as `batman` (Kreidberg 2015).

We show an example of a transit grid simulated with `flatstar` in Fig. A.1.

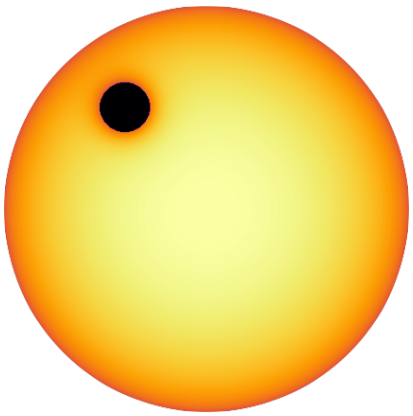

Fig. A.1. `flatstar` simulation of a transit of HD 209458 b with sizes, limb-darkening, and metastable He absorption to scale. The limb-darkening law and coefficients were taken based on the 922-1019 nm wavelength band from Knutson et al. (2007).

Appendix B: Other posterior distributions for the fits to HAT-P-11 b and GJ 436 b data

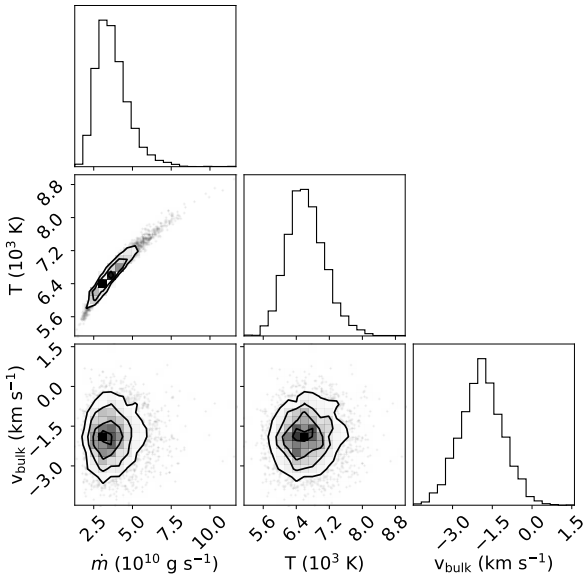

Fig. B.1. Posterior distribution of parameters of HAT-P-11 b fit to the CARMENES transmission spectrum using a model with a quadratic limb-darkening law and coefficients $c_1 = 0.63$ and $c_2 = 0.09$.

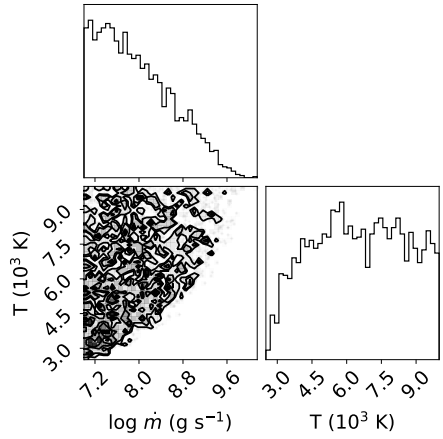

Fig. B.2. Same as Fig. B.1, but for GJ 436 b with H/He fraction fixed to 0.90.

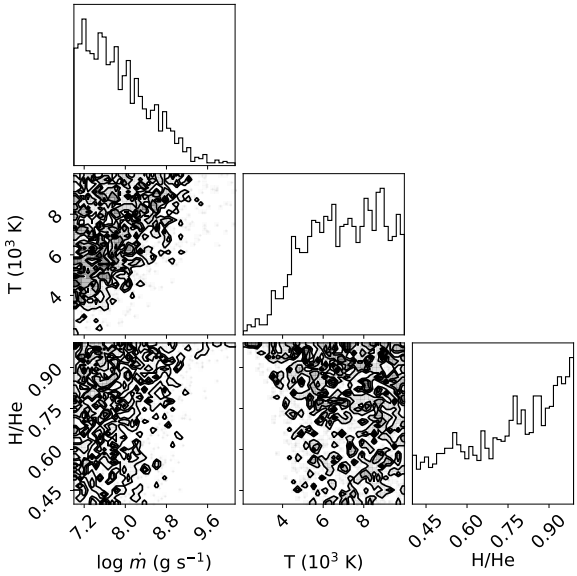

Fig. B.3. Same as Fig. B.2, but with H/He fraction as a free parameter.

Appendix B

Publications as co-author

B.1 Exoplanets, brown dwarfs and their atmospheres

During my doctorate I was involved with the CORALIE survey of exoplanets, the development of the MAROON-X spectrograph, and the *HST* PanCET program. In the following pages I list all the publications about exoplanets, brown dwarfs, and their atmospheres, in which I was a co-author. They encompass new discoveries, atmospheric characterization, and instrumentation. The articles published on A&A are reproduced partially with permission © ESO.

Monthly Notices
of the
ROYAL ASTRONOMICAL SOCIETY

MNRAS **482,** 1690–1700 (2019)
Advance Access publication 2018 October 17

doi:10.1093/mnras/sty2791

Thorium in solar twins: implications for habitability in rocky planets

R. B. Botelho,[1★] A. de C. Milone,[1★] J. Meléndez,[2] M. Bedell,[3] L. Spina,[4] M. Asplund,[5] L. dos Santos,[6] J. L. Bean,[7] I. Ramírez,[8] D. Yong,[5] S. Dreizler,[9] A. Alves-Brito[10] and J. Yana Galarza[2]

[1]*Divisão de Astrofísica, Instituto Nacional de Pesquisas Espaciais, Av. dos Astronautas 1758 São José dos Campos, 12227-010, Brazil*
[2]*Departamento de Astronomia, IAG, Universidade de São Paulo, Rua do Matão 1226 São Paulo, 05509-900, Brazil*
[3]*Center for Computational Astrophysics, Flatiron Institute, 162 5th Ave, New York, NY 10010, USA*
[4]*Monash Centre for Astrophysics, School of Physics and Astronomy, Monash University, VIC 3800, Australia*
[5]*Research School of Astronomy and Astrophysics, The Australian National University, Cotter Road, Canberra, ACT 2611, Australia*
[6]*Observatoire de l'Université de Genéve, 51 chemin des Maillettes, CH-1290 Versoix, Switzerland*
[7]*Department of Astronomy & Astrophysics, 5640 S. Ellis Ave, Chicago, IL 60637, USA*
[8]*Tacoma Community College, 6501 South 19th Street, Tacoma, WA 98466-7400, USA*
[9]*Institut für Astrophysik, Georg-August Universität Göttingen, Wilhelmsplatz 1, D-37073, Göttingen, Germany*
[10]*Universidade Federal do Rio Grande do Sul, Instituto de Física, Av. Bento Gonçalves 9500, Porto Alegre, RS, Brazil*

Accepted 2018 October 8. Received 2018 October 3; in original form 2018 August 16

ABSTRACT

We have investigated the thorium (Th) abundance in a sample of 53 thin disc solar twins covering a wide range of ages. These data provide constrains on the mantle energy budget of terrestrial planets that can be formed over the evolution of the Galaxy's thin disc. We have estimated Th abundances with an average precision of 0.025 dex (in both [Th/H] and [Th/Fe]) through comprehensive spectral synthesis of a Th II line present at 4019.1290 Å, using very high resolution ($R = 115\,000$) high quality HARPS spectra obtained at the ESO La Silla Observatory. We have confirmed that there is a large energy budget from Th decay for maintaining mantle convection inside potential rocky planets around solar twins, from the Galactic thin disc formation until now, because the pristine $[Th/H]_{ZAMS}$ is super-solar on average under a uniform dispersion of 0.056 dex (varying from +0.037 up to +0.138 dex based on linear fits against isochrone stellar age). Comparing to neodymium (Nd) and europium (Eu), two others neutron-capture elements, the stellar pristine abundance of Th follows Eu along the Galactic thin disc evolution, but it does not follow Nd, probably because neodymium has a significant contribution from the *s*-process (about 60 per cent).

Key words: stars: abundances – stars: fundamental parameters – stars: solar-type – Galaxy: disc – solar neighbourhood; planets and satellites: terrestrial planets.

1 INTRODUCTION

The structure of a terrestrial planet is driven by the formation process itself based on the collision and accretion of planetesimals with differential mineralogical settling and also by the internal heat budget. As the prototype geologically dynamic planet, Earth has a partially crystallized metallic dynamo core, and a silicate liquid mantle, whose convection maintains plate tectonics of a rocky crust. The major internal heat sources of Earth come from the secular cooling of core and mantle, and the radioactive decay of Th, U and K isotopes in the mantle (Huang et al. 2013). The mantle thickness and convection inside telluric planets are directly linked to the abundances of these isotopes in the mantle (basically ^{232}Th, ^{235}U and ^{238}U) (McDonough 2003). The volcanic activity generated by the plate tectonics recycles gases such as carbon dioxide between the atmosphere and the mantle, contributing to habitability by keeping the planet surface at moderate temperatures (Walker, Hays & Kasting 1981). A geologically active planet could even play a role for the origin of life and its long-term maintenance (e.g. Misra et al. 2015, and references therein).

Unterborn, Johnson & Panero (2015) were the first to speculate about the potential energy budget of terrestrial planets directly connected to the stellar photospheric abundance of thorium (Th). They measured $\log \varepsilon(\mathrm{Th})$[1] varying from 59 up to 251 per cent of the solar value in a sample of 13 solar twins and analogues,

★ E-mail: rafael.botelho@inpe.br (RBB); andre.milone@inpe.br (ADCM)

[1]$\mathrm{Log}\,\varepsilon(\mathrm{X}) = \log(n(\mathrm{X})/n(\mathrm{H})) + 12$, where n is number density.

A&A 625, A71 (2019)
https://doi.org/10.1051/0004-6361/201935356

Astronomy & Astrophysics

The CORALIE survey for southern extrasolar planets

XVIII. Three new massive planets and two low-mass brown dwarfs at greater than 5 AU separation★,★★

E. L. Rickman[1], D. Ségransan[1], M. Marmier[1], S. Udry[1], F. Bouchy[1], C. Lovis[1], M. Mayor[1], F. Pepe[1], D. Queloz[1], N. C. Santos[2,3], R. Allart[1], V. Bonvin[4], P. Bratschi[1], F. Cersullo[1], B. Chazelas[1], A. Choplin[1], U. Conod[1], A. Deline[1], J.-B. Delisle[1], L. A. Dos Santos[1], P. Figueira[5,2], H. A. C. Giles[1], M. Girard[1], B. Lavie[1], D. Martin[1,★★★,6], F. Motalebi[1], L. D. Nielsen[1], H. Osborn[7,8], G. Ottoni[1], M. Raimbault[1], J. Rey[1,9], T. Roger[1,10], J. V. Seidel[1], M. Stalport[1], A. Suárez Mascareño[1,11], A. Triaud[12], O. Turner[1], L. Weber[1], and A. Wyttenbach[1,13]

(Affiliations can be found after the references)

Received 25 February 2019 / Accepted 2 April 2019

ABSTRACT

Context. Since 1998, a planet-search around main sequence stars within 50 pc in the southern hemisphere has been underway with the CORALIE spectrograph at La Silla Observatory.
Aims. With an observing time span of more than 20 yr, the CORALIE survey is able to detect long-term trends in data with masses and separations large enough to select ideal targets for direct imaging. Detecting these giant companion candidates will allow us to start bridging the gap between radial-velocity-detected exoplanets and directly imaged planets and brown dwarfs.
Methods. Long-term precise Doppler measurements with the CORALIE spectrograph reveal radial-velocity signatures of massive planetary companions and brown dwarfs on long-period orbits.
Results. In this paper, we report the discovery of new companions orbiting HD 181234, HD 13724, HD 25015, HD 92987 and HD 50499. We also report updated orbital parameters for HD 50499b, HD 92788b and HD 98649b. In addition, we confirm the recent detection of HD 92788c. The newly reported companions span a period range of 15.6–40.4 yr and a mass domain of 2.93–26.77 $M_{\rm Jup}$, the latter of which straddles the nominal boundary between planets and brown dwarfs.
Conclusions. We report the detection of five new companions and updated parameters of four known extrasolar planets. We identify at least some of these companions to be promising candidates for imaging and further characterisation.

Key words. techniques: radial velocities – planets and satellites: detection – binaries: visual – planetary systems

1. Introduction

Little is known about massive giant planets and brown dwarfs at orbital separations between 5 and 50 AU due to their low occurrence rate (Bowler 2016) and to the lower sensitivity of the different observing methods in this separation range. Indeed, radial velocity (RV) and transit techniques are extremely efficient at detecting planets around older stars at short separations (Fischer et al. 2014). On the other hand, direct imaging is most efficient at detecting younger planets at separations larger than several times the diffraction limit of the telescope (typically 5–10 λ/D). This translates into several tens of astronomical units for the closest young stellar associations (e.g. β Pic and 51 Eri as part of the β Pic moving group (Zuckerman et al. 2001; Feigelson et al. 2006) and HR 8799 as part of the Columba association (Zuckerman et al. 2011). Nevertheless, the population of massive giant exoplanets at intermediate orbital separations between 5 and 50 AU is an important puzzle piece needed for constraining the uncertainties that exist in planet formation and evolution models.

The historical CORALIE planet-search survey has been ongoing for more than 20 yr in the southern hemisphere and monitors a volume-limited sample of 1647 main sequence (MS) stars from F8 down to K0 located within 50 pc of the Sun (Udry et al. 2000). With an individual measurement precision ranging between 3.5 and 6 ms^{-1}, CORALIE has permitted (or has contributed to) the detection of more than 140 extra-solar planet candidates (Pepe et al. 2002; Udry et al. 2002; Tamuz et al. 2008; Ségransan et al. 2010; Marmier et al. 2013). Such a long and continuous monitoring of nearby MS stars is unique among all planet search surveys; it allows us to detect massive giant planets at separations larger 5 AU as well as to identify small RV drifts

★ The radial velocity measurements and additional data products discussed in this paper are available on the DACE web platform at https://dace.unige.ch/radialVelocities. See the appendix for a direct link to the individual target data products. A copy of the data is also available at the CDS via anonymous ftp to cdsarc.u-strasbg.fr (130.79.128.5) or via http://cdsarc.u-strasbg.fr/viz-bin/qcat?J/A+A/625/A71

★★ Based on observations collected with the CORALIE spectrograph mounted on the 1.2 m Swiss telescope at La Silla Observatory and with the HARPS spectrograph on the ESO 3.6 m telescope at La Silla (ESO, Chile).

★★★ Fellow of the Swiss National Science Foundation.

Monthly Notices of the ROYAL ASTRONOMICAL SOCIETY

MNRAS **492,** 5399–5412 (2020) doi:10.1093/mnras/staa197
Advance Access publication 2020 January 23

Mass determinations of the three mini-Neptunes transiting TOI-125

L. D. Nielsen [1]★ D. Gandolfi,[2] D. J. Armstrong [3,4] J. S. Jenkins [5] M. Fridlund,[6,7] N. C. Santos,[8,9] F. Dai,[10] V. Adibekyan,[8] R. Luque [11,12] J. H. Steffen,[13] M. Esposito,[14] F. Meru [3,4] S. Sabotta [14] E. Bolmont [1] D. Kossakowski,[15] J. F. Otegi,[1,16] F. Murgas,[11,12] M. Stalport,[1] F. Rodler,[17] M. R. Díaz,[5] N. T. Kurtovic,[5] G. Ricker,[18] R. Vanderspek,[18] D. W. Latham,[19] S. Seager,[18,20,21] J. N. Winn,[22] J. M. Jenkins,[23] R. Allart [1] J. M. Almenara [1] D. Barrado,[24] S. C. C. Barros,[8] D. Bayliss [3,4] Z. M. Berdiñas,[5] I. Boisse,[25] F. Bouchy,[1] P. Boyd,[26] D. J. A. Brown [3,4] E. M. Bryant,[3,4] C. Burke,[18] W. D. Cochran,[27] B. F. Cooke [3,4] O. D. S. Demangeon [8] R. F. Díaz [28,29] J. Dittman,[20] C. Dorn,[6] X. Dumusque,[1] R. A. García,[30,31] L. González-Cuesta,[11,12] S. Grziwa,[32] I. Georgieva,[7] N. Guerrero,[18] A. P. Hatzes,[14] R. Helled,[6] C. E. Henze,[23] S. Hojjatpanah,[8,9] J. Korth,[32] K. W. F. Lam,[33] J. Lillo-Box,[24] T. A. Lopez [25] J. Livingston [34] S. Mathur,[11,12] O. Mousis,[25] N. Narita,[11,35,36,37] H. P. Osborn [25,38] E. Palle,[11,12] P. A. Peña Rojas,[5] C. M. Persson,[7] S. N. Quinn,[19] H. Rauer,[33,39,40] S. Redfield [41] A. Santerne [25] L. A. dos Santos [1] J. V. Seidel [1] S. G. Sousa [8] E. B. Ting,[23] M. Turbet,[1] S. Udry,[1] A. Vanderburg,[42]† V. Van Eylen,[43] J. I. Vines,[5] P. J. Wheatley [3,4] and P. A. Wilson[3,4]

Affiliations are listed at the end of the paper

Accepted 2020 January 17. Received 2020 January 17; in original form 2019 December 3

ABSTRACT

The Transiting Exoplanet Survey Satellite, *TESS*, is currently carrying out an all-sky search for small planets transiting bright stars. In the first year of the *TESS* survey, a steady progress was made in achieving the mission's primary science goal of establishing bulk densities for 50 planets smaller than Neptune. During that year, the *TESS*'s observations were focused on the southern ecliptic hemisphere, resulting in the discovery of three mini-Neptunes orbiting the star TOI-125, a $V = 11.0$ K0 dwarf. We present intensive HARPS radial velocity observations, yielding precise mass measurements for TOI-125b, TOI-125c, and TOI-125d. TOI-125b has an orbital period of 4.65 d, a radius of 2.726 ± 0.075 R_E, a mass of 9.50 ± 0.88 M_E, and is near the 2:1 mean motion resonance with TOI-125c at 9.15 d. TOI-125c has a similar radius of 2.759 ± 0.10 R_E and a mass of 6.63 ± 0.99 M_E, being the puffiest of the three planets. TOI-125d has an orbital period of 19.98 d and a radius of 2.93 ± 0.17 R_E and mass 13.6 ± 1.2 M_E. For TOI-125b and d, we find unusual high eccentricities of 0.19 ± 0.04 and $0.17^{+0.08}_{-0.06}$, respectively. Our analysis also provides upper mass limits for the two low-SNR planet candidates in the system; for TOI-125.04 ($R_P = 1.36$ R_E, $P = 0.53$ d), we find a 2σ upper mass limit of 1.6 M_E, whereas TOI-125.05 ($R_P = 4.2^{+2.4}_{-1.4}$ R_E, $P = 13.28$ d) is unlikely a viable planet candidate with an upper mass limit of 2.7 M_E. We discuss the internal structure of the three confirmed planets, as well as dynamical stability and system architecture for this intriguing exoplanet system.

★ E-mail: Louise.Nielsen@unige.ch
† NASA Sagan Fellow.

A&A 639, A76 (2020)
https://doi.org/10.1051/0004-6361/202037941

Astronomy & Astrophysics

Three short-period Jupiters from TESS

HIP 65Ab, TOI-157b, and TOI-169b

L. D. Nielsen[1], R. Brahm[2,3], F. Bouchy[1], N. Espinoza[4], O. Turner[1], S. Rappaport[5], L. Pearce[6], G. Ricker[5], R. Vanderspek[5], D. W. Latham[7], S. Seager[6,8,9], J. N. Winn[10], J. M. Jenkins[11], J. S. Acton[12], G. Bakos[10], T. Barclay[13,14], K. Barkaoui[15,16], W. Bhatti[10], C. Briceño[17], E. M. Bryant[18,19], M. R. Burleigh[12], D. R. Ciardi[20], K. A. Collins[9], K. I. Collins[21], B. F. Cooke[18,19], Z. Csubry[10], L. A. dos Santos[1], Ph. Eigmüller[22], M. M. Fausnaugh[5], T. Gan[23], M. Gillon[15], M. R. Goad[12], N. Guerrero[5], J. Hagelberg[1], R. Hart[24], T. Henning[25], C. X. Huang[5], E. Jehin[26], J. S. Jenkins[27,28], A. Jordán[2,3], J. F. Kielkopf[29], D. Kossakowski[25], B. Lavie[1], N. Law[30], M. Lendl[1,31], J. P. de Leon[32], C. Lovis[1], A. W. Mann[30], M. Marmier[1], J. McCormac[18,19], M. Mori[32], M. Moyano[33], N. Narita[34,35,36,37,38], D. Osip[39], J. F. Otegi[1,40], F. Pepe[1], F. J. Pozuelos[25,15], L. Raynard[12], H. M. Relles[7], P. Sarkis[25], D. Ségransan[1], J. V. Seidel[1], A. Shporer[5], M. Stalport[1], C. Stockdale[41], V. Suc[2], M. Tamura[32,34,36], T. G. Tan[42], R. H. Tilbrook[12], E. B. Ting[11], T. Trifonov[25], S. Udry[1], A. Vanderburg[43], P. J. Wheatley[18,19], G. Wingham[44], Z. Zhan[8,9], and C. Ziegler[45]

(Affiliations can be found after the references)

Received 12 March 2020 / Accepted 28 May 2020

ABSTRACT

We report the confirmation and mass determination of three hot Jupiters discovered by the Transiting Exoplanet Survey Satellite (TESS) mission: HIP 65Ab (TOI-129, TIC-201248411) is an ultra-short-period Jupiter orbiting a bright ($V = 11.1$ mag) K4-dwarf every 0.98 days. It is a massive 3.213 ± 0.078 M_J planet in a grazing transit configuration with an impact parameter of $b = 1.17^{+0.10}_{-0.08}$. As a result the radius is poorly constrained, $2.03^{+0.61}_{-0.49}$ R_J. The planet's distance to its host star is less than twice the separation at which it would be destroyed by Roche lobe overflow. It is expected to spiral into HIP 65A on a timescale ranging from 80 Myr to a few gigayears, assuming a reduced tidal dissipation quality factor of $Q'_s = 10^7 - 10^9$. We performed a full phase-curve analysis of the TESS data and detected both illumination- and ellipsoidal variations as well as Doppler boosting. HIP 65A is part of a binary stellar system, with HIP 65B separated by 269 AU (3.95 arcsec on sky). TOI-157b (TIC 140691463) is a typical hot Jupiter with a mass of 1.18 ± 0.13 M_J and a radius of 1.29 ± 0.02 R_J. It has a period of 2.08 days, which corresponds to a separation of just 0.03 AU. This makes TOI-157 an interesting system, as the host star is an evolved G9 sub-giant star ($V = 12.7$). TOI-169b (TIC 183120439) is a bloated Jupiter orbiting a $V = 12.4$ G-type star. It has a mass of 0.79 ± 0.06 M_J and a radius of $1.09^{+0.08}_{-0.05}$ R_J. Despite having the longest orbital period ($P = 2.26$ days) of the three planets, TOI-169b receives the most irradiation and is situated on the edge of the Neptune desert. All three host stars are metal rich with [Fe/H] ranging from 0.18 to 0.24.

Key words. planets and satellites: detection – planets and satellites: individual: TOI-129 – planets and satellites: individual: HIP 65A – planets and satellites: individual: TOI-157

1. Introduction

Since July 2018, the Transiting Exoplanet Survey Satellite (TESS; Ricker et al. 2015) has surveyed the Southern and Northern Hemispheres for exoplanets transiting bright stars. Based on the first year of observations in the south (Sectors 1–13), a total number of 1117 TESS objects-of-interest (TOIs; Guerrero et al. 2020) have been identified. Currently, 667 of these are still considered as planet candidates and 55 have been confirmed as new TESS-planets and four as transiting brown dwarfs (including studies in preparation and published results, see e.g. Cañas et al. 2019; Jones et al. 2019; Esposito et al. 2019; Günther et al. 2019; Eisner et al. 2020; Díaz et al. 2020; Nielsen et al. 2020; Šubjak et al. 2020; Carmichael et al. 2020). We note that 146 of the TOIs from Sectors 1–13 are previously known planets.

A recent study by Zhou et al. (2019) offers a first estimate of the occurrence rate of hot Jupiters discovered by TESS by analysing a sample of bright ($T_{mag} < 10$) main sequence stars observed by TESS. They find an occurrence rate of $0.40 \pm 0.10\%$ which is in agreement with statistics based on the *Kepler* mission (Fressin et al. 2013; Santerne et al. 2016). An even rarer sub-population of hot Jupiters are the ultra-short-period (USP) Jupiters with orbital periods shorter than one day. To date, the following eight such planets are known: WASP-18b (Hellier et al. 2009), WASP-19b (Hebb et al. 2010), WASP-43b (Hellier et al. 2011), WASP-103b (Gillon et al. 2014), HATS-18b (Penev et al. 2016), KELT-16b (Oberst et al. 2017), NGTS-6b (Vines et al. 2019), and NGTS-10b (McCormac et al. 2020).

Hot Jupiters, and in particular USP Jupiters, can offer insights into planet-star interactions such as photo-evaporation and atmospheric escape (Bourrier et al. 2020; Owen & Lai 2018; Murray-Clay et al. 2009), atmospheric structure and chemistry (Parmentier et al. 2018; Kataria et al. 2015; Kreidberg et al. 2014; Murgas et al. 2014), and tidal decay (Yee et al. 2020). These planets shape the upper edge of the Neptune desert (Mazeh et al. 2016; Szabó & Kiss 2011) which constitutes a dearth of sub-Jovian planets at short periods. The proposed mechanisms

A&A 641, L7 (2020)
https://doi.org/10.1051/0004-6361/202038497

Astronomy & Astrophysics

LETTER TO THE EDITOR

Hot Exoplanet Atmospheres Resolved with Transit Spectroscopy (HEARTS)

V. Detection of sodium on the bloated super-Neptune WASP-166b*

J. V. Seidel[1], D. Ehrenreich[1], V. Bourrier[1], R. Allart[1], O. Attia[1], H. J. Hoeijmakers[1,2,3], M. Lendl[1,4], E. Linder[2], A. Wyttenbach[5], N. Astudillo-Defru[6], D. Bayliss[7], H. M. Cegla[1,7], K. Heng[2], B. Lavie[1], C. Lovis[1], C. Melo[8], F. Pepe[1], L. A. dos Santos[1], D. Ségransan[1], and S. Udry[1]

[1] Observatoire Astronomique de l'Université de Genève, Chemin des Maillettes 51, 1290 Versoix, Switzerland
e-mail: julia.seidel@unige.ch
[2] University of Bern, Center for Space and Habitability, Gesellschaftsstrasse 6, 3012 Bern, Switzerland
[3] Lund Observatory, Department of Astronomy and Theoretical Physics, Lunds Universitet, Solvegatan 9, 222 24 Lund, Sweden
[4] Space Research Institute, Austrian Academy of Sciences, Schmiedlstr. 6, 8042 Graz, Austria
[5] Université Grenoble Alpes, CNRS, IPAG, 38000 Grenoble, France
[6] Departamento de Matemática y Física Aplicadas, Universidad Católica de la Santísima Concepción, Alonso de Rivera 2850, Concepción, Chile
[7] Department of Physics, University of Warwick, Coventry, UK
[8] European Southern Observatory, Alonso de Córdova 3107, Vitacura, Región Metropolitana, Chile

Received 26 May 2020 / Accepted 3 July 2020

ABSTRACT

Planet formation processes or evolution mechanisms are surmised to be at the origin of the hot Neptune desert. Studying exoplanets currently living within or at the edge of this desert could allow disentangling the respective roles of formation and evolution. We present the High Accuracy Radial velocity Planet Searcher (HARPS) transmission spectrum of the bloated super-Neptune WASP-166b, located at the outer rim of the Neptune desert. Neutral sodium is detected at the 3.4σ level ($0.455 \pm 0.135\%$), with a tentative indication of line broadening, which could be caused by winds blowing sodium farther into space, a possible manifestation of the bloated character of these highly irradiated worlds. We put this detection into context with previous work claiming a non-detection of sodium in the same observations and show that the high noise in the trace of the discarded stellar sodium lines was responsible for the non-detection. We highlight the impact of this low signal-to-noise ratio remnant on detections for exoplanets similar to WASP-166b.

Key words. planetary systems – planets and satellites: atmospheres – planets and satellites: individual: WASP-166b – techniques: spectroscopic – instrumentation: spectrographs – methods: observational

1. Introduction

One of the most prominent features of the current landscape of exoplanets is the Neptune desert, an area in the radius-insolation diagram with a lack of strongly irradiated Neptune-sized planets (Lecavelier Des Etangs 2007; Beaugé & Nesvorný 2013; Mazeh et al. 2016). This feature is not an observational bias; these worlds are accessible via various observational methods. Starting with the first detection of an evaporating atmosphere (Vidal-Madjar et al. 2003), both theoretical (e.g. Owen & Lai 2018; Owen 2019) and observational (e.g. Ehrenreich et al. 2015; Bourrier et al. 2018) results show that atmospheric escape is a dominant process in shaping the desert. The high irradiation received by these close-in planets, both in the UV and X-ray bands, triggers a significant expansion of the upper atmosphere (Lammer et al. 2003), indicating that warm and hot Neptunes potentially erode over time (Lecavelier Des Etangs 2007; Owen & Jackson 2012). In this context, WASP-166b presents a rare opportunity to study a planet within the desert, made especially interesting by its low density ($\rho = 0.54 \pm 0.09\,\mathrm{g\,cm^3}$) suggesting a bloated atmosphere (Hellier et al. 2019; Bryant et al. 2020) (see Fig. 1).

Neptune-sized worlds remain challenging observational targets due to their size and subsequent lower signal-to-noise ratio (S/N) compared to Jupiter-sized targets. In this work, we present the observations our group obtained as part of the HEARTS survey and highlight pitfalls in analysing low S/N data, most importantly effects from the stellar sodium lines. We then present our detection of neutral sodium in the atmosphere of WASP-166b. Lastly, we comment on the previous independent analysis of the same observations and non-detection of sodium in Žák et al. (2019; hereafter Z2019).

2. Observations and data reduction

The observations consist of three spectroscopic transits of the bloated super-Neptune WASP-166b in front of WASP-166, a bright F9 star ($V_{\mathrm{mag}} = 9.36$, distance $= 113.0 \pm 1.0$ pc). The

* Based on observations made at ESO 3.6 m telescope (La Silla, Chile) under ESO programme 098.C-0305 (PI Ehrenreich).

Draft version July 14, 2020
Preprint typeset using LaTeX style emulateapj v. 12/16/11

TOI 694 b AND TIC 220568520 b: TWO LOW-MASS COMPANIONS NEAR THE HYDROGEN BURNING MASS LIMIT ORBITING SUN-LIKE STARS

Ismael Mireles[1], Avi Shporer[1], Nolan Grieves[2], George Zhou[3], Maximilian N. Günther[1,A], Rafael Brahm[4,5], Carl Ziegler[6], Keivan G. Stassun[7], Chelsea X. Huang[1], Louise Nielsen[2], Leonardo A. dos Santos[2], Stéphane Udry[2], Franois Bouchy[2], Michael Ireland[8], Alexander Wallace[8], Paula Sarkis[9], Thomas Henning[9], Andrés Jordán[4,5], Nicholas Law[10], Andrew W. Mann[10], Leonardo A. Paredes[11], Hodari-Sadiki James[11], Wei-Chun Jao[11], Todd J. Henry[12], R. Paul Butler[13], Joseph E. Rodriguez[14], Liang Yu[1], Erin Flowers[15, B], George R. Ricker[1], David W. Latham[3], Roland Vanderspek[1], Sara Seager[1, 16, 17], Joshua N. Winn[15], Jon M. Jenkins[18], Gabor Furesz[1], Katharine Hesse[19], Elisa V. Quintana[20], Mark E. Rose[18], Jeffrey C. Smith[18,21], Peter Tenenbaum[18,21], Michael Vezie[16], Daniel A. Yahalomi[3], Zhuchang Zhan[16]

Draft version July 14, 2020

ABSTRACT

We report the discovery of TOI 694 b and TIC 220568520 b, two low-mass stellar companions in eccentric orbits around metal-rich Sun-like stars, first detected by the Transiting Exoplanet Survey Satellite (*TESS*). TOI 694 b has an orbital period of 48.05131±0.00019 days and eccentricity of 0.51946±0.00081, and we derive a mass of 89.0±5.3 $M_{\rm Jup}$ (0.0849±0.0051 $M_{\odot}$) and radius of 1.111±0.017 $R_{\rm Jup}$ (0.1142±0.0017 $R_{\odot}$). TIC 220568520 b has an orbital period of 18.55769±0.00039 days and eccentricity of 0.0964±0.0032, and we derive a mass of 107.2±5.2 $M_{\rm Jup}$ (0.1023±0.0050 $M_{\odot}$) and radius of 1.248±0.018 $R_{\rm Jup}$ (0.1282±0.0019 $R_{\odot}$). Both binary companions lie close to and above the Hydrogen burning mass threshold that separates brown dwarfs and the lowest mass stars, with TOI 694 b being 2-σ above the canonical mass threshold of 0.075 $M_{\odot}$. The relatively long periods of the systems mean that the magnetic fields of the low-mass companions are not expected to inhibit convection and inflate the radius, which according to one leading theory is common in similar objects residing in short-period tidally-synchronized binary systems. Indeed we do not find radius inflation for these two objects when compared to theoretical isochrones. These two new objects add to the short but growing list of low-mass stars with well-measured masses and radii, and highlight the potential of the *TESS* mission for detecting such rare objects orbiting bright stars.

Subject headings: Low mass stars, M dwarfs, Eclipsing binaries, stars: individual (TOI 694, TIC 55383975, TIC 220568520)

[1] Department of Physics and Kavli Institute for Astrophysics and Space Research, Massachusetts Institute of Technology, Cambridge, MA 02139, USA
[2] Observatoire astronomique de l´Université de Genève, 51 Chemin des Maillettes, 1290 Versoix, Switzerland
[3] Harvard-Smithsonian Center for Astrophysics, 60 Garden Street, Cambridge, MA 02138, USA
[4] Facultad de Ingeniería y Ciencias, Universidad Adolfo Ibáñez, Av. Diagonal las Torres 2640, Peñalolén, Santiago, Chile
[5] Millennium Institute for Astrophysics, Chile
[6] Dunlap Institute for Astronomy and Astrophysics, University of Toronto, 50 St. George Street, Toronto, Ontario M5S 3H4, Canada
[7] Vanderbilt University, Department of Physics & Astronomy, 6301 Stevenson Center Lane, Nashville, TN 37235, USA
[8] Research School of Astronomy and Astrophysics, Australian National University, Canberra, ACT 2611, Australia
[9] Max-Planck-Institut für Astronomie, Königstuhl 17, 69117 Heidelberg, Germany
[10] Department of Physics and Astronomy, The University of North Carolina at Chapel Hill, Chapel Hill, NC 27599-3255, USA
[11] Physics and Astronomy Department, Georgia State University, Atlanta, GA 30302, USA
[12] RECONS Institute, Chambersburg, PA, USA
[13] Earth & Planets Laboratory, Carnegie Institution for Science, 5241 Broad Branch Road, NW, Washington, DC 20015, USA
[14] Center for Astrophysics | Harvard & Smithsonian, 60 Garden St, Cambridge, MA 02138, USA
[15] Department of Astrophysical Sciences, Princeton University, Princeton, NJ 08544, USA
[16] Department of Earth, Atmospheric, and Planetary Sciences, Massachusetts Institute of Technology, Cambridge, MA 02139, USA
[17] Department of Aeronautics and Astronautics, MIT, 77 Massachusetts Avenue, Cambridge, MA 02139, USA
[18] NASA Ames Research Center, Moffett Field, CA 94035, USA
[19] Department of Astronomy, Wesleyan University, Middletown, CT 06459, USA
[20] NASA Goddard Space Flight Center, 8800 Greenbelt Road, Greenbelt, MD 20771, USA
[21] SETI Institute, Mountain View, CA 94043, USA
[A] Juan Carlos Torres Fellow
[B] NSF Graduate Research Fellow

On-sky commissioning of MAROON-X: A new precision radial velocity spectrograph for Gemini North

Andreas Seifahrt[a], Jacob L. Bean[a], Julian Stürmer[a,b], David Kasper[a], Luke Gers[c], Christian Schwab[d], Mathias Zechmeister[e], Guðmundur Stefánsson[f], Ben Montet[g], Leonardo A. Dos Santos[a,h], Alison Peck[i], John White[i], and Eduardo Tapia[i]

[a]The University of Chicago, Chicago, United States
[b]Landessternwarte Heidelberg, Heidelberg, Germany
[c]W. M. Keck Observatory, Kamuela, United States
[d]Macquarie University, Sydney, Australia
[e]Georg-August-Universität Göttingen, Göttingen, Germany
[f]Princeton University, Princeton, United States
[g]University of New South Wales (UNSW), Sydney, Australia
[h]Observatoire de l'Université de Genève, Versoix, Switzerland
[i]Gemini Observatory, Hilo, United States

ABSTRACT

MAROON-X is a fiber-fed, red-optical, high precision radial velocity spectrograph recently commissioned at the Gemini North telescope on Mauna Kea, Hawai'i. With a resolving power of 85,000 and a wavelength coverage of 500–920 nm, it delivers radial velocity measurements for late K and M dwarfs with sub-50 $\mathrm{cm\,s^{-1}}$ precision. MAROON-X is currently the only optical EPRV spectrograph on a 8 m-class telescope in the northern hemisphere and the only EPRV instrument on a large telescope with full access by the entire US community. We report here on the results of the commissioning campaign in December 2019 and early science results.

Keywords: Gemini Observatory, EPRV, Radial velocity, Exoplanets, Echelle spectrograph, Optical fibers, Pupil slicer

1. INTRODUCTION

Our team at The University of Chicago has recently commissioned a new red-optical (500 – 920 nm), high-resolution ($\mathrm{R} \simeq 85{,}000$) radial velocity (RV) spectrograph (named "MAROON-X") that was designed explicitly for the purpose of following up small transiting planets around mid to late M dwarfs with sub-m $\mathrm{s^{-1}}$ RV precision.

MAROON-X was installed at the Gemini North Observatory in May 2019 and saw first light in September 2019. About 20 hours of commissioning and science verification observations were performed in December 2019. The first year of operations was impacted by the COVID-19 pandemic which did not allow for site visits in order to complete all aspects of the commissioning. Notwithstanding, regular science observations have started in May 2020 and we conducted them remotely from Chicago. Despite the incomplete commissioning, a number of successful observing runs allow us to report on important performance figures of the instrument, including the capability to obtain sub-m $\mathrm{s^{-1}}$ precision RVs in the first few months of the instrument's operation.

Although MAROON-X is currently classified as a Visiting Instrument*, it is essentially permanently installed at Gemini North. The instrument was first offered to the Gemini community in the 2020B Call for Proposals, and demand for the instrument skyrocketed with the 2021A CfP.

In the following sections we provide a brief overview of the project timeline, update the as-built specifications of the instrument, discuss its current performance, including an example of an early scientific result highlighting the excellent RV precision delivered by MAROON-X, and present our plans for further improvements in 2021.

Further author information: E-mail: seifahrt@uchicago.edu
*See https://www.gemini.edu/instrumentation/current-instruments/maroon-x for more information.

Draft version October 20, 2020
Typeset using LaTeX default style in AASTeX62

The Hubble PanCET Program: A Metal-rich Atmosphere for the Inflated Hot Jupiter HAT-P-41b

Kyle B. Sheppard,[1,2] Luis Welbanks,[3] Avi M. Mandell,[2] Nikku Madhusudhan,[3] Nikolay Nikolov,[4] Drake Deming,[1] Gregory W. Henry,[5] Michael H. Williamson,[5] David K. Sing,[6,7] Mercedes López-Morales,[8] Jegug Ih,[1] Jorge Sanz-Forcada,[9] Panayotis Lavvas,[10] Gilda E. Ballester,[11] Thomas M. Evans,[12] Antonio García Muñoz,[13] and Leonardo A. dos Santos[14]

[1] *Department of Astronomy, University of Maryland at College Park, College Park, MD, 20742, USA*
[2] *Solar System Exploration Division, NASA's Goddard Space Flight Center, Greenbelt, MD 20771, USA*
[3] *Institute of Astronomy, University of Cambridge, Madingley Road Cambridge CB3 0HA, UK*
[4] *Space Telescope Science Institute, 3700 San Martin Drive, Baltimore, MD 21218, USA*
[5] *Center of Excellence in Information Systems, Tennessee State University, Nashville, TN 37209, USA*
[6] *Department of Physics & Astronomy, Johns Hopkins University, Baltimore, MD 21218, USA*
[7] *Department of Earth & Planetary Sciences, Johns Hopkins University, Baltimore, MD 21218, USA*
[8] *Center for Astrophysics | Harvard & Smithsonian, 60 Garden Street, Cambridge, MA 01238, USA*
[9] *Centro de Astrobiología (CSIC-INTA), Spain*
[10] *Groupe de Spectrométrie Moleculaire et Atmosphérique, Université de Reims Champagne Ardenne, Reims, France*
[11] *Lunar & Planetary Laboratory, Department of Planetary Sciences, University of Arizona, Tucson, AZ, USA*
[12] *Kavli Institute for Astrophysics and Space Research, Massachusetts Institute of Technology, 77 Massachusetts Avenue, 37-241, Cambridge, MA 02139, USA*
[13] *Zentrum für Astronomie und Astrophysik, Technische Universität Berlin, Berlin, Germany*
[14] *Observatoire Astronomique de lÚniversité de Geneve, 51 chemin des Maillettes, 1290 Versoix, Switzerland*

ABSTRACT

We present a comprehensive analysis of the 0.3–5 μm transit spectrum for the inflated hot Jupiter HAT-P-41b. The planet was observed in transit with Hubble STIS and WFC3 as part of the Hubble Panchromatic Comparative Exoplanet Treasury (PanCET) program, and we combine those data with warm *Spitzer* transit observations. We extract transit depths from each of the data sets, presenting the STIS transit spectrum (0.29–0.93 μm) for the first time. We retrieve the transit spectrum both with a free-chemistry retrieval suite (AURA) and a complementary chemical equilibrium retrieval suite (PLATON) to constrain the atmospheric properties at the day-night terminator. Both methods provide an excellent fit to the observed spectrum. Both AURA and PLATON retrieve a metal-rich atmosphere for almost all model assumptions (most likely O/H ratio of $\log_{10} Z/Z_\odot = 1.46^{+0.53}_{-0.68}$ and $\log_{10} Z/Z_\odot = 2.33^{+0.23}_{-0.25}$, respectively); this is driven by a 4.9-σ detection of H_2O as well as evidence of gas absorption in the optical (>2.7-σ detection) due to Na, AlO and/or VO/TiO, though no individual species is strongly detected. Both retrievals determine the transit spectrum to be consistent with a clear atmosphere, with no evidence of haze or high-altitude clouds. Interior modeling constraints on the maximum atmospheric metallicity ($\log_{10} Z/Z_\odot < 1.7$) favor the AURA results. The inferred elemental oxygen abundance suggests that HAT-P-41b has one of the most metal-rich atmospheres of any hot Jupiters known to date. Overall, the inferred high metallicity and high inflation make HAT-P-41b an interesting test case for planet formation theories.

Keywords: Exoplanet Atmospheres, individual objects – HAT-P-41b

1. INTRODUCTION

Transit spectroscopy has been fundamental in understanding the physics and chemistry of hot exoplanet atmospheres. Transit observations with the Hubble Space Telescope (HST) and the *Spitzer* Space Telescope have been

Corresponding author: Kyle Sheppard
kshep23@umd.edu

A&A 650, A73 (2021)
https://doi.org/10.1051/0004-6361/202140487

Astronomy & Astrophysics

The *Hubble* PanCET program: long-term chromospheric evolution and flaring activity of the M dwarf host GJ 3470⋆

V. Bourrier[1], L. A. dos Santos[2], J. Sanz-Forcada[2], A. García Muñoz[7], G. W. Henry[6], P. Lavvas[10], A. Lecavelier[9], M. López-Morales[11], T. Mikal-Evans[8], D. K. Sing[4,5], H. R. Wakeford[3], and D. Ehrenreich[1]

[1] Observatoire Astronomique de l'Université de Genève, Chemin Pegasi 51b, 1290 Versoix, Switzerland
e-mail: vincent.bourrier@unige.ch
[2] Centro de Astrobiologia (CSIC-INTA), ESAC Campus, PO Box 78, 28691 Villanueva de la Canada, Madrid, Spain
[3] School of Physics, University of Bristol, HH Wills Physics Laboratory, Tyndall Avenue, Bristol BS8 1TL, UK
[4] Department of Earth & Planetary Sciences, Johns Hopkins University, Baltimore, MD, USA
[5] Department of Physics & Astronomy, Johns Hopkins University, Baltimore, MD, USA
[6] Center of Excellence in Information Systems, Tennessee State University, Nashville, TN 37209, USA
[7] AIM, CEA, CNRS, Université Paris-Saclay, Université de Paris, 91191 Gif-sur-Yvette, France
[8] Kavli Institute for Astrophysics and Space Research, Massachusetts Institute of Technology, Cambridge, MA, USA
[9] Sorbonne Université, CNRS, UMR 7095, Institut d'Astrophysique de Paris, 98bis bd Arago, 75014 Paris, France
[10] Groupe de Spectrométrie Moleculaire et Atmosphérique, Université de Reims Champagne Ardenne, Reims, France
[11] Center for Astrophysics, Harvard & Smithsonian, 60 Garden Street, Cambridge, MA 01238, USA

Received 3 February 2021 / Accepted 11 March 2021

ABSTRACT

Neptune-size exoplanets seem particularly sensitive to atmospheric evaporation, making it essential to characterize the stellar high-energy radiation that drives this mechanism. This is particularly important with M dwarfs, which emit a large and variable fraction of their luminosity in the ultraviolet and can display strong flaring behavior. The warm Neptune GJ 3470b, hosted by an M2 dwarf, was found to harbor a giant exosphere of neutral hydrogen thanks to three transits observed with the *Hubble* Space Telescope Imaging Spectrograph (HST/STIS). Here we report on three additional transit observations from the Panchromatic Comparative Exoplanet Treasury program, obtained with the HST Cosmic Origin Spectrograph. These data confirm the absorption signature from GJ 3470b's exosphere in the stellar Lyman-α line and demonstrate its stability over time. No planetary signatures are detected in other stellar lines, setting a 3σ limit on GJ 3470b's far-ultraviolet (FUV) radius at 1.3 times its Roche lobe radius. We detect three flares from GJ 3470. They show different spectral energy distributions but peak consistently in the Si III line, which traces intermediate-temperature layers in the transition region. These layers appear to play a particular role in GJ 3470's activity as emission lines that form at lower or higher temperatures than Si III evolved differently over the long term. Based on the measured emission lines, we derive synthetic X-ray and extreme-ultraviolet (X+EUV, or XUV) spectra for the six observed quiescent phases, covering one year, as well as for the three flaring episodes. Our results suggest that most of GJ 3470's quiescent high-energy emission comes from the EUV domain, with flares amplifying the FUV emission more strongly. The neutral hydrogen photoionization lifetimes and mass loss derived for GJ 3470b show little variation over the epochs, in agreement with the stability of the exosphere. Simulations informed by our XUV spectra are required to understand the atmospheric structure and evolution of GJ 3470b and the role played by evaporation in the formation of the hot-Neptune desert.

Key words. techniques: spectroscopic – planets and satellites: atmospheres – planets and satellites: individual: GJ 3470 – ultraviolet: stars – stars: chromospheres

1. Introduction

High-energy stellar radiation plays an important role in the structure and chemistry of exoplanetary atmospheres and their evolution. X-ray and extreme ultraviolet (XUV) radiation was proposed as the source for the hydrodynamical expansion (e.g., Vidal-Madjar et al. 2003; Lammer et al. 2003; Lecavelier des Etangs et al. 2004; García Muñoz 2007; Johnstone et al. 2015; Guo & Ben-Jaffel 2016) that leads to the evaporation of close-in hot Jupiters (Vidal-Madjar et al. 2003, 2004, 2008; Ehrenreich et al. 2008; Ben-Jaffel & Sona Hosseini 2010; Lecavelier des Etangs et al. 2010, 2012; Bourrier et al. 2013, 2020). The structure of the close-in planet population (e.g., Lecavelier des Etangs 2007; Davis & Wheatley 2009; Sanz-Forcada et al. 2010a,b; Szabó & Kiss 2011; Mazeh et al. 2016), direct observations (e.g., Ehrenreich et al. 2015; Bourrier et al. 2018a), and evolution simulations (e.g., Owen & Jackson 2012; Lopez & Fortney 2013; Jin et al. 2014; Kurokawa & Nakamoto 2014; Owen & Lai 2018) all suggest that Neptune-size exoplanets are much more sensitive than hot Jupiters to atmospheric escape. Giant clouds of neutral hydrogen, in particular, have been observed around the warm Neptunes GJ 436b (Kulow et al. 2014; Ehrenreich et al. 2015) and GJ 3470b (Bourrier et al. 2018a). Yet it is not clear whether the evaporation of this class of planets stems from

⋆ Synthetic XUV spectra of GJ 3470 associated with the quiescent phases and flaring episodes of the six epochs of observations (Fig. C.4) are only available at the CDS via anonymous ftp to cdsarc.u-strasbg.fr (130.79.128.5) or via http://cdsarc.u-strasbg.fr/viz-bin/cat/J/A+A/650/A73

Astronomy & Astrophysics manuscript no. Hburn_sub3
July 9, 2021

Populating the brown dwarf and stellar boundary: Five stars with transiting companions near the hydrogen-burning mass limit

Nolan Grieves[1,⋆], François Bouchy[1], Monika Lendl[1], Theron Carmichael[2,3], Ismael Mireles[4], Avi Shporer[5], Kim K. McLeod[6], Karen A. Collins[3], Rafael Brahm[7,8], Keivan G. Stassun[9], Sam Gill[10,11], Luke G. Bouma[12], Tristan Guillot[13], Marion Cointepas[1,14], Leonardo A. Dos Santos[1], Sarah L. Casewell[15], Jon M. Jenkins[16], Thomas Henning[17], Louise D. Nielsen[1], Angelica Psaridi[1], Stéphane Udry[1], Damien Ségransan[1], Jason D. Eastman[3], George Zhou[3], Lyu Abe[13], Abelkrim Agabi[13], Gaspar Bakos[12,18], David Charbonneau[3], Kevin I. Collins[18], Knicole D. Colon[19], Nicolas Crouzet[20], Georgina Dransfield[21], Phil Evans[22], Robert F. Goeke[5], Rhodes Hart[23], Jonathan M. Irwin[3], Eric L.N. Jensen[24], Andrés Jordán[7,8], John F. Kielkopf[25], David W. Latham[3], Wenceslas Marie-Sainte[26], Djamel Mékarnia[13], Peter Nelson[27], Samuel N. Quinn[3], Don J. Radford[28], David R. Rodriguez[29], Pamela Rowden[30], François–Xavier Schmider[13], Richard P. Schwarz[31], Jeffrey C. Smith[32,16], Chris Stockdale[33], Olga Suarez[13], Thiam-Guan Tan[34], Amaury H.M.J. Triaud[21], William Waalkes[35], and Geof Wingham[36]

(Affiliations can be found after the references)

Received XX; accepted XX

ABSTRACT

We report the discovery of five transiting companions near the hydrogen-burning mass limit in close orbits around main sequence stars originally identified by the Transiting Exoplanet Survey Satellite (TESS) as TESS Objects of Interest (TOIs): TOI-148, TOI-587, TOI-681, TOI-746, and TOI-1213. Using TESS and ground-based photometry as well as radial velocities from the CORALIE, CHIRON, TRES, and FEROS spectrographs, we found the companions have orbital periods between 4.8 and 27.2 days, masses between 77 and 98 M_{Jup}, and radii between 0.81 and 1.66 R_{Jup}. These targets have masses near the uncertain lower limit of hydrogen core fusion (~73-96 M_{Jup}), which separates brown dwarfs and low-mass stars. We constrained young ages for TOI-587 (0.2 ± 0.1 Gyr) and TOI-681 (0.17 ± 0.03 Gyr) and found them to have relatively larger radii compared to other transiting companions of a similar mass. Conversely we estimated older ages for TOI-148 and TOI-746 and found them to have relatively smaller companion radii. With an effective temperature of 9800 ± 200 K, TOI-587 is the hottest known main-sequence star to host a transiting brown dwarf or very low-mass star. We found evidence of spin-orbit synchronization for TOI-148 and TOI-746 as well as tidal circularization for TOI-148. These companions add to the population of brown dwarfs and very low-mass stars with well measured parameters ideal to test formation models of these rare objects, the origin of the brown dwarf desert, and the distinction between brown dwarfs and hydrogen-burning main sequence stars.

Key words. Stars: low-mass, brown dwarfs; binaries: eclipsing

1. Introduction

Brown dwarfs are objects with masses in between giant planets and low-mass stars. They are often defined with a lower limit of ~13 M_{Jup}, the approximate mass at which an object can begin to ignite deuterium fusion in its core, and with an upper limit of ~80 M_{Jup}, the approximate mass at which an object becomes sufficiently massive to fuse hydrogen nuclei into helium nuclei within its core: the principal characteristic of a main-sequence star. However, these boundaries are not clear-cut as the exact masses where deuterium and hydrogen fusion occur depend on the chemical composition of the object (e.g., Baraffe et al. 2002; Spiegel et al. 2011; Dieterich et al. 2014). A defining characteristic of brown dwarfs is their relative low occurrence rate ($\lessapprox$1%) in close orbits ($\lessapprox$5 AU) around main-sequence stars compared to giant planets and other stars, or the 'brown dwarf desert' (e.g., Marcy & Butler 2000; Grether & Lineweaver 2006; Sahlmann et al. 2011; Santerne et al. 2016; Grieves et al. 2017), with recent studies finding a dry desert for periods < 100 days (e.g., Kiefer et al. 2019, 2021).

The relative lack of brown dwarf companions may be related to a transition of the formation mechanisms required to form giant planets and low-mass stars. In this case, lower mass brown dwarfs may form similar to giant planets via core accretion (Pollack et al. 1996) or disk instability (Cameron 1978; Boss 1997) and higher mass brown dwarfs may form similar to stars from gravitational collapse and turbulent fragmentation of molecular clouds (Padoan & Nordlund 2004; Hennebelle & Chabrier 2008). The boundary of these formation mechanisms is unclear and certainly depends on an object's initial environment.

Using a statistical study of 62 brown dwarfs Ma & Ge (2014) found the "driest" part of the desert in the mass range $35\ M_{Jup} < M_b \sin i < 55\ M_{Jup}$ with periods less than 100 days. Ma & Ge (2014) also suggest 42.5 M_{Jup} may represent a transition between brown dwarfs that formed more similar to giant planets and those that formed more similar to main-sequence stars, as they found that brown dwarfs with masses above 42.5 M_{Jup} have an eccentricity distribution more consistent with binaries. However, Ma & Ge (2014) were limited by a small sample size and more brown dwarfs have been found even in the driest part of the desert (e.g., Persson et al. 2019; Carmichael et al. 2019). Other studies have also suggested two separate populations for lower

⋆ e-mail: nolangrieves@gmail.com

Draft version July 15, 2021
Typeset using LaTeX **twocolumn** style in AASTeX63

The Hubble PanCET program: Transit and Eclipse Spectroscopy of the Strongly Irradiated Giant Exoplanet WASP-76b

Guangwei Fu,[1] Drake Deming,[1] Joshua Lothringer,[2] Nikolay Nikolov,[2] David K. Sing,[2] Eliza M.-R. Kempton,[1] Jegug Ih,[1] Thomas M. Evans,[3] Kevin Stevenson,[4] H.R. Wakeford,[5] Joseph E. Rodriguez,[6] Jason D. Eastman,[6] Keivan Stassun,[7] Gregory W. Henry,[8] Mercedes López-Morales,[6] Monika Lendl,[9] Dennis M. Conti,[10] Chris Stockdale,[10] Karen Collins,[6] John Kielkopf,[11] Joanna K. Barstow,[12] Jorge Sanz-Forcada,[13] David Ehrenreich,[14] Vincent Bourrier,[14] and Leonardo A. dos Santos[14]

[1] *Department of Astronomy, University of Maryland, College Park, MD 20742, USA; gfu@astro.umd.edu*
[2] *Department of Physics and Astronomy, Johns Hopkins University, Baltimore, MD 21218, USA*
[3] *Kavli Institute for Astrophysics and Space Research, Massachusetts Institute of Technology, 77 Massachusetts Avenue, 37-241, Cambridge, MA 02139, USA*
[4] *Space Telescope Science Institute, 3700 San Martin Drive, Baltimore, MD 21218, USA*
[5] *School of Physics, University of Bristol, HH Wills Physics Laboratory, Tyndall Avenue, Bristol BS8 1TL, UK*
[6] *Center for Astrophysics — Harvard & Smithsonian, 60 Garden Street, Cambridge, MA 02138, USA*
[7] *Vanderbilt University, Department of Physics and Astronomy, 6301 Stevenson Center Lane, Nashville, TN 37235, USA*
[8] *Tennessee State University, Center of Excellence in Information Systems, Nashville, TN 37209, USA*
[9] *Space Research Institute, Austrian Academy of Sciences, Schmiedlstr. 6, A-8042 Graz, Austria*
[10] *American Association of Variable Star Observers, 49 Bay State Road, Cambridge, MA 02138, USA*
[11] *University of Louisville, 102 Natural Science Building, Louisville, KY 40292, USA*
[12] *The Open University, Walton Hall, Kents Hill, Milton Keynes, MK7 6AA, UK*
[13] *Centro de Astrobiología (CSIC-INTA),Spain*
[14] *Observatoire astronomique de l'Universitè de Genève, 51 chemin des Maillettes 1290 Versoix, Switzerland*

ABSTRACT

Ultra-hot Jupiters with equilibrium temperature greater than 2000K are uniquely interesting targets as they provide us crucial insights into how atmospheres behave under extreme conditions. This class of giant planets receives intense radiation from their host star and usually has strongly irradiated and highly inflated atmospheres. At such high temperature, cloud formation is expected to be suppressed and thermal dissociation of water vapor could occur. We observed the ultra-hot Jupiter WASP-76b with 7 transits and 5 eclipses using the Hubble Space Telescope (HST) and the Spitzer Space Telescope (*Spitzer*) for a comprehensive study of its atmospheric chemical and physical processes. We detected TiO and H_2O absorption in the optical and near-infrared transit spectrum. Additional absorption by a number of neutral and ionized heavy metals like Fe, Ni, Ti, and SiO help explain the short wavelength transit spectrum. The secondary eclipse spectrum shows muted water feature but a strong CO emission feature in Spitzer's 4.5 μm band indicating an inverted temperature pressure profile. We analyzed both the transit and eclipse spectra with a combination of self-consistent PHOENIX models and atmospheric retrieval (ATMO). Both spectra were well fitted by the self-consistent PHOENIX forward atmosphere model in chemical and radiative equilibrium at solar metallicity, adding to the growing evidence that both TiO/VO and NUV heavy metals opacity are prominent NUV-optical opacity sources in the stratospheres of ultra-hot Jupiters.

Keywords: planets and satellites: atmospheres - techniques: spectroscopic

1. INTRODUCTION

Transiting exoplanets can offer us detailed insights into their atmospheres during the transit and eclipse phases. When transiting in front of the parent star, the limb of planetary atmosphere filters out a portion of the starlight. The amplitude of that effect varies with wavelength, depending on the composition of the atmosphere. The spectral features of the upper exoplanetary atmosphere (∼1mbar) are thereby imprinted onto the stellar light. During the secondary eclipse, the planet passes behind the host star, and deep (10-100 mbar) thermal emission of the atmosphere can be measured via the total flux difference before and after the eclipse

B.2 Characterization of planet-hosting stars

During my doctorate I was also involved with the survey of exoplanets around Solar Twins (PI: J. Meléndez). In the following pages I list all the publications resulting from this collaboration. They encompass new discoveries about the chemical homogeneity, rotational evolution, and Li abundances of Sun-like stars, as well as the evolution of chemical abundances for Galactic-disk stars.

Draft version August 8, 2018
Typeset using LaTeX **twocolumn** style in AASTeX62

The Chemical Homogeneity of Sun-like Stars in the Solar Neighborhood

Megan Bedell,[1,2] Jacob L. Bean,[2] Jorge Meléndez,[3] Lorenzo Spina,[4,3] Ivan Ramírez,[5] Martin Asplund,[6] Alan Alves-Brito,[7] Leonardo dos Santos,[8,3] Stefan Dreizler,[9] David Yong,[6] TalaWanda Monroe,[10] and Luca Casagrande[6]

[1] *Center for Computational Astrophysics, Flatiron Institute, 162 5th Ave., New York, NY 10010, USA*
[2] *Department of Astronomy and Astrophysics, University of Chicago, 5640 S. Ellis Ave, Chicago, IL 60637, USA*
[3] *Departamento de Astronomia do IAG/USP, Universidade de São Paulo, Rua do Matão 1226, Cidade Universitária, 05508-900 São Paulo, SP, Brazil*
[4] *Monash Centre for Astrophysics, School of Physics and Astronomy, Monash University, VIC 3800, Australia*
[5] *Tacoma Community College, 6501 South 19th Street, Tacoma, Washington 98466, USA*
[6] *Research School of Astronomy and Astrophysics, The Australian National University, Cotter Road, Canberra, ACT 2611, Australia*
[7] *Universidade Federal do Rio Grande do Sul, Instituto de Física, Av. Bento Gonçalves 9500, Porto Alegre, RS, Brazil*
[8] *Observatoire de l'Université de Genève, 51 chemin des Maillettes, 1290 Versoix, Switzerland*
[9] *Institut für Astrophysik, Georg-August-Universität, Friedrich-Hund-Platz 1, 37077 Göttingen, Germany*
[10] *Space Telescope Science Institute, 3700 San Martin Drive, Baltimore, MD 21218, USA*

ABSTRACT

The compositions of stars are a critical diagnostic tool for many topics in astronomy such as the evolution of our Galaxy, the formation of planets, and the uniqueness of the Sun. Previous spectroscopic measurements indicate a large intrinsic variation in the elemental abundance patterns of stars with similar overall metal content. However, systematic errors arising from inaccuracies in stellar models are known to be a limiting factor in such studies, and thus it is uncertain to what extent the observed diversity of stellar abundance patterns is real. Here we report the abundances of 30 elements with precisions of 2% for 79 Sun-like stars within 100 parsecs. Systematic errors are minimized in this study by focusing on solar twin stars and performing a line-by-line differential analysis using high-resolution, high-signal-to-noise spectra. We resolve [X/Fe] abundance trends in galactic chemical evolution at precisions of 10^{-3} dex Gyr^{-1} and reveal that stars with similar ages and metallicities have nearly identical abundance patterns. Contrary to previous results, we find that the ratios of carbon-to-oxygen and magnesium-to-silicon in solar metallicity stars are homogeneous to within 10% throughout the solar neighborhood, implying that exoplanets may exhibit much less compositional diversity than previously thought. Finally, we demonstrate that the Sun has a subtle deficiency in refractory material relative to >80% of solar twins (at 2σ confidence), suggesting a possible signpost for planetary systems like our own.

Keywords: Sun: abundances, stars: abundances, stars: solar-type, techniques: spectroscopic

1. INTRODUCTION

The photosphere of a Sun-like star acts as a fossil record of the nebular cloud from which the star formed, making spectroscopic measurements of stellar compositions an informative probe of chemical evolution throughout the galaxy. Stellar compositions can also support exoplanet studies: because the star and its planets form side-by-side from the same primordial material, the relative compositions of stars that host different types of planets yield constraints on planet formation processes (e.g. Gonzalez 1997; Fischer & Valenti 2005; Thiabaud et al. 2015) and may even indicate the detailed physical properties of known planets (e.g. Dorn et al. 2015; Santos et al. 2015; Unterborn et al. 2014; Unterborn & Panero 2017).

Previous investigations on this topic indicate that stars with similar overall metal content display significant diversity in their elemental abundance patterns (Adibekyan et al. 2012; Bensby et al. 2014; Brewer & Fischer 2016). This implies a wide range in the possible

Corresponding author: Megan Bedell
E-mail: mbedell@flatironinstitute.org

Monthly Notices
of the
ROYAL ASTRONOMICAL SOCIETY

MNRAS **474,** 2580–2593 (2018)
Advance Access publication 2017 November 21

doi:10.1093/mnras/stx2938

The temporal evolution of neutron-capture elements in the Galactic discs

Lorenzo Spina,[1,2★] Jorge Meléndez,[1] Amanda I. Karakas,[2] Leonardo dos Santos,[1,3] Megan Bedell,[4,5] Martin Asplund,[6] Ivan Ramírez,[7] David Yong,[6] Alan Alves-Brito,[8] Jacob L. Bean[4] and Stefan Dreizler[9]

[1]*Universidade de São Paulo, IAG, Departamento de Astronomia, Rua do Matão 1226, São Paulo, 05509-900 SP, Brasil*
[2]*Monash Centre for Astrophysics, School of Physics and Astronomy, Monash University, VIC 3800, Australia*
[3]*Observatoire de l'Université de Genève, 51 chemin des Maillettes, CH-1290 Versoix, Switzerland*
[4]*Department of Astronomy & Astrophysics, 5640 S. Ellis Ave, Chicago, IL 60637, USA*
[5]*Center for Computational Astrophysics, Flatiron Institute, 162 5th Ave, New York, NY 10010, USA*
[6]*Research School of Astronomy and Astrophysics, The Australian National University, Cotter Road, Canberra, ACT 2611, Australia*
[7]*Tacoma Community College, 6501 South 19th Street, Tacoma, WA 98466-7400, USA*
[8]*Universidade Federal do Rio Grande do Sul, Instituto de Física, Av. Bento Gonçalves 9500, Porto Alegre, RS, Brazil*
[9]*Institut für Astrophysik, Georg-August Universität Göttingen, Wilhelmsplatz 1, D-37073, Göttingen, Germany*

Accepted 2017 November 9. Received 2017 November 9; in original form 2017 September 29

ABSTRACT

Important insights into the formation and evolution of the Galactic disc(s) are contained in the chemical compositions of stars. We analysed high-resolution and high signal-to-noise HARPS spectra of 79 solar twin stars in order to obtain precise determinations of their atmospheric parameters, ages (σ ∼0.4 Gyr) and chemical abundances (σ <0.01 dex) of 12 neutron-capture elements (Sr, Y, Zr, Ba, La, Ce, Pr, Nd, Sm, Eu, Gd and Dy). This valuable data set allows us to study the [X/Fe]-age relations over a time interval of ∼10 Gyr and among stars belonging to the thin and thick discs. These relations show that (i) the *s*-process has been the main channel of nucleosynthesis of *n*-capture elements during the evolution of the thin disc; (ii) the thick disc is rich in *r*-process elements which suggests that its formation has been rapid and intensive. In addition, the heavy (Ba, La, Ce) and light (Sr, Y, Zr) *s*-process elements revealed details on the dependence between the yields of AGB stars and the stellar mass or metallicity. Finally, we confirmed that both [Y/Mg] and [Y/Al] ratios can be employed as stellar clocks, allowing ages of solar twin stars to be estimated with an average precision of ∼0.5 Gyr.

Key words: stars: abundances – Galaxy: abundances – Galaxy: disc – Galaxy: evolution.

1 INTRODUCTION

The history of matter in galaxies is written in the chemical composition of stellar populations. Akin to archaeologists, who use fossils to infer the past of ancient civilizations, astronomers can decrypt the information locked into stellar spectra to trace the history of the Milky Way.

The pristine material from which our Galaxy has formed was extremely poor in metals. All the elements heavier than Li have been subsequently produced in stars through different sites of nucleosynthesis [e.g. Type II or Type Ia supernovae, asymptotic giant branch (AGB) stars], with their own unique pattern of species produced and delivered into the insterstellar medium (ISM). Due to this variety of channels, the abundance ratios of two species having different origin change with time and can be used to study the formation and evolution of stellar populations (e.g. Gilmore, Wyse & Kuijken 1989; Chiappini, Matteucci & Gratton 1997; Recio-Blanco et al. 2014; Rojas-Arriagada et al. 2016, 2017). Recent studies have shown that the knowledge of the relations between the abundance ratios and the stellar ages can provide insights on the variables that are controlling the evolution of our Galaxy, such as the star formation rate, the initial mass function, the mass and metallicity of the supernovae (SNe) progenitors and their yields (Haywood et al. 2015; Nissen 2015, 2016; Snaith et al. 2015; Battistini & Bensby 2016; Spina, Meléndez & Ramírez 2016a; Spina et al. 2016b).

These latter studies proceed along a well-defined path enabled by an increasingly precise abundance analysis of stars that aims to unravel the chemical enrichment history of the Galactic disc. In this context, the study of the elements heavier than zinc ($Z > 30$) play a crucial role, as they trace yields of a broad range of sites of nucleosynthesis with very different time-scales (Sneden, Cowan & Gallino 2008). These species are produced via neutron capture of isotopes heavier than iron: neutrons are captured by nuclei that, if unstable, can β decay transforming neutrons into protons. The group of elements that are synthesized through this process are

★ E-mail: lorenzo.spina@monash.esu

Monthly Notices
of the
ROYAL ASTRONOMICAL SOCIETY

MNRAS **485,** L68–L72 (2019)
Advance Access publication 2019 March 19

doi:10.1093/mnrasl/slz034

Constraining the evolution of stellar rotation using solar twins

Diego Lorenzo-Oliveira [1]★ Jorge Meléndez,[1] Jhon Yana Galarza,[1] Geisa Ponte [2] Leonardo A. dos Santos [3] Lorenzo Spina,[4] Megan Bedell [5] Iván Ramírez,[6] Jacob L. Bean[7] and Martin Asplund[8]

[1]*Departamento de Astronomia do IAG/USP, Universidade de São Paulo, Rua do Matão 1226, Cidade Universitária, 05508-900 São Paulo, SP, Brazil*
[2]*Observatório do Valongo, Universidade Federal do Rio de Janeiro, Ladeira do Pedro Antonio 43, CEP: 20080-090 Rio de Janeiro, RJ, Brazil*
[3]*Observatoire astronomique de l'Université de Genève, 51 chemin des Maillettes, CH-1290 Versoix, Switzerland*
[4]*Monash Centre for Astrophysics, School of Physics and Astronomy, Monash University, VIC 3800, Australia*
[5]*Center for Computational Astrophysics, Flatiron Institute, 162 5th Ave., New York, NY 10010, USA*
[6]*Tacoma Community College, 6501 South 19th Street, Tacoma, WA 98466, USA*
[7]*Department of Astronomy and Astrophysics, 5640 Ellis Ave., Chicago, IL 60637, USA*
[8]*Research School of Astronomy and Astrophysics, The Australian National University, Cotter Road, Weston, ACT 2611, Australia*

Accepted 2019 March 5. Received 2019 February 28; in original form 2019 January 14

ABSTRACT

The stellar rotation versus age relation is commonly considered a useful tool to derive reliable ages for Sun-like stars. However, in the light of *Kepler* data, the presence of apparently old and fast rotators that do not obey the usual gyrochronology relations led to the hypothesis of weakened magnetic breaking in some stars. In this letter, we constrain the solar rotation evolutionary track using solar twins. Predicted rotational periods as a function of mass, age, [Fe/H], and given critical Rossby number ($Ro_{\rm crit}$) were estimated for the entire rotational sample. Our analysis favours the smooth rotational evolution scenario and suggests that if the magnetic weakened breaking scenario takes place at all, it should arise after $Ro_{\rm crit} \gtrsim 2.29$ or ages $\gtrsim$5.3 Gyr (at 95 per cent confidence level).

Key words: Sun: rotation – stars: fundamental parameters – stars: rotation – stars: solar-type.

1 INTRODUCTION

Rotation-based ages of old Sun-like stars are rooted in a complex and intricate dependence on age, rotation, turbulent convection, structural variations, and mass-loss due to magnetized winds (Skumanich 1972; Reiners & Mohanty 2012; Guerrero et al. 2013; O'Fionnagáin & Vidotto 2018). Classically, the age-dating method that relies on this phenomenon assumes that the rotational periods ($P_{\rm rot}$) can be expressed in well-defined functions of the age and mass (or a proxy of it), the so-called gyrochronology relations (Barnes 2007; Mamajek & Hillenbrand 2008). These relations had successfully confirmed the paradigm of rotation-activity-age coupling that powers the global dynamo evolution along the main-sequence (Barnes 2007; do Nascimento et al. 2014; Vidotto et al. 2014; Lorenzo-Oliveira, Porto de Mello & Schiavon 2016; Lorenzo-Oliveira et al. 2018) and reproduced the main features observed in open clusters spanning a wide range of ages (Meibom et al. 2015).

Apart from this inspiring agreement, some of the old *Kepler* field stars show unexpected fast rotation, especially hotter ones with ages greater than 2–3 Gyr (Angus et al. 2015; Metcalfe, Egeland & van Saders 2016). This tension led to the idea that after a critical Rossby number ($Ro \equiv P_{\rm rot}/\tau_{\rm CZ}$, where $\tau_{\rm CZ}$ is the convective turnover time; Noyes et al. 1984) a drastic change of the stellar differential rotation (SDR) pattern might hamper the production and maintenance of magnetic field large-scale components over secular time-scales. One of the most important (and accessible) effects of this drastic transition would be the presence of old and fast rotating stars with reduced angular momentum loss caused by magnetized winds. However, recent observational results gave us alternative hints about the possible smooth nature of the Sun-like rotational evolution in the light of *Kepler* asteroseismic data (Benomar et al. 2018).

Motivated by this up-to-date discussion about the smooth nature of the age–rotation relations, we can ask ourselves: *what solar twins can tell us about the solar rotational evolution*? This letter uses solar twins to evaluate a recent claim (van Saders et al. 2016) about the solar rotational transition at a given critical Rossby number. Section 2 describes our working sample, selection criteria of solar twin rotators and determination of $P_{\rm rot}$ through activity time series. In Section 3 we discuss the age-rotation evolution of solar twins and the suitability of standard rotational evolution models. The conclusions are drawn in Section 4.

★ E-mail: diegolorenzo@usp.br

Monthly Notices
of the
ROYAL ASTRONOMICAL SOCIETY

MNRAS **485,** 4052–4059 (2019)
Advance Access publication 2019 March 8

doi:10.1093/mnras/stz681

The Li–age correlation: the Sun is unusually Li deficient for its age

M. Carlos,[1★] J. Meléndez,[1] L. Spina,[2] L. A. dos Santos,[3] M. Bedell,[4] I. Ramirez,[5] M. Asplund,[6] J. L. Bean,[7] D. Yong,[6] J. Yana Galarza[1] and A. Alves-Brito[8]

[1]*Departamento de Astronomia, IAG, Universidade de São Paulo, Rua do Matão 1226, São Paulo 05509-900, Brazil*
[2]*Monash Centre for Astrophysics, School of Physics and Astronomy, Monash University, VIC 3800, Australia*
[3]*Observatoire de l'Université de Genéve, 51 chemin des Maillettes, CH-1290 Versoix, Switzerland*
[4]*Center for Computational Astrophysics, Flatiron Institute, 162 5th Avenue, New York, NY 10010, USA*
[5]*Tacoma Community College, 6501 South 19th Street, Tacoma, WA 98466-7400, USA*
[6]*Research School of Astronomy and Astrophysics, The Australian National University, Cotter Road, Canberra, ACT 2611, Australia*
[7]*Department of Astronomy and Astrophysics, 5640 S. Ellis Ave, Chicago, IL 60637, USA*
[8]*Instituto de Física, Universidade Federal do Rio Grande do Sul, Av. Bento Gonçalves 9500, 90040-060 Porto Alegre, RS, Brazil*

Accepted 2019 March 5. Received 2019 February 21; in original form 2019 January 8

ABSTRACT

This work aims to examine in detail the depletion of lithium in solar twins to better constrain stellar evolution models and investigate its possible connection with exoplanets. We employ spectral synthesis in the region of the asymmetric 6707.75 Å Li I line for a sample of 77 stars plus the Sun. As in previous works based on a smaller sample of solar twins, we find a strong correlation between Li depletion and stellar age. In addition, for the first time we show that the Sun has the lowest Li abundance in comparison with solar twins at similar age (4.6 ± 0.5 Gyr). We compare the lithium content with the condensation temperature slope for a subsample of the best solar twins and determine that the most lithium-depleted stars also have fewer refractory elements. We speculate whether the low lithium content in the Sun might be related to the particular configuration of our Solar system.

Key words: techniques: spectroscopic – Sun: abundances – stars: abundances – stars: evolution – planetary systems – stars: solar-type.

1 INTRODUCTION

The importance of lithium in astronomy ranges from cosmological to stellar evolution questions, and could even be related to exoplanets. The *cosmological Li problem* is related to the mismatch between the Li content produced during big bang nucleosynthesis and the one measured in old halo dwarf stars (Spite & Spite 1982); a disagreement of about a factor of four is found (Ryan, Norris & Beers 1999; Asplund et al. 2006; Bonifacio et al. 2007; Matsuno et al. 2017).

In the context of Galactic chemical evolution, Li abundances obtained in thin disc stars indicate a production of this element at this component of the Galaxy, with the production mechanisms still in debate (Ramírez et al. 2012; Bensby & Lind 2018; Cescutti & Molaro 2018; Fu et al. 2018).

Regarding stellar evolution, the Li-rich giant problem is related to how some observed giant stars have higher content of Li despite the expectation that this element is destroyed during their first dredge-up phase due to its fragile nature (Casey et al. (Aguilera-Gómez et al. 2016; Casey et al. 2016), as seen in standard stellar evolution models. The work of Charbonnel & Lagarde (2010) presented a non-standard stellar evolution model considering thermohaline instability and rotation-induced mixing and they were able to reproduce the Li behaviour in red giants. The non-standard stellar nucleosynthesis presented in Yan et al. (2018) might explain the observations of Li-rich giants in a particular short stellar evolution phase. See also recent papers by Deepak & Reddy (2019) and Casey et al. (2019).

Despite many observational and theoretical efforts, the origin of the observed Li depletion in solar-like stars is not well established yet and remains hotly debated in the literature. Albeit likely related to internal depletion during the lifetime of the star, more Li abundances are necessary to better constrain non-standard evolution stellar models that take into consideration different internal motions of stars. The extra mixing is necessary since Li is destroyed through the reaction ^{7}Li(p, α)α at temperatures of $\sim 2.5 \times 10^6$ K near the base of the convective envelope in sun-like stars. Those non-standard evolution models can include gravity waves (Charbonnel & Talon 2005), rotation-induced mixing and diffusion (Do Nascimento et al. 2009), rotation-driven turbulent diffusion (Denissenkov 2010), and overshooting and gravitational settling (Xiong & Deng 2009).

Several works in the literature discuss the factors influencing lithium depletion in solar-type stars such as occurrence of planets (Delgado Mena et al. 2014), binarity (Zahn 1994; Beck et al. 2017),

★ E-mail: marilia.carlos@usp.br

Draft version August 10, 2021
Typeset using LaTeX **modern** style in AASTeX63

Radial velocity precision of ESPRESSO through the analysis of the solar twin HIP 11915

Yuri Netto,[1] Diego Lorenzo-Oliveira,[1] Jorge Meléndez,[1] Jhon Yana Galarza,[1] Raphaëlle D. Haywood,[2] Lorenzo Spina,[3] and Leonardo A. dos Santos[4]

[1] *Universidade de São Paulo, Instituto de Astronomia, Geofísica e Ciências Atmosféricas (IAG), Departamento de Astronomia, Rua do Matão 1226, Cidade Universitária, 05508-900, SP, Brazil*
[2] *Astrophysics Group, University of Exeter, Exeter EX4 4QL, UK*
[3] *INAF Osservatorio Astronomico di Padova, vicolo dell'Osservatorio 5, 35122, Padova, Italy*
[4] *Observatoire Astronomique de l'Université de Genève, Chemin Pegasi 51, 1290 Versoix, Switzerland*

(Received xxxx; Revised yyyy; Accepted zzzz)

ABSTRACT

Different stellar phenomena affect radial velocities (RVs), causing variations large enough to make it difficult to identify planet signals from the stellar variability. RV variations caused by stellar oscillations and granulation can be reduced through some methods, but the impact of rotationally modulated magnetic activity on RV, due to stellar active regions is harder to correct. New instrumentation promises an improvement in precision of one order of magnitude, from about 1 m/s, to about 10 cm/s. In this context, we report our first results from 24 spectroscopic ESPRESSO/VLT observations of the solar twin star HIP 11915, spread over 60 nights. We used a Gaussian Process approach and found for HIP 11915 a RV residual RMS scatter of about 20 cm s^{-1}, representing an upper limit for the performance of ESPRESSO.

Keywords: techniques: radial velocities - methods: data analysis - stars: individual: HIP 11915

1. INTRODUCTION

The radial velocity (RV) method has been used to discover exoplanets, or to confirm exoplanets detected by the transit method and estimate their mass. Earth analogs orbiting the habitable zone of a Sun-like star, induce a RV signal on the order of 10 cm s^{-1} (e.g., Langellier et al. 2020). However, the measured RV variations are not entirely due to planets; stellar activity, oscillations and granulation also cause changes in RV

Corresponding author: Yuri Netto
yurinetto@usp.br